Ph.D. DISSERTATION

Channel Acquisition and Beam Management for Millimeter and Terahertz Communications

밀리미터파 및 테라헤르츠 통신을 위한 채널 획득 및 빔 관리 기법

BY

SEUNGNYUN KIM

AUGUST 2023

DEPARTMENT OF ELECTRICAL AND
COMPUTER ENGINEERING
COLLEGE OF ENGINEERING
SEOUL NATIONAL UNIVERSITY

Ph.D. DISSERTATION

Channel Acquisition and Beam Management for Millimeter and Terahertz Communications

밀리미터파 및 테라헤르츠 통신을 위한 채널 획득 및 빔 관리 기법

BY

SEUNGNYUN KIM

AUGUST 2023

DEPARTMENT OF ELECTRICAL AND
COMPUTER ENGINEERING
COLLEGE OF ENGINEERING
SEOUL NATIONAL UNIVERSITY

Channel Acquisition and Beam Management for Millimeter and Terahertz Communications

밀리미터파 및 테라헤르츠 통신을 위한 채널 획득 및 빔 관리 기법

지도교수 심 병 효

이 논문을 공학박사 학위논문으로 제출함

2023년 8월

서울대학교 대학원

전기 정보 공학부

김 승 년

김승년의 공학박사 학위 논문을 인준함

2023년 8월

위 원 장:	김 성 철
부위원장:	심 병 효
위 원:	이 경 한
위 원:	최 준 원
위 원:	이 병 주

Abstract

Recently, terahertz (THz) communications have received much attention to alleviate spectrum bottleneck and support high data rates for 6G wireless communications. Using the abundant spectrum resource in the THz frequency band ($0.1 \sim 10\,$THz), THz communications can support immersive mobile services such as digital twin, metaverse realized by XR devices, and high-fidelity mobile holographic displays. Well-known drawback of the THz communications is the severe attenuation of the signal power caused by the high diffraction and penetration losses and atmospheric absorption. To deal with the problem, a beamforming technique realized by the massive multiple-input multiple-output (MIMO) has been widely used. Since the beamforming gain is maximized only when the beams are properly aligned with the signal propagation paths, the base station (BS) needs to acquire the accurate channel information.

In the first part of the dissertation, we study a channel feedback technique for the frequency-division-duplexing (FDD)-based cell-free mmWave and THz systems. Cell-free system where a group of base stations (BSs) cooperatively serves users has received much attention as a promising technology for the future wireless systems. In order to maximize the cooperation gain in the cell-free systems, acquisition of downlink channel state information (CSI) at the BSs is crucial. While this task is relatively easy for the time division duplexing (TDD) systems due to the channel reciprocity, it is not easy for the frequency division duplexing (FDD) systems due to the CSI feedback overhead. This issue is even more pronounced in the cell-free systems since the user needs to feed back the CSIs of multiple BSs. In our work, we propose a novel feedback reduction technique for the FDD-based cell-free systems. Key feature of the proposed technique is to choose a few dominating paths and then feed back the path gain information (PGI) of the chosen paths. By exploiting the property that the angles of departure (AoDs) are quite similar in the uplink and downlink channels (this property is referred to as angle reciprocity), the BSs obtain the AoDs directly from the uplink pilot signal.

In the second part of the dissertation, we study a channel estimation technique for reconfigurable intelligent surface-assisted THz systems. Recently, an RIS that controls the reflection characteristics of incident signals has received a great deal of attention. To make the most of the RIS-aided systems, an acquisition of RIS reflected channel information at the base station (BS) is crucial. However, this task is by no means easy due to the pilot overhead induced by the large number of reflecting elements. In our work, we propose an efficient channel estimation and phase shift control technique reducing the pilot overhead of the RIS-aided mmWave systems. Key idea of the proposed scheme is to decompose the RIS reflected channel into three major components, i.e., static BS-RIS angles, quasi-static RIS-UE angles, and time-varying BS-RIS-UE path gains, and then estimate them in different time scales. By estimating the BS-RIS and RIS-UE angles occasionally and estimating only the path gains frequently, the proposed scheme achieves a significant reduction on the pilot overhead. Further, by optimizing the phase shifts using the channel components with relatively long coherence time, we can improve the channel estimation accuracy.

In the third part of the dissertation, we study a channel estimation technique for time-division-duplexing (TDD)-based THz ultra-massive (UM) multiple-input multiple-output (MIMO) systems. THz UM-MIMO system is envisioned as a key technology to support ever-increasing data rates in 6G communication systems. To make the most of THz UM-MIMO systems, acquisition of accurate channel information is crucial. However, the THz channel acquisition is not easy due to the humongous pilot overhead that scales linearly with the number of antennas. In our work, we propose a novel deep learning (DL)-based channel acquisition technique for the THz UM-MIMO systems. By learning the complicated mapping function between the received pilot signal and the sparse channel parameters (e.g., angles, distances, path gains) using Transformer, the proposed scheme can make a fast yet accurate channel estimation with a relatively small amount of pilot resources. Moreover, using the attention mechanism of Transformer, we can promote the correlation structure of the received pilot signals in the feature extraction, thereby improving the channel parameter estimation quality significantly.

In the fourth part of the dissertation, we study a beam management technique for wideband THz systems. One main difficulty of the THz communications is the severe attenuation of signal power caused by the high diffraction and penetration losses and atmospheric absorption. To compensate for the severe path loss, a beamforming technique realized by the massive multiple-input multiple-output (MIMO) has been widely used. Since the beamforming gain is maximized only when the beams are appropriately aligned with the signal propagation paths, acquisition of accurate beam directions is of great importance. A major issue of the conventional beam management schemes is the considerable latency being proportional to the number of training beams. In this chapter, we propose a THz beam management technique that simultaneously generates multiple frequency-dependent beams using the true time delay (TTD)-based phase shifters. By closing the gap between the frequency-dependent beamforming vectors and the desired directional beamforming vectors using the TTD-based signal propagation network called intensifier, we generate very sharp training beams maximizing the beamforming gain.

keywords: 6G, wireless communications, terahertz, channel estimation, channel feedback, beam management
student number: 2016-25925

Contents

List of Tables

List of Figures

Chapter 1

Introduction

1.1 Background

Recently, terahertz (THz) communications have received much attention to alleviate spectrum bottleneck and support high data rates for 6G wireless communications. Using the abundant spectrum resource in the THz frequency band ($0.1 \sim 10\,\mathrm{THz}$), THz communications can support immersive mobile services such as digital twin, metaverse realized by XR devices, and high-fidelity mobile holographic displays. Well-known drawback of the THz communications is the severe attenuation of the signal power caused by the high diffraction and penetration losses and atmospheric absorption. To deal with the problem, a beamforming technique realized by the massive multiple-input multiple-output (MIMO) has been widely used. Since the beamforming gain is maximized only when the beams are properly aligned with the signal propagation paths, the base station (BS) needs to acquire the accurate channel information.

1.1.1 Terahertz Channel Characteristics

In this subsection, we discuss a few useful properties of THz channel. We first explain the LoS-dominant property that the transmit energy is mostly concentrated on the LoS path in the THz channel and then explain the THz near-field effect that the channel is a function of the communication distance.

Due to the high directivity and path loss, the scattering and refraction of signal are negligible in the THz band so that the LoS path becomes the dominant means of propagation. Two major factors contributing to the LoS-dominant property of THz channel are 1) highly directional propagation of THz signal and 2) significant power gap between the LoS and NLoS path signals. First, since the power of diffracted signal decreases sharply with the signal frequency, diffraction is almost negligible in the high frequency band like THz band, meaning that the signal power is concentrated on a few dominant paths. Indeed, from the extensive measurements on the THz channel, it has been shown that the number of dominant paths in 256-antenna UM-MIMO systems operating at $0.3\,$THz band is less than 4 [1]. Second, the power gap between the LoS and NLoS path signals is significant due to the huge reflection and diffuse scattering losses. The reflection of signal can be roughly categorized into two types: 1) specular reflection where the signal is reflected to a definite angle at smooth surfaces and 2) diffuse scattering where the signal is reflected to all directions at rough surfaces. In the THz band, the wavelength (e.g., $100\,\mu$m in $3\,$THz band) is smaller than the surface roughness[1] of objects (e.g., the roughness of concrete wall is $300 \sim 1000\,\mu$m) so that the diffuse scattering is the dominant means of reflection. Since the reflected signal is not focused on a specific direction but scattered over an area, the power of reflected signal in the NLoS path is much smaller than that of the LoS path signal. For example, the Rician K-factor, a ratio of the power of the strongest path over the sum of powers of other paths, is around $20\,$dB in $0.4\,$THz band [2], which implies that the power of LoS path signal is almost 100 times stronger than that of NLoS path signals.

Due to the short communication distance and the extremely large number of antennas in the THz systems, the THz channel is categorized as the near-field channel where the EM radiation is modeled as spherical waves. In the near-field THz channel, the array steering vector is expressed as a joint function of the azimuth/elevation angles

---

[1] The surface roughness is defined as the standard deviation of surface heights from the mean line.

and the distance. In general, the EM radiation field can be divided into two categories: 1) far-field region where the EM radiation can be approximated as plane waves and 2) near-field region where the EM radiation is modeled by the spherical waves. To distinguish two regions, the Rayleigh distance $Z = \frac{N^2\lambda}{2}$ (N is the number of antennas and λ is the signal wavelength) is widely used. In the THz systems, due to the extremely large number of antennas, the Rayleigh distance can be up to a hundred meters, covering most of the small cell area [3]. For example, in the 256-antenna UM-MIMO systems operating at $0.1\,$THz band, the Rayleigh distance is around $100\,$m. In the near-field region, the signal wavefronts have spherical shapes so that the phase delay between two adjacent antenna elements is affected not only by the azimuth angle θ, the elevation angle φ, but also the distance r. Thus, the near-field array steering vector should be expressed as a function of spherical coordinates (r, θ, φ).

1.1.2 Terahertz Channel Estimation

In FDD systems, where separate frequency bands are allocated for uplink and downlink communication, the downlink channel estimation process plays a vital role in establishing reliable communication between the transmitter and receiver. One common technique is the use of pilot signals or reference symbols. The transmitter inserts known symbols into the downlink transmission at regular intervals. The receiver detects and analyzes these symbols to estimate the channel response. By comparing the known symbols with the received ones, the receiver can determine the effects of the channel on the transmitted signal. Another approach is channel sounding, where the transmitter actively transmits signals with specific properties to probe the channel. The receiver measures the channel response by analyzing these transmitted signals. This technique provides more detailed information about the channel's characteristics. Through these methods, the receiver estimates the downlink channel response, including its gain, phase, and frequency response. This information is crucial for adapting the receiver's equalization and decoding techniques to compensate for channel impairments, such as fading and interference. In some cases, the receiver may provide feedback to the transmitter in the form of channel state information (CSI). This feedback conveys the estimated channel characteristics, enabling the transmitter to adapt its transmission parameters accordingly. For example, based on the CSI, the transmitter can adjust the transmit power, modulation scheme, or even perform beamforming to enhance the quality and reliability of the downlink communication.

In TDD systems, where transmission and reception occur in the same frequency band but at different time intervals, the downlink channel estimation process differs slightly. Similar to FDD, synchronization is the first step, ensuring accurate timing and frequency references. However, in TDD, channel estimation takes advantage of the reciprocity property of wireless channels. During specific time slots allocated for channel estimation, the receiver transmits known pilot symbols or reference signals. The receiver then measures the channel response by analyzing the received signals during these time slots. By comparing the known pilot symbols with the received ones, the receiver estimates the downlink channel characteristics. Similar to FDD, TDD systems may also involve feedback mechanisms where the receiver provides channel state information (CSI) to the transmitter. This feedback helps the transmitter adjust its transmission parameters based on the estimated channel characteristics.

1.2 Contribution and Organization

In this dissertation, we introduce a DL-based wireless communication systems for 6G.

In Chapter 2, we propose a novel feedback reduction technique for FDD-based cell-free systems. The key feature of the proposed scheme is to choose a few dominating paths among all possible propagation paths and then feed back the path gain information (PGI) of the chosen paths. Key observations in our work are that 1) the spatial domain channel is represented by a small number of multi-path components (AoDs and path gains) and 2) the AoDs are quite similar in the uplink and downlink channel owing to the angle reciprocity so that the BSs can acquire AoD information directly from the uplink pilot signal. Thus, by choosing a few dominating paths and only feed back the path gain of the chosen paths, we can achieve a significant reduction in the feedback overhead.

In Chapter 3, we propose an efficient channel estimation framework to reduce the pilot overhead of RIS-aided mmWave systems. Key idea of the proposed scheme is to decompose the RIS reflected channel into three major components, i.e., static BS-RIS angles, quasi-static RIS-UE angles, and time-varying BS-RIS-UE path gains, and then estimate these components in different time scales. In doing so, the number of channel parameters to be estimated at each stage can be reduced significantly, resulting in a reduction of pilot overhead. Also, by optimizing the RIS phase shifts using the channel components with relatively long coherence time, we could further improve the channel estimation accuracy without requiring additional pilot resources.

In Chapter 4, we propose a DL-based channel acquisition technique for the THz UM-MIMO systems. In recent years, a remarkable success of DL in various disciplines (e.g., image classification, speech recognition, and language translation) has stimulated increasing interest in applying this paradigm to wireless communication systems. Intriguing feature of the proposed scheme is to promote the nonuniform and irregular correlation structures of the received pilot signals using Transformer, a DL architecture that differently weights each input data based on the correlations between the input data. By exploiting the attention mechanism of Transformer, T-PCA can facilitate the extraction of spatially and temporally-correlated features inherent in the THz UM-MIMO systems. In doing so, fast yet accurate channel parameter estimation can be made with small pilot overhead.

In Chapter 5, we propose a THz beam management scheme that simultaneously generates multiple frequency-dependent beams using the TTD-based phase shifters. By employing the generated FDB beams as the training beams, the proposed technique can search multiple directions simultaneously, thereby reducing the beam management latency. Intriguing feature of the proposed frequency-dependent beamforming (FDB) is to exploit a deliberately designed true time delay (TTD)-based signal propagation network called intensifier to bridge the gap between the desired beamforming vectors and the frequency-dependent beamforming vectors. In doing so, RSRP of the beam aligned with the channel propagation path gets larger while those of the misaligned beams get smaller, resulting in a significant improvement of the beam direction accuracy.

Chapter 6 summarizes the contribution of the dissertation and discuss the future research directions based on studies of this dissertation.

Chapter 2

Downlink Pilot Precoding and Compressed Channel Feedback for FDD-Based Cell-Free Systems

In this chapter, we introduce a channel feedback technique for the frequency-division-duplexing (FDD)-based cell-free mmWave and THz systems. Cell-free system where a group of base stations (BSs) cooperatively serves users has received much attention as a promising technology for the future wireless systems. In order to maximize the cooperation gain in the cell-free systems, acquisition of downlink channel state information (CSI) at the BSs is crucial. While this task is relatively easy for the time division duplexing (TDD) systems due to the channel reciprocity, it is not easy for the frequency division duplexing (FDD) systems due to the CSI feedback overhead. This issue is even more pronounced in the cell-free systems since the user needs to feed back the CSIs of multiple BSs. In our work, we propose a novel feedback reduction technique for the FDD-based cell-free systems. Key feature of the proposed technique is to choose a few dominating paths and then feed back the path gain information (PGI) of the chosen paths. By exploiting the property that the angles of departure (AoDs) are quite similar in the uplink and downlink channels (this property is referred to as angle reciprocity), the BSs obtain the AoDs directly from the uplink pilot signal.

2.1 Introduction

In recent years, ultra dense network (UDN) has received a great deal of attention as a means to achieve a thousand-fold throughput improvement in 5G wireless communications [4]. Network densification can improve the capacity of cellular systems by overlaying the existing macro cells with a large number of small (femto, pico) cells. However, throughput improvement of dense networks might not be dramatic as expected due to the poor cell-edge performance. This is because the portion of users in the cell-boundary (cell-edge users) increases sharply yet cell-edge users suffer from significant inter-cell interference due to the reduced cell size. To address this problem, an approach to entirely remove the notion of cell from the cellular systems, called *cell-free* systems, has been introduced recently [5]. When compared to the conventional cellular systems in which a single base station (BS) serves all the users in a cell, a group of BSs cooperatively serves users in the cell-free systems (see Fig. 2.1). In the cell-free systems, BSs are connected to the digital unit (DU) via advanced backhaul links to share the channel state information (CSI) and the transmit data. Since the cell association is not strictly limited by the regional cell, notions like *cell* and *cell boundary* are unnecessary in the cell-free systems. Also, since the DU intelligently recognizes the user's communication environments and then organizes the associated BSs for each user, cell-free systems can control inter-cell interference efficiently, thereby achieving significant improvement in the spectral efficiency and coverage.

In order to maximize the gain obtained by the BS cooperation, acquisition of accurate downlink CSI at the BS is crucial. While this task is relatively easy for the time division duplexing (TDD) systems due to the channel reciprocity, it is not easy for the frequency division duplexing (FDD) systems due to the CSI feedback overhead [6, 7]. For this reason, most efforts on the cell-free systems to date are based on the TDD systems [8,9]. In practice, however, TDD-based cell-free systems have some potential problems. For example, due to the switching between the uplink and downlink transmission in the TDD systems, users may not be able to obtain the instantaneous

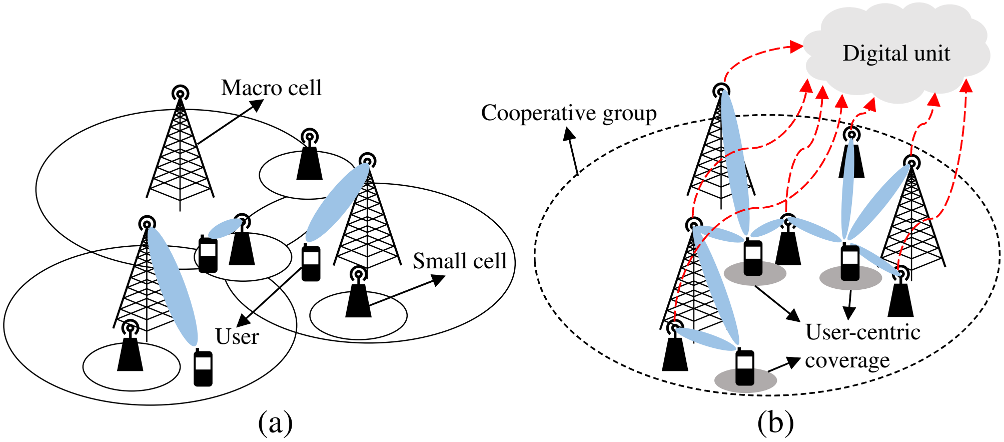

Figure 2.1: Comparison between (a) the conventional cellular systems and (b) the cell-free systems.

CSI when the transmission direction is directed to the uplink [10]. Further, the channel reciprocity in TDD systems might not be accurate due to the calibration error in the RF chains [6]. These observations, together with the fact that the FDD systems have many benefits over the TDD systems (e.g., continuous channel estimation and small latency), motivate us to study FDD-based cell-free systems. One well-known drawback of the FDD systems is that the amount of CSI feedback needs to be proportional to the number of transmit antennas to achieve the rate comparable to the system with the perfect CSI [11]. This issue is even more pronounced in the cell-free systems since the user needs to estimate and feed back the downlink CSIs of multiple BSs. Therefore, it is of a great importance to come up with an effective means to relax the feedback overhead in the FDD-based cell-free systems.

The primary purpose of this paper is to propose an approach to reduce the CSI feedback overhead in the FDD-based cell-free systems. Key feature of the proposed technique is that the spatial domain channel can be represented by a small number of multi-path components (angle of departure (AoD) and path gain) [12]. By exploiting the property referred to as *angle reciprocity* [13] that the AoDs are quite similar in the uplink and downlink channels, we only feed back the path gain information (PGI) to the BSs. As a result, the number of bits required for the channel vector quantization scales linearly with the number of dominating paths, not the number of transmit antennas. Moreover, by choosing a few dominating paths maximizing the sum rate, we can further reduce the feedback overhead considerably. In order to support the dominating PGI acquisition and feedback at the user, we use spatially precoded downlink pilot signal.

Through the performance analysis, we show that the proposed dominating PGI feedback scheme exhibits a smaller quantization distortion than that generated by the conventional CSI feedback scheme. In fact, the number of feedback bits required to maintain a constant gap to the system with perfect PGI scales linearly with the number of dominating paths which is much smaller than the number of transmit antennas. From the simulations on realistic scenarios, we show that the proposed dominating PGI feedback scheme achieves more than 60% reduction in the feedback overhead over the conventional scheme relying on the CSI feedback. We also show that the performance gain of the proposed dominating PGI feedback scheme increases with the number of propagation paths while no such benefit can be obtained from the conventional CSI feedback scheme. This implies that the proposed dominating PGI feedback scheme is an appealing solution to reduce the feedback overhead for both the limited scattering and rich scattering environment.

Notations: Lower and upper case symbols are used to denote vectors and matrices, respectively. The superscripts $(\cdot)^{\mathrm{T}}$, $(\cdot)^{\mathrm{H}}$, and $(\cdot)^{+}$ denote transpose, Hermitian transpose, and pseudo-inverse, respectively. $\otimes$ denotes the Kronecker product. $\|\mathbf{x}\|$ and $\|\mathbf{X}\|_{\mathrm{F}}$ are used as the Euclidean norm of a vector $\mathbf{x}$ and the Frobenius norm of a matrix $\mathbf{X}$, respectively. $\mathrm{tr}\left(\mathbf{X}\right)$ and $\mathrm{vec}\left(\mathbf{X}\right)$ denote the trace and vectorization of $\mathbf{X}$, respectively. Also, $\mathrm{diag}\left(\mathbf{X}_1, \mathbf{X}_2\right)$ denotes a block diagonal matrix whose diagonal elements are $\mathbf{X}_1$ and $\mathbf{X}_2$. In addition, $\mathbf{x}_\Lambda$ is a subvector of $\mathbf{x}$ whose i-th entry is $\mathbf{x}(\Lambda(i))$ and $\mathbf{X}_\Lambda$ is a submatrix of $\mathbf{X}$ whose i-th column is the $\Lambda(i)$-th column of $\mathbf{X}$ for $i = 1, \cdots, |\Lambda|$ (Λ is the set of partial indices and $|\Lambda|$ is the cardinality of Λ).

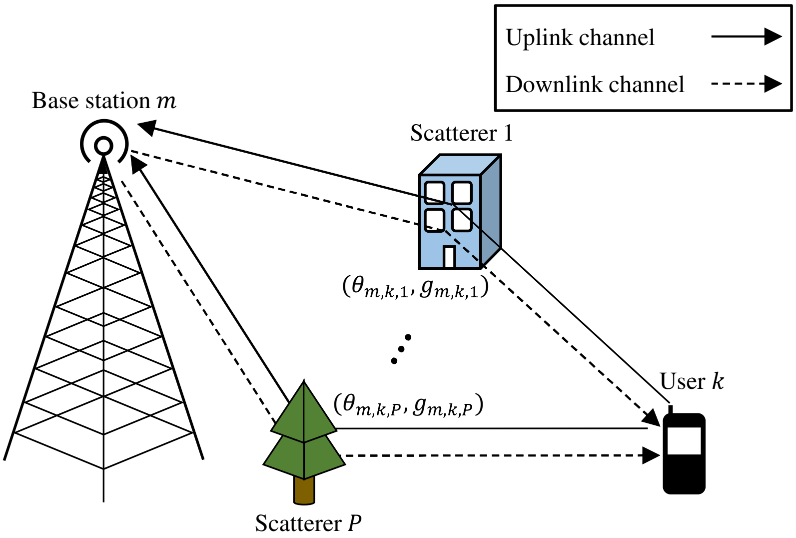

Figure 2.2: Narrowband ray-based channel model and angle reciprocity between the uplink and downlink channels.

2.2 Cell-Free System Model

In this section, we introduce the FDD-based cell-free systems and the multi-path channel model. We also discuss the angle reciprocity between the uplink and downlink channels and the conventional quantized channel feedback scheme.

2.2.1 Cell-Free System Model

We consider the FDD-based cell-free systems with M BSs and K users. Each BS is equipped with a uniform linear array of N antennas and each user is equipped with a single antenna. Let $\mathcal{B} = \{1, \cdots, M\}$ and $\mathcal{U} = \{1, \cdots, K\}$ be the sets of BSs and users, respectively. In our work, we consider the narrowband ray-based channel model consisting of P paths (see Fig. 2.2) [14]. The downlink channel vector $\mathbf{h}_{m,k} \in \mathbb{C}^N$ from the BS m to the user k is expressed as

$$\mathbf{h}_{m,k} = \sum_{i=1}^{P} g_{m,k,i}\mathbf{a}(\theta_{m,k,i}), \tag{2.1}$$

where $\theta_{m,k,i}$ is the AoD and $g_{m,k,i}$ is the complex path gain of the i-th path, respectively. We assume that for every m, k, and i, $g_{m,k,i} \sim \mathcal{CN}(0,1)$ are independent and identically distributed (i.i.d.) random variables. In addition, $\mathbf{a}(\theta_{m,k,i}) \in \mathbb{C}^N$ is the array steering vector given by

$$\mathbf{a}(\theta_{m,k,i}) = \left[1, e^{-j\frac{2\pi d}{\lambda}\sin\theta_{m,k,i}}, \cdots, e^{-j(N-1)\frac{2\pi d}{\lambda}\sin\theta_{m,k,i}}\right]^{\mathrm{T}}, \tag{2.2}$$

where d is the antenna spacing and λ is the signal wavelength. The matrix-vector form of $\mathbf{h}_{m,k}$ is

$$\mathbf{h}_{m,k} = \mathbf{A}_{m,k}\mathbf{g}_{m,k}, \tag{2.3}$$

where $\mathbf{A}_{m,k} = [\mathbf{a}(\theta_{m,k,1}), \cdots, \mathbf{a}(\theta_{m,k,P})] \in \mathbb{C}^{N\times P}$ is the array steering matrix and $\mathbf{g}_{m,k} = [g_{m,k,1}, \cdots, g_{m,k,P}]^{\mathrm{T}} \in \mathbb{C}^P$ is the PGI vector. It is worth mentioning that the AoDs vary much slower than the path gains. In fact, since scatterers affecting the signal transmission do not change their positions significantly, the AoDs are readily considered as constant during the channel coherence time. Also, it has been shown that the number of propagation paths P is quite smaller than the number of transmit antennas N [15]. We note that P is completely determined by the scattering geometry around the BS. Since the BSs are usually located at high places such as a rooftop of a building, only a few scatterers affect the signal transmission. For example, P is $2\sim 8$ for $6\sim 60$ GHz band due to the limited scattering of the millimeter-wave signal [16]. Also, for the sub-6 GHz band, P is set to $10\sim 20$ (3GPP spatial channel model [17]) while N is $32\sim 256$ in the massive multiple-input multiple-output (MIMO) regime. In this setting, the received signal $y_k \in \mathbb{C}$ of the user k is given by

$$y_k = \sum_{m=1}^{M} \mathbf{h}_{m,k}^{\mathrm{H}}\mathbf{w}_{m,k}s_k + \sum_{j\neq k}^{K}\sum_{m=1}^{M} \mathbf{h}_{m,k}^{\mathrm{H}}\mathbf{w}_{m,j}s_j + n_k, \tag{2.4}$$

where $\mathbf{w}_{m,k} \in \mathbb{C}^N$ is the precoding vector from the BS m to the user k, $s_k \in \mathbb{C}$ is the data symbol for the user k, and $n_k \sim \mathcal{CN}(0, \sigma_n^2)$ is the additive Gaussian noise. The corresponding achievable rate R_k of the user k is

$$R_k = \mathbb{E}\left[\log_2\left(1+\frac{\left|\sum_{m=1}^{M}\mathbf{h}_{m,k}^{\mathrm{H}}\mathbf{w}_{m,k}\right|^2}{\sum_{j\neq k}^{K}\left|\sum_{m=1}^{M}\mathbf{h}_{m,k}^{\mathrm{H}}\mathbf{w}_{m,j}\right|^2+\sigma_n^2}\right)\right]. \tag{2.5}$$

Approximately, we have[1]

$$R_k \approx \log_2\left(1+\frac{\mathbb{E}\left[\left|\sum_{m=1}^{M}\mathbf{h}_{m,k}^{\mathrm{H}}\mathbf{w}_{m,k}\right|^2\right]}{\sum_{j\neq k}^{K}\mathbb{E}\left[\left|\sum_{m=1}^{M}\mathbf{h}_{m,k}^{\mathrm{H}}\mathbf{w}_{m,j}\right|^2\right]+\sigma_n^2}\right). \tag{2.6}$$

2.2.2 Angle Reciprocity between Uplink and Downlink Channels

As mentioned, the AoDs in the uplink and downlink channels are fairly similar in the FDD systems when their carrier frequencies do not differ too much (typically less than a few GHz). The reason is because only the signal components that physically reverse the uplink propagation path can reach the user during the downlink transmission [13] (see Fig. 2.2). Since the changes of relative permittivity and conductivity of the scatterers are negligible in the scale of several GHz, reflection and deflection properties determining the propagation paths in the uplink and downlink transmissions are fairly similar [19], which in turn implies that the propagation paths of the uplink and downlink channels are more or less similar. This so-called *angle reciprocity* is very useful since the BS can acquire the AoDs from the uplink pilot signal. In estimating the AoDs, various algorithms such as multiple signal classification (MUSIC) [20] or estimation of signal parameters via rotational invariance techniques (ESPRIT) [21] can be employed.

2.2.3 Conventional Quantized Channel Feedback

In the conventional quantized channel feedback, a user estimates the downlink channel vector from the downlink pilot signal. Then, the user quantizes the channel direction

---

[1] This approximation becomes more accurate as the number of transmit antennas N increases [18, Lemma 1].

$\bar{\mathbf{h}}_{m,k} = \frac{\mathbf{h}_{m,k}}{\|\mathbf{h}_{m,k}\|}$ and then feeds it back to the BS. Specifically, a codeword $\mathbf{c}_{\hat{i}_{m,k}}$ is chosen from a pre-defined B-bit codebook $\mathcal{C} = \{\mathbf{c}_1, \cdots, \mathbf{c}_{2^B}\}$ as

$$\mathbf{c}_{\hat{i}_{m,k}} = \arg\max_{\mathbf{c}\in\mathcal{C}} \left|\bar{\mathbf{h}}_{m,k}^{\mathrm{H}}\mathbf{c}\right|^2. \tag{2.7}$$

Then, the selected index $\hat{i}_{m,k}$ is fed back to the BS. It has been shown that the number of feedback bits B needs to be scaled linearly with the channel dimension N and SNR (in decibels) to properly control the quantization distortion as [11]

$$B \approx \frac{(N-1)}{3} \times \text{SNR}. \tag{2.8}$$

In the FDD-based cell-free systems, since multiple BSs cooperatively serve users, a user should send the downlink CSIs to multiple BSs. Thus, the feedback overhead should also increase with the number of associated BSs M. For example, if $M = 6$, $N = 16$, and SNR $= 10\,\text{dB}$, then a user has to send $B = 300$ bits ($2 \sim 3$ resource blocks in LTE systems) just for the CSI feedback.

2.3 Dominating Path Gain Information Feedback in Cell-Free Systems

The key idea of the proposed dominating PGI feedback scheme is to select a small number of paths based on the AoD information and then feed back the measured path gains of the chosen paths. As mentioned, the AoDs are acquired from the uplink pilot signal by using the angle reciprocity. Since the number of propagation paths is smaller than the number of transmit antennas, we can achieve a considerable reduction in the quantized channel dimension using the dominating PGI feedback. We can further reduce the feedback overhead from multiple BSs by choosing a few dominating paths among all possible multi-paths.

In a nutshell, overall operations of the proposed dominating PGI feedback scheme are as follows: 1) user transmits the uplink pilot signal and then BSs acquire AoDs

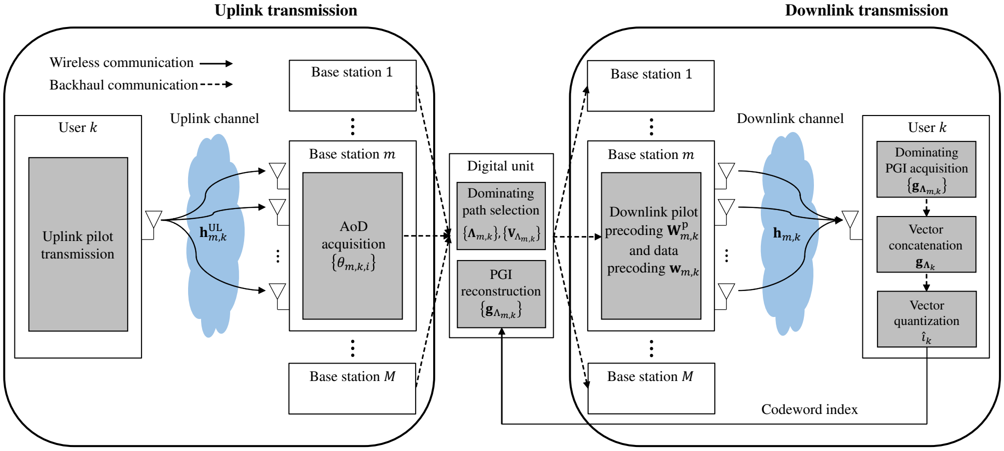

Figure 2.3: Overall transceiver structure of the proposed dominating PGI feedback scheme.

from the received pilot signal, 2) DU performs the dominating path selection based on the acquired AoDs, 3) BSs transmit the precoded downlink pilot signal, 4) each user acquires the dominating PGI from the precoded downlink pilot signal and then feeds it back to the BSs, and 5) BSs perform the downlink data transmission based on the dominating PGI feedback (see Fig. 2.3).

2.3.1 Uplink AoD Acquisition

Since the AoDs are quite similar in the uplink and downlink channels, the BS can acquire the AoD information from the uplink pilot signal. Roughly speaking, there are two types of AoD estimation technique: 1) noise subspace-based methods (e.g., MUSIC [20], Capon [22]) and 2) signal subspace-based methods (e.g., ESPRIT [21], ML [23]). In this work, we used the MUSIC algorithm since it is easy to implement and performs comparable to the subspace-based approaches[2]. In the MUSIC algorithm, the

---

[2] This is because the MUSIC algorithm exploits the information about the whole array geometry of the transmit antennas while the ESPRIT algorithm exploits only the partial information related to the array geometry.

BS estimates the uplink channel vector $\mathbf{h}_{m,k}^{\mathrm{UL}}$ and then computes the channel covariance matrix $\mathbf{R}_{m,k}^{\mathrm{UL}} = \mathbb{E}\left[\mathbf{h}_{m,k}^{\mathrm{UL}}\mathbf{h}_{m,k}^{\mathrm{UL,H}}\right]$. Key idea of the MUSIC algorithm is to decompose the eigenspace of $\mathbf{R}_{m,k}^{\mathrm{UL}}$ into two orthogonal subspaces: signal subspace and noise subspace. The eigenvectors of $\mathbf{R}_{m,k}^{\mathrm{UL}}$ corresponding to the P largest eigenvalues form the signal subspace matrix $\mathbf{E}_s$ and the rest form the noise subspace matrix $\mathbf{E}_n$. Since $\mathbf{E}_n$ is orthogonal to the signal subspace, the AoD θ should satisfy $\mathbf{E}_n^{\mathrm{H}}\mathbf{a}(\theta) = \mathbf{0}_P$. Thus, the AoDs are obtained from the peak of spectrum function f_{MUSIC} given by

$$f_{\mathrm{MUSIC}}(\theta) = \frac{1}{\mathbf{a}^{\mathrm{H}}(\theta)\,\mathbf{E}_n\mathbf{E}_n^{\mathrm{H}}\mathbf{a}(\theta)}. \tag{2.9}$$

2.3.2 Dominating Path Selection Problem Formulation

Main advantage of the dominating PGI feedback over the conventional CSI feedback is the reduction of the channel vector dimension to be quantized. However, since the user should feed back the PGI to multiple BSs, feedback overhead is still considerable. In the proposed scheme, by choosing a few dominating paths among all possible multi-paths between each user and the associated BSs, we can control the feedback overhead at the expense of marginal degradation in the sum rate.

In order to choose the paths that contribute to the sum rate most, we first need to express the sum rate as a function of the dominating paths. Let $\Lambda_{m,k} \subseteq \{1, \cdots, P\}$ be the index set of the dominating paths from the BS m to the user k and $\mathbf{g}_{\Lambda_{m,k}} = [g_{m,k,i},\ i \in \Lambda_{m,k}]^{\mathrm{T}} \in \mathbb{C}^{|\Lambda_{m,k}|}$ be the dominating PGI vector. For example, if the first and the third paths are chosen as the dominating paths, then $\Lambda_{m,k} = \{1, 3\}$ and $\mathbf{g}_{\Lambda_{m,k}} = [g_{m,k,1},\ g_{m,k,3}]^{\mathrm{T}}$. Also, let $\Lambda_k = \{\Lambda_{1,k}, \cdots, \Lambda_{M,k}\}$ be the combined index set for the user k and $\mathbf{g}_{\Lambda_k} = \left[\mathbf{g}_{\Lambda_{1,k}}^{\mathrm{T}}, \cdots, \mathbf{g}_{\Lambda_{M,k}}^{\mathrm{T}}\right]^{\mathrm{T}} \in \mathbb{C}^L$ be the corresponding dominating PGI vector. Note that L is the total number of dominating paths for each user. For example, if $M = 3$, $L = 4$, and $\Lambda_{1,k} = \{1\}$, $\Lambda_{2,k} = \{1, 3\}$, and $\Lambda_{3,k} = \{2\}$, then $\Lambda_k = \{\{1\}, \{1, 3\}, \{2\}\}$ and $\mathbf{g}_{\Lambda_k} = \left[g_{1,k,1}, g_{2,k,1}, g_{2,k,3}, g_{3,k,2}\right]^{\mathrm{T}}$ (see Fig. 2.4). Then, the user k estimates and feeds back $\mathbf{g}_{\Lambda_k}$ to the DU. The downlink precoding vector $\mathbf{w}_{m,k} \in \mathbb{C}^N$ from the BS m to the user k, constructed from the dominating PGI

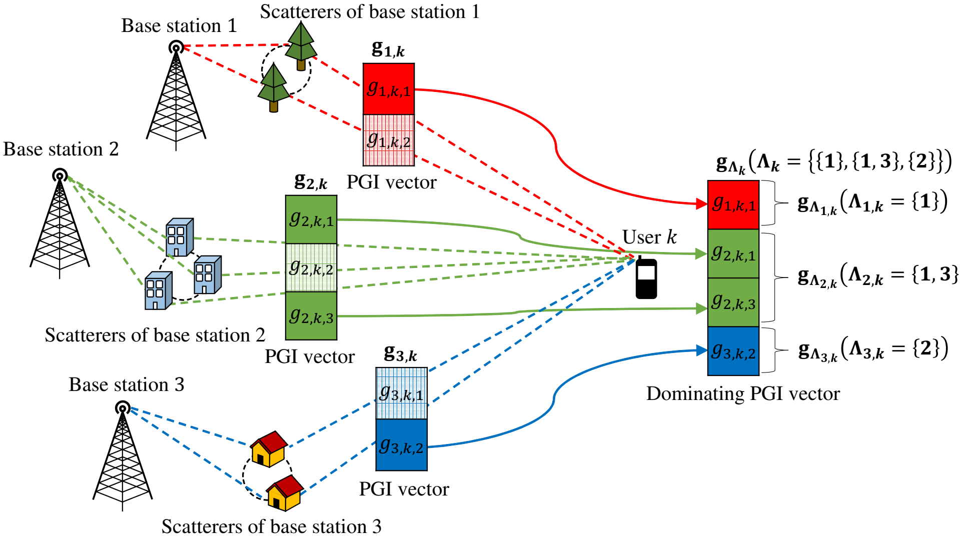

Figure 2.4: Illustration of the dominating path selection

feedback, is

$$\mathbf{w}_{m,k} = \mathbf{V}_{\Lambda_{m,k}} \hat{\mathbf{g}}_{\Lambda_{m,k}}, \tag{2.10}$$

where $\mathbf{V}_{\Lambda_{m,k}} \in \mathbb{C}^{N \times |\Lambda_{m,k}|}$ is the precoding matrix to transform $|\Lambda_{m,k}|$-dimensional vector $\hat{\mathbf{g}}_{\Lambda_{m,k}}$ into N-dimensional vector $\mathbf{w}_{m,k}$ and $\hat{\mathbf{g}}_{\Lambda_{m,k}} \in \mathbb{C}^{|\Lambda_{m,k}|}$ is the dominating PGI vector fed back from the user. In the following theorem, we express the achievable rate of the dominating PGI feedback scheme as a function of the dominating path indices $\{\Lambda_{m,k}\}$ and the precoding matrices $\{\mathbf{V}_{\Lambda_{m,k}}\}$. Using this theorem, we can find out $\{\Lambda_{m,k}\}$ and $\{\mathbf{V}_{\Lambda_{m,k}}\}$ maximizing the sum rate performance of the dominating PGI feedback.

Theorem 1. *The achievable rate $R_k^{(\text{ideal})}$ of the user k for the ideal system with perfect PGI is*

$$R_k^{(\text{ideal})} \approx \log_2 \left(1 + \frac{\left| \sum_{m=1}^{M} \operatorname{tr}\left(\mathbf{A}^{\mathrm{H}}_{\Lambda_{m,k}} \mathbf{V}_{\Lambda_{m,k}} \right) \right|^2 + \sum_{m=1}^{M} \left\| \mathbf{A}^{\mathrm{H}}_{m,k} \mathbf{V}_{\Lambda_{m,k}} \right\|_{\mathrm{F}}^2}{\sum_{j \neq k}^{K} \sum_{m=1}^{M} \left\| \mathbf{A}^{\mathrm{H}}_{m,k} \mathbf{V}_{\Lambda_{m,j}} \right\|_{\mathrm{F}}^2 + \sigma_n^2} \right), \tag{2.11}$$

where $\mathbf{A}_{\Lambda_{m,k}} = [\mathbf{a}(\theta_{m,k,i}),\, i \in \Lambda_{m,k}] \in \mathbb{C}^{N \times |\Lambda_{m,k}|}$ *is the submatrix of* $\mathbf{A}_{m,k}$*.*

Proof. See Appendix A. $\square$

Then, the dominating path selection problem to choose L paths maximizing the sum rate for each user can be formulated as

$$\mathcal{P}_1 : \max_{\{\Lambda_{m,k}, \mathbf{V}_{\Lambda_{m,k}}\}} \sum_{k=1}^{K} R_k^{(\text{ideal})} \tag{2.12a}$$

$$\text{s.t.} \quad \sum_{m=1}^{M} |\Lambda_{m,k}| = L, \quad \forall k \in \mathcal{U} \tag{2.12b}$$

$$\sum_{k=1}^{K} \left\| \mathbf{V}_{\Lambda_{m,k}} \right\|_{\mathrm{F}}^2 = P_m^{\text{tx}}, \quad \forall m \in \mathcal{B}, \tag{2.12c}$$

where P_m^{tx} is the transmission power of BS m. Note that (2.12b) is the dominating path number constraint and (2.12c) is the transmit power constraint.

2.3.3 Alternating Dominating Path Selection and Precoding Algorithm

Major obstacle in solving $\mathcal{P}_1$ is the strong correlation between the dominating path index set $\Lambda_{m,k}$ and the precoding matrix $\mathbf{V}_{\Lambda_{m,k}}$. In fact, since the column dimension of $\mathbf{V}_{\Lambda_{m,k}}$ is the number of dominating paths $|\Lambda_{m,k}|$, $\Lambda_{m,k}$ and $\mathbf{V}_{\Lambda_{m,k}}$ cannot be determined simultaneously. Since it is not possible to solve $\mathcal{P}_1$ directly, we propose an algorithm to determine $\{\Lambda_{m,k}\}$ and $\{\mathbf{V}_{\Lambda_{m,k}}\}$ in an alternating way (see Table 2.1): 1) First, we fix $\{\Lambda_{m,k}\}$ and then find out the optimal precoding matrices $\{\mathbf{V}_{\Lambda_{m,k}}\}$ maximizing the sum rate. 2) We then update $\{\Lambda_{m,k}\}$ by removing the path index giving the minimal impact on the sum rate. We repeat these procedures until L dominating paths remain for each user. Although this relaxation will be sub-optimal, it helps to reduce the computational complexity required for solving $\mathcal{P}_1$.

Table 2.1 Alternating dominating path selection and precoding algorithm

```
Input: Path AoDs $\{\theta_{m,k,i}\}$, BS set $\mathcal{B}$, user set $\mathcal{U}$, number of propagation paths $P$,
    number of dominating paths $L$, BS maximum transmit power $\{P_m^{\text{tx}}\}$
Initialization: $\Lambda_{m,k} = \{1, \cdots, P\}, \ \forall m \in \mathcal{B}, \forall k \in \mathcal{U}$, $\{\mathbf{V}_{\Lambda_{m,k}}\} =$
    Precoding_matrix_optimization $(\{\Lambda_{m,k}\})$
Iteration:
    while $\sum_{m=1}^{M} |\Lambda_{m,k}| > L$ for some $k$ do
    (Check the number of dominating paths)
        for $k \in \mathcal{U}$ do
            if $\sum_{m=1}^{M} |\Lambda_{m,k}| > L$ then
                $(\hat{m}_k, \hat{i}_k) = \arg \min_{m \in \mathcal{B}, \, i \in \Lambda_{m,k}} \text{SLNR}_{m,k,i}$
                (Find the path index with minimum SLNR)
                $\Lambda_{\hat{m}_k,k} = \Lambda_{\hat{m}_k,k} \setminus \{\hat{i}_k\}$
                (Remove the chosen path index)
            end if
        end for
        $\{\mathbf{V}_{\Lambda_{m,k}}\} =$ Precoding_matrix_optimization $(\{\Lambda_{m,k}\})$
    end while
Output: $\{\Lambda_{m,k}\}$, $\{\mathbf{V}_{\Lambda_{m,k}}\}$
```

Precoding Matrix Optimization

We first discuss the way to find out the optimal precoding matrices $\{\mathbf{V}_{\Lambda_{m,k}}\}$ when $\{\Lambda_{m,k}\}$ are fixed[3]. Unfortunately, the problem $\mathcal{P}_2$ is highly non-convex and also contains multiple matrix variables. To address these issues, we first vectorize and concatenate the variables of multiple BSs $\mathbf{V}_{\Lambda_{1,k}}, \cdots, \mathbf{V}_{\Lambda_{M,k}}$ into $\mathbf{x}_{\Lambda_k}$. Then, by exploiting the

---

[3] Even though L is chosen to be larger than the effective number of propagation paths, the precoding matrix would be optimized such that the transmit power is focused on the best column vectors (corresponding to the dominant paths).

notion of *leakage*, we decompose the sum rate maximization problem into the distributed leakage minimization problems for each $\mathbf{x}_{\Lambda_k}$. After obtaining $\mathbf{x}_{\Lambda_k}$, we de-vectorize and de-concatenate $\mathbf{x}_{\Lambda_k}$ to obtain the desired precoding matrices $\mathbf{V}_{\Lambda_{1,k}}, \cdots, \mathbf{V}_{\Lambda_{M,k}}$.

When $\{\Lambda_{m,k}\}$ are fixed, the precoding optimization problem $\mathcal{P}_2$ is formulated as

$$\mathcal{P}_2 : \max_{\{\mathbf{V}_{\Lambda_{m,k}}\}} \sum_{k=1}^{K} R_k^{(\text{ideal})} \tag{2.13a}$$

$$\text{s.t.} \quad \sum_{k=1}^{K} \left\| \mathbf{V}_{\Lambda_{m,k}} \right\|_{\text{F}}^2 = P_m^{\text{tx}}, \quad \forall m \in \mathcal{B}. \tag{2.13b}$$

Then, using the rate expression in (2.11), we vectorize the variables ($\mathbf{x}_{\Lambda_{m,k}} = \text{vec}(\mathbf{V}_{\Lambda_{m,k}})$, $\boldsymbol{\mu}_{\Lambda_{m,k}} = \text{vec}(\mathbf{A}_{\Lambda_{m,k}})$) and then concatenate the variables of multiple BSs ($\mathbf{x}_{\Lambda_k} = [\mathbf{x}_{\Lambda_{1,k}}^{\text{T}}, \cdots, \mathbf{x}_{\Lambda_{M,k}}^{\text{T}}]^{\text{T}}$, $\boldsymbol{\mu}_{\Lambda_k} = [\boldsymbol{\mu}_{\Lambda_{1,k}}^{\text{T}}, \cdots, \boldsymbol{\mu}_{\Lambda_{M,k}}^{\text{T}}]^{\text{T}}$) to obtain

$$\mathcal{P}_3 : \max_{\{\mathbf{x}_{\Lambda_k}\}} \sum_{k=1}^{K} \log_2 \left(1 + \frac{\left| \boldsymbol{\mu}_{\Lambda_k}^{\text{H}} \mathbf{x}_{\Lambda_k} \right|^2 + \left\| \boldsymbol{\Gamma}_{k,k}^{\text{H}} \mathbf{x}_{\Lambda_k} \right\|^2}{\sum_{j \neq k}^{K} \left\| \boldsymbol{\Gamma}_{j,k}^{\text{H}} \mathbf{x}_{\Lambda_j} \right\|^2 + \sigma_n^2} \right) \tag{2.14a}$$

$$\text{s.t.} \quad \sum_{k=1}^{K} \left\| \mathbf{x}_{\Lambda_{m,k}} \right\|^2 = P_m^{\text{tx}}, \quad \forall m \in \mathcal{B}, \tag{2.14b}$$

where $\boldsymbol{\Gamma}_{m,j,k} = \mathbf{I}_{|\Lambda_{m,j}|} \otimes \mathbf{A}_{m,k}$ and $\boldsymbol{\Gamma}_{j,k} = \text{diag}(\boldsymbol{\Gamma}_{1,j,k}, \cdots, \boldsymbol{\Gamma}_{M,j,k})$. Here, we use the properties $\text{tr}(\mathbf{A}_{\Lambda_{m,k}}^{\text{H}} \mathbf{V}_{\Lambda_{m,k}}) = \text{vec}(\mathbf{A}_{\Lambda_{m,k}})^{\text{H}} \text{vec}(\mathbf{V}_{\Lambda_{m,k}})$ and $\left\| \mathbf{A}_{m,k}^{\text{H}} \mathbf{V}_{\Lambda_{m,j}} \right\|_{\text{F}} = \left\| \left(\mathbf{I}_{|\Lambda_{m,j}|} \otimes \mathbf{A}_{m,k} \right)^{\text{H}} \text{vec}(\mathbf{V}_{\Lambda_{m,j}}) \right\|$.

The modified problem $\mathcal{P}_3$ looks simpler than the original problem $\mathcal{P}_2$, but it is still hard to find out the optimal solution because the rate expression in (2.14a) is a non-convex quadratic fractional function (i.e., both numerator and denominator are quadratic functions) so that $\mathcal{P}_3$ is a non-convex optimization problem. Furthermore, $\mathcal{P}_3$ requires joint optimization for $\mathbf{x}_{\Lambda_1}, \cdots, \mathbf{x}_{\Lambda_K}$, and thus it is difficult to find out the global solutions simultaneously. As a remedy, we introduce the notion of *leakage*, a measure of how much signal power leaks into the other users [24]. To be specific, the signal-to-leakage-and-noise-ratio (SLNR) of the user k is given by

$$\mathrm{SLNR}_k = \frac{\mathbb{E}\left[\left|\sum_{m=1}^{M} \mathbf{h}_{m,k}^{\mathrm{H}} \mathbf{w}_{m,k}\right|^2\right]}{\sum_{j\neq k}^{K} \mathbb{E}\left[\left|\sum_{m=1}^{M} \mathbf{h}_{m,j}^{\mathrm{H}} \mathbf{w}_{m,k}\right|^2\right] + \sigma_n^2} \tag{2.15}$$

$$\overset{(a)}{=} \frac{\left|\boldsymbol{\mu}_{\Lambda_k}^{\mathrm{H}} \mathbf{x}_{\Lambda_k}\right|^2 + \left\|\boldsymbol{\Gamma}_{k,k}^{\mathrm{H}} \mathbf{x}_{\Lambda_k}\right\|^2}{\sum_{j\neq k}^{K} \left\|\boldsymbol{\Gamma}_{k,j}^{\mathrm{H}} \mathbf{x}_{\Lambda_k}\right\|^2 + \sigma_n^2}, \tag{2.16}$$

where (a) comes from (2.14a)[4]. While (2.14a) is a function of $\mathbf{x}_{\Lambda_1}, \cdots, \mathbf{x}_{\Lambda_K}$, SLNR_k in (2.16) is a sole function of $\mathbf{x}_{\Lambda_k}$. Thus, for each user k, we can find out the optimal $\mathbf{x}_{\Lambda_k}^*$ maximizing SLNR_k separately. While this solution is sub-optimal, it is simple and easy to calculate because we can obtain the tractable closed-form solution.

The distributed SLNR maximization problem for the user k is given by

$$\mathcal{P}_4 : \mathbf{x}_{\Lambda_k}^* = \arg \max_{\|\mathbf{x}_{\Lambda_k}\| = \sqrt{P_k^{\mathrm{tx}}}} \frac{\left|\boldsymbol{\mu}_{\Lambda_k}^{\mathrm{H}} \mathbf{x}_{\Lambda_k}\right|^2 + \left\|\boldsymbol{\Gamma}_{k,k}^{\mathrm{H}} \mathbf{x}_{\Lambda_k}\right\|^2}{\sum_{j\neq k}^{K} \left\|\boldsymbol{\Gamma}_{k,j}^{\mathrm{H}} \mathbf{x}_{\Lambda_k}\right\|^2 + \sigma_n^2}, \tag{2.17}$$

where $P_{m,k}^{\mathrm{tx}}$ is the transmit power allocated to the user k from the BS m and $P_k^{\mathrm{tx}} = \sum_{m=1}^{M} P_{m,k}^{\mathrm{tx}}$ is the total transmit power allocated to the user k. When we try to solve $\mathcal{P}_4$, we should know the information about the allocated power P_k^{tx}. In this chapter, we use a simple yet effective proportional power allocation strategy satisfying the per-BS transmit power constraint. In this scheme, the transmit power is set to be proportional to the channel magnitude as [25]

$$P_{m,k}^{\mathrm{tx}} = \left\|\mathbf{x}_{\Lambda_{m,k}}\right\|_{\mathrm{F}}^2 = \frac{\|\boldsymbol{\Gamma}_{m,k,k}\|_{\mathrm{F}}^2}{\sum_{j=1}^{K} \|\boldsymbol{\Gamma}_{m,j,j}\|_{\mathrm{F}}^2} P_m^{\mathrm{tx}}. \tag{2.18}$$

Note that since the BSs have information about the AoDs and the dominating PGIs only, we use $\boldsymbol{\Gamma}_{m,k,k} = \mathbf{I}_{|\Lambda_{m,k}|} \otimes \mathbf{A}_{m,k}$ as an effective channel matrix instead. One can easily see that the power constraint (2.14b) is satisfied ($\sum_{k=1}^{K} P_{m,k}^{\mathrm{tx}} = P_m^{\mathrm{tx}}$).

---

[4] When compared to the signal-to-interference-and-noise-ratio (SINR) of the user k in (2.5), one can observe that the only difference is the exchange of user index at the denominator between $\mathbf{h}_{m,j}^{\mathrm{H}} \mathbf{w}_{m,k}$ and $\mathbf{h}_{m,k}^{\mathrm{H}} \mathbf{w}_{m,j}$. Hence, we can easily obtain the closed-form expression of SLNR_k from (2.14a).

Once the transmit power allocation is determined, we can convert the objective function (i.e., SLNR_k) of $\mathcal{P}_4$ as a Rayleigh quotient form as

$$\text{SLNR}_k = \frac{\mathbf{x}_{\Lambda_k}^{\text{H}}(\boldsymbol{\mu}_{\Lambda_k}\boldsymbol{\mu}_{\Lambda_k}^{\text{H}} + \boldsymbol{\Gamma}_{k,k}\boldsymbol{\Gamma}_{k,k}^{\text{H}})\mathbf{x}_{\Lambda_k}}{\mathbf{x}_{\Lambda_k}^{\text{H}}\big(\sum_{j\neq k}^{K}\boldsymbol{\Gamma}_{k,j}\boldsymbol{\Gamma}_{k,j}^{\text{H}} + \frac{\sigma_n^2}{P_k^{\text{tx}}}\mathbf{I}_{N|\Lambda_k|}\big)\mathbf{x}_{\Lambda_k}} \tag{2.19}$$

$$= \frac{\mathbf{x}_{\Lambda_k}^{\text{H}}\mathbf{U}_k\mathbf{x}_{\Lambda_k}}{\mathbf{x}_{\Lambda_k}^{\text{H}}\mathbf{W}_k\mathbf{x}_{\Lambda_k}}, \tag{2.20}$$

where $\mathbf{U}_k = \boldsymbol{\mu}_{\Lambda_k}\boldsymbol{\mu}_{\Lambda_k}^{\text{H}} + \boldsymbol{\Gamma}_{k,k}\boldsymbol{\Gamma}_{k,k}^{\text{H}}$ and $\mathbf{W}_k = \sum_{j\neq k}^{K}\boldsymbol{\Gamma}_{k,j}\boldsymbol{\Gamma}_{k,j}^{\text{H}} + \frac{\sigma_n^2}{P_k^{\text{tx}}}\mathbf{I}_{N|\Lambda_k|}$. Then, $\mathcal{P}_4$ is re-expressed as

$$\mathcal{P}_4 : \mathbf{x}_{\Lambda_k}^{*} = \arg \max_{\|\mathbf{x}_{\Lambda_k}\|=\sqrt{P_k^{\text{tx}}}} \frac{\mathbf{x}_{\Lambda_k}^{\text{H}}\mathbf{U}_k\mathbf{x}_{\Lambda_k}}{\mathbf{x}_{\Lambda_k}^{\text{H}}\mathbf{W}_k\mathbf{x}_{\Lambda_k}}. \tag{2.21}$$

In the following lemma, we provide a closed-form solution of $\mathcal{P}_4$.

Lemma 1. *The solution* $\mathbf{x}_{\Lambda_k}^{*}$ *of* $\mathcal{P}_4$ *is given by [24]*

$$\mathbf{x}_{\Lambda_k}^{*} = \sqrt{P_k^{\text{tx}}}\frac{\mathbf{u}_{k,max}}{\|\mathbf{u}_{k,max}\|}, \tag{2.22}$$

where $\mathbf{u}_{k,max}$ *is the eigenvector corresponding to the largest eigenvalue of* $\mathbf{W}_k^{-1}\mathbf{U}_k$.

Using Lemma 1, we can obtain the closed-form solution $\mathbf{x}_{\Lambda_k}^{*}$ of $\mathcal{P}_4$. Then, from the de-concatenation and de-vectorization of $\mathbf{x}_{\Lambda_k}^{*}$, we obtain the desired precoding matrices $\mathbf{V}_{\Lambda_{1,k}}^{*}, \cdots, \mathbf{V}_{\Lambda_{M,k}}^{*}$ for each BS. Finally, we normalize each $\mathbf{V}_{\Lambda_{m,k}}^{*}$ and multiply the allocated power $P_{m,k}^{\text{tx}}$ in (2.18) to satisfy the per-BS transmit power constraint. The proposed precoding matrix optimization algorithm is summarized in Table 2.2.

Dominating Path Index Update

Once we obtain $\{\mathbf{V}_{\Lambda_{m,k}}\}$ from the precoding matrix optimization, we then update the dominating path indices $\{\Lambda_{m,k}\}$ by removing the path index giving the minimal impact on the sum rate. While this task is conceptually simple, it is very difficult to find out the desired path index since the sum rate is a joint function of precoding matrices and

Table 2.2 Precoding matrix optimization

```
Input: Path index set $\{\Lambda_{m,k}\}$, BS set $\mathcal{B}$, user set $\mathcal{U}$, number of propagation paths $P$,
    number of dominating paths $L$, BS maximum transmit power $\{P_m^{\text{tx}}\}$

    $\boldsymbol{\mu}_{\Lambda_{m,k}} = \text{vec}(\mathbf{A}_{\Lambda_{m,k}}),\ \boldsymbol{\mu}_{\Lambda_k} = \left[\boldsymbol{\mu}_{\Lambda_{1,k}}^{\text{T}}, \cdots, \boldsymbol{\mu}_{\Lambda_{M,k}}^{\text{T}}\right]^{\text{T}},\ \forall m \in \mathcal{B},\ \forall k \in \mathcal{U}$
    $\boldsymbol{\Gamma}_{m,j,k} = \mathbf{I}_{|\Lambda_{m,j}|} \otimes \mathbf{A}_{m,k},\ \boldsymbol{\Gamma}_{j,k} = \text{diag}(\boldsymbol{\Gamma}_{1,j,k}, \cdots, \boldsymbol{\Gamma}_{M,j,k}),$
    $\forall m \in \mathcal{B},\ \forall j, k \in \mathcal{U}$
    $P_{m,k}^{\text{tx}} = \frac{\|\boldsymbol{\Gamma}_{m,k,k}\|_{\text{F}}^2}{\sum_{j=1}^{K}\|\boldsymbol{\Gamma}_{m,j,j}\|_{\text{F}}^2} P_m^{\text{tx}},\ P_k^{\text{tx}} = \sum_{m=1}^{M} P_{m,k}^{\text{tx}}, \forall m \in \mathcal{B}, k \in \mathcal{U}$
    for $k \in \mathcal{U}$ do
        $\mathbf{U}_k = \boldsymbol{\mu}_{\Lambda_k}\boldsymbol{\mu}_{\Lambda_k}^{\text{H}} + \boldsymbol{\Gamma}_{k,k}\boldsymbol{\Gamma}_{k,k}^{\text{H}}$
        $\mathbf{W}_k = \sum_{j \neq k}^{K} \boldsymbol{\Gamma}_{k,j}\boldsymbol{\Gamma}_{k,j}^{\text{H}} + \frac{\sigma_n^2}{P_k^{\text{tx}}}\mathbf{I}_{N|\Lambda_k|}$
        $\mathbf{u}_{k,\text{max}} = \text{max\_eigenvector}\left(\mathbf{W}_k^{-1}\mathbf{U}_k\right)$
        $\mathbf{x}_{\Lambda_k}^* = \sqrt{P_k^{\text{tx}}}\frac{\mathbf{u}_{k,\text{max}}}{\|\mathbf{u}_{k,\text{max}}\|}$
        $\left[(\mathbf{x}_{\Lambda_{1,k}}^*)^{\text{T}}, \cdots, (\mathbf{x}_{\Lambda_{M,k}}^*)^{\text{T}}\right]^{\text{T}} = \mathbf{x}_{\Lambda_k}^*$
        $\mathbf{V}_{\Lambda_{m,k}}^* = \sqrt{P_{m,k}^{\text{tx}}}\frac{\text{vec}^{-1}\left(\mathbf{x}_{\Lambda_{m,k}}^*\right)}{\left\|\mathbf{x}_{\Lambda_{m,k}}^*\right\|}, \quad \forall m \in \mathcal{B}$
    end for
    return $\{\mathbf{V}_{\Lambda_{m,k}}^*\}$
end function
Output: $\{\mathbf{V}_{\Lambda_{m,k}}\}$
```

dominating path indices. As a remedy, we remove the path index generating minimum SLNR as

$$(\hat{m}_k,\ \hat{i}_k) = \arg \min_{m \in \mathcal{B},\, i \in \Lambda_{m,k}} \text{SLNR}_{m,k,i}, \tag{2.23}$$

where $\mathrm{SLNR}_{m,k,i}$ the SLNR of i-th path between the BS m and the user k given by

$$\mathrm{SLNR}_{m,k,i} = \frac{\mathbb{E}\left[\left|\mathbf{h}_{m,k}^{\mathrm{H}}\mathbf{v}_{m,k,i}\right|^2\right]}{\sum_{j\neq k}^{K}\mathbb{E}\left[\left|\mathbf{h}_{m,j}^{\mathrm{H}}\mathbf{v}_{m,k,i}\right|^2\right] + \sigma_n^2} \tag{2.24}$$

$$\overset{(a)}{=} \frac{\left|\mathbf{a}^{\mathrm{H}}(\theta_{m,k,i})\mathbf{v}_{m,k,i}\right|^2 + \left\|\mathbf{A}_{m,k}^{\mathrm{H}}\mathbf{v}_{m,k,i}\right\|^2}{\sum_{j\neq k}^{K}\left\|\mathbf{A}_{m,j}^{\mathrm{H}}\mathbf{v}_{m,k,i}\right\|^2 + \sigma_n^2}, \tag{2.25}$$

where $\mathbf{v}_{m,k,i}$ is the column vector of $\mathbf{V}_{\Lambda_{m,k}}$ corresponding to the i-th path and (a) is obtained in a similar way with (2.16). Since $\mathrm{SLNR}_{m,k,i}$ is a sole function of the dominating path index i, we can easily find out the path index generating minimum SLNR. In our simulation results in Section VI, we show that this approach can achieve performance comparable to the optimal path selection strategy obtained from the exhaustive combinatorial search. The precoding matrix optimization and the dominating path index update are repeated iteratively until only L paths remain for each user.

Once the dominating paths maximizing the sum rate are chosen, each user acquires the corresponding dominating PGI from the downlink pilot signal, quantizes the acquired dominating PGI, and then feeds it back to the BSs. In the following section, we will discuss this issue in detail.

2.4 Downlink Pilot Precoding for Dominating Path Gain Information Acquisition

In the FDD systems, a user acquires the downlink CSI from the downlink pilot signal and then feeds the quantized channel vector back to the BS [26]. In contrast, in the proposed scheme, a user acquires the dominating PGI and then feeds back the quantized dominating PGI vector to the BS. However, there are some difficulties in the dominating PGI acquisition. First, since each user needs to selectively feed back PGIs of the dominating paths, the BS must assign additional resources to indicate the desired path information. Also, it is computationally inefficient for the user to estimate the gains of

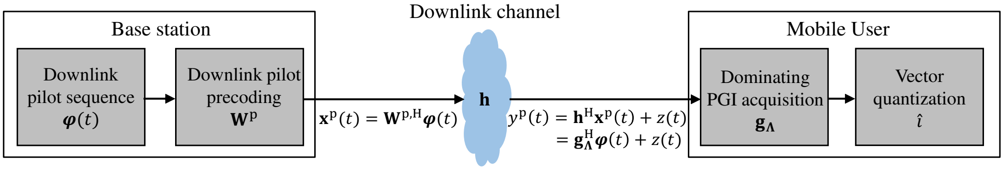

Figure 2.5: Downlink pilot precoding for dominating PGI acquisition

all possible paths. To handle this issue, we propose a new downlink training scheme based on the spatially precoded pilot signal in the acquisition of dominating PGI.

In essence, a key idea of precoded pilot signal is to convert the downlink channel vector into the dominating PGI vector so that the user can easily estimate the dominating PGI using the conventional channel estimation techniques such as the linear minimum mean square error (LMMSE) estimator [27] (see Fig. 2.5). Additionally, since the dimension of dominating PGI (i.e., the number of dominating paths) is reduced and thus becomes much smaller than that of the downlink CSI (i.e., the number of transmit antennas), we can reduce the pilot resources for the downlink pilot signal.

When the pilot precoding matrix $\mathbf{W}^{\mathrm{p}}_{m,k} \in \mathbb{C}^{|\Lambda_{m,k}| \times N}$ is applied, the downlink precoded pilot signal $\mathbf{x}^{\mathrm{p}}_m(t) \in \mathbb{C}^N$ of the BS m at time slot t is given by

$$\mathbf{x}^{\mathrm{p}}_m(t) = \sum_{k=1}^{K} \mathbf{W}^{\mathrm{p,H}}_{m,k} \boldsymbol{\psi}_{m,k}(t), \quad t = 1, \cdots, \tau, \tag{2.26}$$

where $\{\boldsymbol{\psi}_{m,k}(t)\}_{t=1}^{\tau} \subseteq \mathbb{C}^{|\Lambda_{m,k}|}$ is the downlink pilot sequence from the BS m to the user k. Then, the received signal $y^{\mathrm{p}}_k(t) \in \mathbb{C}$ of the user k at time slot t is

$$y^{\mathrm{p}}_k(t) = \sum_{m=1}^{M} \left(\mathbf{W}^{\mathrm{p}}_{m,k}\mathbf{h}_{m,k}\right)^{\mathrm{H}} \boldsymbol{\psi}_{m,k}(t) + \sum_{j \neq k}^{K} \sum_{m=1}^{M} \left(\mathbf{W}^{\mathrm{p}}_{m,j}\mathbf{h}_{m,k}\right)^{\mathrm{H}} \boldsymbol{\psi}_{m,j}(t) + z_k(t), \tag{2.27}$$

where $z_k(t) \sim \mathcal{CN}(0, \sigma_z^2)$ is the Gaussian noise. The user k collects this received signal for each slot, i.e., $\mathbf{y}^{\mathrm{p}}_k = \left[y^{\mathrm{p}}_k(1), \cdots, y^{\mathrm{p}}_k(\tau)\right]^{\mathrm{H}} \in \mathbb{C}^{\tau}$ and then multiplies $\boldsymbol{\Psi}_{m,k} =$

$\left[\boldsymbol{\psi}_{m,k}(1), \cdots, \boldsymbol{\psi}_{m,k}(\tau)\right] \in \mathbb{C}^{|\Lambda_{m,k}| \times \tau}$ to get

$$\boldsymbol{\Psi}_{m,k}\mathbf{y}_k^{\mathrm{p}} = \boldsymbol{\Psi}_{m,k}\left(\sum_{m=1}^{M} \boldsymbol{\Psi}_{m,k}^{\mathrm{H}}\mathbf{W}_{m,k}^{\mathrm{p}}\mathbf{h}_{m,k} + \sum_{m=1}^{M}\sum_{j\neq k}^{K} \boldsymbol{\Psi}_{m,j}^{\mathrm{H}}\mathbf{W}_{m,j}^{\mathrm{p}}\mathbf{h}_{m,k} + \mathbf{z}_k\right) \tag{2.28}$$

$$\overset{(a)}{=} \mathbf{W}_{m,k}^{\mathrm{p}}\mathbf{h}_{m,k} + \mathbf{n}_k, \tag{2.29}$$

where $\mathbf{z}_k = [z_k(1), \cdots, z_k(\tau)]^{\mathrm{H}} \in \mathbb{C}^{\tau}$ and $\mathbf{n}_k = \boldsymbol{\Psi}_{m,k}\mathbf{z}_k \in \mathbb{C}^{|\Lambda_{m,k}|}$. Note that (a) is due to the orthogonality of pilot sequence.

From (2.29), we observe that if the BS uses a pilot precoding matrix $\mathbf{W}_{m,k}^{\mathrm{p}}$ satisfying $\mathbf{W}_{m,k}^{\mathrm{p}}\mathbf{h}_{m,k} = \mathbf{g}_{\Lambda_{m,k}}$, then the user can extract the dominating PGI vector $\mathbf{g}_{\Lambda_{m,k}}$ from $\boldsymbol{\Psi}_{m,k}\mathbf{y}_k^{\mathrm{p}}$. To generate the desired precoding matrix $\mathbf{W}_{m,k}^{\mathrm{p}}$, we basically need to perform two operations: 1) application of the matrix inversion of $\mathbf{A}_{m,k}^{+} = (\mathbf{A}_{m,k}^{\mathrm{H}}\mathbf{A}_{m,k})^{-1}\mathbf{A}_{m,k}^{\mathrm{H}}$ and 2) compression of $\mathbf{g}_{m,k}$ into $\mathbf{g}_{\Lambda_{m,k}}$. Note that $\mathbf{A}_{m,k}^{+}$ exists as long as $\mathbf{A}_{m,k}^{\mathrm{H}}\mathbf{A}_{m,k}$ is invertible, which is easily guaranteed by the fact that the array steering vectors corresponding to different AoDs are independent and the number of transmit antennas N is larger then the number of paths P. Thus,

$$\mathbf{A}_{m,k}^{+}\mathbf{h}_{m,k} \overset{(a)}{=} \mathbf{A}_{m,k}^{+}\mathbf{A}_{m,k}\mathbf{g}_{m,k} = \mathbf{g}_{m,k}, \tag{2.30}$$

where (a) is from (2.3). Once $\mathbf{g}_{m,k}$ is obtained, we then extract $\mathbf{g}_{\Lambda_{m,k}}$ from $\mathbf{g}_{m,k}$ using the path selection matrix $\mathbf{G}_{m,k}$. For example, if the number of paths is 3 and $\Lambda_{m,k} = \{1,\, 3\}$, then $\mathbf{G}_{m,k} = \begin{bmatrix} 1 & 0 & 0 \\ 0 & 0 & 1 \end{bmatrix}$ and thus,

$$\mathbf{G}_{m,k}\mathbf{g}_{m,k} = \begin{bmatrix} 1 & 0 & 0 \\ 0 & 0 & 1 \end{bmatrix}\begin{bmatrix} g_{m,k,1} \\ g_{m,k,2} \\ g_{m,k,3} \end{bmatrix} = \begin{bmatrix} g_{m,k,1} \\ g_{m,k,3} \end{bmatrix} = \mathbf{g}_{\Lambda_{m,k}}. \tag{2.31}$$

In summary, the pilot precoding matrix $\mathbf{W}_{m,k}^{\mathrm{p}}$ from the BS m to the user k is given by

$$\mathbf{W}_{m,k}^{\mathrm{p}} = \mathbf{G}_{m,k}\mathbf{A}_{m,k}^{+}. \tag{2.32}$$

Using $\mathbf{W}_{m,k}^{\mathrm{p}}$ in (2.32), we can convert $\mathbf{h}_{m,k}$ into $\mathbf{g}_{\Lambda_{m,k}}$ (i.e., $\mathbf{W}_{m,k}^{\mathrm{p}}\mathbf{h}_{m,k} = \mathbf{g}_{\Lambda_{m,k}}$). Hence, (2.29) can be re-expressed as

$$\mathbf{\Psi}_{m,k}\mathbf{y}_k^{\mathrm{p}} = \mathbf{g}_{\Lambda_{m,k}} + \mathbf{n}_k. \tag{2.33}$$

Finally, the user k acquires $\hat{\mathbf{g}}_{\Lambda_{m,k}}$ from $\mathbf{\Psi}_{m,k}\mathbf{y}_k^{\mathrm{p}}$ by using the linear MMSE estimation [27] as

$$\hat{\mathbf{g}}_{\Lambda_{m,k}} = \frac{1}{1+\sigma_z^2}\mathbf{\Psi}_{m,k}\mathbf{y}_k^{\mathrm{p}}. \tag{2.34}$$

After the estimation of the dominating PGI, each user quantizes it and then feeds it back to the BS. To be specific, the user k concatenates $\mathbf{g}_{\Lambda_{1,k}}, \cdots, \mathbf{g}_{\Lambda_{M,k}}$ into a single vector $\mathbf{g}_{\Lambda_k} = \left[\mathbf{g}_{\Lambda_{1,k}}^{\mathrm{T}}, \cdots, \mathbf{g}_{\Lambda_{M,k}}^{\mathrm{T}}\right]^{\mathrm{T}} \in \mathbb{C}^L$ and then quantizes $\mathbf{g}_{\Lambda_k}$ into a codeword index $\hat{i}_k$ as

$$\hat{i}_k = \arg\max_i \left|\bar{\mathbf{g}}_{\Lambda_k}^{\mathrm{H}}\mathbf{c}_i\right|^2 \tag{2.35}$$

where $\bar{\mathbf{g}}_{\Lambda_k} = \frac{\mathbf{g}_{\Lambda_{m,k}}}{\left\|\mathbf{g}_{\Lambda_{m,k}}\right\|}$ and $\mathbf{c}_i$ is the codeword. In the codebook generation, for example, one can use the random vector quantization (RVQ) codebook [11]. Note that the user k also quantizes the dominating PGI magnitude $\|\mathbf{g}_{\Lambda_k}\|$ and then feeds it back to the DU. After receiving $\hat{i}_k$ and $\|\mathbf{g}_{\Lambda_k}\|$, DU reconstructs the original dominating PGI as $\hat{\mathbf{g}}_{\Lambda_k} = \|\mathbf{g}_{\Lambda_k}\|\,\mathbf{c}_{\hat{i}_k}$.

2.5 Performance Analysis of the Dominating Path Gain Information Feedback

In this section, we provide the performance analysis of the proposed dominating PGI feedback scheme. Specifically, we analyze the upper bound of rate gap between the ideal system with perfect PGI and the realistic system with finite rate PGI feedback. To this end, we first express the rate gap as a function of the normalized distortion induced from the quantization of dominating PGI vector $\mathbf{g}_{\Lambda_k}$. We then find out the upper bound of the normalized quantization distortion and also the rate gap. Finally, we obtain the number of feedback bits required to maintain a constant rate gap with the ideal system.

2.5.1 Rate Gap Analysis of the Dominating PGI Feedback

The achievable rate R_k of the user k in the realistic system with finite rate feedback is

$$R_k = \log_2\left(1 + \frac{\mathbb{E}\left[\left|\sum_{m=1}^{M} \mathbf{g}_{m,k}^{\mathrm{H}} \mathbf{A}_{m,k}^{\mathrm{H}} \mathbf{V}_{\Lambda_{m,k}} \hat{\mathbf{g}}_{\Lambda_{m,k}}\right|^2\right]}{\sum_{j\neq k}^{K} \mathbb{E}\left[\left|\sum_{m=1}^{M} \mathbf{g}_{m,k}^{\mathrm{H}} \mathbf{A}_{m,k}^{\mathrm{H}} \mathbf{V}_{\Lambda_{m,j}} \hat{\mathbf{g}}_{\Lambda_{m,j}}\right|^2\right] + \sigma_n^2}\right) \tag{2.36}$$

$$= \log_2\left(1 + \frac{\mathrm{DS}_k + \mathrm{US}_k}{\mathrm{IS}_k + \sigma_n^2}\right), \tag{2.37}$$

where $\hat{\mathbf{g}}_{\Lambda_{m,k}}$ is the dominating PGI feedback and

$$\mathrm{DS}_k = \mathbb{E}\left[\left|\sum_{m=1}^{M} \mathbf{g}_{\Lambda_{m,k}}^{\mathrm{H}} \mathbf{A}_{\Lambda_{m,k}}^{\mathrm{H}} \mathbf{V}_{\Lambda_{m,k}} \hat{\mathbf{g}}_{\Lambda_{m,k}}\right|^2\right] \tag{2.38}$$

$$\mathrm{US}_k = \mathbb{E}\left[\left|\sum_{m=1}^{M} \mathbf{g}_{\Lambda_{m,k}^{\mathsf{C}}}^{\mathrm{H}} \mathbf{A}_{\Lambda_{m,k}^{\mathsf{C}}}^{\mathrm{H}} \mathbf{V}_{\Lambda_{m,k}} \hat{\mathbf{g}}_{\Lambda_{m,k}}\right|^2\right] \tag{2.39}$$

$$\mathrm{IS}_k = \sum_{j\neq k}^{K} \mathbb{E}\left[\left|\sum_{m=1}^{M} \mathbf{g}_{m,k}^{\mathrm{H}} \mathbf{A}_{m,k}^{\mathrm{H}} \mathbf{V}_{\Lambda_{m,j}} \hat{\mathbf{g}}_{\Lambda_{m,j}}\right|^2\right]. \tag{2.40}$$

Note that R_k consists of the desired signal part DS_k, the unselected signal part US_k, and the interference signal part IS_k, respectively. Since $\mathbf{g}_{\Lambda_{m,k}}$ is independent of $\mathbf{g}_{\Lambda_{m,k}^{\mathsf{C}}}$ and $\mathbf{g}_{m,j}$ $(j \neq k)$, $\hat{\mathbf{g}}_{\Lambda_{m,k}}$ is also independent of $\mathbf{g}_{\Lambda_{m,k}^{\mathsf{C}}}$ and $\mathbf{g}_{m,j}$ $(j \neq k)$ so that the quantization of $\mathbf{g}_{\Lambda_{m,k}}$ only affects DS_k. This means that US_k and IS_k remain unchanged regardless of the quantization. Thus, the achievable rates for the realistic system R_k and the ideal system $R_k^{(\text{ideal})}$ are given by

$$R_k = \log_2\left(1 + \frac{\mathrm{DS}_k + \mathrm{US}_k}{\mathrm{IS}_k + \sigma_n^2}\right) \tag{2.41}$$

$$R_k^{(\text{ideal})} = \log_2\left(1 + \frac{\mathrm{DS}_k^{(\text{ideal})} + \mathrm{US}_k}{\mathrm{IS}_k + \sigma_n^2}\right), \tag{2.42}$$

where $\mathrm{DS}_k^{(\text{ideal})}$ is the desired signal constructed from perfect PGI as $\mathrm{DS}_k^{(\text{ideal})} = \mathbb{E}\left[\left|\sum_{m=1}^{M} \mathbf{g}_{\Lambda_{m,k}}^{\mathrm{H}} \mathbf{A}_{\Lambda_{m,k}}^{\mathrm{H}} \mathbf{V}_{\Lambda_{m,k}} \mathbf{g}_{\Lambda_{m,k}}\right|^2\right]$. Then the rate gap ΔR_k is

$$\Delta R_k = R_k^{(\text{ideal})} - R_k \tag{2.43}$$

$$= \log_2\left(1+\frac{\mathrm{DS}_k^{(\text{ideal})} + \mathrm{US}_k}{\mathrm{IS}_k + \sigma_n^2}\right) - \log_2\left(1+\frac{\mathrm{DS}_k + \mathrm{US}_k}{\mathrm{IS}_k + \sigma_n^2}\right). \tag{2.44}$$

As mentioned, the only difference between R_k^{ideal} and R_k is the desired signal part. Based on this observation, we express ΔR_k as a function of signal-to-noise-ratio (SNR) and the normalized quantization distortion D_k of the desired signal DS_k. D_k is defined as

$$D_k = \frac{\mathrm{DS}_k^{(\text{ideal})} - \mathrm{DS}_k}{\mathrm{DS}_k^{(\text{ideal})}}. \tag{2.45}$$

Proposition 1. *The upper bound of rate gap ΔR_k between the ideal system with perfect PGI and the realistic system with finite rate feedback of the user k is expressed as a function of SNR and D_k. That is,*

$$\Delta R_k \leq \log_2\left(1 + \frac{D_k}{1-D_k}\frac{\mathrm{SNR}}{1+\mathrm{SNR}}\right). \tag{2.46}$$

Proof. From (2.44), the rate gap ΔR_k is expressed as

$$\Delta R_k = \log_2\left(1+\frac{\mathrm{DS}_k^{(\text{ideal})} - \mathrm{DS}_k}{\mathrm{DS}_k+\mathrm{US}_k+\mathrm{IS}_k+\sigma_n^2}\right) \tag{2.47}$$

$$= \log_2\left(1+\frac{\mathrm{DS}_k^{(\text{ideal})}-\mathrm{DS}_k}{\mathrm{DS}_k}\frac{\mathrm{DS}_k}{\mathrm{DS}_k+\mathrm{US}_k+\mathrm{IS}_k+\sigma_n^2}\right) \tag{2.48}$$

$$\overset{(a)}{=} \log_2\left(1+\frac{D_k}{1-D_k}\frac{\mathrm{DS}_k}{\mathrm{DS}_k+\mathrm{US}_k+\mathrm{IS}_k+\sigma_n^2}\right), \tag{2.49}$$

where (a) is from the definition of D_k in (2.45). By using the fact that $\mathrm{SNR} = \frac{\mathrm{DS}_k+\mathrm{US}_k+\mathrm{IS}_k}{\sigma_n^2}$, we obtain the desired upper bound of ΔR_k as

$$\Delta R_k = \log_2\left(1+\frac{D_k}{1-D_k}\frac{\mathrm{DS}_k}{\left(1+\frac{1}{\mathrm{SNR}}\right)(\mathrm{DS}_k+\mathrm{US}_k+\mathrm{IS}_k)}\right) \tag{2.50}$$

$$\leq \log_2\left(1+\frac{D_k}{1-D_k}\frac{\mathrm{SNR}}{1+\mathrm{SNR}}\right). \tag{2.51}$$

□

Now, we analyze the upper bound of the normalized quantization distortion D_k to find out the closed-form upper bound of the rate gap ΔR_k. In order to simplify the expression in (2.45), we use the notation $\mathbf{A}_{\Lambda_k} = \text{diag}(\mathbf{A}_{\Lambda_{1,k}}, \cdots, \mathbf{A}_{\Lambda_{M,k}})$ and $\mathbf{V}_{\Lambda_k} = \text{diag}(\mathbf{V}_{\Lambda_{1,k}}, \cdots, \mathbf{V}_{\Lambda_{M,k}})$. Then, we have

$$D_k = \frac{\mathbb{E}\left[\left|\mathbf{g}_{\Lambda_k}^{\text{H}} \mathbf{A}_{\Lambda_k}^{\text{H}} \mathbf{V}_{\Lambda_k} \mathbf{g}_{\Lambda_k}\right|^2\right] - \mathbb{E}\left[\left|\mathbf{g}_{\Lambda_k}^{\text{H}} \mathbf{A}_{\Lambda_k}^{\text{H}} \mathbf{V}_{\Lambda_k} \hat{\mathbf{g}}_{\Lambda_k}\right|^2\right]}{\mathbb{E}\left[\left|\mathbf{g}_{\Lambda_k}^{\text{H}} \mathbf{A}_{\Lambda_k}^{\text{H}} \mathbf{V}_{\Lambda_k} \mathbf{g}_{\Lambda_k}\right|^2\right]} \tag{2.52}$$

$$= 1 - \frac{\mathbb{E}\left[\left|\mathbf{g}_{\Lambda_k}^{\text{H}} \mathbf{A}_{\Lambda_k}^{\text{H}} \mathbf{V}_{\Lambda_k} \hat{\mathbf{g}}_{\Lambda_k}\right|^2\right]}{\mathbb{E}\left[\left|\mathbf{g}_{\Lambda_k}^{\text{H}} \mathbf{A}_{\Lambda_k}^{\text{H}} \mathbf{V}_{\Lambda_k} \mathbf{g}_{\Lambda_k}\right|^2\right]} \tag{2.53}$$

$$\overset{(a)}{=} 1 - \frac{\mathbb{E}\left[\|\mathbf{g}_{\Lambda_k}\|^4 \left|\bar{\mathbf{g}}_{\Lambda_k}^{\text{H}} \mathbf{A}_{\Lambda_k}^{\text{H}} \mathbf{V}_{\Lambda_k} \mathbf{c}_{\hat{i}_k}\right|^2\right]}{\mathbb{E}\left[\|\mathbf{g}_{\Lambda_k}\|^4 \left|\bar{\mathbf{g}}_{\Lambda_k}^{\text{H}} \mathbf{A}_{\Lambda_k}^{\text{H}} \mathbf{V}_{\Lambda_k} \bar{\mathbf{g}}_{\Lambda_k}\right|^2\right]} \tag{2.54}$$

$$= 1 - \frac{\mathbb{E}\left[\left|\bar{\mathbf{g}}_{\Lambda_k}^{\text{H}} \mathbf{A}_{\Lambda_k}^{\text{H}} \mathbf{V}_{\Lambda_k} \mathbf{c}_{\hat{i}_k}\right|^2\right]}{\mathbb{E}\left[\left|\bar{\mathbf{g}}_{\Lambda_k}^{\text{H}} \mathbf{A}_{\Lambda_k}^{\text{H}} \mathbf{V}_{\Lambda_k} \bar{\mathbf{g}}_{\Lambda_k}\right|^2\right]}, \tag{2.55}$$

where (a) is due to the independence of the dominating PGI magnitude $\|\mathbf{g}_{\Lambda_k}\|$ and the dominating PGI direction $\bar{\mathbf{g}}_{\Lambda_k}$. In the following proposition, we provide an upper bound of D_k.

Proposition 2. *The normalized quantization distortion D_k of the user k is upper bounded as*

$$D_k \leq \frac{L - \delta_k}{(L-1)(1+\delta_k)} 2^{-\frac{B}{L-1}}, \tag{2.56}$$

where $\delta_k = \frac{\sum_{m=1}^{M} \|\mathbf{A}_{\Lambda_{m,k}}^{\text{H}} \mathbf{V}_{\Lambda_{m,k}}\|_{\text{F}}^2}{|\sum_{m=1}^{M} \text{tr}(\mathbf{A}_{\Lambda_{m,k}}^{\text{H}} \mathbf{V}_{\Lambda_{m,k}})|^2}$. Furthermore, D_k is generally upper bounded as $D_k \leq 2^{-\frac{B}{L-1}}$.

Proof. From the simplified expression in (2.55), what we need to do is to compute the closed-form expression of the numerator $\mathbb{E}\left[\left|\bar{\mathbf{g}}_{\Lambda_k}^{\text{H}} \mathbf{A}_{\Lambda_k}^{\text{H}} \mathbf{V}_{\Lambda_k} \mathbf{c}_{\hat{i}_k}\right|^2\right]$ and the denominator $\mathbb{E}\left[\left|\bar{\mathbf{g}}_{\Lambda_k}^{\text{H}} \mathbf{A}_{\Lambda_k}^{\text{H}} \mathbf{V}_{\Lambda_k} \bar{\mathbf{g}}_{\Lambda_k}\right|^2\right]$. When the B-bit RVQ codebook $\mathcal{C}_k = \{\mathbf{c}_1, \cdots, \mathbf{c}_{2^B}\}$ is used, the correlation $\left|\bar{\mathbf{g}}_{\Lambda_k}^{\text{H}} \mathbf{c}_{\hat{i}_k}\right|^2$ between the dominating PGI direction $\bar{\mathbf{g}}_{\Lambda_k}$ and the chosen codeword $\mathbf{c}_{\hat{i}_k}$ is the maximum of 2^B independent β-distributed random variables with parameters 1 and $L-1$ [11]. Moreover, it has been proved that the expectation of this correlation is lower bounded as

$$\gamma = \mathbb{E}\left[\left|\bar{\mathbf{g}}_{\Lambda_k}^{\mathrm{H}} \mathbf{c}_{\hat{i}_k}\right|^2\right] = 1 - 2^B \beta\left(2^B, \frac{L}{L-1}\right) \geq 1 - 2^{-\frac{B}{L-1}}, \tag{2.57}$$

where $\beta(a,b)$ is the beta function defined as $\beta(a,b) = \frac{\Gamma(a)\Gamma(b)}{\Gamma(a+b)}$. Unfortunately, we cannot directly use this result since $\mathbf{A}_{\Lambda_k}^{\mathrm{H}} \mathbf{V}_{\Lambda_k}$ is inserted in the middle of $\mathbb{E}\left[\left|\bar{\mathbf{g}}_{\Lambda_k}^{\mathrm{H}} \mathbf{A}_{\Lambda_k}^{\mathrm{H}} \mathbf{V}_{\Lambda_k} \mathbf{c}_{\hat{i}_k}\right|^2\right]$. To handle this, we exploit the property that the dominating PGI direction $\bar{\mathbf{g}}_{\Lambda_k}$ can be written as a sum of two vectors: one in the direction of the chosen codeword $\mathbf{c}_{\hat{i}_k}$ and the other s isotropically distributed in the null space of $\mathbf{c}_{\hat{i}_k}$ [11]:

$$\bar{\mathbf{g}}_{\Lambda_k} = \sqrt{Z}\mathbf{c}_{\hat{i}_k} + \sqrt{1-Z}\mathbf{s}, \tag{2.58}$$

where Z is β-distributed according to $\left|\bar{\mathbf{g}}_{\Lambda_k}^{\mathrm{H}} \mathbf{c}_{\hat{i}_k}\right|^2$ so that $\mathbb{E}\left[Z\right] = \gamma$ and is independent with s. By plugging (2.58) into the nominator $\mathbb{E}\left[\left|\bar{\mathbf{g}}_{\Lambda_k}^{\mathrm{H}} \mathbf{A}_{\Lambda_k}^{\mathrm{H}} \mathbf{V}_{\Lambda_k} \mathbf{c}_{\hat{i}_k}\right|^2\right]$, we obtain

$$\mathbb{E}\left[\left|\bar{\mathbf{g}}_{\Lambda_k}^{\mathrm{H}} \mathbf{A}_{\Lambda_k}^{\mathrm{H}} \mathbf{V}_{\Lambda_k} \mathbf{c}_{\hat{i}_k}\right|^2\right] = \mathbb{E}\left[\mathbf{c}_{\hat{i}_k}^{\mathrm{H}} \mathbf{V}_{\Lambda_k}^{\mathrm{H}} \mathbf{A}_{\Lambda_k}\Big(Z\mathbf{c}_{\hat{i}_k}\mathbf{c}_{\hat{i}_k}^{\mathrm{H}} + (1-Z)\mathbf{s}\mathbf{s}^{\mathrm{H}}\Big)\mathbf{A}_{\Lambda_k}^{\mathrm{H}} \mathbf{V}_{\Lambda_k} \mathbf{c}_{\hat{i}_k}\right] \tag{2.59}$$

$$= \gamma\mathbb{E}\left[\left|\mathbf{c}_{\hat{i}_k}^{\mathrm{H}} \mathbf{A}_{\Lambda_k}^{\mathrm{H}} \mathbf{V}_{\Lambda_k} \mathbf{c}_{\hat{i}_k}\right|^2\right] + (1-\gamma)\,\mathbb{E}\left[\left|\mathbf{s}^{\mathrm{H}} \mathbf{A}_{\Lambda_k}^{\mathrm{H}} \mathbf{V}_{\Lambda_k} \mathbf{c}_{\hat{i}_k}\right|^2\right]. \tag{2.60}$$

Using Lemma 3 (see Appendix A), we obtain the closed-form expression of the first term of (2.60) as

$$\mathbb{E}\left[\left|\mathbf{c}_{\hat{i}_k}^{\mathrm{H}} \mathbf{A}_{\Lambda_k}^{\mathrm{H}} \mathbf{V}_{\Lambda_k} \mathbf{c}_{\hat{i}_k}\right|^2\right] = \frac{1}{L(L+1)}\left(\left|\mathrm{tr}\big(\mathbf{A}_{\Lambda_k}^{\mathrm{H}} \mathbf{V}_{\Lambda_k}\big)\right|^2 + \left\|\mathbf{A}_{\Lambda_k}^{\mathrm{H}} \mathbf{V}_{\Lambda_k}\right\|_{\mathrm{F}}^2\right). \tag{2.61}$$

Since s is in the null space of $\mathbf{c}_{\hat{i}_k}$ and s and $\mathbf{c}_{\hat{i}_k}$ are correlated, it is difficult to obtain the closed-form expression of the second term of (2.60). As a remedy, we use the law of total expectation given by

$$\mathbb{E}_{\mathbf{s},\mathbf{c}_{\hat{i}_k}}\left[\left|\mathbf{s}^{\mathrm{H}}\mathbf{A}_{\Lambda_k}^{\mathrm{H}}\mathbf{V}_{\Lambda_k}\mathbf{c}_{\hat{i}_k}\right|^2\right] = \mathbb{E}_{\mathbf{c}_{\hat{i}_k}}\left[\mathbb{E}_{\mathbf{s}}\left[\left|\mathbf{s}^{\mathrm{H}}\mathbf{A}_{\Lambda_k}^{\mathrm{H}}\mathbf{V}_{\Lambda_k}\mathbf{c}_{\hat{i}_k}\right|^2 \mid \mathbf{c}_{\hat{i}_k}\right]\right] \tag{2.62}$$

$$= \mathbb{E}_{\mathbf{c}_{\hat{i}_k}}\left[\mathbf{c}_{\hat{i}_k}^{\mathrm{H}}\mathbf{V}_{\Lambda_k}^{\mathrm{H}}\mathbf{A}_{\Lambda_k}\mathbb{E}_{\mathbf{s}}\left[\mathbf{s}\mathbf{s}^{\mathrm{H}} \mid \mathbf{c}_{\hat{i}_k}\right]\mathbf{A}_{\Lambda_k}^{\mathrm{H}}\mathbf{V}_{\Lambda_k}\mathbf{c}_{\hat{i}_k}\right]. \tag{2.63}$$

In the following lemma, we present the closed-form expression of $\mathbb{E}_{\mathbf{s}}\left[\mathbf{s}\mathbf{s}^{\mathrm{H}} \mid \mathbf{c}_{\hat{i}_k}\right]$.

Lemma 2. *The conditional covariance of* s *for a given* $\mathbf{c}_{\hat{i}_k}$ *is*

$$\mathbb{E}_{\mathbf{s}}\left[\mathbf{s}\mathbf{s}^{H} \mid \mathbf{c}_{\hat{i}_k}\right] = \frac{1}{L-1}\left(\mathbf{I}_L - \mathbf{c}_{\hat{i}_k}\mathbf{c}_{\hat{i}_k}^{H}\right). \tag{2.64}$$

Proof. See Appendix B. □

By plugging (2.64) into the second term of (2.60), we obtain

$$\mathbb{E}\left[\left|\mathbf{s}^{\mathrm{H}}\mathbf{A}_{\Lambda_k}^{\mathrm{H}}\mathbf{V}_{\Lambda_k}\mathbf{c}_{\hat{i}_k}\right|^2\right] = \frac{1}{L-1}\mathbb{E}_{\mathbf{c}_{\hat{i}_k}}\left[\mathbf{c}_{\hat{i}_k}^{\mathrm{H}}\mathbf{V}_{\Lambda_k}^{\mathrm{H}}\mathbf{A}_{\Lambda_k}\left(\mathbf{I}_L - \mathbf{c}_{\hat{i}_k}\mathbf{c}_{\hat{i}_k}^{\mathrm{H}}\right)\mathbf{A}_{\Lambda_k}^{\mathrm{H}}\mathbf{V}_{\Lambda_k}\mathbf{c}_{\hat{i}_k}\right] \tag{2.65}$$

$$= \frac{1}{L-1}\left(\mathbb{E}_{\mathbf{c}_{\hat{i}_k}}\left[\left|\mathbf{A}_{\Lambda_k}^{\mathrm{H}}\mathbf{V}_{\Lambda_k}\mathbf{c}_{\hat{i}_k}\right|^2\right] - \mathbb{E}_{\mathbf{c}_{\hat{i}_k}}\left[\left|\mathbf{c}_{\hat{i}_k}^{\mathrm{H}}\mathbf{A}_{\Lambda_k}^{\mathrm{H}}\mathbf{V}_{\Lambda_k}\mathbf{c}_{\hat{i}_k}\right|^2\right]\right) \tag{2.66}$$

$$= \frac{1}{L-1}\left(\frac{1}{L}\left\|\mathbf{A}_{\Lambda_k}^{\mathrm{H}}\mathbf{V}_{\Lambda_k}\right\|_{\mathrm{F}}^2 - \frac{1}{L(L+1)}\left(\left|\mathrm{tr}\left(\mathbf{A}_{\Lambda_k}^{\mathrm{H}}\mathbf{V}_{\Lambda_k}\right)\right|^2 + \left\|\mathbf{A}_{\Lambda_k}^{\mathrm{H}}\mathbf{V}_{\Lambda_k}\right\|_{\mathrm{F}}^2\right)\right) \tag{2.67}$$

$$= \frac{1}{L^2-1}\left(\left\|\mathbf{A}_{\Lambda_k}^{\mathrm{H}}\mathbf{V}_{\Lambda_k}\right\|_{\mathrm{F}}^2 - \frac{1}{L}\left|\mathrm{tr}\left(\mathbf{A}_{\Lambda_k}^{\mathrm{H}}\mathbf{V}_{\Lambda_k}\right)\right|^2\right). \tag{2.68}$$

Finally, by plugging (2.61) and (2.68) into (2.60), we get the closed-form expression of the nominator $\mathbb{E}\left[\left|\bar{\mathbf{g}}_{\Lambda_k}^{\mathrm{H}}\mathbf{A}_{\Lambda_k}^{\mathrm{H}}\mathbf{V}_{\Lambda_k}\mathbf{c}_{\hat{i}_k}\right|^2\right]$ as

$$\mathbb{E}\left[\left|\bar{\mathbf{g}}_{\Lambda_k}^{\mathrm{H}}\mathbf{A}_{\Lambda_k}^{\mathrm{H}}\mathbf{V}_{\Lambda_k}\mathbf{c}_{\hat{i}_k}\right|^2\right] = \frac{\gamma}{L(L+1)}\left(\left|\mathrm{tr}\left(\mathbf{A}_{\Lambda_k}^{\mathrm{H}}\mathbf{V}_{\Lambda_k}\right)\right|^2 + \left\|\mathbf{A}_{\Lambda_k}^{\mathrm{H}}\mathbf{V}_{\Lambda_k}\right\|_{\mathrm{F}}^2\right) + \frac{1-\gamma}{L^2-1}\left(\left\|\mathbf{A}_{\Lambda_k}^{\mathrm{H}}\mathbf{V}_{\Lambda_k}\right\|_{\mathrm{F}}^2 - \frac{1}{L}\left|\mathrm{tr}\left(\mathbf{A}_{\Lambda_k}^{\mathrm{H}}\mathbf{V}_{\Lambda_k}\right)\right|^2\right) \tag{2.69}$$

$$= \frac{L\gamma-1}{L(L^2-1)}\left|\mathrm{tr}\left(\mathbf{A}_{\Lambda_k}^{\mathrm{H}}\mathbf{V}_{\Lambda_k}\right)\right|^2 + \frac{L-\gamma}{L(L^2-1)}\left\|\mathbf{A}_{\Lambda_k}^{\mathrm{H}}\mathbf{V}_{\Lambda_k}\right\|_{\mathrm{F}}^2. \tag{2.70}$$

Next, we consider the denominator $\mathbb{E}\left[\left|\bar{\mathbf{g}}_{\Lambda_k}^{\mathrm{H}}\mathbf{A}_{\Lambda_k}^{\mathrm{H}}\mathbf{V}_{\Lambda_k}\bar{\mathbf{g}}_{\Lambda_k}\right|^2\right]$ in (2.55). Since both $\bar{\mathbf{g}}_{\Lambda_k}$ and $\mathbf{c}_{\hat{i}_k}$ are uniformly distributed on the surface of a L-dimensional unit sphere, the closed-form expression of $\mathbb{E}\left[\left|\bar{\mathbf{g}}_{\Lambda_k}^{\mathrm{H}}\mathbf{A}_{\Lambda_k}^{\mathrm{H}}\mathbf{V}_{\Lambda_k}\bar{\mathbf{g}}_{\Lambda_k}\right|^2\right]$ can be obtained in the same way to (2.61). Combining (2.61) and (2.70), the closed-form expression of the upper bound of D_k is simplified as

$$D_k = 1 - \frac{\frac{L\gamma-1}{L(L^2-1)}\left|\mathrm{tr}\left(\mathbf{A}_{\Lambda_k}^{\mathrm{H}}\mathbf{V}_{\Lambda_k}\right)\right|^2 + \frac{L-\gamma}{L(L^2-1)}\left\|\mathbf{A}_{\Lambda_k}^{\mathrm{H}}\mathbf{V}_{\Lambda_k}\right\|_{\mathrm{F}}^2}{\frac{1}{L(L+1)}\left(\left|\mathrm{tr}\left(\mathbf{A}_{\Lambda_k}^{\mathrm{H}}\mathbf{V}_{\Lambda_k}\right)\right|^2 + \left\|\mathbf{A}_{\Lambda_k}^{\mathrm{H}}\mathbf{V}_{\Lambda_k}\right\|_{\mathrm{F}}^2\right)} \tag{2.71}$$

$$= \frac{1-\gamma}{L-1}\frac{L\left|\mathrm{tr}\left(\mathbf{A}_{\Lambda_k}^{\mathrm{H}}\mathbf{V}_{\Lambda_k}\right)\right|^2 - \left\|\mathbf{A}_{\Lambda_k}^{\mathrm{H}}\mathbf{V}_{\Lambda_k}\right\|_{\mathrm{F}}^2}{\left|\mathrm{tr}\left(\mathbf{A}_{\Lambda_k}^{\mathrm{H}}\mathbf{V}_{\Lambda_k}\right)\right|^2 + \left\|\mathbf{A}_{\Lambda_k}^{\mathrm{H}}\mathbf{V}_{\Lambda_k}\right\|_{\mathrm{F}}^2} \tag{2.72}$$

$$= \frac{L-\delta_k}{(L-1)(1+\delta_k)}(1-\gamma) \tag{2.73}$$

$$\overset{(a)}{\leq} \frac{L-\delta_k}{(L-1)(1+\delta_k)}2^{-\frac{B}{L-1}}, \tag{2.74}$$

where $\delta_k = \frac{\sum_{m=1}^{M}\|\mathbf{A}_{\Lambda_{m,k}}^{\mathrm{H}}\mathbf{V}_{\Lambda_{m,k}}\|_{\mathrm{F}}^2}{|\sum_{m=1}^{M}\mathrm{tr}(\mathbf{A}_{\Lambda_{m,k}}^{\mathrm{H}}\mathbf{V}_{\Lambda_{m,k}})|^2}$ and (a) is due to (2.57). Noting that $\frac{1}{L} \leq \frac{\|\mathbf{C}\|_{\mathrm{F}}^2}{|\mathrm{tr}(\mathbf{C})|^2}$, we obtain a simple upper bound of D_k as

$$D_k \leq \frac{L-\frac{1}{L}}{(L-1)(1+\frac{1}{L})}2^{-\frac{B}{L-1}} = 2^{-\frac{B}{L-1}}. \tag{2.75}$$

$\square$

Since $\frac{1}{L} \leq \delta_k$, D_k is smaller than the quantization distortion of the conventional L-dimensional vector quantization $1-\gamma$ in (2.57). Note also that D_k is a function of the number of dominating paths L, not the number of transmit antennas N.

In Fig. 2.6, we plot the normalized quantization distortion D_k as a function of the number of dominating paths L. In this figure, we plot the numerical evaluation of D_k, the upper bound in (2.74), the simplified upper bound in (2.75), and the conventional L-dimensional vector quantization using RVQ codebook in (2.57). One can observe that the numerical evaluation is close to the derived upper bound. One can also observe

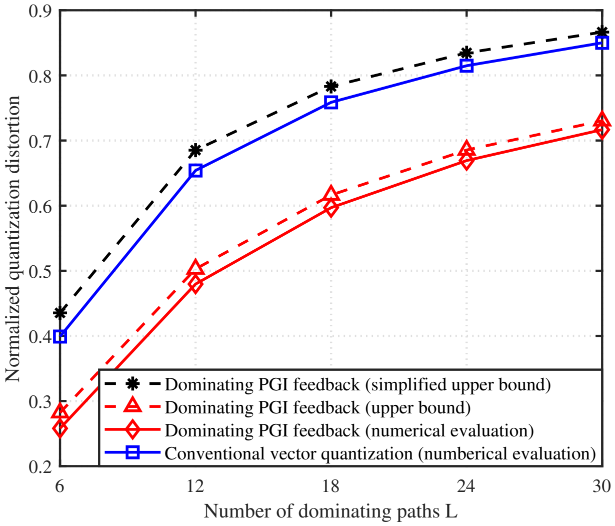

Figure 2.6: Normalized quantization distortion as a function of the number of dominating paths L ($M = 5$, $K = 5$, $N = 8$, $P = 6$, $B = 9$, SNR $= 17\,$dB)

that the normalized quantization distortion of the proposed scheme is much smaller than that of the conventional vector quantization.

Finally, by using Proposition 2, we obtain the closed-form expression on the upper bound of ΔR_k.

Theorem 2. *The per user rate gap ΔR_k between the ideal system using the perfect PGI and the realistic system using the finite rate feedback of the user k is upper bounded as*

$$\Delta R_k \leq \log_2\left(1+\frac{\text{SNR}}{1+\text{SNR}}\frac{(L-\delta_k)2^{-\frac{B}{L-1}}}{(L-1)(1+\delta_k)-(L-\delta_k)2^{-\frac{B}{L-1}}}\right), \tag{2.76}$$

where SNR *is the signal-to-noise-ratio.*

Proof. By plugging (2.56) into (2.46), we get

$$\Delta R_k \leq \log_2\left(1+\frac{\text{SNR}}{1+\text{SNR}}\frac{\frac{L-\delta_k}{(L-1)(1+\delta_k)}2^{-\frac{B}{L-1}}}{1-\frac{L-\delta_k}{(L-1)(1+\delta_k)}2^{-\frac{B}{L-1}}}\right) \tag{2.77}$$

$$=\log_2\left(1+\frac{\text{SNR}}{1+\text{SNR}}\frac{(L-\delta_k)2^{-\frac{B}{L-1}}}{(L-1)(1+\delta_k)-(L-\delta_k)2^{-\frac{B}{L-1}}}\right). \tag{2.78}$$

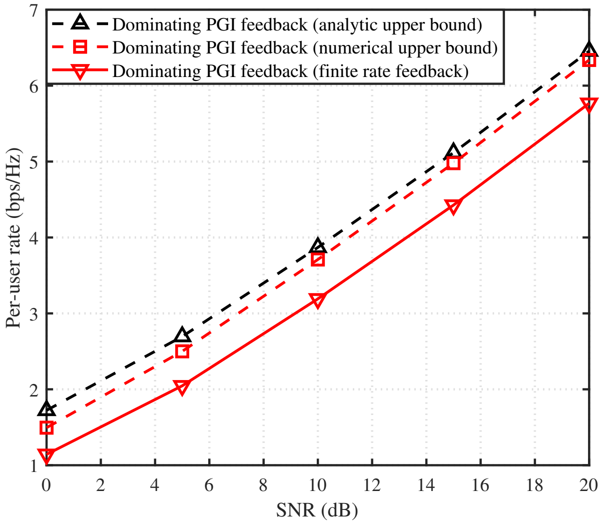

Figure 2.7: Per user rate as a function of SNR ($M = 5$, $K = 5$, $N = 8$, $P = 6$, $L = 8$, $B = 9$)

□

We can also obtain the number of feedback bits required to maintain a certain rate gap with the ideal system.

Proposition 3. *To maintain a rate gap between the proposed scheme with the ideal system with perfect PGI within* $\log_2(b)$ bps/Hz *per user, the number of feedback bits should satisfy*

$$B \geq (L-1)\log_2\left(\frac{b(\mathrm{SNR}+1)-1}{(\mathrm{SNR}+1)(b-1)}\frac{L-\delta_k}{(L-1)(1+\delta_k)}\right). \tag{2.79}$$

Proof. To maintain $\Delta R_k \leq \log_2(b)$, the number of feedback bits B should satisfy

$$1+\frac{\mathrm{SNR}}{1+\mathrm{SNR}}\frac{(L-\delta_k)2^{-\frac{B}{L-1}}}{(L-1)(1+\delta_k)-(L-\delta_k)2^{-\frac{B}{L-1}}} \leq b. \tag{2.80}$$

After simple manipulations, we get the desired result. □

In Fig. 2.7, we plot the per user rate as a function of SNR. We observe that the analytic upper bound obtained from the Theorem 2 is close to the upper bound obtained from the numerical evaluation. This means that by using a proper scaling of feedback bits in Proposition 3, the rate gap can be controlled effectively.

2.5.2 Dominating Path Number Selection

In the subsection, we discuss how to choose the dominating path number. In a nutshell, we compute the lower bound of the sum rate $\sum_{k=1}^{K} R_k\left(l\right)$ for each l ($l = 1, \cdots, MP$) and then choose the value L maximizing the sum rate. That is

$$L = \arg \max_{l=1,\cdots,MP} \sum_{k=1}^{K} R_k(l). \tag{2.81}$$

Note that $R_k(l)$ is obtained from the dominating path selection algorithm. In each iteration of this algorithm (see Section III.C), we obtain the dominating path indices $\{\Lambda_{m,k}\}$ and the precoding matrices $\{\mathbf{V}_{\Lambda_{m,k}}\}$ and then compute the lower bound of the rate using $\{\Lambda_{m,k}\}$ and $\{\mathbf{V}_{\Lambda_{m,k}}\}$[5].

2.6 Simulation Results

In this section, we investigate the sum rate performance of the proposed dominating PGI feedback scheme. For comparison, we use the conventional CSI feedback schemes with the AoD-adaptive subspace codebook [15] and the RVQ codebook [11]. Note that we use the same precoding scheme (centralized SLNR precoding [28]) and the power allocation strategy [25] for the conventional schemes as well as the proposed scheme.

In our simulations, we consider the FDD-based cell-free systems where $M = 5$ BSs equipped with $N = 8$ transmit antennas cooperatively serve $K = 5$ users equipped with a single antenna. We set the maximum transmit power of BS to 2 W and the total transmit power of cooperating BS group to 10 W. Also, we distribute the BSs and

---

[5] To be specific, the lower bound of the rate is $R_k(l) = R_k^{(\text{ideal})}(l) - \Delta R_k(l)$ where $R_k^{(\text{ideal})}(l)$ is the rate of ideal system with perfect PGI (see Theorem 1) and $\Delta R_k(l)$ is the upper bound of the rate gap over the ideal system (see Theorem 2).

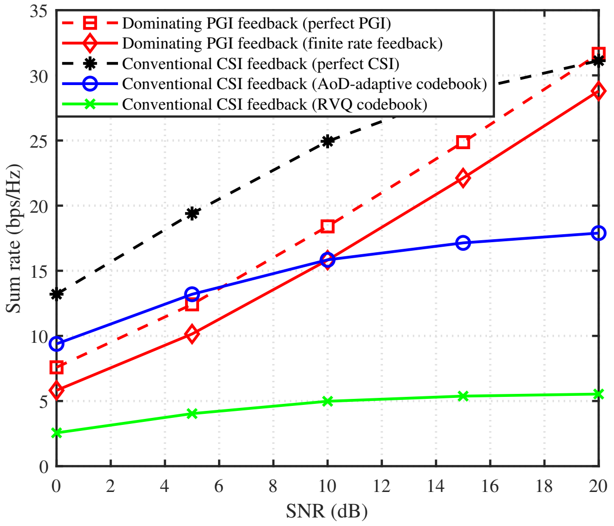

Figure 2.8: Sum rate as a function of SNR ($M = 5$, $K = 5$, $N = 8$, $P = 6$, $L = 8$, $B = 9$)

users randomly in a square area (size of a square is $1 \times 1\,\text{km}^2$). We use the downlink narrowband multi-path channel model whose carrier frequency is $f_c = 2\,\text{GHz}$ and set the number of propagation paths to $P = 6$. The angular spread of AoD is set to 10°. In the proposed dominating PGI feedback scheme, we select $L = 8$ dominating paths among all possible $MP = 30$ paths. Further, we use $B_{\text{CSI}} = 6$ and $B_{\text{CQI}} = 3$ for the channel direction and channel magnitude feedbacks so that the total number of feedback bits is $B = B_{\text{CSI}} + B_{\text{CQI}} = 9$. In addition, we fix the transmit SNR into 17 dB. To avoid special scenarios where the proposed technique is favorable (or unfavorable), we used 1000 randomly generated cell-free system realizations.

In Fig. 2.8, we plot the sum rate performance as a function of SNR. We observe that the proposed scheme outperforms the conventional schemes by a large margin in the mid and high SNR regions. For example, at 17 bps/Hz region, the proposed scheme achieves 8 dB gain over the conventional CSI feedback schemes. We also observe that the sum rate loss of the proposed scheme over the perfect PGI system is within 3 dB

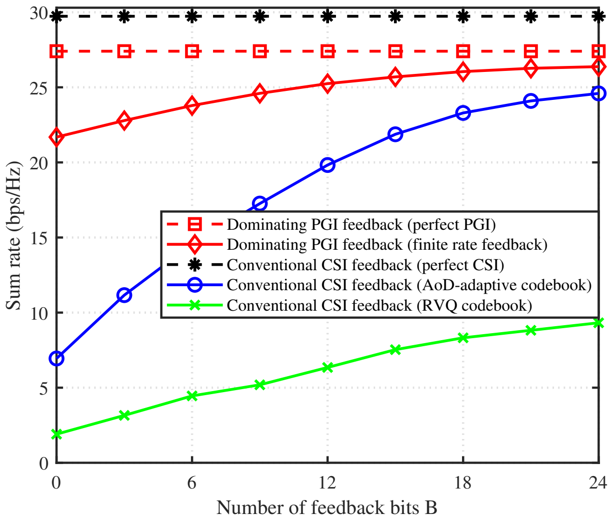

Figure 2.9: Sum rate as a function of the number of feedback bits B ($M = 5$, $K = 5$, $N = 8$, $P = 6$, $L = 8$, SNR $= 17\,\mathrm{dB}$)

whereas the conventional AoD-adaptive codebook scheme and the RVQ codebook scheme suffer more than 5 dB and 15 dB loss. As mentioned, this is because the number of feedback bits of the proposed scheme required to control the rate gap scales linearly with the number of dominating paths L while such is not the case for the conventional schemes. Further, it is worth mentioning that in the high SNR region, the performance of the proposed scheme increases linearly while no such behavior is observed for the conventional scheme. This is because the proposed scheme allocates power to a few dominating paths maximizing the sum rate while the conventional schemes allocates the power uniformly to every propagation paths.

In Fig. 2.9, we plot the sum rate as a function of the number of feedback bits B. We observe that the proposed dominating PGI feedback scheme achieves a significant feedback overhead reduction over the conventional schemes. For example, in achieving 23 bps/Hz, the proposed dominating PGI feedback scheme requires $B = 6$ bits while the AoD-adaptive subspace codebook scheme requires more than $B = 18$ bits, resulting

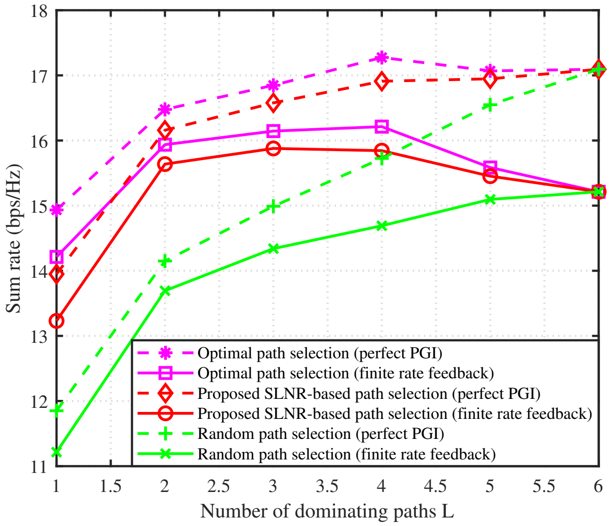

Figure 2.10: Sum rate as a function of the number of dominating paths L ($M = 3$, $K = 3$, $N = 8$, $P = 2$, $B = 9$, SNR $= 17$ dB)

in more than 60% reduction in feedback overhead. Further, the proposed scheme requires only $B = 9$ bits to maintain 3 bps/Hz rate gap with the ideal system while the conventional AoD-adaptive codebook scheme requires more than $B = 24$ bits to maintain the same rate gap.

In order to show the effectiveness of the proposed SLNR-based dominating path selection, we compare the proposed dominating path selection with the optimal path selection and the random path selection in Fig. 2.10. In the optimal path selection approach, we exhaustively search all possible choices of dominating paths and then find out the one maximizing the sum rate. Also, in the random path selection, we feed back the PGI of randomly selected paths. Note that due to the huge computational complexity of the optimal path selection (e.g., if $M = 5$, $K = 5$, $P = 6$, and $L = 8$, we need to search over $K^{\binom{MP}{L}} = 5^{5852925}$ possible choices), we set $M = 3$, $K = 3$, and $P = 2$ so that the total number of paths is $MP = 6$. Overall, we observe that the proposed SLNR-based dominating path selection performs comparable to the optimal

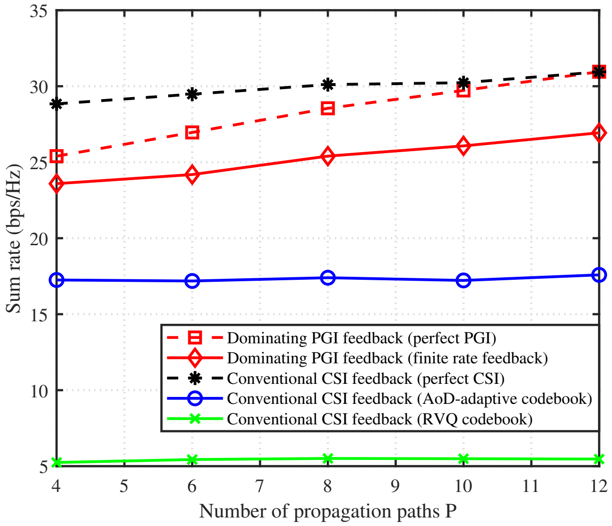

Figure 2.11: Sum rate as a function of the number of propagation paths P ($M = 5$, $K = 5$, $N = 8$, $L = \left\lfloor \frac{4MP}{-5-fig16} \right\rfloor$, $B = 9$, SNR $= 17\,\text{dB}$)

path selection and also provides a considerable sum rate gain over the random path selection.

In Fig. 2.11, we plot the sum rate as a function of the number of propagation paths P. We set $L = \left\lfloor \frac{4MP}{-5-fig16} \right\rfloor$ so that the number of dominating paths increases linearly with the number of propagation paths. Interestingly, the performance of the proposed dominating PGI scheme increases with the number of propagation paths while no such effect is observed from the conventional CSI feedback schemes. The reason is because when the number of propagation paths increases, we can choose the dominating paths from increased number of total paths so that we can achieve the gain obtained from the path diversity. Indeed, the performance gain of the proposed scheme over the conventional scheme increases from 6 bps/Hz to 9 bps/Hz when P increases from 4 to 12. This clearly demonstrates that the proposed scheme performs well even in the rich scattering environment.

In Fig. 2.12, we plot the sum rate as a function of the number of BSs. Similar to Fig.

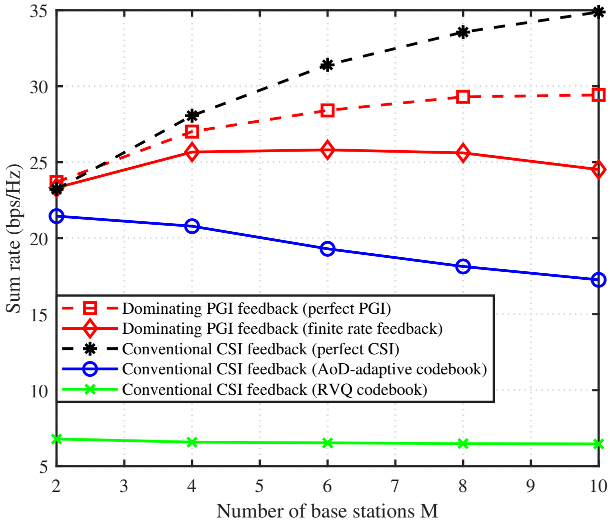

Figure 2.12: Sum rate as a function of the number of BSs M ($K = 5$, $N = 8$, $P = 6$, $L = \left\lfloor \frac{4MP}{-5-fig16} \right\rfloor$, $B = 12$, SNR $= 17$ dB)

11, we set $L = \left\lfloor \frac{4MP}{-5-fig16} \right\rfloor$. We observe that when the number of BSs increases, the rate loss of the proposed scheme is much smaller than that of the conventional schemes. In particular, when M increases from 2 to 10, the rate loss of the proposed scheme increases from 0.5 bps/Hz to 5 bps/Hz while that of the conventional scheme increases sharply from 3 bps/Hz to 17 bps/Hz.

In Fig. 2.13, we investigate the performance of proposed dominating PGI feedback when only one BS serves users in a cell. Although the gain obtained from the BS cooperation would not be significant in this scenario, we can still obtain fairly accurate dominating PGI and use this to control the inter-cell interference. As a result, the proposed scheme achieves more than 2.5 dB gain in the high SNR region over the AoD-adaptive subspace codebook scheme.

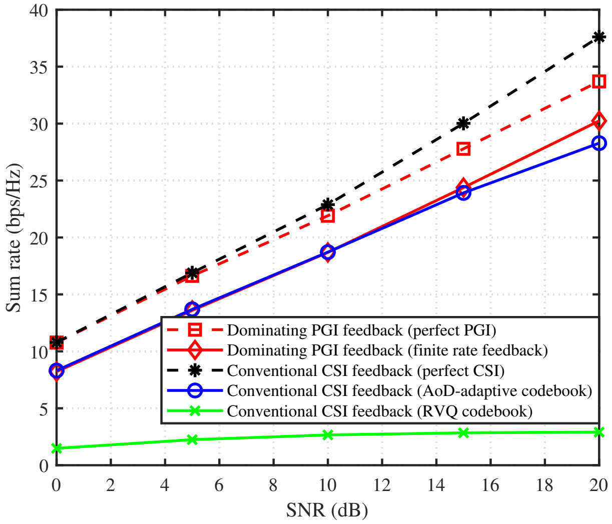

Figure 2.13: Sum rate as a function of SNR ($M = 1$, $K = 5$, $N = 16$, $P = 16$, $L = 12$, $B = 3$)

2.7 Summary

In this chapter, we proposed a novel feedback reduction technique for FDD-based cell-free systems. The key feature of the proposed scheme is to choose a few dominating paths among all possible propagation paths and then feed back the PGI of the chosen paths. Key observations in our work are that 1) the spatial domain channel is represented by a small number of multi-path components (AoDs and path gains) and 2) the AoDs are quite similar in the uplink and downlink channel owing to the angle reciprocity so that the BSs can acquire AoD information directly from the uplink pilot signal. Thus, by choosing a few dominating paths and only feed back the path gain of the chosen paths, we can achieve a significant reduction in the feedback overhead. We observed from the extensive simulations that the proposed scheme can achieve more than 60% of feedback overhead reduction over the conventional schemes relying on the CSI feedback.

2.8 Proofs

2.8.1 Proof of Theorem 1

We first compute the closed-form expression of numerator of R_k and then compute the closed-form expression of denominator of R_k. Since the channel vector is decomposed as

$$\begin{align} \mathbf{h}_{m,k} &= \mathbf{A}_{m,k}\mathbf{g}_{m,k} \tag{2.82} \\ &= \mathbf{A}_{\Lambda_{m,k}}\mathbf{g}_{\Lambda_{m,k}} + \mathbf{A}_{\Lambda^{\mathsf{C}}_{m,k}}\mathbf{g}_{\Lambda^{\mathsf{C}}_{m,k}}, \tag{2.83} \end{align}$$

the numerator of R_k is given by

$$\begin{align} \mathbb{E}\left[\left|\sum_{m=1}^{M}\mathbf{h}^{\mathrm{H}}_{m,k}\mathbf{w}_{m,k}\right|^2\right] &= \mathbb{E}\left[\left|\sum_{m=1}^{M}\mathbf{g}^{\mathrm{H}}_{m,k}\mathbf{A}^{\mathrm{H}}_{m,k}\mathbf{V}_{\Lambda_{m,k}}\mathbf{g}_{\Lambda_{m,k}}\right|^2\right] \tag{2.84} \\ &= \mathbb{E}\left[\left|\mathbf{g}^{\mathrm{H}}_{\Lambda_k}\mathbf{A}^{\mathrm{H}}_{\Lambda_k}\mathbf{V}_{\Lambda_k}\mathbf{g}_{\Lambda_k}\right|^2\right] + \mathbb{E}\left[\left|\mathbf{g}^{\mathrm{H}}_{\Lambda^{\mathsf{C}}_k}\mathbf{A}^{\mathrm{H}}_{\Lambda^{\mathsf{C}}_k}\mathbf{V}_{\Lambda_k}\mathbf{g}_{\Lambda_k}\right|^2\right] \tag{2.85} \\ &\overset{(a)}{=} \mathbb{E}\left[\|\mathbf{g}_{\Lambda_k}\|^4\right]\mathbb{E}\left[\left|\bar{\mathbf{g}}^{\mathrm{H}}_{\Lambda_k}\mathbf{A}^{\mathrm{H}}_{\Lambda_k}\mathbf{V}_{\Lambda_k}\bar{\mathbf{g}}_{\Lambda_k}\right|^2\right] \nonumber \\ &\quad + \mathbb{E}\left[\|\mathbf{g}_{\Lambda_k}\|^2\|\mathbf{g}_{\Lambda^{\mathsf{C}}_k}\|^2\right]\mathbb{E}\left[\left|\bar{\mathbf{g}}^{\mathrm{H}}_{\Lambda^{\mathsf{C}}_k}\mathbf{A}^{\mathrm{H}}_{\Lambda^{\mathsf{C}}_k}\mathbf{V}_{\Lambda_k}\bar{\mathbf{g}}_{\Lambda_k}\right|^2\right] \tag{2.86} \\ &= L(L+1)\mathbb{E}\left[\left|\bar{\mathbf{g}}^{\mathrm{H}}_{\Lambda_k}\mathbf{A}^{\mathrm{H}}_{\Lambda_k}\mathbf{V}_{\Lambda_k}\bar{\mathbf{g}}_{\Lambda_k}\right|^2\right] + L^2\mathbb{E}\left[\left|\bar{\mathbf{g}}^{\mathrm{H}}_{\Lambda^{\mathsf{C}}_k}\mathbf{A}^{\mathrm{H}}_{\Lambda^{\mathsf{C}}_k}\mathbf{V}_{\Lambda_k}\bar{\mathbf{g}}_{\Lambda_k}\right|^2\right], \tag{2.87} \end{align}$$

where (a) is due to the independence of the vector norm $\|\mathbf{g}_{\Lambda_k}\|$ and the vector direction $\bar{\mathbf{g}}_{\Lambda_k}$. Since $\bar{\mathbf{g}}_{\Lambda_k}$ and $\bar{\mathbf{g}}_{\Lambda^{\mathsf{C}}_k}$ are independent, the closed-form expression of the second term in (2.87) is

$$\begin{align} \mathbb{E}\left[\left|\bar{\mathbf{g}}^{\mathrm{H}}_{\Lambda^{\mathsf{C}}_k}\mathbf{A}^{\mathrm{H}}_{\Lambda^{\mathsf{C}}_k}\mathbf{V}_{\Lambda_k}\bar{\mathbf{g}}_{\Lambda_k}\right|^2\right] &= \mathbb{E}\left[\mathrm{tr}\left(\bar{\mathbf{g}}^{\mathrm{H}}_{\Lambda_k}\mathbf{V}^{\mathrm{H}}_{\Lambda_k}\mathbf{A}_{\Lambda^{\mathsf{C}}_k}\bar{\mathbf{g}}_{\Lambda^{\mathsf{C}}_k}\bar{\mathbf{g}}^{\mathrm{H}}_{\Lambda^{\mathsf{C}}_k}\mathbf{A}^{\mathrm{H}}_{\Lambda^{\mathsf{C}}_k}\mathbf{V}_{\Lambda_k}\bar{\mathbf{g}}_{\Lambda_k}\right)\right] \tag{2.88} \\ &= \mathrm{tr}\left(\mathbb{E}\left[\bar{\mathbf{g}}_{\Lambda_k}\bar{\mathbf{g}}^{\mathrm{H}}_{\Lambda_k}\right]\mathbf{V}^{\mathrm{H}}_{\Lambda_k}\mathbf{A}_{\Lambda^{\mathsf{C}}_k}\mathbb{E}\left[\bar{\mathbf{g}}_{\Lambda^{\mathsf{C}}_k}\bar{\mathbf{g}}^{\mathrm{H}}_{\Lambda^{\mathsf{C}}_k}\right]\mathbf{A}^{\mathrm{H}}_{\Lambda^{\mathsf{C}}_k}\mathbf{V}_{\Lambda_k}\right) \tag{2.89} \\ &= \frac{1}{L^2}\left\|\mathbf{A}^{\mathrm{H}}_{\Lambda^{\mathsf{C}}_k}\mathbf{V}_{\Lambda_k}\right\|^2_{\mathrm{F}}. \tag{2.90} \end{align}$$

Whereas, the closed-form expression of the first term in (2.87) is not easy to compute. To address this issue, we use the following lemma.

Lemma 3. *Let* $\mathbf{A}$ *be a* $L \times L$ *matrix,* $\mathbf{g}$ *be a* $L \times 1$ *complex normal vector, and* $\bar{\mathbf{g}} = \frac{\mathbf{g}}{|\mathbf{g}|}$. *Then,*

$$\mathbb{E}\Big[\big|\bar{\mathbf{g}}^{\mathrm{H}}\mathbf{A}\bar{\mathbf{g}}\big|^2\Big] = \frac{1}{L(L+1)}\big(|\mathrm{tr}(\mathbf{A})|^2 + \|\mathbf{A}\|_{\mathrm{F}}^2\big). \tag{2.91}$$

Proof. Let (i,j)-th element of $\mathbf{A}$ be $a_{i,j}$ and i-th element of $\bar{\mathbf{g}}$ be g_i. Then,

$$\begin{aligned}
\mathbb{E}\Big[\big|\bar{\mathbf{g}}^{\mathrm{H}}\mathbf{A}\bar{\mathbf{g}}\big|^2\Big] &= \mathbb{E}\Big[\Big|\sum_{i,j} a_{i,j} g_i^* g_j\Big|^2\Big] &(2.92)\\
&= \mathbb{E}\Big[\Big|\sum_{i} a_{i,i} |g_i|^2\Big|^2\Big] + \mathbb{E}\Big[\Big|\sum_{i\neq j} a_{i,j} g_i^* g_j\Big|^2\Big] &(2.93)\\
&= \sum_i |a_{i,i}|^2 \mathbb{E}\big[|g_i|^4\big] + \sum_{i\neq j} a_{i,i}^* a_{j,j}\mathbb{E}\big[|g_i|^2|g_j|^2\big]\\
&\quad + \sum_{i\neq j}|a_{i,j}|^2\mathbb{E}\big[|g_i|^2|g_j|^2\big] &(2.94)\\
&\overset{(a)}{=} \frac{2}{L(L+1)}\sum_i |a_{i,i}|^2 + \frac{1}{L(L+1)}\sum_{i\neq j} a_{i,i}^* a_{j,j}\\
&\quad + \frac{1}{L(L+1)}\sum_{i\neq j}|a_{i,j}|^2 &(2.95)\\
&= \frac{1}{L(L+1)}\bigg(\Big|\sum_i a_{i,i}\Big|^2 + \sum_{i,j}|a_{i,j}|^2\bigg) &(2.96)\\
&= \frac{1}{L(L+1)}\big(|\mathrm{tr}\,(\mathbf{A})|^2 + \|\mathbf{A}\|_{\mathrm{F}}^2\big), &(2.97)
\end{aligned}$$

where (a) is due to the fact that $\mathbb{E}\big[|g_i|^4\big] = \frac{2}{L(L+1)}$ and $\mathbb{E}\big[|g_i|^2\big] = \mathbb{E}\big[|g_i|^2|g_j|^2\big] = \frac{1}{L(L+1)}$. □

By plugging the result of Lemma 3 and (2.90) into (2.87), we get

$$\begin{aligned}
\mathbb{E}\Big[\Big|\sum_{m=1}^{M}\mathbf{h}_{m,k}^{\mathrm{H}}\mathbf{w}_{m,k}\Big|^2\Big] &= \Big|\mathrm{tr}\big(\mathbf{A}_{\Lambda_k}^{\mathrm{H}}\mathbf{V}_{\Lambda_k}\big)\Big|^2 + \big\|\mathbf{A}_{\Lambda_k}^{\mathrm{H}}\mathbf{V}_{\Lambda_k}\big\|_{\mathrm{F}}^2 + \Big\|\mathbf{A}_{\Lambda_k^{\mathrm{C}}}^{\mathrm{H}}\mathbf{V}_{\Lambda_k}\Big\|_{\mathrm{F}}^2 &(2.98)\\
&= \Big|\mathrm{tr}\big(\mathbf{A}_{\Lambda_k}^{\mathrm{H}}\mathbf{V}_{\Lambda_k}\big)\Big|^2 + \big\|\mathbf{A}_{k}^{\mathrm{H}}\mathbf{V}_{\Lambda_k}\big\|_{\mathrm{F}}^2 &(2.99)\\
&= \Big|\sum_{m=1}^{M}\mathrm{tr}\big(\mathbf{A}_{\Lambda_{m,k}}^{\mathrm{H}}\mathbf{V}_{\Lambda_{m,k}}\big)\Big|^2 + \sum_{m=1}^{M}\big\|\mathbf{A}_{m,k}^{\mathrm{H}}\mathbf{V}_{\Lambda_{m,k}}\big\|_{\mathrm{F}}^2. &(2.100)
\end{aligned}$$

Next, since $\mathbf{g}_{m,k}$ and $\mathbf{g}_{\Lambda_{m,j}}$ are independent, the denominator of R_k can be obtained similarly to (2.88)–(2.90) as

$$\sum_{j\neq k}^{K}\mathbb{E}\left[\left|\sum_{m=1}^{M}\mathbf{h}_{m,k}^{\mathrm{H}}\mathbf{w}_{m,j}\right|^2\right]=\sum_{j\neq k}^{K}\mathbb{E}\left[\left|\sum_{m=1}^{M}\mathbf{g}_{m,k}^{\mathrm{H}}\mathbf{A}_{m,k}^{\mathrm{H}}\mathbf{V}_{\Lambda_{m,j}}\mathbf{g}_{\Lambda_{m,j}}\right|^2\right] \tag{2.101}$$

$$=\sum_{j\neq k}^{K}\sum_{m=1}^{M}\left\|\mathbf{A}_{m,k}^{\mathrm{H}}\mathbf{V}_{\Lambda_{m,j}}\right\|_{\mathrm{F}}^2. \tag{2.102}$$

Combining (2.100) and (2.102), we obtain the data rate expression in Theorem 1.

2.8.2 Proof of Proposition 2

Let $\{\mathbf{c}_{\hat{i}_k},\mathbf{u}_1,\cdots,\mathbf{u}_{L-1}\}$ be the orthonormal basis of $\mathbb{C}^L$. Also, let $\mathbf{U}=[\mathbf{u}_1,\cdots,\mathbf{u}_{L-1}]\in\mathbb{C}^{L\times(L-1)}$. Then, the null space of $\mathbf{c}_{\hat{i}_k}$ can be represented as $\{\mathbf{U}\boldsymbol{\alpha}\mid\|\boldsymbol{\alpha}\|=1\}$ where $\boldsymbol{\alpha}$ is isotropically distributed on the $(L-1)$-dimensional unit sphere. Hence, we have

$$\mathbb{E}\left[\mathbf{s}\mathbf{s}^{\mathrm{H}}\mid\mathbf{c}_{\hat{i}_k}\right]=\mathbf{U}\mathbb{E}\left[\boldsymbol{\alpha}\boldsymbol{\alpha}^{\mathrm{H}}\right]\mathbf{U}^{\mathrm{H}} \tag{2.103}$$

$$=\frac{1}{L-1}\mathbf{U}\mathbf{U}^{\mathrm{H}} \tag{2.104}$$

$$\overset{(a)}{=}\frac{1}{L-1}\left(\mathbf{I}_L-\mathbf{c}_{\hat{i}_k}\mathbf{c}_{\hat{i}_k}^{\mathrm{H}}\right), \tag{2.105}$$

where (a) is due to the fact that

$$\mathbf{I}_L=[\mathbf{c}_{\hat{i}_k},\mathbf{U}][\mathbf{c}_{\hat{i}_k},\mathbf{U}]^{\mathrm{H}} \tag{2.106}$$

$$=\mathbf{c}_{\hat{i}_k}\mathbf{c}_{\hat{i}_k}^{\mathrm{H}}+\mathbf{U}\mathbf{U}^{\mathrm{H}}. \tag{2.107}$$

Chapter 3

Efficient Channel Probing and Phase Shift Control for mmWave Reconfigurable Intelligent Surface-Aided Communications

In this chapter, we introduce a channel estimation technique for reconfigurable intelligent surface-assisted THz systems. Recently, an RIS that controls the reflection characteristics of incident signals has received a great deal of attention. To make the most of the RIS-aided systems, an acquisition of RIS reflected channel information at the base station (BS) is crucial. However, this task is by no means easy due to the pilot overhead induced by the large number of reflecting elements. In our work, we propose an efficient channel estimation and phase shift control technique reducing the pilot overhead of the RIS-aided mmWave systems. Key idea of the proposed scheme is to decompose the RIS reflected channel into three major components, i.e., static BS-RIS angles, quasi-static RIS-UE angles, and time-varying BS-RIS-UE path gains, and then estimate them in different time scales. By estimating the BS-RIS and RIS-UE angles occasionally and estimating only the path gains frequently, the proposed scheme achieves a significant reduction on the pilot overhead. Further, by optimizing the phase shifts using the channel components with relatively long coherence time, we can improve the channel estimation accuracy.

3.1 Introduction

As the standardization of 5G phase 2 (Rel. 16) has been completed and the commercialization is in progress, the visioning and planning of 6G communications have been initiated recently, with an aim to accomplish a hyper-connected society in 2030. The IMT vision forecasts that 6G will provide two orders of magnitude improvement over 5G in terms of throughput, energy efficiency, and operation cost [4]. As a means to achieve this relentless goal, reconfigurable intelligent surface (RIS)-aided communications have received a great deal of attention recently [29]. In essence, RIS is a planar array consisting of a large number of low-cost passive reflecting elements, each of which can induce a phase shift to the incident signal. In contrast to the traditional communication systems where the wireless channel is unchangeable, RIS-aided systems proactively modify the wireless channel by adjusting the phase shifts of reflecting elements, thereby enhancing the throughput significantly. For instance, when the direct link between the base station (BS) and the user equipment (UE) is blocked by obstacles, RIS can provide a virtual line-of-sight (LoS) link via intelligent signal reflection, resulting in an improvement of coverage.

To make the most of the RIS-aided systems, the phase shifts of RIS reflecting elements should be properly configured based on the wireless propagation environments. To do so, an acquisition of downlink channel information at the BS is of great importance[1]. However, this task is by no means easy due to the huge pilot overhead induced by the large number of RIS reflecting elements. In fact, in the RIS-aided systems, the BS needs to acquire not only the conventional direct channel between the BS and UE but also the channels reflected by RIS (i.e., BS to RIS and RIS to UE channels). Since the reflecting elements have no dedicated RF chains to transmit or receive the pilot signals,

---

[1] To avoid the necessity of RIS reflected channel estimation, a beam training-based RIS phase shift control techniques have been proposed in [30, 31]. Potential drawback of these schemes is that the RIS phase shifts are chosen from a pre-defined codebook with finite number of codewords so that the BS cannot obtain the optimal RIS phase shifts maximizing the throughput.

the BS needs to indirectly estimate the RIS reflected channels from the pilot signals. This clearly indicates that a considerable amount of pilot resources is needed for the acquisition of RIS reflected channel information. Indeed, this issue is pronounced in the RIS-aided mmWave systems due to the short coherence time of mmWave channel.

Recently, various approaches have been proposed to address the channel estimation issue of RIS-aided systems [32–35]. In [32], an on/off-based technique that turns on only a single reflecting element at a time and then estimates the channel of corresponding reflecting element has been proposed. In [33], a minimum mean squared error (MMSE)-based channel estimation has been proposed. In [34], a channel estimation technique that employs the parallel factor decomposition of RIS-aided channels has been proposed. Also, in [35], a technique that estimates the BS-RIS channel in a large time scale and estimates the RIS-UE channel in a small time scale has been proposed. Potential problem of these approaches is that the pilot overhead is considerable since the full-dimensional RIS reflected channel should be estimated.

To reduce the dimension of channel to be estimated, approaches that convert the original spatial-domain channel to the angular-domain channel have gained much interest recently [36–39]. In [36], a compressed sensing (CS)-based channel estimation scheme has been proposed. In [37], a channel estimation technique using the double-structured sparsity of the RIS reflected channels for multi-user RIS-aided systems has been proposed. Also, in [38, 39], manifold optimization (MO)-based channel estimation techniques that exploit the low-rank property of RIS reflected channel have been proposed. In these schemes, the total number of angular bins is unduly large (e.g., order of hundreds or thousands) since the BS-RIS angles, the RIS-UE angles, and the path gains are estimated simultaneously. In this case, the columns of system matrix (a.k.a. sensing matrix) will be highly correlated, degrading the estimation accuracy considerably.

An aim of this paper is to propose an efficient channel estimation framework reducing the pilot overhead of RIS-aided mmWave systems. Main idea of proposed scheme, henceforth referred to as *three-stage angular-domain channel estimation* (TAD-CE), is to decompose the angular-domain RIS reflected channel into three major components, i.e., *static BS-RIS angles*, *quasi-static RIS-UE angles*, and *time-varying BS-RIS-UE path gains*, and then estimate these components in different time scales. Our strategy is justified by two crucial observations that 1) the coherence time of angles is an order of magnitude longer than that of path gains [40] and 2) BS-RIS angles are quasi-static over the RIS-UE angles [35]. Using the proposed strategy, we can reduce the number of multi-path components to be estimated at each stage significantly over the conventional schemes estimating all components simultaneously. This, together with the fact that the number of multi-path components is much smaller than the number of reflecting elements, implies that TAD-CE requires far smaller pilot resources than the conventional scheme requires.

The main contributions of this work are as follows:

- We propose a novel three-stage channel estimation technique for the RIS-aided mmWave systems. Specifically, since the BS-RIS angles are determined primarily by the scattering geometry around the BS and RIS, they are not affected by the UE, and thus we estimate the BS-RIS angles before the UE connection. After the UE connection, since the angles vary much slower than the path gains, we estimate the RIS-UE angles occasionally and estimate only the BS-RIS-UE path gains frequently. In doing so, we can avoid the waste of pilot resources required for the frequent estimation of static or quasi-static channel components.

- We propose a phase shift control scheme to assist the proposed channel estimation framework. While the conventional studies focus on the design of phase shifts maximizing the throughput, not much work has been done on the design of phase shifts improving the channel estimation accuracy. Indeed, an accurate phase shift control in the channel estimation process is difficult since the BS cannot acquire the channel information used for the phase shift control before the channel estimation. In the proposed TAD-CE scheme, we exploit the channel components with relatively long coherence time to optimize the RIS phase shifts. By adjusting the RIS phase shifts to satisfy the desirable properties of system matrix (e.g., column orthogonality), we can improve the channel estimation accuracy without requiring additional pilot resources.

- We analyze the channel estimation error induced by the mismatch between the true angles and the discretized angular bin from which we demonstrate that the channel estimation error of TAD-CE is much smaller than that of the CS-based scheme. Also, from the numerical evaluations on the realistic RIS-aided mmWave systems, we show that TAD-CE outperforms the conventional schemes in terms of the normalized mean squared error (NMSE) and the pilot overhead reduction. For example, TAD-CE achieves more than $7\,\text{dB}$ NMSE gain and 80% pilot overhead reduction over the MMSE-based scheme. Even when compared with the CS-based scheme, TAD-CE achieves $5\,\text{dB}$ NMSE gain and 60% pilot overhead reduction.

Notations: Lower and upper case symbols are used to denote vectors and matrices, respectively. The superscripts $(\cdot)^{\mathrm{T}}$, $(\cdot)^{\mathrm{H}}$, and $(\cdot)^{\dagger}$ denote the transpose, hermitian transpose, and pseudo-inverse, respectively. $\|\mathbf{x}\|$ and $\|\mathbf{X}\|_{\mathrm{F}}$ are used as the Euclidean norm of a vector $\mathbf{x}$ and the Frobenius norm of a matrix $\mathbf{X}$, respectively. $\operatorname{tr}(\mathbf{X})$ denotes the trace of $\mathbf{X}$ and $\operatorname{diag}(\mathbf{x})$ denotes a diagonal matrix whose diagonal elements are $\mathbf{x}$. $\mathbf{X} \otimes \mathbf{Y}$ and $\mathbf{X} \odot \mathbf{Y}$ denote the Kronecker and Hadamard products of $\mathbf{X}$ and $\mathbf{Y}$, respectively. In addition, $\mathbf{X} * \mathbf{Y}$ and $\mathbf{X} \bullet \mathbf{Y}$ denote the column-wise and row-wise Khatri-Rao products of $\mathbf{X}$ and $\mathbf{Y}$, respectively.

3.2 RIS-Aided mmWave Systems

In this section, we discuss the RIS-aided mmWave systems and the conventional channel estimation scheme. We then present useful properties to develop our channel estimation framework.

3.2.1 RIS-Aided mmWave System Model

We consider the RIS-aided mmWave systems where a single-antenna UE transmits an uplink pilot signal and the BS equipped with a linear array of M antennas estimates the uplink channel from the pilot signal of UE. An RIS is equipped with a planar array of $N = N_x \times N_y$ passive reflecting elements, each of which is connected to the RIS controller responsible for the phase shift control. By exploiting the channel reciprocity of time-division duplexing (TDD) systems, the BS can recycle the acquired uplink channel information for the downlink data transmission.

In the RIS-aided systems, other than the direct channel between the BS and UE, the reflected channels (BS-RIS channel $\mathbf{G} \in \mathbb{C}^{M \times N}$ and RIS-UE channel $\mathbf{h}_r \in \mathbb{C}^N$) need to be considered. Since we focus on the estimation of RIS reflected channels, we assume that the direct link is blocked so that the uplink channel $\mathbf{h} \in \mathbb{C}^M$ from the UE to the BS is[2]

$$\mathbf{h} = \mathbf{G}\text{diag}(\boldsymbol{\phi})\mathbf{h}_r = \mathbf{G}\text{diag}(\mathbf{h}_r)\boldsymbol{\phi} = \mathbf{H}\boldsymbol{\phi}, \tag{3.1}$$

where $\mathbf{H} = \mathbf{G}\text{diag}(\mathbf{h}_r) \in \mathbb{C}^{M \times N}$ is the RIS reflected channel matrix, $\boldsymbol{\phi} = [e^{j\omega_1} \cdots e^{j\omega_N}]^{\mathrm{T}} \in \mathbb{C}^N$ is the phase shift vector, and $\omega_n \in [0, 2\pi)$ is the phase shift of n-th reflecting element[3].

3.2.2 RIS-aided mmWave Channel Model

We assume the narrowband block-fading multi-path channel model where the channel remains unchanged within a block of τ symbols and changes from block-to-block (see Fig. 3.1) [6, 14].

---

[2] By switching off all the reflecting elements, the direct channel can be acquired via conventional channel estimation technique.

[3] We assume the ideal phase shift model where the reflection amplitude and the phase shift are independent and the phase shifts can take a continuous value in $[0, 2\pi)$. Note that the proposed scheme can be readily extended to the practical systems with finite level of phase shifts via the phase quantization.

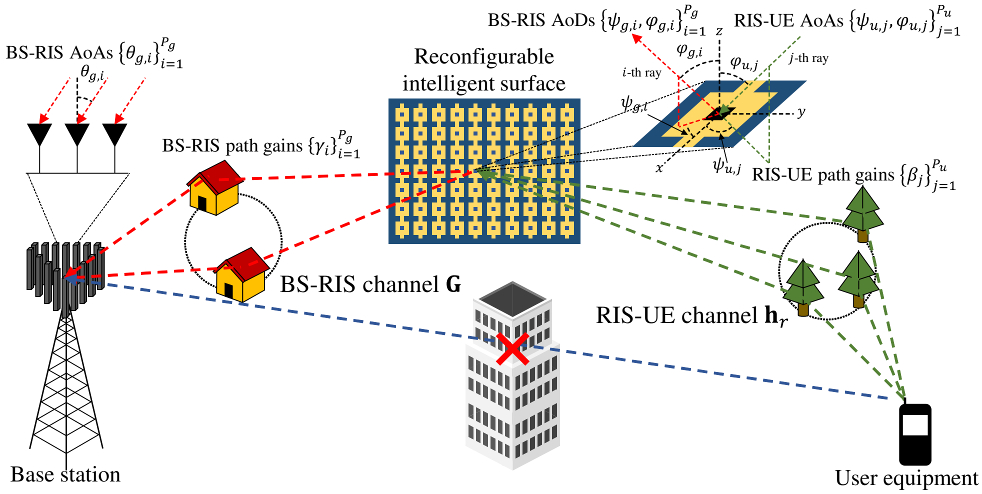

Figure 3.1: RIS-aided mmWave multi-path channel model.

The uplink channel matrix $\mathbf{G} \in \mathbb{C}^{M \times N}$ from the RIS to the BS is expressed as

$$\mathbf{G} = \sum_{i=1}^{P_g} \gamma_{g,i} \mathbf{a}_\text{B}(\theta_{g,i}) \mathbf{a}_\text{R}^\text{H}(\psi_{g,i}, \varphi_{g,i}) \tag{3.2}$$

$$= \mathbf{A}_\text{B}(\boldsymbol{\theta}_g) \text{diag}(\boldsymbol{\gamma}_g) \mathbf{A}_\text{R}^\text{H}(\boldsymbol{\psi}_g, \boldsymbol{\varphi}_g), \tag{3.3}$$

where P_g is the path number, $\theta_{g,i}$ is the angle of arrival (AoA), $(\psi_{g,i}, \varphi_{g,i})$ are the azimuth and elevation angles of departures (AoDs), $\gamma_{g,i} \sim \mathcal{CN}(0, \rho_g)$ is the gain of the i-th path where ρ_g is the large-scale fading coefficient. We assume that the path gains in adjacent blocks are uncorrelated. Also, $\mathbf{a}_\text{B}(\theta_{g,i}) = [1 \cdots e^{-j\pi(M-1)\sin\theta_{g,i}}]^\text{T} \in \mathbb{C}^M$ and $\mathbf{a}_\text{R}(\psi_{g,i}, \varphi_{g,i}) = \mathbf{a}_{\text{R},x}(\psi_{g,i}, \varphi_{g,i}) \otimes \mathbf{a}_{\text{R},y}(\varphi_{g,i}) \in \mathbb{C}^N$ are the BS and RIS array response vectors where $\mathbf{a}_{\text{R},x}(\psi_{g,i}, \varphi_{g,i}) = [1 \cdots e^{-j\pi(N_x-1)\sin\psi_{g,i}\cos\varphi_{g,i}}]^\text{T} \in \mathbb{C}^{N_x}$ and $\mathbf{a}_{\text{R},y}(\varphi_{g,i}) = [1 \cdots e^{-j\pi(N_y-1)\sin\varphi_{g,i}}]^\text{T} \in \mathbb{C}^{N_y}$. In addition, $\mathbf{A}_\text{B}(\boldsymbol{\theta}_g) = [\mathbf{a}_\text{B}(\theta_{g,1}) \cdots \mathbf{a}_\text{B}(\theta_{g,P_g})] \in \mathbb{C}^{M \times P_g}$ is the BS-RIS AoA matrix, $\mathbf{A}_\text{R}(\boldsymbol{\psi}_g, \boldsymbol{\varphi}_g) = [\mathbf{a}_\text{R}(\psi_{g,1}, \varphi_{g,1}) \cdots \mathbf{a}_\text{R}(\psi_{g,P_g}, \varphi_{g,P_g})] \in \mathbb{C}^{N \times P_g}$ is the BS-RIS AoD matrix, and $\boldsymbol{\gamma}_g = [\gamma_{g,1} \cdots \gamma_{g,P_g}]^\text{T} \in \mathbb{C}^{P_g}$ is the BS-RIS path gain vector where $\boldsymbol{\theta}_g = [\theta_{g,1} \cdots \theta_{g,P_g}]^\text{T}$, $\boldsymbol{\psi}_g = [\psi_{g,1} \cdots \psi_{g,P_g}]^\text{T}$, and $\boldsymbol{\varphi}_g = [\varphi_{g,1} \cdots \varphi_{g,P_g}]^\text{T}$.

Similarly, the uplink channel vector $\mathbf{h}_r \in \mathbb{C}^N$ from the UE to the RIS is expressed as

$$\mathbf{h}_r = \sum_{i=1}^{P_r} \gamma_{r,i} \mathbf{a}_{\mathrm{R}}(\psi_{r,i}, \varphi_{r,i}) \tag{3.4}$$

$$= \mathbf{A}_{\mathrm{R}}(\boldsymbol{\psi}_r, \boldsymbol{\varphi}_r)\boldsymbol{\gamma}_r, \tag{3.5}$$

where P_r is the path number, $(\psi_{r,i}, \varphi_{r,i})$ are the azimuth and elevation AoAs, and $\gamma_{r,i} \sim \mathcal{CN}(0, \rho_r)$ is the gain of the i-th path where ρ_r is the large-scale fading coefficient. Also, $\mathbf{A}_{\mathrm{R}}(\boldsymbol{\psi}_r, \boldsymbol{\varphi}_r) = [\mathbf{a}_{\mathrm{R}}(\psi_{r,1}, \varphi_{r,1}) \cdots \mathbf{a}_{\mathrm{R}}(\psi_{r,P_r}, \varphi_{r,P_r})] \in \mathbb{C}^{N \times P_r}$ is the RIS-UE AoA matrix and $\boldsymbol{\gamma}_r = [\gamma_{r,1} \cdots \gamma_{r,P_r}]^{\mathrm{T}} \in \mathbb{C}^{P_r}$ is the RIS-UE path gain vector where $\boldsymbol{\psi}_r = [\psi_{r,1} \cdots \psi_{r,P_r}]^{\mathrm{T}}$ and $\boldsymbol{\varphi}_r = [\varphi_{r,1} \cdots \varphi_{r,P_r}]^{\mathrm{T}}$.

The RIS reflected channel $\mathbf{H}$ can be expressed as a function of multi-path components [36].

Lemma 4. *The RIS reflected channel matrix* $\mathbf{H} = \mathbf{G}\mathrm{diag}(\mathbf{h}_r)$ *can be expressed as [36]*

$$\mathbf{H} = (\mathbf{1}_{P_r}^{\mathrm{T}} \otimes \mathbf{A}_{\mathrm{B}}(\boldsymbol{\theta}_g))\mathrm{diag}(\boldsymbol{\gamma})(\mathbf{A}_{\mathrm{R}}^*(\boldsymbol{\psi}_r, \boldsymbol{\varphi}_r) \bullet \mathbf{A}_{\mathrm{R}}(\boldsymbol{\psi}_g, \boldsymbol{\varphi}_g))^{\mathrm{H}}, \tag{3.6}$$

where $\boldsymbol{\gamma} = \boldsymbol{\gamma}_r \otimes \boldsymbol{\gamma}_g$*. Also, the vectorized RIS reflected channel* $\mathrm{vec}(\mathbf{H})$ *can be expressed as*

$$\mathrm{vec}(\mathbf{H}) = \big((\mathbf{A}_{\mathrm{R}}(\boldsymbol{\psi}_r, \boldsymbol{\varphi}_r) \bullet \mathbf{A}_{\mathrm{R}}^*(\boldsymbol{\psi}_g, \boldsymbol{\varphi}_g)) * (\mathbf{1}_{P_r}^{\mathrm{T}} \otimes \mathbf{A}_{\mathrm{B}}(\boldsymbol{\theta}_g))\big)\boldsymbol{\gamma}. \tag{3.7}$$

Typically, the number of paths P is much smaller than the number of reflecting elements N (e.g., $P = 2 \sim 8$ while $N = 64 \sim 1024$) due to the high path loss and directivity of mmWave signal [17]. Thus, one can greatly reduce the pilot overhead by estimating the channel parameters, i.e., $\boldsymbol{\theta}_g$, $(\boldsymbol{\psi}_g, \boldsymbol{\varphi}_g)$, $(\boldsymbol{\psi}_r, \boldsymbol{\varphi}_r)$, $\boldsymbol{\gamma}$, instead of the full-dimensional RIS reflected channel matrix $\mathbf{H}$.

3.2.3 Conventional RIS Reflected Channel Estimation

In the conventional channel estimation strategy, the BS directly estimates $\mathbf{H}$ from the uplink pilot signal of UE. To be specific, the received pilot signal $\mathbf{y}_t \in \mathbb{C}^M$ of BS at the t-th symbol is

$$\mathbf{y}_t = \mathbf{H}\boldsymbol{\phi}_t p_t + \mathbf{n}_t, \quad t = 1, \cdots, \tau_p, \tag{3.8}$$

where τ_p is the number of pilot symbols, p_t is the uplink pilot symbol of UE, and $\boldsymbol{\phi}_t \in \mathbb{C}^N$ is the phase shift vector at the t-th symbol. The received signal matrix $\mathbf{Y} = [\mathbf{y}_1 \cdots \mathbf{y}_{\tau_p}] \in \mathbb{C}^{M \times \tau_p}$ is

$$\mathbf{Y} = \mathbf{H}[\boldsymbol{\phi}_1 p_1 \cdots \boldsymbol{\phi}_{\tau_p} p_{\tau_p}] + [\mathbf{n}_1 \cdots \mathbf{n}_{\tau_p}] = \mathbf{H}\boldsymbol{\Pi} + \mathbf{N}, \tag{3.9}$$

where $\boldsymbol{\Pi} = [\boldsymbol{\phi}_1 p_1 \cdots \boldsymbol{\phi}_{\tau_p} p_{\tau_p}] \in \mathbb{C}^{N \times \tau_p}$ and $\mathbf{N} = [\mathbf{n}_1 \cdots \mathbf{n}_{\tau_p}] \in \mathbb{C}^{M \times \tau_p}$. After the vectorization of $\mathbf{Y}$ into $\mathbf{y} = \text{vec}(\mathbf{Y}) \in \mathbb{C}^{M\tau_p}$, we obtain a simple linear system model:

$$\begin{aligned} \mathbf{y} &= \text{vec}(\mathbf{H}\boldsymbol{\Pi} + \mathbf{N}) && (3.10) \\ &= (\boldsymbol{\Pi}^{\mathrm{T}} \otimes \mathbf{I}_M)\text{vec}(\mathbf{H}) + \mathbf{n} && (3.11) \\ &= \boldsymbol{\Sigma}(\boldsymbol{\Phi})\text{vec}(\mathbf{H}) + \mathbf{n}, && (3.12) \end{aligned}$$

where $\boldsymbol{\Sigma}(\boldsymbol{\Phi}) = \boldsymbol{\Pi}^{\mathrm{T}} \otimes \mathbf{I}_M$ is the system matrix and $\boldsymbol{\Phi} = [\boldsymbol{\phi}_1 \cdots \boldsymbol{\phi}_{\tau_p}]$ is the RIS phase shift matrix. Note that $\boldsymbol{\Sigma}(\boldsymbol{\Phi})$ is a function of $\boldsymbol{\Phi}$. Since the estimation accuracy of $\text{vec}(\mathbf{H})$ is determined by $\boldsymbol{\Sigma}(\boldsymbol{\Phi})$, one can improve the channel estimation accuracy by deliberately designing $\boldsymbol{\Phi}$.

To accurately estimate $\mathbf{H}$ from $\mathbf{y}$, the number of pilot symbols τ_p should be larger than the number of reflecting elements N. For example, when $N = 1024$, at least 13 resource blocks (RBs) (12×7 resources for each RB) are needed just for the pilot transmission.

3.2.4 Angular-Domain Channel Coherence Property

In this subsection, we discuss useful properties to develop our channel estimation framework.

Remark 1. *The coherence time of angles (i.e., AoAs and AoDs) is typically an order of magnitude (around* 40*) longer than that of path gains [41]. Specifically, the angle* *coherence time T_θ and the path gain coherence time T_γ are given by [40]*

$$T_\theta = \frac{D_r}{v \sin\theta} \mathbb{E}_\beta \big[\cos^{-1}((\beta^2 + \gamma^2) \log\zeta + 1) \big], \tag{3.13}$$

$$T_\gamma = \sqrt{\frac{1 - (1 + \gamma^2 \log\zeta)^2}{\frac{1}{4}(1 + \gamma^2 \log\zeta)(\frac{v \sin\theta}{D_r})^2 + (2\pi f_D)^2 \gamma^4}}, \tag{3.14}$$

where $f_D = \frac{v}{\lambda}$ is the maximum Doppler frequency, v is the speed of UE, λ is the signal wavelength, θ is the angle, γ is the beamwidth, β is the spatial lobe width which is modeled as a Gaussian random variable, D_r is the scattering radius, and $\zeta \approx 0.5$ is the coherence coefficient.

Remark 1 is due to the fact that the angles are determined by the dominant scatterers (e.g., buildings and trees) which do not change their positions significantly. In contrast, the path gains depend on dynamically varying scatterers (e.g., cars and leaves) around UE. By plugging the RIS speed $v_{\text{RIS}} = 0\,\text{m/s}$ and the UE speed $v_{\text{UE}} = 1 \sim 5\,\text{m/s}$ to (3.13), we obtain the following property.

Remark 2. *The BS-RIS angles remain unchanged whereas the RIS-UE angles vary over time due to the UE mobility [35, 42].*

Using Remark 1 and 2, we obtain the angular-domain channel coherence property.

Remark 3 (angular-domain channel coherence property)**.** *The RIS reflected channel matrix* $\mathbf{H}$ *can be decomposed into three major components with different coherence time:*

1. *Static BS-RIS AoAs ($\boldsymbol{\theta}_g$) and AoDs ($\boldsymbol{\psi}_g, \boldsymbol{\varphi}_g$),*
2. *Quasi-static RIS-UE AoAs ($\boldsymbol{\psi}_r, \boldsymbol{\varphi}_r$),*
3. *Time-varying BS-RIS-UE path gains ($\boldsymbol{\gamma} = \boldsymbol{\gamma}_r \otimes \boldsymbol{\gamma}_g$).*

This property justifies the three-stage processing of our channel estimation framework.

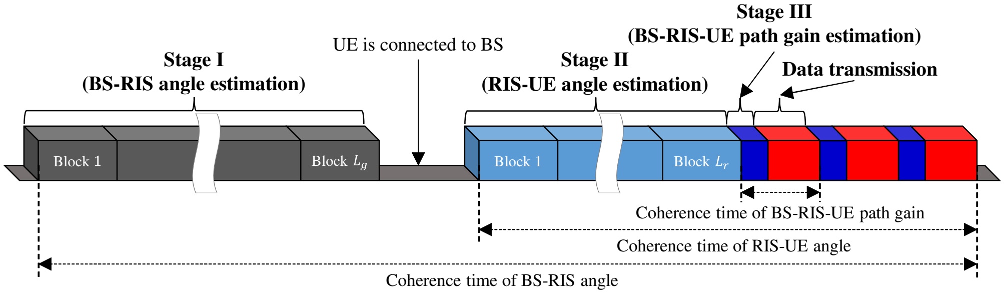

Figure 3.2: Overall structure of proposed three-stage angular-domain channel estimation.

3.3 Three-Stage Angular-Domain Channel Estimation for RIS-Aided mmWave Systems

A potential problem in the RIS reflected channel estimation is that the pilot overhead is considerable due to the large number of reflecting elements. To address this issue, we exploit the angular-domain channel coherence property that the RIS reflected channel $\mathbf{H}$ can be decomposed into three channel components: 1) static BS-RIS angles $\boldsymbol{\theta}_g$ and (ψ_g, φ_g), 2) quasi-static RIS-UE angles (ψ_r, φ_r), and 3) time-varying BS-RIS-UE path gains γ. Since the BS-RIS angles are determined by the scattering geometry around the BS and RIS, they are not affected by UE so that we can estimate them before the UE connection. Whereas, components related to UE such as the RIS-UE angles and the BS-RIS-UE path gains are estimated after the UE is connected to the BS. Also, since the coherence time of angle is much longer than that of path gains, we can estimate the RIS-UE angles infrequently, achieving a substantial reduction of the pilot overhead. Further, by optimizing the phase shifts of RIS reflecting elements using the channel components with relatively long coherence time (e.g., BS-RIS and RIS-UE angles), we can improve the channel estimation accuracy without using additional pilot resources.

In a nutshell, the proposed TAD-CE scheme consists of three major steps (see Fig. 3.2). First, the BS estimates the BS-RIS angles before the UE connection. Second, when

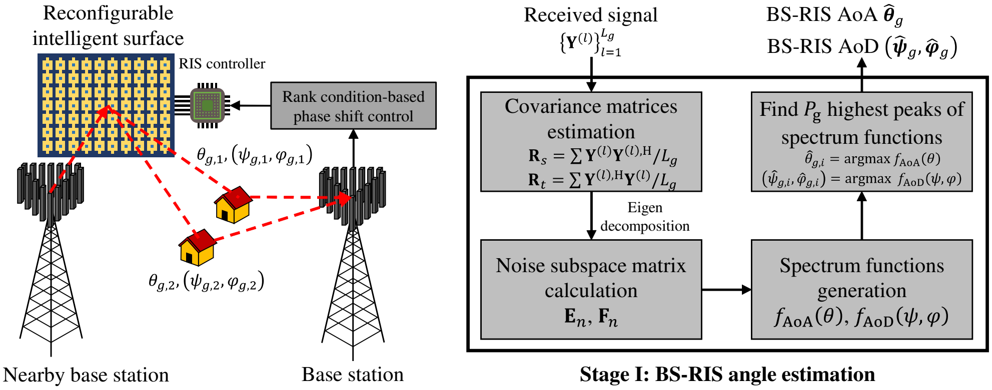

Figure 3.3: Block diagram of BS-RIS angle estimation.

the UE is connected to BS, the BS estimates the RIS-UE angles occasionally. Third, the BS estimates the BS-RIS-UE path gains in each channel coherence block.

3.3.1 Stage I: BS-RIS Angle Estimation

Before the UE connection, the BS estimates the BS-RIS AoAs $\boldsymbol{\theta}_g$ and AoDs $(\boldsymbol{\psi}_g, \boldsymbol{\varphi}_g)$ from the uplink pilot signal of adjacent BS[4] (see Fig. 3.3). Since the locations of BS and RIS are fixed, the BS-RIS angles can be considered to be static, meaning that the BS can collect a large number of pilot measurements. In any case, to account for the situations where the BS-RIS angles might change, the BS periodically estimates the BS-RIS angles when the RIS is not serving the UE. One option to estimate the BS-RIS angles is the subspace-based methods (e.g., MUSIC, ESPRIT [20]). When compared to the CS-based angle estimation scheme where the mismatch between the true angle and the discretized angular bin is unavoidable, the subspace-based method can estimate the continuous BS-RIS angle without quantization [43]. In the subspace-based method, we

---

[4] Since the BS-RIS angles remain unchanged, the BS-RIS angles can be measured at any time before the UE connection (e.g., during the initial installation of the RIS from the network operator). When there is no BS near the RIS, one can utilize an RF signal generator, which is typically used for wireless channel measurements, to transmit the uplink pilot signal to the RIS. By collecting the uplink pilot measurements reflected at the RIS, the BS can acquire the BS-RIS angle information.

construct the sample covariance matrix[5] and then decompose its eigenspace to signal and noise subspaces. Since the signal subspace is spanned by the array response vectors of BS-RIS angles while the noise subspace is orthogonal to the signal subspace, we can acquire the BS-RIS angles from the null space of the noise subspace.

When we use the subspace-based technique, we need to make sure that the signal covariance matrix is a full-rank matrix since otherwise its eigenspace (i.e., signal subspace) would be spanned by the array response vectors of incorrect angles [20]. To guarantee the accurate estimation of BS-RIS angles, we first express the signal covariance matrices as functions of RIS phase shifts and then find out the phase shifts ensuring the full-rank condition.

BS-RIS Angle Estimation

In this stage, the BS collects the pilot measurements for L_g blocks and then estimates the BS-RIS AoAs $\boldsymbol{\theta}_g$ and AoDs $(\boldsymbol{\psi}_g, \boldsymbol{\varphi}_g)$. Let $p_t \in \mathbb{C}$ be the uplink pilot symbol of adjacent BS and $\boldsymbol{\phi}_t \in \mathbb{C}^N$ be the phase shift vector at the t-th symbol. Then the received signal $\mathbf{y}_t^{(l)} \in \mathbb{C}^M$ of BS at the t-th symbol of l-th block is

$$\mathbf{y}_t^{(l)} = \mathbf{H}^{(l)}\boldsymbol{\phi}_t p_t + \mathbf{n}_t^{(l)}, \quad t = 1, \cdots, \tau,\, l = 1, \cdots, L_g, \tag{3.15}$$

where $\mathbf{H}^{(l)}$ is the RIS reflected channel at the l-th block and $\mathbf{n}_t^{(l)} \sim \mathcal{CN}(\mathbf{0}, \sigma_n^2 \mathbf{I}_M)$ is the Gaussian noise. The combined received signal matrix $\mathbf{Y}^{(l)} = [\mathbf{y}_1^{(l)} \cdots \mathbf{y}_\tau^{(l)}] \in \mathbb{C}^{M \times \tau}$ is

$$\mathbf{Y}^{(l)} = \mathbf{H}^{(l)}[\boldsymbol{\phi}_1 \cdots \boldsymbol{\phi}_\tau]\text{diag}(p_1, \cdots, p_\tau) + [\mathbf{n}_1^{(l)} \cdots \mathbf{n}_\tau^{(l)}] \tag{3.16}$$

$$\overset{(a)}{=} (\mathbf{1}_{P_r}^{\mathrm{T}} \otimes \mathbf{A}_{\mathrm{B}}(\boldsymbol{\theta}_g))\text{diag}(\boldsymbol{\gamma}^{(l)})(\mathbf{A}_{\mathrm{R}}^*(\boldsymbol{\psi}_r, \boldsymbol{\varphi}_r) \bullet \mathbf{A}_{\mathrm{R}}(\boldsymbol{\psi}_g, \boldsymbol{\varphi}_g))^{\mathrm{H}}\boldsymbol{\Phi}\mathbf{P} + \mathbf{N}^{(l)}, l = 1, \cdots, L_g, \tag{3.17}$$

where (a) is from Lemma 1, $\boldsymbol{\Phi} = [\boldsymbol{\phi}_1 \cdots \boldsymbol{\phi}_\tau] \in \mathbb{C}^{N \times \tau}$ is the phase shift matrix, and $\mathbf{P} = \text{diag}(p_1 \cdots p_\tau)$ is the pilot matrix.

By collecting the received signals $\mathbf{Y}^{(l)}$ for L_g blocks, the BS constructs the sample covariance matrices $\mathbf{R}_s = \mathbb{E}[\mathbf{Y}^{(l)}\mathbf{Y}^{(l),\mathrm{H}}] \approx \frac{1}{L_g}\sum_{i=1}^{L_g} \mathbf{Y}^{(l)}\mathbf{Y}^{(l),\mathrm{H}}$ and $\mathbf{R}_t =$

---

[5] Note that the sample covariance matrix is different with the channel covariance matrix in [44].

$\mathbb{E}[\mathbf{Y}^{(l),\mathrm{H}}\mathbf{Y}^{(l)}] \approx \frac{1}{L_g}\sum_{i=1}^{L_g}\mathbf{Y}^{(l),\mathrm{H}}\mathbf{Y}^{(l)}$. In our experience, we could not observe any meaningful difference in acquiring the sample covariance matrices when L_g is larger than 100. In the following proposition, we obtain the closed-form expressions of $\mathbf{R}_s$ and $\mathbf{R}_t$.

Proposition 4. *The sample covariance matrices* $\mathbf{R}_s$ *and* $\mathbf{R}_t$ *can be expressed as*

$$\begin{aligned}\mathbf{R}_s =& \rho_g\rho_r\mathbf{A}_{\mathrm{B}}(\boldsymbol{\theta}_g)\mathrm{diag}(\|\mathbf{P}^{\mathrm{H}}\boldsymbol{\Phi}^{\mathrm{H}}\mathbf{B}_1\mathbf{A}_{\mathrm{R}}^*(\boldsymbol{\psi}_r,\boldsymbol{\varphi}_r)\|_{\mathrm{F}}^2\cdots\\ &\|\mathbf{P}^{\mathrm{H}}\boldsymbol{\Phi}^{\mathrm{H}}\mathbf{B}_{P_g}\mathbf{A}_{\mathrm{R}}^*(\boldsymbol{\psi}_r,\boldsymbol{\varphi}_r)\|_{\mathrm{F}}^2)\mathbf{A}_{\mathrm{B}}^{\mathrm{H}}(\boldsymbol{\theta}_g)+\sigma_n^2\mathbf{I}_M \quad (3.18)\\ \mathbf{R}_t =& M\rho_g\rho_r\mathbf{P}^{\mathrm{H}}\boldsymbol{\Phi}^{\mathrm{H}}(\mathbf{A}_{\mathrm{R}}^*(\boldsymbol{\psi}_r,\boldsymbol{\varphi}_r)\bullet\mathbf{A}_{\mathrm{R}}(\boldsymbol{\psi}_g,\boldsymbol{\varphi}_g))\\ &(\mathbf{A}_{\mathrm{R}}^*(\boldsymbol{\psi}_r,\boldsymbol{\varphi}_r)\bullet\mathbf{A}_{\mathrm{R}}(\boldsymbol{\psi}_g,\boldsymbol{\varphi}_g))^{\mathrm{H}}\boldsymbol{\Phi}\mathbf{P}+\sigma_n^2\mathbf{I}_\tau, \quad (3.19)\end{aligned}$$

where $\mathbf{B}_i = \mathrm{diag}(\mathbf{a}_{\mathrm{R}}(\psi_{g,i},\varphi_{g,i})) \in \mathbb{C}^{N\times N}$ *for* $i = 1\cdots P_g$.

Proof. See Appendix A. □

One can see that $\mathbf{R}_s$ has the form of $\mathbf{R}_s = \mathbf{S}+\sigma_n^2\mathbf{I}$ where $\mathbf{S}$ is the signal covariance matrix. Since $\mathbf{S}$ has the same column space with the BS-RIS AoA matrix $\mathbf{A}_{\mathrm{B}}(\boldsymbol{\theta}_g)$, the BS can acquire the BS-RIS AoA $\boldsymbol{\theta}_g$ from $\mathbf{R}_s$ via the subspace-based algorithms. In the MUSIC algorithm, for example, the BS computes the signal subspace matrix $\mathbf{E}_s$ and the noise subspace matrix $\mathbf{E}_n$ from the eigenspace of $\mathbf{R}_s$. Since $\mathbf{E}_n$ is orthogonal to $\mathbf{E}_s$, $\hat{\boldsymbol{\theta}}_g$ is obtained from P_g highest peaks of AoA spectrum function $f_{\mathrm{AoA}}(\theta) = 1/\|\mathbf{E}_n^{\mathrm{H}}\mathbf{a}_{\mathrm{B}}(\theta)\|^2$:

$$\hat{\theta}_{g,i} = \arg\max_{\theta} f_{\mathrm{AoA}}(\theta), \quad i = 1,\cdots,P_g. \tag{3.20}$$

The estimation of BS-RIS AoD $(\boldsymbol{\psi}_g,\boldsymbol{\varphi}_g)$ from $\mathbf{R}_t$ is a bit difficult since the BS-RIS AoD matrix $\mathbf{A}_{\mathrm{R}}(\boldsymbol{\psi}_g,\boldsymbol{\varphi}_g)$ is coupled with the RIS-BS AoA matrix $\mathbf{A}_{\mathrm{R}}(\boldsymbol{\psi}_r,\boldsymbol{\varphi}_r)$ which is unknown to the BS at stage I. To deal with this issue, the BS exploits the RIS-BS AoA of the LoS path $(\psi_{r,\mathrm{LoS}},\varphi_{r,\mathrm{LoS}})$ which can be obtained directly from the relative locations of RIS and BS. In the MUSIC algorithm, for example, $(\hat{\boldsymbol{\psi}}_g,\hat{\boldsymbol{\varphi}}_g)$ is obtained from the P_g highest peaks of AoD spectrum function $f_{\mathrm{AoD}}(\psi,\varphi) =$

$1/\|\mathbf{F}_n^{\mathrm{H}}\mathbf{P}^{\mathrm{H}}\mathbf{\Phi}^{\mathrm{H}}(\mathbf{a}_{\mathrm{R}}^*(\psi_{r,\mathrm{LoS}},\varphi_{r,\mathrm{LoS}}) \odot \mathbf{a}_{\mathrm{R}}(\psi,\varphi))\|^2$ as

$$(\hat{\psi}_{g,i},\hat{\varphi}_{g,i}) = \arg\max_{(\psi,\varphi)} f_{\mathrm{AoD}}(\psi,\varphi), \quad i = 1,\cdots,P_g, \tag{3.21}$$

where $\mathbf{F}_n$ is the noise subspace matrix constructed from $\mathbf{R}_t$.

RIS Phase Shift Control

As mentioned, for the accurate estimation of the BS-RIS angles using the subspace-based method, the signal covariance matrix should be full-rank:

$$\operatorname{rank}\left(\mathbf{A}_{\mathrm{B}}(\boldsymbol{\theta}_g)\operatorname{diag}(\|\mathbf{P}^{\mathrm{H}}\mathbf{\Phi}^{\mathrm{H}}\mathbf{B}_1\mathbf{A}_{\mathrm{R}}^*(\boldsymbol{\psi}_r,\boldsymbol{\varphi}_r)\|_{\mathrm{F}},\cdots,\|\mathbf{P}^{\mathrm{H}}\mathbf{\Phi}^{\mathrm{H}}\mathbf{B}_{P_g}\mathbf{A}_{\mathrm{R}}^*(\boldsymbol{\psi}_r,\boldsymbol{\varphi}_r)\|_{\mathrm{F}})\right) = P_g, \tag{3.22}$$

$$\operatorname{rank}\left(\mathbf{P}^{\mathrm{H}}\mathbf{\Phi}^{\mathrm{H}}(\mathbf{A}_{\mathrm{R}}^*(\boldsymbol{\psi}_r,\boldsymbol{\varphi}_r) \bullet \mathbf{A}_{\mathrm{R}}(\boldsymbol{\psi}_g,\boldsymbol{\varphi}_g))\right) = P_r P_g. \tag{3.23}$$

If these conditions are not satisfied, then the eigenspace of signal covariance matrix would be spanned by the array response vectors of incorrect angles, deteriorating the angle estimation performance severely [20]. Since the covariance matrices are functions of phase shift matrix $\mathbf{\Phi}$ (see Proposition 1), we design $\mathbf{\Phi}$ such that (3.22) and (3.23) are satisfied.

Proposition 5. *The phase shift matrix* $\mathbf{\Phi} = [\mathbf{f}_1 \cdots \mathbf{f}_\tau] \in \mathbb{C}^{N\times\tau}$ *satisfies* (3.22) *and* (3.23) *where* $\mathbf{f}_1,\cdots,\mathbf{f}_\tau$ *are* τ *randomly chosen column vectors of* N*-point DFT matrix.*

Proof. See Appendix B. □

3.3.2 Stage II: RIS-UE Angle Estimation

When the UE is connected to the BS, the BS estimates the RIS-UE AoAs $(\boldsymbol{\psi}_r,\boldsymbol{\varphi}_r)$ from the pilot signal of UE (see Fig. 3.4). Due to the UE mobility, the coherence time of RIS-UE angles is shorter than that of BS-RIS angles, which means that the BS cannot collect a large number of measurements for the RIS-UE angle estimation. In this case, the CS-based technique can be useful since it can generate the angle estimate even

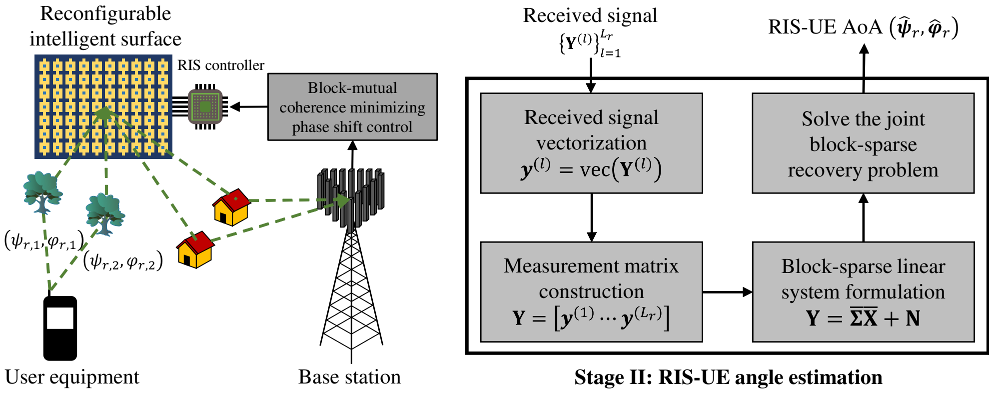

Figure 3.4: Block diagram of RIS-UE angle estimation.

with a small amount of measurements [45]. In the CS-based technique, we formulate the block-sparse linear system model where the RIS-UE angles and the path gains are mapped to the positions of non-zero blocks (i.e., support) of a block-sparse vector. By employing the block-sparse recovery algorithm, we can find out the support of the block-sparse vector using which we can recover the RIS-UE angles.

It is worth mentioning that the block-sparse recovery performance of the CS algorithm depends on the correlations between the submatrices of the sensing matrix. Since the sensing matrix is a function of RIS phase shifts, we can improve the RIS-UE angle estimation accuracy by adjusting the phase shifts such that the adjusted phases minimize the column correlation of sensing matrix.

RIS-UE Angle Estimation

In this stage, the BS estimates the RIS-UE AoAs (ψ_r, φ_r) for L_r blocks. Specifically, the CS-based angle estimation consists of three major steps:

- **Angular-domain sparse mapping**: We map (ψ_r, φ_r) and γ_r to the positions of non-zero blocks (i.e., support $\mathbf{\Omega}$) of the block-sparse path gain vector.
- **Block-sparse representation**: We formulate the block-sparse linear system

$\mathbf{Y} = \bar{\mathbf{\Sigma}}\bar{\mathbf{\Gamma}} + \mathbf{N}$ where $\bar{\mathbf{\Sigma}}$ is the angular-domain sensing matrix and $\bar{\mathbf{\Gamma}}$ is the block-sparse path gain matrix.

- **Block-sparse recovery and angle reconstruction**: Using the block-sparse recovery algorithm, we find out the support $\mathbf{\Omega}$ of $\bar{\mathbf{\Gamma}}$ from which we recover $(\boldsymbol{\psi}_r, \boldsymbol{\varphi}_r)$.

Let $(\bar{\boldsymbol{\psi}}, \bar{\boldsymbol{\varphi}}) = \{(\bar{\psi}_i, \bar{\varphi}_i) \mid i = 1, \cdots, W\}$ be the quantized angle set where W is the number of angular bins and $\bar{\boldsymbol{\gamma}}_r^{(l)} \in \mathbb{C}^W$ be the corresponding sparse RIS-UE path gain vector such that $\|\bar{\boldsymbol{\gamma}}_r^{(l)}\|_0 = P_r$ and $\mathrm{supp}(\bar{\boldsymbol{\gamma}}_r^{(l)}) = \mathbf{\Omega}$. Then the combined block-sparse BS-RIS-UE path gain vector is $\bar{\boldsymbol{\gamma}}^{(l)} = \bar{\boldsymbol{\gamma}}_r^{(l)} \otimes \boldsymbol{\gamma}_g^{(l)} \in \mathbb{C}^{WP_g}$. Using $(\bar{\boldsymbol{\psi}}, \bar{\boldsymbol{\varphi}})$ and $\bar{\boldsymbol{\gamma}}^{(l)}$, the received signal matrix $\mathbf{Y}^{(l)} \in \mathbb{C}^{M \times \tau}$ of BS at the l-th block $\mathbf{Y}^{(l)}$ can be expressed as

$$\mathbf{Y}^{(l)} = \mathbf{H}^{(l)}\mathbf{\Phi}\mathbf{P} + \mathbf{N}^{(l)} \tag{3.24}$$

$$= (\mathbf{1}_W^{\mathrm{T}} \otimes \mathbf{A}_{\mathrm{B}}(\boldsymbol{\theta}_g))\mathrm{diag}(\bar{\boldsymbol{\gamma}}^{(l)})(\mathbf{A}_{\mathrm{R}}^{*}(\bar{\boldsymbol{\psi}}, \bar{\boldsymbol{\varphi}}) \bullet \mathbf{A}_{\mathrm{R}}(\boldsymbol{\psi}_g, \boldsymbol{\varphi}_g))^{\mathrm{H}}\mathbf{\Phi}\mathbf{P} + \mathbf{N}^{(l)}, l = 1, \cdots, L_r, \tag{3.25}$$

where $\mathbf{\Phi} = [\boldsymbol{\phi}_1 \cdots \boldsymbol{\phi}_\tau] \in \mathbb{C}^{N \times \tau}$ is the phase shift matrix and $\mathbf{P} = \mathrm{diag}(p_1 \cdots p_\tau)$ is the pilot matrix.

Now, to convert (3.25) to the block-sparse linear system, we vectorize $\mathbf{Y}^{(l)}$ to $\mathbf{y}^{(l)} = \mathrm{vec}(\mathbf{Y}^{(l)})$:

$$\mathbf{y}^{(l)} = (\mathbf{P}\mathbf{\Phi}^{\mathrm{T}} \otimes \mathbf{I}_M)\mathrm{vec}(\mathbf{H}^{(l)}) + \mathbf{n}^{(l)} \tag{3.26}$$

$$\overset{(a)}{=} \big((\mathbf{P}\mathbf{\Phi}^{\mathrm{T}}(\mathbf{A}_{\mathrm{R}}(\bar{\boldsymbol{\psi}}, \bar{\boldsymbol{\varphi}}) \bullet \mathbf{A}_{\mathrm{R}}^{*}(\boldsymbol{\psi}_g, \boldsymbol{\varphi}_g))) * (\mathbf{1}_W^{\mathrm{T}} \otimes \mathbf{A}_{\mathrm{B}}(\boldsymbol{\theta}_g))\big)\bar{\boldsymbol{\gamma}}^{(l)} + \mathbf{n}^{(l)} \tag{3.27}$$

$$= \bar{\mathbf{\Sigma}}\bar{\boldsymbol{\gamma}}^{(l)} + \mathbf{n}^{(l)}, \quad l = 1, \cdots, L_r, \tag{3.28}$$

where (a) is from Lemma 1 and the property of Khatri-Rao product such that $(\mathbf{A} \otimes \mathbf{B})(\mathbf{C} * \mathbf{D}) = (\mathbf{AC}) * (\mathbf{BD})$. Also, $\bar{\mathbf{\Sigma}} \in \mathbb{C}^{M\tau \times WP_g}$ is the angular-domain sensing matrix defined as

$$\bar{\mathbf{\Sigma}} = (\mathbf{P}\mathbf{\Phi}^{\mathrm{T}}(\mathbf{A}_{\mathrm{R}}(\bar{\boldsymbol{\psi}}, \bar{\boldsymbol{\varphi}}) \bullet \mathbf{A}_{\mathrm{R}}^{*}(\boldsymbol{\psi}_g, \boldsymbol{\varphi}_g))) * (\mathbf{1}_W^{\mathrm{T}} \otimes \mathbf{A}_{\mathrm{B}}(\boldsymbol{\theta}_g)). \tag{3.29}$$

In the following remark, we explain the block-sparse structure of $\bar{\boldsymbol{\gamma}}^{(l)}$.

Remark 4. *Since $\bar{\gamma}_r^{(l)}$ is a sparse vector, $\bar{\gamma}^{(l)} = \bar{\gamma}_r^{(l)} \otimes \gamma_g^{(l)}$ is a block-sparse vector*[6]*. By a block-sparse vector, we mean that non-zero elements appear in a few blocks of the vector. Also, since the RIS-UE AoAs are constant in the RIS-UE angle estimation stage, $\bar{\gamma}^{(1)}, \cdots, \bar{\gamma}^{(L_r)}$ have a common index set of non-zero blocks $\mathbf{\Omega}$.*

Since $\bar{\gamma}^{(1)}, \cdots, \bar{\gamma}^{(L_r)}$ have the common support $\mathbf{\Omega}$, the problem to identify $\mathbf{\Omega}$ from $\{\mathbf{y}^{(l)}\}_{l=1}^{L_r}$ can be modeled as a joint block-sparse recovery problem. Thus, by exploiting the measurements of L_r blocks simultaneously, one can greatly enhance the block-sparse recovery performance.

To do so, we combine $\{\mathbf{y}^{(l)}\}_{l=1}^{L_r}$ into a measurement matrix $\mathbf{Y} = [\mathbf{y}^{(1)} \cdots \mathbf{y}^{(L_r)}] \in \mathbb{C}^{M\tau \times L_r}$ as

$$\mathbf{Y} = \bar{\mathbf{\Sigma}}\bar{\mathbf{\Gamma}} + \mathbf{N}, \tag{3.30}$$

where $\bar{\mathbf{\Sigma}} \in \mathbb{C}^{M\tau \times WP_g}$ is the angular-domain sensing matrix in (3.29) and $\bar{\mathbf{\Gamma}} = [\bar{\gamma}^{(1)} \cdots \bar{\gamma}^{(L_r)}] \in \mathbb{C}^{WP_g \times L_r}$ is the block-sparse path gain matrix such that the non-zero rows appear in a few $P_g \times L_r$ size blocks[7]. Then the joint block-sparse recovery problem $\mathcal{P}$ to find out $\mathbf{\Omega}$ from $\mathbf{Y}$ is

$$\mathcal{P}: \min_{\bar{\mathbf{\Gamma}} = [\bar{\mathbf{\Gamma}}_1^{\mathrm{T}} \cdots \bar{\mathbf{\Gamma}}_W^{\mathrm{T}}]^{\mathrm{T}}} \quad \|\mathbf{Y} - \bar{\mathbf{\Sigma}}\bar{\mathbf{\Gamma}}\|_{\mathrm{F}}^2, \tag{3.31a}$$

$$\text{s.t.} \quad \sum_{i=1}^{W} \mathcal{I}(\|\bar{\mathbf{\Gamma}}_i\|_{\mathrm{F}}) = P_r, \tag{3.31b}$$

where $\mathcal{I}(x)$ is the indicator function such that $\mathcal{I}(x) = 1$ if $x \neq 0$ and $\mathcal{I}(x) = 0$ otherwise.

In solving $\mathcal{P}$, one can use the block-sparse recovery algorithm such as BOMP [45]. When using the BOMP algorithm, an index of the submatrix of the sensing matrix is chosen at a time using a greedy strategy and then the residual is updated. To be specific,

---

[6] For example, if $\bar{\gamma}_r^{(l)} = [1,0,0,1]^{\mathrm{T}}$ and $\gamma_g^{(l)} = [1,2]^{\mathrm{T}}$, then $\bar{\gamma}^{(l)} = \bar{\gamma}_r^{(l)} \otimes \gamma_g^{(l)} = [1,2,0,0,0,0,1,2]^{\mathrm{T}}$.

[7] For example, if $P_g = 2$, $L_r = 2$, $\gamma_g^{(1)} = [1,2]^{\mathrm{T}}$, $\gamma_g^{(2)} = [3,4]^{\mathrm{T}}$, and $\bar{\gamma}_r^{(1)} = \bar{\gamma}_r^{(2)} = [1,0,0,1]^{\mathrm{T}}$, then $\bar{\mathbf{\Gamma}} = [\bar{\gamma}^{(1)} \otimes \gamma_g^{(1)}, \bar{\gamma}^{(2)} \otimes \gamma_g^{(2)}] = \left[\begin{smallmatrix} 1 & 2 & 0 & 0 & 0 & 0 & 1 & 2 \\ 3 & 4 & 0 & 0 & 0 & 0 & 3 & 4 \end{smallmatrix}\right]^{\mathrm{T}}$. The indices of non-zero 2×2 block matrices are $\mathbf{\Omega} = \{1, 4\}$.

in the n-th iteration, an index $\hat{\omega}_n$ corresponding to the submatrix $\bar{\mathbf{\Sigma}}_{\hat{\omega}_n} \in \mathbb{C}^{M\tau \times P_g}$ ($\bar{\mathbf{\Sigma}} = [\bar{\mathbf{\Sigma}}_1 \cdots \bar{\mathbf{\Sigma}}_W]$) which is maximally correlated with the residual is chosen:

$$\hat{\omega}_n = \arg \max_{i=1,\cdots,W} \|\bar{\mathbf{\Sigma}}_i^{\mathrm{H}} \mathbf{Z}_{n-1}\|_{\mathrm{F}}^2, \quad n = 1, \cdots, P_r, \tag{3.32}$$

where $\mathbf{Z}_{n-1} = (\mathbf{I} - \bar{\mathbf{\Sigma}}_{\hat{\mathbf{\Omega}}_{n-1}} \bar{\mathbf{\Sigma}}_{\hat{\mathbf{\Omega}}_{n-1}}^{\dagger})\mathbf{Y}$ is the residual, $\hat{\mathbf{\Omega}}_{n-1} = \{\hat{\omega}_1, \cdots, \hat{\omega}_{n-1}\}$, and $\bar{\mathbf{\Sigma}}_{\hat{\mathbf{\Omega}}_{n-1}} = [\bar{\mathbf{\Sigma}}_{\hat{\omega}_1} \cdots \bar{\mathbf{\Sigma}}_{\hat{\omega}_{n-1}}]$. The iteration is repeated until P_r indices are chosen[8]. Once $\hat{\mathbf{\Omega}}$ is recovered, the RIS-UE AoAs are obtained from the quantized angle set as $(\hat{\psi}_r, \hat{\varphi}_r) = (\bar{\psi}_{\mathbf{\Omega}}, \bar{\varphi}_{\mathbf{\Omega}})$.

RIS Phase Shift Control

As mentioned, the block-sparse recovery performance depends on the correlations between the submatrices $\{\bar{\mathbf{\Sigma}}_i\}_{i=1}^{W}$ (i.e., block-mutual coherence) of the sensing matrix $\bar{\mathbf{\Sigma}} = [\bar{\mathbf{\Sigma}}_1 \cdots \bar{\mathbf{\Sigma}}_W]$. Since $\bar{\mathbf{\Sigma}}$ is a function of the RIS phase shift matrix $\mathbf{\Phi}$ (see (3.29)), we can improve the block-sparse recovery performance by designing $\mathbf{\Phi}$ such that the block-mutual coherence of $\bar{\mathbf{\Sigma}}$ is minimized. To be specific, the block-mutual coherence μ of $\bar{\mathbf{\Sigma}}$ is defined as

$$\mu(\mathbf{\Phi}) = \max_{1 \leq i < j \leq W} \frac{\|\bar{\mathbf{\Sigma}}_i^{\mathrm{H}}(\mathbf{\Phi})\bar{\mathbf{\Sigma}}_j(\mathbf{\Phi})\|_2}{\|\bar{\mathbf{\Sigma}}_i(\mathbf{\Phi})\|_2 \|\bar{\mathbf{\Sigma}}_j(\mathbf{\Phi})\|_2}. \tag{3.33}$$

Then the block-mutual coherence minimization problem $\mathcal{P}_{\mathrm{II}}$ to find out the optimal phase shift matrix $\mathbf{\Phi}$ minimizing $\mu(\mathbf{\Phi})$ is formulated as

$$\mathcal{P}_{\mathrm{II}} : \min_{\mathbf{\Phi}} \ \mu(\mathbf{\Phi}), \tag{3.34a}$$

$$\text{s.t.} \ \left|[\mathbf{\Phi}]_{n,t}\right| = 1, \ n = 1, \cdots, N, \ t = 1, \cdots, \tau. \tag{3.34b}$$

---

[8] To estimate the block-sparsity level, one can use the cross-validation technique [46]. In this scheme, the measurement matrix is divided into two parts: a training matrix and a validation matrix. In the first step, using the training matrix, a sequence of supports with different block-sparsity levels is generated. In the second step, using the acquired supports and the validation matrix, the validation error is computed. Finally, a block-sparsity level corresponding to the minimum validation error is returned.

By defining the auxiliary matrix $\mathbf{Y}_{i,j} = \frac{\bar{\mathbf{\Sigma}}_i^{\mathrm{H}}(\mathbf{\Phi})\bar{\mathbf{\Sigma}}_j(\mathbf{\Phi})}{\|\bar{\mathbf{\Sigma}}_i(\mathbf{\Phi})\|_2\|\bar{\mathbf{\Sigma}}_j(\mathbf{\Phi})\|_2}$, $\mathcal{P}_{\mathrm{II}}$ can be reformulated as

$$\begin{aligned}
\mathcal{P}_{\mathrm{II}} : \min_{\mathbf{Y},\mathbf{\Phi}} \quad & \max_{1\le i<j\le W} \|\mathbf{Y}_{i,j}\|_2, && \text{(3.35a)}\\
\text{s.t.} \quad & \mathbf{Y}_{i,j} = \frac{\bar{\mathbf{\Sigma}}_i^{\mathrm{H}}(\mathbf{\Phi})\bar{\mathbf{\Sigma}}_j(\mathbf{\Phi})}{\|\bar{\mathbf{\Sigma}}_i(\mathbf{\Phi})\|_2\|\bar{\mathbf{\Sigma}}_j(\mathbf{\Phi})\|_2}, \quad 1 \le i < j \le W, && \text{(3.35b)}\\
& \left|[\mathbf{\Phi}]_{n,t}\right| = 1,\ n = 1, \cdots, N,\ t = 1, \cdots, \tau, && \text{(3.35c)}
\end{aligned}$$

Due to the quadratic fractional structure of (3.35b) and the unit-modulus constraints (3.35c), $\mathcal{P}_{\mathrm{II}}$ is a non-convex problem in which finding out the global optimal solution is very difficult. Also, since $\mathbf{\Sigma}$ and $\mathbf{\Phi}$ are coupled with each other in (3.35b), it is not easy to optimize them simultaneously.

To find out a tractable solution of $\mathcal{P}_{\mathrm{II}}$, we employ the augmented Lagrangian relaxation technique that converts a complicated constrained problem to an unconstrained problem by adding a quadratic penalty term to the objective function. Specifically, the modified objective function L, so-called the augmented Lagrangian, is given by

$$\begin{aligned}
L(\mathbf{Y}, \mathbf{\Phi}, \mathbf{\Lambda}) = & \max_{1\le i<j\le W} \|\mathbf{Y}_{i,j}\|_2 + \mathbb{1}_{\mathcal{M}}(\mathbf{\Phi}) + \\
& \frac{\rho}{2} \sum_{1\le i<j\le W} \left\| \mathbf{Y}_{i,j} - \frac{\bar{\mathbf{\Sigma}}_i^{\mathrm{H}}(\mathbf{\Phi})\bar{\mathbf{\Sigma}}_j(\mathbf{\Phi})}{\|\bar{\mathbf{\Sigma}}_i(\mathbf{\Phi})\|_2\|\bar{\mathbf{\Sigma}}_j(\mathbf{\Phi})\|_2} + \frac{\mathbf{\Lambda}_{i,j}}{\rho} \right\|_{\mathrm{F}}^2
\end{aligned} \tag{3.36}$$

where $\mathcal{M} = \{\mathbf{\Phi} \in \mathbb{C}^{N\times\tau} : \left|[\mathbf{\Phi}]_{n,t}\right| = 1, \forall n, \forall t\}$ is the complex circle manifold, a set of the phase shift matrices satisfying the unit-modulus constraints (3.35c), $\mathbf{\Lambda}$ is the Lagrangian multiplier matrix, and $\rho > 0$ is the scaling factor. Using $L(\mathbf{Y}, \mathbf{\Phi}, \mathbf{\Lambda})$, the dual problem $\mathcal{P}'_{\mathrm{II}}$ can be expressed as

$$\mathcal{P}'_{\mathrm{II}} : \max_{\mathbf{\Lambda}} \ \min_{\mathbf{Y},\mathbf{\Phi}} L(\mathbf{Y}, \mathbf{\Phi}, \mathbf{\Lambda}). \tag{3.37}$$

Since $\mathcal{P}'_{\mathrm{II}}$ is an unconstrained problem, it would be much easier to handle than the primary problem $\mathcal{P}_{\mathrm{II}}$. Note, based on the weak duality, the optimal value of $\mathcal{P}'_{\mathrm{II}}$ corresponds to the lower bound of the optimal value of $\mathcal{P}_{\mathrm{II}}$. Unfortunately, it is still not easy to solve $\mathcal{P}'_{\mathrm{II}}$ since the augmented Lagrangian L is a joint function of $\mathbf{Y}$, $\mathbf{\Phi}$, and

$\mathbf{\Lambda}$. To address this issue, we use an approach that alternately updates the block-mutual coherence matrix $\mathbf{Y}$, the phase shift matrix $\mathbf{\Phi}$, and the Lagrangian multiplier matrix $\mathbf{\Lambda}$:

$$\mathbf{Y}^{(t+1)} = \arg\min_{\mathbf{\Sigma}} L(\mathbf{Y}, \mathbf{\Phi}^{(t)}, \mathbf{\Lambda}^{(t)}), \tag{3.38}$$

$$\mathbf{\Phi}^{(t+1)} = \arg\min_{\mathbf{\Phi}} L(\mathbf{Y}^{(t+1)}, \mathbf{\Phi}, \mathbf{\Lambda}^{(t)}), \tag{3.39}$$

$$\mathbf{\Lambda}_{i,j}^{(t+1)} = \mathbf{\Lambda}_{i,j}^{(t)} + \rho\left(\mathbf{Y}_{i,j}^{(t+1)} - \frac{\bar{\mathbf{\Sigma}}_i^{\mathrm{H}}(\mathbf{\Phi}^{(t+1)})\bar{\mathbf{\Sigma}}_j(\mathbf{\Phi}^{(t+1)})}{\|\bar{\mathbf{\Sigma}}_i(\mathbf{\Phi}^{(t+1)})\|_2\|\bar{\mathbf{\Sigma}}_j(\mathbf{\Phi}^{(t+1)})\|_2}\right). \tag{3.40}$$

First, the block-mutual coherence matrix optimization problem $\mathcal{P}_{\mathbf{Y}}$ corresponding to (3.38) is

$$\mathcal{P}_{\mathbf{Y}} : \min_{\mathbf{Y}} \max_{1 \le i < j \le W} \|\mathbf{Y}_{i,j}\|_2 + \frac{\rho}{2} \sum_{1 \le i < j \le W} \|\mathbf{Y}_{i,j} - \mathbf{Z}_{i,j}^{(t)}\|_{\mathrm{F}}^2, \tag{3.41}$$

where $\mathbf{Z}_{i,j}^{(t)} = \frac{\bar{\mathbf{\Sigma}}_i^{\mathrm{H}}(\mathbf{\Phi}^{(t)})\bar{\mathbf{\Sigma}}_j(\mathbf{\Phi}^{(t)})}{\|\bar{\mathbf{\Sigma}}_i(\mathbf{\Phi}^{(t)})\|_2\|\bar{\mathbf{\Sigma}}_j(\mathbf{\Phi}^{(t)})\|_2} - \frac{1}{\rho}\mathbf{\Lambda}_{i,j}^{(t)}$. Note that $\mathcal{P}_{\mathbf{Y}}$ is a spectral norm minimization problem which can be equivalently converted to the convex semidefinite program (SDP)[9] [47]. Thus, we can obtain the global optimal solution $\mathbf{Y}^*$ using the convex optimization tool (e.g., CVX).

Second, the optimization problem $\mathcal{P}_{\mathbf{\Phi}}$ corresponding to (3.39) is given by

$$\mathcal{P}_{\mathbf{\Phi}} : \min_{\mathbf{\Phi}} \sum_{1 \le i < j \le W} \left\| \frac{\bar{\mathbf{\Sigma}}_i^{\mathrm{H}}(\mathbf{\Phi})\bar{\mathbf{\Sigma}}_j(\mathbf{\Phi})}{\|\bar{\mathbf{\Sigma}}_i(\mathbf{\Phi})\|_2\|\bar{\mathbf{\Sigma}}_j(\mathbf{\Phi})\|_2} - \mathbf{W}_{i,j}^{(t)} \right\|_{\mathrm{F}}^2, \tag{3.42a}$$

$$\text{s.t.} \left|[\mathbf{\Phi}]_{n,t}\right| = 1, n = 1, \cdots, N, \, t = 1, \cdots, \tau, \tag{3.42b}$$

where $\mathbf{W}_{i,j}^{(t)} = \mathbf{Y}_{i,j}^{(t+1)} + \frac{\mathbf{\Lambda}_{i,j}^{(t)}}{\rho}$. One major obstacle in solving $\mathcal{P}_{\mathbf{\Phi}}$ is the non-convex unit-modulus constraint (3.42b). To handle this issue, one can exploit the smooth Riemannian manifold structure of the set of unit-modulus phase shift matrices such that $\mathcal{P}_{\mathbf{\Phi}}$ is converted to an unconstrained optimization problem on the Riemannian manifold. Since the optimization over the Riemannian manifold is conceptually analogous to that in the Euclidean space, optimization tools of Euclidean space (e.g., conjugate gradient

---

[9] The spectral norm constraint $\|\mathbf{Y}\|_2 \le t$ can be equivalently converted to the linear matrix inequality constraint $\mathbf{Y}^{\mathrm{H}}\mathbf{Y} \preceq t\mathbf{I}$.

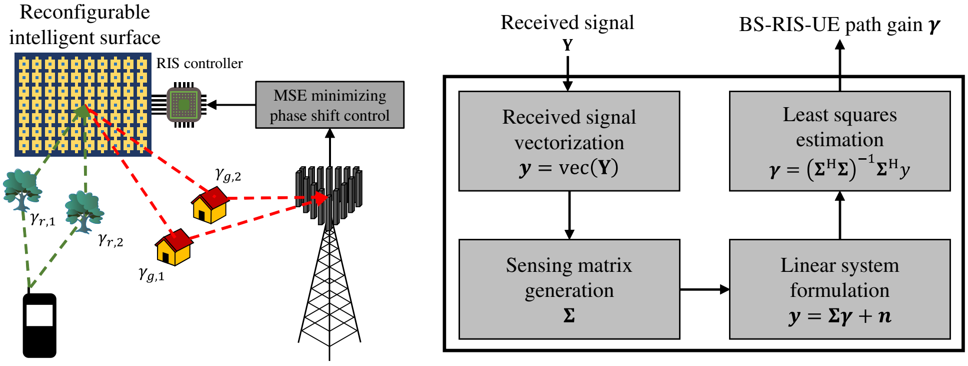

Stage III: BS-RIS-UE angle estimation

Figure 3.5: Block diagram of BS-RIS-UE path gain estimation.

method) can be readily employed to solve the problem on the Riemannian manifold (e.g., Riemannian conjugate gradient (RCG) method) [29].

Lastly, once we obtain $\mathbf{Y}^{(t+1)}$ and $\mathbf{\Phi}^{(t+1)}$, we update $\mathbf{\Lambda}$ using the dual ascent method. The update procedures (3.38)-(3.40) are repeated until $\mathbf{\Phi}$ converges.

We briefly discuss the computational complexity of the proposed RIS phase shift control scheme. First, in the block-mutual coherence matrix update process, the primal-dual interior-point method is used to solve the SDP. The computational complexity of the block-mutual coherence matrix update process is $\mathcal{C}_{\mathbf{Y}} = \mathcal{O}(P_g^4 W^6)$ [48]. Second, in the RIS phase shift matrix update process, the RCG method is used to solve the problem. The computational complexity of this process is $\mathcal{C}_{\mathbf{\Phi}} = \mathcal{O}(M^2 N \tau^3 P_g W^2)$. Third, the computational complexity of the Lagrangian multiplier matrix update process is $\mathcal{C}_{\mathbf{\Lambda}} = \mathcal{O}(M^2 \tau^2 P_g W^2)$.

3.3.3 Stage III: BS-RIS-UE Path Gain Estimation

After the RIS-UE angle estimation, the BS estimates the BS-RIS-UE path gains from the pilot signal of UE (see Fig. 3.5). Since the coherence time of path gains is relatively shorter than that of the path angles, the BS-RIS-UE path gains are estimated at each channel coherence block. Recall that in the previous stage, the BS formulates a block-sparse linear system for the recovery of the block-sparse path gain vector (see (3.28)). By solving the linear system using the LS estimation technique, one can obtain the path gains after which the BS reconstructs the RIS reflected channel matrix using the acquired channel components (see Lemma 1).

We note that the MSE of the LS estimate is determined by the sensing matrix. For example, it has been shown that MSE is minimized when the columns of the sensing matrix are mutually orthogonal [49]. Since the sensing matrix is a function of the RIS phase shifts (see (3.46)), by designing the RIS phase shifts such that the columns of the sensing matrix are mutually orthogonal, we can improve the estimation accuracy of the path gains.

BS-RIS-UE Path Gain Estimation

In this stage, the BS estimates the BS-RIS-UE path gains from the uplink pilot signal for τ_p symbols and then transmits the downlink data for $\tau - \tau_p$ remaining symbols. To be specific, the received matrix $\mathbf{Y} = [\mathbf{y}_1 \cdots \mathbf{y}_{\tau_p}] \in \mathbb{C}^{M \times \tau_p}$ of BS is given by

$$\begin{aligned} \mathbf{Y} =& \mathbf{H}\mathbf{\Phi}\mathbf{P} + \mathbf{N} && (3.43) \\ =& (\mathbf{1}_{P_r}^{\mathrm{T}} \otimes \mathbf{A}_{\mathrm{B}}(\boldsymbol{\theta}_g))\mathrm{diag}(\gamma)(\mathbf{A}_{\mathrm{R}}^*(\boldsymbol{\psi}_r, \boldsymbol{\varphi}_r \bullet \mathbf{A}_{\mathrm{R}}(\boldsymbol{\psi}_g, \boldsymbol{\varphi}_g))^{\mathrm{H}}\mathbf{\Phi}\mathbf{P} + \mathbf{N}, && (3.44) \end{aligned}$$

where $\mathbf{\Phi} = [\boldsymbol{\phi}_1 \cdots \boldsymbol{\phi}_{\tau_p}] \in \mathbb{C}^{N \times \tau_p}$ is the phase shift matrix and $\mathbf{P} = \mathrm{diag}(p_1, \cdots, p_{\tau_p})$ is the pilot matrix. By vectorizing $\mathbf{Y}$ to $\mathbf{y} = \mathrm{vec}(\mathbf{Y})$, we obtain the linear system with respect to the BS-RIS-UE path gain vector γ as (see (3.26)-(3.28))

$$\mathbf{y} = \mathbf{\Sigma}\gamma + \mathbf{n}, \tag{3.45}$$

where $\mathbf{\Sigma} \in \mathbb{C}^{M\tau_p \times P_r P_g}$ is the sensing matrix given by

$$\mathbf{\Sigma} = (\mathbf{P}\mathbf{\Phi}^{\mathrm{T}}(\mathbf{A}_{\mathrm{R}}(\boldsymbol{\psi}_r, \boldsymbol{\varphi}_r) \bullet \mathbf{A}_{\mathrm{R}}^*(\boldsymbol{\psi}_g, \boldsymbol{\varphi}_g))) * (\mathbf{1}_{P_r}^{\mathrm{T}} \otimes \mathbf{A}_{\mathrm{B}}(\boldsymbol{\theta}_g)) \tag{3.46}$$

Then the LS estimate of BS-RIS-UE path gains is

$$\hat{\gamma} = (\mathbf{\Sigma}^{\mathrm{H}}\mathbf{\Sigma})^{-1}\mathbf{\Sigma}^{\mathrm{H}}\mathbf{y}. \tag{3.47}$$

Once we obtain the BS-RIS-UE path gains $\hat{\gamma}$, together with the BS-RIS angles $\hat{\boldsymbol{\theta}}_g$, $(\hat{\boldsymbol{\psi}}_g, \hat{\boldsymbol{\varphi}}_g)$ and the RIS-UE angles $(\hat{\boldsymbol{\psi}}_r, \hat{\boldsymbol{\varphi}}_r)$, we reconstruct $\hat{\mathbf{H}}$ as

$$\hat{\mathbf{H}} = (\mathbf{1}_{P_r}^{\mathrm{T}} \otimes \mathbf{A}_{\mathrm{B}}(\hat{\boldsymbol{\theta}}_g))\mathrm{diag}(\boldsymbol{\gamma})(\mathbf{A}_{\mathrm{R}}^*(\hat{\boldsymbol{\psi}}_r, \hat{\boldsymbol{\varphi}}_r) \bullet \mathbf{A}_{\mathrm{R}}(\hat{\boldsymbol{\psi}}_g, \hat{\boldsymbol{\varphi}}_g))^{\mathrm{H}}. \tag{3.48}$$

RIS Phase Shift Control

Note that the MSE of the LS estimate is given by

$$\mathrm{MSE} = \mathbb{E}\big[\|\hat{\gamma} - \boldsymbol{\gamma}\|^2\big] = \sigma_n^2 \mathrm{tr}((\boldsymbol{\Sigma}^{\mathrm{H}}\boldsymbol{\Sigma})^{-1}), \tag{3.49}$$

where σ_n^2 is the noise variance. Since $\boldsymbol{\Sigma}$ is a function of RIS phase shift matrix $\boldsymbol{\Phi}$ (see (3.46)), we can improve the path gain estimation accuracy by optimizing $\boldsymbol{\Phi}$ to minimize the MSE.

Specifically, the MSE minimization problem is formulated as

$$\mathcal{P}_{\mathrm{III}} : \min_{\boldsymbol{\Phi} \in \mathcal{M}} \ \mathrm{tr}((\boldsymbol{\Sigma}^{\mathrm{H}}(\boldsymbol{\Phi})\boldsymbol{\Sigma}(\boldsymbol{\Phi}))^{-1}), \tag{3.50a}$$

where $\mathcal{M} = \{\boldsymbol{\Phi} \in \mathbb{C}^{N \times \tau} : \big|[\boldsymbol{\Phi}]_{n,t}\big| = 1, \forall n, \forall t\}$ is the complex circle manifold, a set of the phase shift matrices satisfying the unit-modulus constraints. By exploiting the linear matrix inequality and the Cauchy-Schwarz inequality, we obtain the lower bound of the optimal value of $\mathcal{P}_{\mathrm{III}}$:

$$\begin{aligned} \min_{\boldsymbol{\Phi} \in \mathcal{M}} \mathrm{tr}((\boldsymbol{\Sigma}^{\mathrm{H}}(\boldsymbol{\Phi})\boldsymbol{\Sigma}(\boldsymbol{\Phi}))^{-1}) &\geq \min_{\boldsymbol{\Phi} \in \mathcal{M}} \sum_{i=1}^{P_r P_g} \frac{1}{[(\boldsymbol{\Sigma}^{\mathrm{H}}(\boldsymbol{\Phi})\boldsymbol{\Sigma}(\boldsymbol{\Phi}))]_{i,i}} & (3.51) \\ &\geq \frac{(P_r P_g)^2}{\max_{\boldsymbol{\Phi} \in \mathcal{M}} \mathrm{tr}(\boldsymbol{\Sigma}^{\mathrm{H}}(\boldsymbol{\Phi})\boldsymbol{\Sigma}(\boldsymbol{\Phi}))}, & (3.52) \end{aligned}$$

where the first inequality is from [49, Example 4.3] and the second inequality is from the Cauchy-Schwarz inequality. Note that the equality condition of (3.52) is $\boldsymbol{\Sigma}^{\mathrm{H}}(\boldsymbol{\Phi})\boldsymbol{\Sigma}(\boldsymbol{\Phi}) = c\mathbf{I}$ for some c. Thus, one can see that the optimal solution of $\mathcal{P}_{\mathrm{III}}$ can be re-expressed as

$$\arg \min_{\boldsymbol{\Phi} \in \mathcal{M}} \mathrm{tr}((\boldsymbol{\Sigma}^{\mathrm{H}}(\boldsymbol{\Phi})\boldsymbol{\Sigma}(\boldsymbol{\Phi}))^{-1}) = \arg \max_{\substack{\boldsymbol{\Sigma}^{\mathrm{H}}(\boldsymbol{\Phi})\boldsymbol{\Sigma}(\boldsymbol{\Phi}) = c\mathbf{I} \\ \boldsymbol{\Phi} \in \mathcal{M}}} \mathrm{tr}(\boldsymbol{\Sigma}^{\mathrm{H}}(\boldsymbol{\Phi})\boldsymbol{\Sigma}(\boldsymbol{\Phi})). \tag{3.53}$$

In the following proposition, we provide the asymptotic optimal solution of (3.53).

Proposition 6. *The feasible solution of* (3.53) *exists only when* $\tau_p \geq P_r P_g$. *Also, when* $\tau_p = P_r P_g$, *the asymptotic optimal solution of* $\mathcal{P}_{\text{III}}$ *satisfying* (3.53) *is given by*

$$\mathbf{\Phi} = \mathbf{A}_{\text{R}}^{*}(\boldsymbol{\psi}_r, \boldsymbol{\varphi}_r) \bullet \mathbf{A}_{\text{R}}(\boldsymbol{\psi}_g, \boldsymbol{\varphi}_g). \tag{3.54}$$

Proof. See Appendix C. □

3.4 Performance Analysis of Three-Stage Angular-Domain Channel Estimation

3.4.1 Channel Estimation Error Analysis

Since the RIS-UE angles are chosen from the quantized angle set, a mismatch between the true angle $(\boldsymbol{\psi}_r, \boldsymbol{\varphi}_r)$ and the quantized angle $(\hat{\boldsymbol{\psi}}_r, \hat{\boldsymbol{\varphi}}_r)$ is unavoidable in the RIS-UE angle estimation, which causes a distortion of the linear system at the BS-RIS-UE path gain estimation and the degradation of the RIS reflected channel estimation performance.

In this section, we analyze the RIS reflected channel estimation error induced by the RIS-UE angle quantization[10]. To this end, we first derive the distortions $\Delta\mathbf{A}_{\text{R},r}$ and $\Delta\mathbf{\Phi}$ of RIS-UE AoA matrix in (3.5) and phase shift matrix in (3.54). We then derive the distortions $\Delta\mathbf{\Sigma}$ and $\Delta\boldsymbol{\gamma}$ of sensing matrix in (3.46) and BS-RIS-UE path gain estimate in (3.47), from which we find out the NMSE of constructed RIS reflected channel $\mathbb{E}[||\Delta\mathbf{H}||_{\text{F}}^2/||\mathbf{H}||_{\text{F}}^2]$. For notational simplicity, we use the notations $\mathbf{A}_{\text{B}} = \mathbf{A}_{\text{B}}(\boldsymbol{\theta}_g)$, $\mathbf{A}_{\text{R},g} = \mathbf{A}_{\text{R}}(\boldsymbol{\psi}_g, \boldsymbol{\varphi}_g)$, and $\mathbf{A}_{\text{R},r} = \mathbf{A}_{\text{R}}(\boldsymbol{\psi}_r, \boldsymbol{\varphi}_r)$. Also, we assume the noiseless scenario to simplify the analysis.

Let $(\Delta\boldsymbol{\psi}_r, \Delta\boldsymbol{\varphi}_r) = (\hat{\boldsymbol{\psi}}_r, \hat{\boldsymbol{\varphi}}_r) - (\boldsymbol{\psi}_r, \boldsymbol{\varphi}_r)$ be the quantization error vectors. Using the first-order Taylor expansion, we can obtain the distortion of RIS-UE AoA matrix

---

[10] Note that in this analysis, we do not consider the BS-RIS angle estimation error. This is because since the BS-RIS angle can be readily approximated as static information, the BS can collect a large number of pilot measurements for the BS-RIS angle estimation. Hence, the BS-RIS angle estimation error is almost negligible compared to the RIS-UE angle estimation error.

$\Delta\mathbf{A}_{\mathrm{R},r}$ as

$$\Delta\mathbf{A}_{\mathrm{R},r} \approx \nabla_{\boldsymbol{\psi}_r}\mathbf{A}_{\mathrm{R},r}\Delta\boldsymbol{\psi}_r + \nabla_{\boldsymbol{\varphi}_r}\mathbf{A}_{\mathrm{R},r}\Delta\boldsymbol{\varphi}_r \tag{3.55}$$

$$= \mathbf{R} \odot \mathbf{A}_{\mathrm{R},r}. \tag{3.56}$$

Here, $\mathbf{R} = [\mathbf{r}_1 \cdots \mathbf{r}_{P_r}] \in \mathbb{C}^{N \times P_r}$ where $\mathbf{r}_i = \mathbf{p}_i\Delta\psi_{r,i} + \mathbf{q}_i\Delta\varphi_{r,i}$ and

$$\mathbf{p}_i = -j\pi \sin\varphi_{r,i}(\cos\psi_{r,i}(\mathbf{n}_y \otimes \mathbf{1}_{N_x}) - \sin\psi_{r,i}(\mathbf{1}_{N_y} \otimes \mathbf{n}_x)), \tag{3.57}$$

$$\mathbf{q}_i = -j\pi \cos\varphi_{r,i}(\sin\psi_{r,i}(\mathbf{n}_y \otimes \mathbf{1}_{N_x}) + \cos\psi_{r,i}(\mathbf{1}_{N_y} \otimes \mathbf{n}_x)), \tag{3.58}$$

where $\mathbf{n}_x = [0 \cdots N_x - 1]^{\mathrm{T}}$ and $\mathbf{n}_y = [0 \cdots N_y - 1]^{\mathrm{T}}$. Recall that the phase shift matrix at the BS-RIS-UE path gain estimation stage is $\boldsymbol{\Phi} = \mathbf{A}^*_{\mathrm{R},r} \bullet \mathbf{A}_{\mathrm{R},g}$ (see (3.54)). Thus, the distortion of the phase shift matrix $\Delta\boldsymbol{\Phi}$ is given by

$$\Delta\boldsymbol{\Phi} = \Delta\mathbf{A}^*_{\mathrm{R},r} \bullet \mathbf{A}_{\mathrm{R},g} \approx (\mathbf{R} \odot \mathbf{A}_{\mathrm{R},r})^* \bullet \mathbf{A}_{\mathrm{R},g}. \tag{3.59}$$

In the BS-RIS-UE path gain estimation stage, the sensing matrix is given by $\boldsymbol{\Sigma} = (\mathbf{P}\boldsymbol{\Phi}^{\mathrm{T}}(\mathbf{A}_{\mathrm{R},r} \bullet \mathbf{A}^*_{\mathrm{R},g})) * (\mathbf{1}^{\mathrm{T}}_{P_r} \otimes \mathbf{A}_{\mathrm{B}})$ (see (3.46)). Then the distortion of sensing matrix $\Delta\boldsymbol{\Sigma}$ can be approximated as

$$\Delta\boldsymbol{\Sigma} \approx \big(\mathbf{P}\Delta\boldsymbol{\Phi}^{\mathrm{T}}(\mathbf{A}_{\mathrm{R},r} \bullet \mathbf{A}^*_{\mathrm{R},g}) + \mathbf{P}\boldsymbol{\Phi}^{\mathrm{T}}(\Delta\mathbf{A}_{\mathrm{R},r} \bullet \mathbf{A}^*_{\mathrm{R},g})\big) * (\mathbf{1}^{\mathrm{T}}_{P_r} \otimes \mathbf{A}_{\mathrm{B}}). \tag{3.60}$$

Due to the distortion of the sensing matrix, the performance of LS estimation of BS-RIS-UE path gains will be degraded. In the following proposition, we provide the distortion of $\boldsymbol{\gamma}$.

Proposition 7. *The distortion of BS-RIS-UE path gain estimate in* (3.47) *can be approximated as*

$$\Delta\boldsymbol{\gamma} \approx -(\boldsymbol{\Sigma}^{\mathrm{H}}\boldsymbol{\Sigma})^{-1}\boldsymbol{\Sigma}^{\mathrm{H}}\big((\mathbf{P}\boldsymbol{\Phi}^{\mathrm{T}}(\Delta\mathbf{A}_{\mathrm{R},r} \bullet \mathbf{A}^*_{\mathrm{R},g})) * (\mathbf{1}^{\mathrm{T}}_{P_r} \otimes \mathbf{A}_{\mathrm{B}})\big)\boldsymbol{\gamma}. \tag{3.61}$$

Proof. See Appendix D. □

Finally, using (3.56), (3.59), (3.60), and (3.61), we obtain the asymptotic closed-form expression of the NMSE of RIS reflected channel estimation.

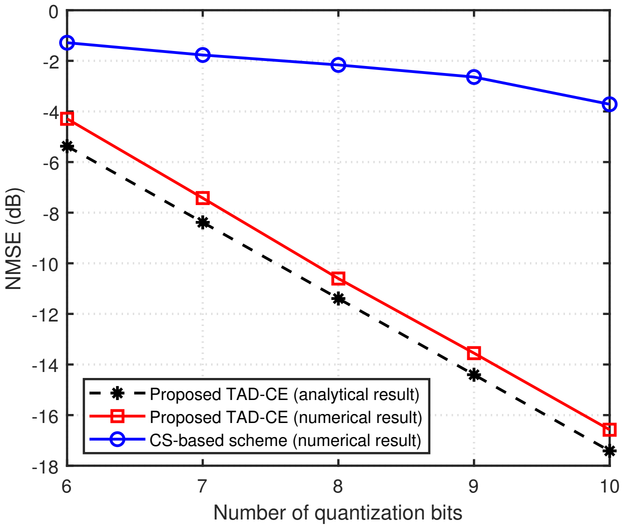

Figure 3.6: NMSE vs. number of RIS-UE angle quantization bits.

Theorem 3. *When the number of RIS reflecting elements N is large, the NMSE of RIS reflected channel estimation induced by the RIS-UE angle quantization can be approximated as*

$$\mathbb{E}\left[\frac{\|\Delta\mathbf{H}\|_{\mathrm{F}}^2}{\|\mathbf{H}\|_{\mathrm{F}}^2}\right] \approx \frac{(N_x^2 + N_y^2 - 2)\pi^4}{144}\left(\frac{1}{W_{\mathrm{az}}^2} + \frac{1}{4W_{\mathrm{el}}^2}\right), \tag{3.62}$$

where $N = N_x \times N_y$ is the number of RIS reflecting antennas and $W = W_{\mathrm{az}} \times W_{\mathrm{el}}$ is the number of angular bins for the RIS-UE angle quantization.

Proof. See Appendix E. □

In Fig. 3.6, we plot the NMSE as a function of the number of RIS-UE angle quantization bits. We observe that the analytic NMSE obtained from Theorem 1 is close to the numerical result. We can infer from these results that by properly scaling the number of RIS-UE angle quantization bits using Theorem 1, one can effectively control the RIS reflected channel estimation error. We also observe that the NMSE of TAD-CE is much smaller than that of the conventional CS-based channel estimation scheme [36]. Since the conventional CS-based scheme quantizes and estimates the BS-RIS and the

RIS-UE angles simultaneously, the quantization distortion of the estimated channel is considerable. Whereas, using the property that the BS-RIS angles remain unchanged, TAD-CE continuously estimates the BS-RIS angles before the UE connection. Then, when the BS is connected to the UE, the BS quantizes and estimates only the RIS-UE angles.

3.4.2 Pilot Overhead Analysis

In this subsection, we analyze the pilot overhead of the proposed TAD-CE scheme. As mentioned, TAD-CE consists of three major steps: 1) estimation of the BS-RIS angles before the UE connection, 2) estimation of the RIS-UE angles occasionally (once every L_r blocks[11]), and 3) estimation of the BS-RIS-UE path gains at each channel coherence block. Note that the number of pilot symbols used for the BS-RIS angle estimation is not considered in the pilot overhead analysis since the BS-RIS angles are estimated before the UE connection. Recall that in the RIS-UE angle estimation, we use the block-sparse recovery algorithm to estimate the BS-RIS angles. Thus, the number of measurements required for the RIS-UE angle estimation is $\tau_2 = P_r \log WP_g$ [50]. After the RIS-UE angle estimation, we estimate the BS-RIS-UE path gains using the LS estimation. Thus, the number of pilot measurements required for the BS-RIS-UE path gain estimation is $\tau_3 = P_r P_g$. In conclusion, the pilot overhead of TAD-CE is

$$\tau = \left\lceil \frac{1}{L_r}\tau_2 \right\rceil + \tau_3 = \left\lceil \frac{P_r}{L_r} \log WP_g \right\rceil + P_r P_g. \tag{3.63}$$

In Table 3.1, we compare the pilot overhead of TAD-CE with two benchmark schemes: 1) CS-based scheme [36] and 2) BALS scheme [34]. One can see that TAD-CE achieves a significant pilot overhead reduction over the benchmark schemes. One can also see that while the pilot overheads of conventional schemes increase sharply with the number of reflecting elements, that of TAD-CE does not change significantly.

---

[11] L_r is the RIS-UE angle coherence time in terms of channel coherence block.

Table 3.1: Pilot overhead comparison of different channel estimation schemes

	Pilot overhead	Pilot overhead for various N		
		$N = 256$	$N = 512$	$N = 1024$
Proposed TAD-CE	$\lceil \frac{P_r}{L_r} \log WP_g \rceil + P_rP_g$	11	11	12
CS-based scheme	$\lceil P_rP_g \log W^2 \rceil$	44	49	55
BALS scheme	N	256	512	1024

3.5 Simulation Results

3.5.1 Simulation Setup

In this section, we investigate the channel estimation performance of the proposed TAD-CE technique. We consider the RIS-aided mmWave systems where a BS equipped with $M = 8$ antennas serves a single-antenna UE with the aid of an RIS equipped with $N = 16 \times 16$ reflecting elements. The RIS and UE are located randomly around the BS within the cell radius of $R = 50\,\text{m}$. We use the block-fading multi-path channel model where the number of path is $P_g = P_r = 3$, the carrier frequency is $f_c = 28\,\text{GHz}$, and the channel bandwidth is $100\,\text{MHz}$. The channel remains unchanged within a block of $\tau = 14 \times 9 = 126$ symbols (9 subframes $= 9\,\text{ms}$). By exploiting the angular-domain channel coherence property, we assume that the BS-RIS angles are constant and the RIS-UE angles are coherent for 40 blocks whereas the BS-RIS-UE path gains vary over block [40]. The large-scale fading coefficients are modeled as $\rho = \text{PL} \times 10^{\frac{\sigma_{\text{sh}} z_{\text{sh}}}{10}}$ where PL represents the path loss and $10^{\frac{\sigma_{\text{sh}} z_{\text{sh}}}{10}}$ represents the shadow fading where $\sigma_{\text{sh}} = 4\,\text{dB}$ and $z_{\text{sh}} \sim \mathcal{CN}(0, 1)$. Also, we use the path loss model in 3GPP Rel. 16 [17]. The small-scale fading coefficients are generated according to the complex normal distribution (i.e. $\gamma \sim \mathcal{CN}(0, 1)$). We set the uplink transmit power of UE and the noise power to $1\,\text{W}$ and $-110\,\text{dBm/Hz}$, respectively.

For comparison, we use 5 benchmark schemes: 1) oracle-LS scheme where the

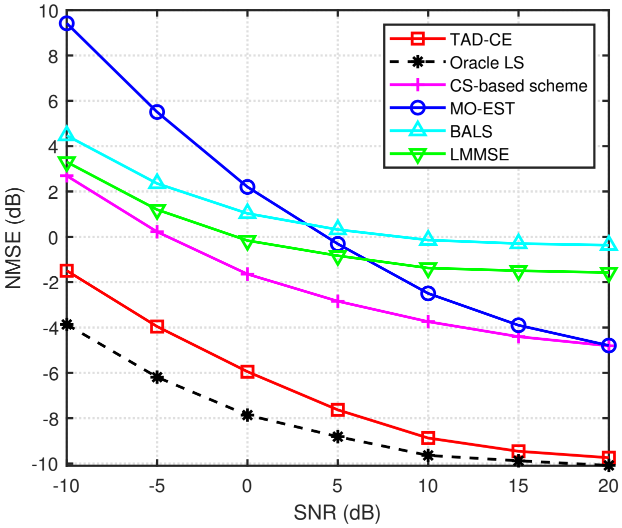

Figure 3.7: NMSE vs. transmit SNR.

BS-RIS and RIS-UE angles are perfectly estimated and only the BS-RIS-UE path gains are estimated using the LS technique, 2) MO-EST scheme that uses the optimization technique on the Riemannian manifold of low-rank RIS reflected channel matrices [51], 3) CS-based scheme that estimates the BS-RIS angles, the RIS-UE angles, and the BS-RIS-UE path gains simultaneously using the OMP algorithm [36], 4) BALS scheme that uses the parallel factor decomposition of RIS reflected channel [34], and 5) LMMSE-based scheme [33]. As a performance metric, we use the NMSE defined as $\mathbb{E}[\|\hat{\mathbf{H}} - \mathbf{H}\|_{\mathrm{F}}^2 / \|\mathbf{H}\|_{\mathrm{F}}^2]$. In the proposed TAD-CE scheme, by exploiting the angular-domain channel coherence property, the BS-RIS angles are estimated only once before the UE connection, the RIS-UE angles are estimated once every 40 blocks, and the BS-RIS-UE path gains are estimated at each block. Specifically, we use $L_g = 50$ blocks for the BS-RIS angle estimation, $L_r = 5$ blocks for the RIS-UE angle estimation, and $\tau_p = 14 \times 4 = 56$ uplink symbols for the BS-RIS-UE path gain estimation. We measure the NMSE for $40 - 5 = 35$ blocks after the RIS-UE angle estimation. To make fair comparisons with the benchmark schemes, we measure the NMSEs of

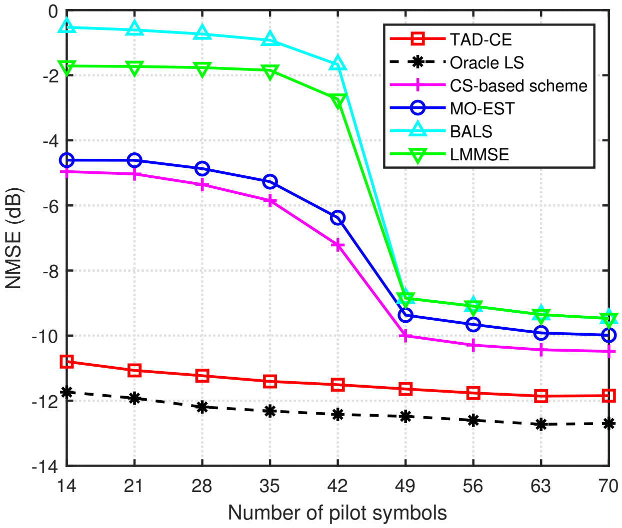

Figure 3.8: NMSE vs. number of pilot symbols.

benchmark schemes for 35 blocks but with different numbers of uplink symbols (i.e., $\tau_{p,\text{conv}} = \tau_p + \lceil \frac{L_r \tau}{35} \rceil$) so that the total number of pilot symbols used for the RIS reflected channel estimation would be the same with that of TAD-CE[12].

3.5.2 Simulation Results

In Fig. 3.7, we plot the NMSE as a function of the transmit SNR. We observe that the proposed TAD-CE scheme outperforms the conventional channel estimation schemes by a large margin. For instance, when SNR $= 10\,$dB, the proposed scheme achieves almost $7\,$dB and $9\,$dB NMSE gains over the conventional MO-EST scheme and BALS scheme. Even when compared to the conventional CS-based channel estimation scheme, the NMSE gain of the proposed scheme is more than $5\,$dB. In fact, in the high SNR regime, the performance of TAD-CE is similar to that of the oracle-LS scheme, meaning that the estimated BS-RIS and RIS-UE angles of TAD-CE are close to the genie angles.

---

[12] The pilot symbols used for the estimation of BS-RIS angles is not counted since they are estimated before the UE connection.

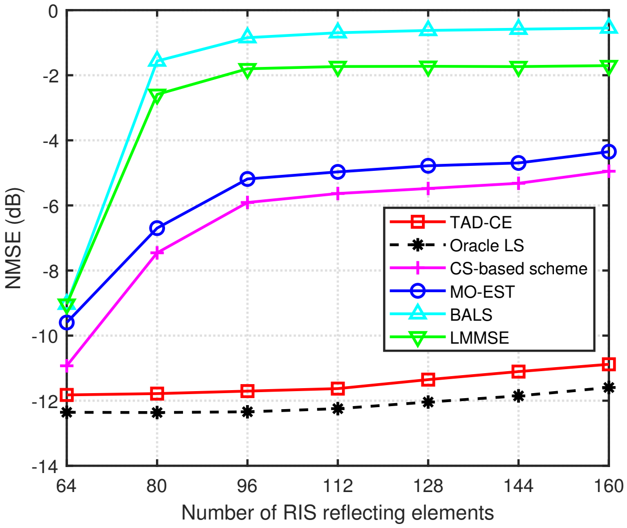

Figure 3.9: NMSE vs. number of reflecting elements.

This is because TAD-CE estimates the BS-RIS and RIS-UE angles sporadically and estimates the path gains frequently so that the number of channel parameters to be estimated in each stage is quite small. Thus, TAD-CE can accurately estimate the channel parameters even with a small amount of pilot measurements.

In Fig. 3.8, we set $N = 64$ and then plot the NMSE as a function of the number of pilot symbols τ_p. To make a fair comparison, we also change the number of pilot symbols of conventional schemes $\tau_{p,\text{conv}} = \tau_p + \lceil \frac{L_r \tau}{35} \rceil$ as well. We observe that the proposed TAD-CE achieves more than 80% pilot overhead reduction over the conventional schemes. For example, to achieve the NMSE of -11 dB, TAD-CE requires only $\tau_p = 14$ symbols whereas both the conventional LS and BALS schemes require more than $\tau_p = 70$ symbols. This is because the number of pilot symbols of TAD-CE required to estimate the sparse channel parameters scales with the number of propagation paths while those of conventional schemes required to estimate the full-dimensional RIS reflected channel matrix scale with the number of reflecting elements.

In Fig. 3.9, we investigate the NMSEs of the proposed TAD-CE and benchmark

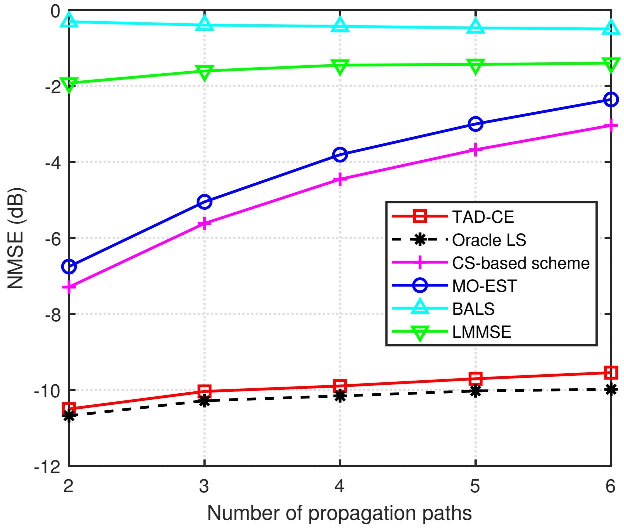

Figure 3.10: NMSE vs. number of propagation paths.

schemes as a function of the number of RIS reflecting elements N. From the simulation results, we observe that the NMSE gain of TAD-CE over the conventional schemes increases with the number of reflecting elements. In particular, when N increases from 64 to 160, the NMSE gain of TAD-CE over the conventional BALS scheme increases from $2.8\,\text{dB}$ to $10\,\text{dB}$. This implies that TAD-CE would be more effective in improving the channel estimation performance of the RIS-aided terahertz (THz) systems where the number of reflecting elements is extremely large.

In Fig. 3.10, we plot the NMSE as a function of the number of propagation paths P. We observe that TAD-CE outperforms the conventional schemes by a large margin. For example, when $P = 6$, TAD-CE achieves $7\,\text{dB}$ and $8.1\,\text{dB}$ NMSE gains over the conventional CS-based and BALS schemes, respectively. We also observe that when the number of paths increases, the NMSEs of conventional schemes increase sharply whereas that of TAD-CE does not increase much. Note that the performance of CS technique depends heavily on the sparsity (in our case, the number of paths). Since the conventional CS-based scheme estimates all channel components simultane-

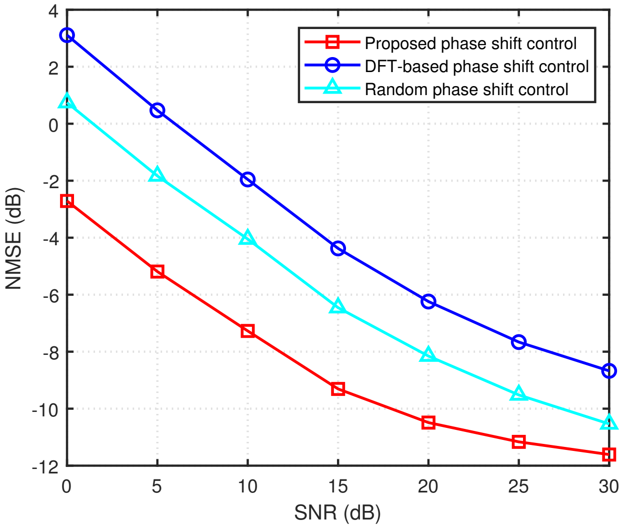

Figure 3.11: NMSE vs. transmit SNR.

ously, the performance degradation is severe when the number of propagation paths is large. In contrast, since TAD-CE separately estimates these channel components, the performance degradation is marginal even in the rich scattering environments.

In order to examine the effectiveness of the proposed phase shift control scheme, we compare the NMSE performance of the proposed scheme with two benchmark schemes: 1) DFT-based phase shift control scheme that uses the columns of DFT matrix as the phase shift vectors and 2) random phase shift control scheme that randomly chooses the phase shifts of RIS reflecting elements. In all schemes under test, we use TAD-CE for the RIS reflected channel estimation. In Fig. 3.11, we observe that the proposed scheme outperforms the benchmark schemes. This is because the proposed scheme optimizes the phase shifts using the channel components with relatively long coherence time but the conventional schemes have no such mechanism to improve the channel estimation accuracy. Interestingly, we observe that the random phase shift control scheme performs better than the DFT-based scheme. The reason is that due to the large number of RIS reflecting elements, the RIS reflected beams are very narrow so that the SNR decreases sharply when the phase shift vectors generated from the DFT matrix are not properly align with the propagation paths of the RIS reflected channel. This implies that the proper phase shift control is crucial for the accurate acquisition of RIS reflected channel information.

3.6 Summary

In this chapter, we proposed an efficient channel estimation framework to reduce the pilot overhead of RIS-aided mmWave systems. Key idea of the proposed TAD-CE scheme is to decompose the RIS reflected channel into three major components, i.e., static BS-RIS angles, quasi-static RIS-UE angles, and time-varying BS-RIS-UE path gains, and then estimate these components in different time scales. In doing so, the number of channel parameters to be estimated at each stage can be reduced significantly, resulting in a reduction of pilot overhead. Also, by optimizing the RIS phase shifts using the channel components with relatively long coherence time, we could further improve the channel estimation accuracy without requiring additional pilot resources. We demonstrated from the channel estimation error and pilot overhead analyses and numerical evaluations that the proposed TAD-CE scheme is effective in saving the pilot resources. In our work, we assumed the ideal phase shift model where the reflection amplitude and the phase shifts are independent, but an extension to the realistic scenarios where the reflection is imperfect and is affected by the RIS phase shifts would be an interesting future work worth pursuing.

3.7 Proofs

For notational simplicity, we denote $\mathbf{A}_{\text{B}} = \mathbf{A}_{\text{B}}(\boldsymbol{\theta}_g)$, $\mathbf{A}_{\text{R},g} = \mathbf{A}_{\text{R}}(\boldsymbol{\psi}_g, \boldsymbol{\varphi}_g)$, and $\mathbf{A}_{\text{R},r} = \mathbf{A}_{\text{R}}(\boldsymbol{\psi}_r, \boldsymbol{\varphi}_r)$.

3.7.1 Proof of Proposition 1

Let $\mathbf{c}_i$ be the i-th column vector of $\mathbf{P}^{\mathrm{H}}\mathbf{\Phi}^{\mathrm{H}}(\mathbf{A}_{\mathrm{R},r}^{*} \bullet \mathbf{A}_{\mathrm{R},g})$. Then we obtain

$$\mathbf{R}_s = (\mathbf{1}_{P_r}^{\mathrm{T}} \otimes \mathbf{A}_{\mathrm{B}})\mathbb{E}\big[[\gamma_1^{(l),*}\mathbf{c}_1 \cdots \gamma_{P_gP_r}^{(l),*}\mathbf{c}_{P_gP_r}]^{\mathrm{H}}[\gamma_1^{(l),*}\mathbf{c}_1 \cdots \gamma_{P_gP_r}^{(l),*}\mathbf{c}_{P_gP_r}]\big](\mathbf{1}_{P_r}^{\mathrm{T}} \otimes \mathbf{A}_{\mathrm{B}})^{\mathrm{H}} \tag{3.64}$$

$$= \rho_g\rho_r(\mathbf{1}_{P_r}^{\mathrm{T}} \otimes \mathbf{A}_{\mathrm{B}})\mathrm{diag}(\|\mathbf{c}_1\|^2, \cdots, \|\mathbf{c}_{P_rP_g}\|^2)(\mathbf{1}_{P_r}^{\mathrm{T}} \otimes \mathbf{A}_{\mathrm{B}})^{\mathrm{H}} \tag{3.65}$$

$$= \rho_g\rho_r\mathbf{A}_{\mathrm{B}}\sum_{i=1}^{P_r}\mathrm{diag}\big(\|\mathbf{c}_{(i-1)P_g+1}\|^2, \cdots, \|\mathbf{c}_{iP_g}\|^2\big)\mathbf{A}_{\mathrm{B}}^{\mathrm{H}} \tag{3.66}$$

$$= \rho_g\rho_r\mathbf{A}_{\mathrm{B}}\mathrm{diag}(\|\mathbf{P}^{\mathrm{H}}\mathbf{\Phi}^{\mathrm{H}}\mathbf{B}_1\mathbf{A}_{\mathrm{R},r}^{*}\|^2, \cdots, \|\mathbf{P}^{\mathrm{H}}\mathbf{\Phi}^{\mathrm{H}}\mathbf{B}_{P_g}\mathbf{A}_{\mathrm{R},r}^{*}\|^2)\mathbf{A}_{\mathrm{B}}^{\mathrm{H}}. \tag{3.67}$$

The closed-form expression of $\mathbf{R}_t$ can be obtained similarly with $\mathbf{R}_s$.

3.7.2 Proof of Proposition 2

We will show that $\mathcal{N}(\mathbf{\Phi}^{\mathrm{H}}(\mathbf{A}_{\mathrm{R},r}^{*} \bullet \mathbf{A}_{\mathrm{R},g})) = \{\mathbf{0}\}$ which is equivalent to $\mathcal{N}(\mathbf{\Phi}^{\mathrm{H}}) \cap \mathcal{C}(\mathbf{A}_{\mathrm{R},r}^{*} \bullet \mathbf{A}_{\mathrm{R},g}) = \{\mathbf{0}\}$ where $\mathcal{N}(\cdot)$ and $\mathcal{C}(\cdot)$ are the null and column spaces, respectively. Let $\mathbf{F}_N = [\mathbf{f}_1 \cdots \mathbf{f}_N]$ be the N-point DFT matrix and without the loss of generality, let $\mathbf{\Phi} = [\mathbf{f}_1 \cdots \mathbf{f}_\tau]$. Then $\mathcal{N}(\mathbf{\Phi}^{\mathrm{H}}) = \mathcal{C}(\mathbf{\Phi})^{\perp} = \mathrm{span}\{\mathbf{f}_{\tau+1}, \cdots, \mathbf{f}_N\}$. Due to the property of Khatri-Rao product, the column vectors of $\mathbf{A}_{\mathrm{R},r}^{*} \bullet \mathbf{A}_{\mathrm{R},g}$ are also array response vectors and thus, they are independent with $\mathbf{f}_{\tau+1}, \cdots, \mathbf{f}_N$. Thus, $\mathcal{N}(\mathbf{\Phi}^{\mathrm{H}}) \cap \mathcal{C}(\mathbf{A}_{\mathrm{R},r}^{*} \bullet \mathbf{A}_{\mathrm{R},g}) = \mathrm{span}\{\mathbf{f}_{\tau+1}, \cdots, \mathbf{f}_N\} \cap \mathcal{C}(\mathbf{A}_{\mathrm{R},r}^{*} \bullet \mathbf{A}_{\mathrm{R},g}) = \{\mathbf{0}\}$.

3.7.3 Proof of Proposition 3

From the definition of $\mathbf{\Sigma}$ in (3.46), one can easily see that we need $\tau_p \geq P_rP_g$ to make $\mathbf{\Sigma}$ into an orthogonal matrix. Also, since the column vectors of $\mathbf{A}_{\mathrm{R},r}^{*} \bullet \mathbf{A}_{\mathrm{R},g}$ are also array response vectors, $\mathbf{\Phi} = \mathbf{A}_{\mathrm{R},r}^{*} \bullet \mathbf{A}_{\mathrm{R},g} \in \mathcal{M}$. Now, to show that $\mathbf{\Sigma}$ asymptotically becomes an orthogonal matrix when $\mathbf{\Phi} = \mathbf{A}_{\mathrm{R},r}^{*} \bullet \mathbf{A}_{\mathrm{R},g}$, we use the mutual orthogonality between the array steering vectors, i.e., $\mathbf{a}_{\mathrm{R}}^{\mathrm{H}}(\psi_{r,i}, \varphi_{r,i})\mathbf{a}_{\mathrm{R}}(\psi_{r,j}, \varphi_{r,j}) \approx N\delta_{i,j}$. Using this property, $\mathbf{\Sigma}$ can be re-expressed as

$$\mathbf{\Sigma} = (\mathbf{P}(\mathbf{A}^*_{\mathrm{R},r} \bullet \mathbf{A}_{\mathrm{R},g})^{\mathrm{T}}(\mathbf{A}_{\mathrm{R},r} \bullet \mathbf{A}^*_{\mathrm{R},g})) * (\mathbf{1}^{\mathrm{T}}_{P_r} \otimes \mathbf{A}_{\mathrm{B}}) \tag{3.68}$$

$$\approx N\mathbf{P} * (\mathbf{1}^{\mathrm{T}}_{P_r} \otimes \mathbf{A}_{\mathrm{B}}). \tag{3.69}$$

Then one can see that $\mathbf{\Sigma}$ becomes an orthogonal matrix as

$$\mathbf{\Sigma}^{\mathrm{H}}\mathbf{\Sigma} \approx N^2(\mathbf{P}^{\mathrm{H}}\mathbf{P}) \odot ((\mathbf{1}^{\mathrm{T}}_{P_r} \otimes \mathbf{A}_{\mathrm{B}})^{\mathrm{H}}(\mathbf{1}^{\mathrm{T}}_{P_r} \otimes \mathbf{A}_{\mathrm{B}})) \tag{3.70}$$

$$= N^2 P_{\mathrm{tx}}\mathbf{I}_{P_rP_g} \odot ((\mathbf{1}_{P_r}\mathbf{1}^{\mathrm{T}}_{P_r}) \otimes (\mathbf{A}^{\mathrm{H}}_{\mathrm{B}}\mathbf{A}_{\mathrm{B}})) \tag{3.71}$$

$$= MN^2 P_{\mathrm{tx}}\mathbf{I}_{P_rP_g}, \tag{3.72}$$

where P_{tx} is the BS transmit power. Also, note that tr$(\mathbf{\Sigma}^{\mathrm{H}}\mathbf{\Sigma})$ can be expressed as

$$\mathrm{tr}(\mathbf{\Sigma}^{\mathrm{H}}\mathbf{\Sigma}) = \|\mathbf{\Sigma}\|^2_{\mathrm{F}} \tag{3.73}$$

$$= \|(\mathbf{P}\mathbf{\Phi}^{\mathrm{T}}(\mathbf{A}_{\mathrm{R}}(\boldsymbol{\psi}_r, \boldsymbol{\varphi}_r) \bullet \mathbf{A}^*_{\mathrm{R}}(\boldsymbol{\psi}_g, \boldsymbol{\varphi}_g))) * (\mathbf{1}^{\mathrm{T}}_{P_r} \otimes \mathbf{A}_{\mathrm{B}}(\boldsymbol{\theta}_g))\|^2_{\mathrm{F}} \tag{3.74}$$

$$\overset{(a)}{=} M\left\|\mathbf{P}\mathbf{\Phi}^{\mathrm{T}}(\mathbf{A}_{\mathrm{R},r} \bullet \mathbf{A}^*_{\mathrm{R},g})\right\|^2_{\mathrm{F}}, \tag{3.75}$$

where (a) is from the definition of column-wise Khatri-Rao product. Due to the mutual orthogonality of array steering vectors, $\mathbf{A}^*_{\mathrm{R},r} \bullet \mathbf{A}_{\mathrm{R},g}$ is an orthogonal matrix, and thus $\|\mathbf{\Sigma}\|^2_{\mathrm{F}}$ is maximized when $\mathbf{\Phi} = \mathbf{A}^*_{\mathrm{R},r} \bullet \mathbf{A}_{\mathrm{R},g}$. Therefore, $\mathbf{\Phi} = \mathbf{A}^*_{\mathrm{R},r} \bullet \mathbf{A}_{\mathrm{R},g}$ is the asymptotic optimal solution of (3.53).

3.7.4 Proof of Proposition 4

The distortion of BS-RIS-UE path gain estimate is

$$\Delta\boldsymbol{\gamma} = (\hat{\mathbf{\Sigma}}^{\mathrm{H}}\hat{\mathbf{\Sigma}})^{-1}\hat{\mathbf{\Sigma}}^{\mathrm{H}}\mathbf{y} - \boldsymbol{\gamma} \tag{3.76}$$

$$= (\hat{\mathbf{\Sigma}}^{\mathrm{H}}\hat{\mathbf{\Sigma}})^{-1}\hat{\mathbf{\Sigma}}^{\mathrm{H}}(\mathbf{\Sigma} + \Delta\mathbf{\Sigma}')\boldsymbol{\gamma} - \boldsymbol{\gamma}, \tag{3.77}$$

where $\hat{\mathbf{\Sigma}}$ is the estimated sensing matrix generated from $(\hat{\boldsymbol{\psi}}_r, \hat{\boldsymbol{\varphi}}_r)$. Note that $\mathbf{y}$ is equal to $(\mathbf{\Sigma} + \Delta\mathbf{\Sigma}')\boldsymbol{\gamma}$, not $\mathbf{\Sigma}\boldsymbol{\gamma}$ where $\Delta\mathbf{\Sigma}' = (\mathbf{P}\Delta\mathbf{\Phi}^{\mathrm{T}}(\mathbf{A}_{\mathrm{R},r} \bullet \mathbf{A}^*_{\mathrm{R},g})) * (\mathbf{1}^{\mathrm{T}}_{P_r} \otimes \mathbf{A}_{\mathrm{B}})$. This is because the BS uses the estimated phase shift matrix $\hat{\mathbf{\Phi}}$ generated from $(\hat{\boldsymbol{\psi}}_r, \hat{\boldsymbol{\varphi}}_r)$

so that the effective uplink channel is a function of $\hat{\boldsymbol{\Phi}}$. Also, $(\hat{\boldsymbol{\Sigma}}^{\mathrm{H}}\hat{\boldsymbol{\Sigma}})^{-1}\hat{\boldsymbol{\Sigma}}^{\mathrm{H}}$ can be approximated as

$$\begin{aligned}
(\hat{\boldsymbol{\Sigma}}^{\mathrm{H}}\hat{\boldsymbol{\Sigma}})^{-1}\hat{\boldsymbol{\Sigma}}^{\mathrm{H}} \approx & (\boldsymbol{\Sigma}^{\mathrm{H}}\boldsymbol{\Sigma} + \Delta\boldsymbol{\Sigma}^{\mathrm{H}}\boldsymbol{\Sigma} + \boldsymbol{\Sigma}^{\mathrm{H}}\Delta\boldsymbol{\Sigma})^{-1}(\boldsymbol{\Sigma} + \Delta\boldsymbol{\Sigma})^{\mathrm{H}} && (3.78)\\
\overset{(a)}{=} & ((\boldsymbol{\Sigma}^{\mathrm{H}}\boldsymbol{\Sigma})^{-1} - (\boldsymbol{\Sigma}^{\mathrm{H}}\boldsymbol{\Sigma})^{-1}(\Delta\boldsymbol{\Sigma}^{\mathrm{H}}\boldsymbol{\Sigma} + \boldsymbol{\Sigma}^{\mathrm{H}}\Delta\boldsymbol{\Sigma})(\boldsymbol{\Sigma}^{\mathrm{H}}\boldsymbol{\Sigma})^{-1})(\boldsymbol{\Sigma} + \Delta\boldsymbol{\Sigma})^{\mathrm{H}} \\
& && (3.79)\\
\approx & (\boldsymbol{\Sigma}^{\mathrm{H}}\boldsymbol{\Sigma})^{-1}\boldsymbol{\Sigma}^{\mathrm{H}} + (\boldsymbol{\Sigma}^{\mathrm{H}}\boldsymbol{\Sigma})^{-1}\Delta\boldsymbol{\Sigma}^{\mathrm{H}} - (\boldsymbol{\Sigma}^{\mathrm{H}}\boldsymbol{\Sigma})^{-1}(\Delta\boldsymbol{\Sigma}^{\mathrm{H}}\boldsymbol{\Sigma} + \boldsymbol{\Sigma}^{\mathrm{H}}\Delta\boldsymbol{\Sigma})\\
& (\boldsymbol{\Sigma}^{\mathrm{H}}\boldsymbol{\Sigma})^{-1}\boldsymbol{\Sigma}^{\mathrm{H}} && (3.80)
\end{aligned}$$

where (a) is from the matrix inversion lemma. By plugging (3.80) into (3.77), we obtain

$$\begin{aligned}
\Delta\boldsymbol{\gamma} \approx & ((\boldsymbol{\Sigma}^{\mathrm{H}}\boldsymbol{\Sigma})^{-1}\boldsymbol{\Sigma}^{\mathrm{H}} + (\boldsymbol{\Sigma}^{\mathrm{H}}\boldsymbol{\Sigma})^{-1}\Delta\boldsymbol{\Sigma}^{\mathrm{H}} - (\boldsymbol{\Sigma}^{\mathrm{H}}\boldsymbol{\Sigma})^{-1}(\Delta\boldsymbol{\Sigma}^{\mathrm{H}}\boldsymbol{\Sigma}\\
& + \boldsymbol{\Sigma}^{\mathrm{H}}\Delta\boldsymbol{\Sigma})(\boldsymbol{\Sigma}^{\mathrm{H}}\boldsymbol{\Sigma})^{-1}\boldsymbol{\Sigma}^{\mathrm{H}})(\boldsymbol{\Sigma} + \Delta\boldsymbol{\Sigma}')\boldsymbol{\gamma} - \boldsymbol{\gamma} && (3.81)\\
\approx & (\boldsymbol{\Sigma}^{\mathrm{H}}\boldsymbol{\Sigma})^{-1}\boldsymbol{\Sigma}^{\mathrm{H}}(\Delta\boldsymbol{\Sigma}' - \Delta\boldsymbol{\Sigma})\boldsymbol{\gamma} && (3.82)\\
= & -(\boldsymbol{\Sigma}^{\mathrm{H}}\boldsymbol{\Sigma})^{-1}\boldsymbol{\Sigma}^{\mathrm{H}}\big((\mathbf{P}\boldsymbol{\Phi}^{\mathrm{T}}(\Delta\mathbf{A}_{\mathrm{R},r} \bullet \mathbf{A}^{*}_{\mathrm{R},g})) * (\mathbf{1}^{\mathrm{T}}_{P_r} \otimes \mathbf{A}_{\mathrm{B}})\big)\boldsymbol{\gamma}. && (3.83)
\end{aligned}$$

3.7.5 Proof of Theorem 1

As shown in Lemma 1, $\mathrm{vec}(\mathbf{H})$ can be expressed as $\mathrm{vec}(\mathbf{H}) = \boldsymbol{\Psi}\boldsymbol{\gamma}$ where $\boldsymbol{\Psi} = (\mathbf{A}_{\mathrm{R},r} \bullet \mathbf{A}^{*}_{\mathrm{R},g}) * (\mathbf{1}^{\mathrm{T}}_{P_r} \otimes \mathbf{A}_{\mathrm{B}})$. Then the distortion of vectorized RIS reflected channel is

$$\Delta\mathrm{vec}(\mathbf{H}) \approx \Delta\boldsymbol{\Psi}\boldsymbol{\gamma} + \boldsymbol{\Psi}\Delta\boldsymbol{\gamma}, \tag{3.84}$$

where $\Delta\boldsymbol{\Psi} = (\Delta\mathbf{A}_{\mathrm{R},r} \bullet \mathbf{A}^{*}_{\mathrm{R},g}) * (\mathbf{1}^{\mathrm{T}}_{P_r} \otimes \mathbf{A}_{\mathrm{B}}) = ((\mathbf{R} \odot \mathbf{A}_{\mathrm{R},r}) \bullet \mathbf{A}^{*}_{\mathrm{R},g}) * (\mathbf{1}^{\mathrm{T}}_{P_r} \otimes \mathbf{A}_{\mathrm{B}})$. In the following lemma, we provide the approximated expression of $\Delta\boldsymbol{\gamma}$.

Lemma 5. *When the number of RIS reflecting elements is large, $\Delta\boldsymbol{\gamma}$ can be approximated as*

$$\Delta\boldsymbol{\gamma} \approx \mathrm{diag}(\mathbf{z} \otimes \mathbf{1}_{P_g})\boldsymbol{\gamma}. \tag{3.85}$$

Here, $\mathbf{z} = [z_1 \cdots z_{P_r}]^{\mathrm{T}}$ where $z_i = x_i\Delta\psi_{r,i} + y_i\Delta\varphi_{r,i}$, $x_i = \sin\varphi_{r,i}(\cos\psi_{r,i}(N_y - 1) - \sin\psi_{r,i}(N_x - 1))$, and $y_i = \cos\varphi_{r,i}(\sin\psi_{r,i}(N_y - 1) + \cos\psi_{r,i}(N_x - 1))$.

Proof. By plugging (3.54), (3.56), (3.69), and (3.72) into (3.61), we obtain

$$\begin{aligned}\Delta\boldsymbol{\gamma} \approx &- \frac{1}{MN^2P_{\text{tx}}}\big(N\mathbf{P} \ast (\mathbf{1}_{P_r}^{\text{T}} \otimes \mathbf{A}_{\text{B}})\big)^{\text{H}}\big((\mathbf{P}(\mathbf{A}_{\text{R},r}^{*} \bullet \mathbf{A}_{\text{R},g})^{\text{T}}((\mathbf{R} \odot \mathbf{A}_{\text{R},r}) \bullet \mathbf{A}_{\text{R},g}^{*})) \\ &\ast (\mathbf{1}_{P_r}^{\text{T}} \otimes \mathbf{A}_{\text{B}})\big)\boldsymbol{\gamma} &(3.86)\\ = &- \frac{1}{MNP_{\text{tx}}}\big((\mathbf{P}^{\text{H}}\mathbf{P}(\mathbf{A}_{\text{R},r}^{*} \bullet \mathbf{A}_{\text{R},g})^{\text{T}}((\mathbf{R} \odot \mathbf{A}_{\text{R},r}) \bullet \mathbf{A}_{\text{R},g}^{*})) \odot ((\mathbf{1}_{P_r}^{\text{T}} \otimes \mathbf{A}_{\text{B}})^{\text{H}}(\mathbf{1}_{P_r}^{\text{T}} \\ &\otimes \mathbf{A}_{\text{B}}))\big)\boldsymbol{\gamma} &(3.87)\\ = &- \frac{1}{MN}\big(((\mathbf{A}_{\text{R},r}^{*} \bullet \mathbf{A}_{\text{R},g})^{\text{T}}((\mathbf{R} \odot \mathbf{A}_{\text{R},r}) \bullet \mathbf{A}_{\text{R},g}^{*})) \odot ((\mathbf{1}_{P_r}\mathbf{1}_{P_r}^{\text{H}}) \otimes (\mathbf{A}_{\text{B}}^{\text{H}}\mathbf{A}_{\text{B}}))\big)\boldsymbol{\gamma}. \\ & &(3.88)\end{aligned}$$

To compute (3.88), we use the property of Khatri-Rao product that $\mathbf{A}\bullet\mathbf{B} = [\text{diag}(\mathbf{a}_1)\mathbf{B} \cdots \text{diag}(\mathbf{a}_M)\mathbf{B}]$ where $\mathbf{A} = [\mathbf{a}_1 \cdots \mathbf{a}_M]$. Using this property, we obtain

$$\mathbf{A}_{\text{R},r}^{*} \bullet \mathbf{A}_{\text{R},g} = [\text{diag}(\mathbf{a}_{\text{R}}^{*}(\psi_{r,1}, \varphi_{r,1}))\mathbf{A}_{\text{R},g} \cdots \text{diag}(\mathbf{a}_{\text{R}}^{*}(\psi_{r,P_r}, \varphi_{r,P_r}))\mathbf{A}_{\text{R},g}], \tag{3.89}$$

$$(\mathbf{R} \odot \mathbf{A}_{\text{R},r}) \bullet \mathbf{A}_{\text{R},g}^{*} = [\text{diag}(\mathbf{r}_1 \odot \mathbf{a}_{\text{R}}(\psi_{r,1}, \varphi_{r,1}))\mathbf{A}_{\text{R},g}^{*} \cdots \text{diag}(\mathbf{r}_{P_r} \odot \mathbf{a}_{\text{R}}(\psi_{r,P_r}, \varphi_{r,P_r}))\mathbf{A}_{\text{R},g}^{*}], \tag{3.90}$$

where $\mathbf{r}_i = \mathbf{p}_i\Delta\psi_{r,i} + \mathbf{q}_i\Delta\varphi_{r,i}$ is the i-th column vector of $\mathbf{R}$ (see (3.56)). Thus, one can easily check that the (i, j)-th submatrix of $(\mathbf{A}_{\text{R},r}^{*} \bullet \mathbf{A}_{\text{R},g})^{\text{T}}((\mathbf{R} \odot \mathbf{A}_{\text{R},r}) \bullet \mathbf{A}_{\text{R},g}^{*})$ has the form of $\mathbf{A}_{\text{R},g}^{\text{T}}\text{diag}(\mathbf{a}_{\text{R}}^{*}(\psi_{r,i}, \varphi_{r,i}) \odot \mathbf{r}_j \odot \mathbf{a}_{\text{R}}(\psi_{r,j}, \varphi_{r,j}))\mathbf{A}_{\text{R},g}^{*}$. Also, the (k, l)-th element of $\mathbf{A}_{\text{R},g}^{\text{T}}\text{diag}(\mathbf{a}_{\text{R}}^{*}(\psi_{r,i}, \varphi_{r,i}) \odot \mathbf{r}_j \odot \mathbf{a}_{\text{R}}(\psi_{r,j}, \varphi_{r,j}))\mathbf{A}_{\text{R},g}^{*}$ is $\mathbf{a}_{\text{R}}^{\text{T}}(\psi_{g,k}, \varphi_{g,k})\text{diag}(\mathbf{a}_{\text{R}}^{*}(\psi_{r,i}, \varphi_{r,i}) \odot \mathbf{r}_j \odot \mathbf{a}_{\text{R}}(\psi_{r,j}, \varphi_{r,j}))\mathbf{a}_{\text{R}}^{*}(\psi_{g,l}, \varphi_{g,l})$. From the mutual orthogonality of array steering vectors, (3.57), and (3.58), we obtain

$$\begin{aligned}\mathbf{a}_{\text{R}}^{\text{H}}(\psi_{r,i}, \varphi_{r,i})\text{diag}(\mathbf{p}_j)\mathbf{a}_{\text{R}}(\psi_{r,j}, \varphi_{r,j}) = &- j\pi \sin\varphi_{r,j}(\mathbf{a}_{\text{R},y}(\psi_{r,i}, \varphi_{r,i}) \otimes \mathbf{a}_{\text{R},x}(\psi_{r,i}, \varphi_{r,i}))^{\text{H}} \\ &(\cos\psi_{r,j}(\mathbf{N}_y \otimes \mathbf{I}_{N_x}) - \sin\psi_{r,j}(\mathbf{I}_{N_y} \otimes \mathbf{N}_x)) \\ &(\mathbf{a}_{\text{R},y}(\psi_{r,j}, \varphi_{r,j}) \otimes \mathbf{a}_{\text{R},x}(\psi_{r,j}, \varphi_{r,j})) &(3.91)\\ = &- \frac{jN\pi\delta_{i,j}}{2}\sin\varphi_{r,j}(\cos\psi_{r,j}(N_y - 1) \\ &- \sin\psi_{r,j}(N_x - 1)) &(3.92)\\ = &- \frac{jN\pi\delta_{i,j}}{2}x_j, &(3.93)\end{aligned}$$

where $\mathbf{N}_x = \text{diag}(0, \cdots, N_x - 1)$ and $\mathbf{N}_y = \text{diag}(0, \cdots, N_y - 1)$. Similarly, we obtain

$$\begin{aligned}\mathbf{a}_{\text{R}}^{\text{H}}(\psi_{r,i}, \varphi_{r,i})\text{diag}(\mathbf{q}_j)\mathbf{a}_{\text{R}}(\psi_{r,j}, \varphi_{r,j}) =& -\frac{jN\pi\delta_{i,j}}{2}\cos\varphi_{r,j}(\sin\psi_{r,j}(N_y - 1) \\ & + \cos\psi_{r,j}(N_x - 1)) \qquad (3.94) \\ =& -\frac{jN\pi\delta_{i,j}}{2}y_j. \qquad (3.95)\end{aligned}$$

This means that the mutual orthogonality between the array response vectors holds even when $\mathbf{R}$ is multiplied in the middle. Based on this observation, we obtain

$$(\mathbf{A}_{\text{R},r}^* \bullet \mathbf{A}_{\text{R},g})^{\text{T}}((\mathbf{R} \odot \mathbf{A}_{\text{R},r}) \bullet \mathbf{A}_{\text{R},g}^*) = -\frac{jN\pi}{2}\text{diag}(\mathbf{z} \otimes \mathbf{1}_{P_g}). \qquad (3.96)$$

By plugging (3.96) into (3.88), we obtain the desired results. □

Using (3.84) and (3.85), the NMSE of RIS reflected channel estimation can be approximated as

$$\begin{aligned}\mathbb{E}\Big[\frac{\|\Delta\mathbf{H}\|_{\text{F}}^2}{\|\mathbf{H}\|_{\text{F}}^2}\Big] =& \mathbb{E}\Big[\frac{\|\Delta\text{vec}(\mathbf{H})\|^2}{\|\text{vec}(\mathbf{H})\|^2}\Big] \qquad (3.97) \\ \approx& \mathbb{E}\Big[\frac{(\Delta\boldsymbol{\Psi}\boldsymbol{\gamma} + \boldsymbol{\Psi}\Delta\boldsymbol{\gamma})^{\text{H}}(\Delta\boldsymbol{\Psi}\boldsymbol{\gamma} + \boldsymbol{\Psi}\Delta\boldsymbol{\gamma})}{\boldsymbol{\gamma}^{\text{H}}\boldsymbol{\Psi}^{\text{H}}\boldsymbol{\Psi}\boldsymbol{\gamma}}\Big] \qquad (3.98) \\ \overset{(a)}{\approx}& \frac{1}{MN}\Big(\mathbb{E}\big[\|\Delta\boldsymbol{\Psi}\bar{\boldsymbol{\gamma}}\|^2\big] - \pi\,\text{Re}\big\{j\mathbb{E}\big[\bar{\boldsymbol{\gamma}}^{\text{H}}\text{diag}(\mathbf{z} \otimes \mathbf{1}_{P_g})^{\text{H}}\boldsymbol{\Psi}^{\text{H}}\Delta\boldsymbol{\Psi}\bar{\boldsymbol{\gamma}}\big]\big\} \\ & + \frac{\pi^2}{4}\mathbb{E}\big[\|\boldsymbol{\Psi}\text{diag}(\mathbf{z} \otimes \mathbf{1}_{P_g})\bar{\boldsymbol{\gamma}}\|^2\big]\Big), \qquad (3.99)\end{aligned}$$

where $\bar{\boldsymbol{\gamma}} = \boldsymbol{\gamma}/\|\boldsymbol{\gamma}\|$ and (a) is from $\boldsymbol{\Psi}^{\text{H}}\boldsymbol{\Psi} \approx MN\mathbf{I}_{P_gP_r}$. The first term of (3.99) is computed as

$$\begin{aligned}\mathbb{E}\big[\|\Delta\boldsymbol{\Psi}\bar{\boldsymbol{\gamma}}\|^2\big] =& \mathbb{E}\big[\text{tr}(\Delta\boldsymbol{\Psi}\bar{\boldsymbol{\gamma}}\bar{\boldsymbol{\gamma}}^{\text{H}}\Delta\boldsymbol{\Psi}^{\text{H}})\big] \qquad (3.100) \\ \overset{(a)}{=}& \frac{1}{P_gP_r}\mathbb{E}[\|\Delta\boldsymbol{\Psi}\|_{\text{F}}^2] \qquad (3.101) \\ =& \frac{1}{P_gP_r}\mathbb{E}\big[\|((\mathbf{R} \odot \mathbf{A}_{\text{R},r}) \bullet \mathbf{A}_{\text{R},g}^*) * (\mathbf{1}_{P_r}^{\text{T}} \otimes \mathbf{A}_{\text{B}})\|_{\text{F}}^2\big], \qquad (3.102)\end{aligned}$$

where (a) is from $\mathbb{E}\big[\bar{\gamma}\bar{\gamma}^{\text{H}}\big] = \frac{1}{P_rP_g}\mathbf{I}_{P_rP_g}$. Similar to (3.89)-(3.96), one can easily check the mutual orthogonality between the column vectors of $(\mathbf{R} \odot \mathbf{A}_{\text{R},r}) \bullet \mathbf{A}_{\text{R},g}^*$. Thus, we obtain

$$((\mathbf{R} \odot \mathbf{A}_{\mathrm{R},r}) \bullet \mathbf{A}_{\mathrm{R},g}^{*})^{\mathrm{H}}((\mathbf{R} \odot \mathbf{A}_{\mathrm{R},r}) \bullet \mathbf{A}_{\mathrm{R},g}^{*})) \approx \mathrm{diag}(\mathbf{t} \otimes \mathbf{1}_{P_g}), \tag{3.103}$$

where $\mathbf{t}$ is the diagonal element vector of $\mathbf{R}^{\mathrm{H}}\mathbf{R}$. Thus, $\mathbb{E}\big[\|\Delta\mathbf{\Psi}\bar{\boldsymbol{\gamma}}\|^2\big]$ can be re-expressed as

$$\begin{aligned}
&\frac{1}{P_g P_r}\mathbb{E}\big[\|((\mathbf{R} \odot \mathbf{A}_{\mathrm{R},r}) \bullet \mathbf{A}_{\mathrm{R},g}^{*}) * (\mathbf{1}_{P_r}^{\mathrm{T}} \otimes \mathbf{A}_{\mathrm{B}})\|_{\mathrm{F}}^2\big] && (3.104)\\
&= \frac{1}{P_g P_r}\mathbb{E}\big[\mathrm{tr}\big(\mathrm{diag}(\mathbf{t} \otimes \mathbf{1}_{P_g}) \odot ((\mathbf{1}_{P_r}\mathbf{1}_{P_r}^{\mathrm{H}}) \otimes (\mathbf{A}_{\mathrm{B}}^{\mathrm{H}}\mathbf{A}_{\mathrm{B}}))\big)\big] && (3.105)\\
&= \frac{M}{P_r}\sum_{i=1}^{P_r}\mathbb{E}\big[\|\mathbf{p}_i\|^2|\Delta\psi_{r,i}|^2 + \|\mathbf{q}_i\|^2|\Delta\varphi_{r,i}|^2\big]. && (3.106)
\end{aligned}$$

From the definition of $\mathbf{p}_i$ in (3.57), we obtain

$$\mathbb{E}\big[\|\mathbf{p}_i\|^2|\Delta\psi_{r,i}|^2\big] = \pi^2\mathbb{E}\big[\sin^2\varphi_{r,i}\|\cos\psi_{r,i}(\mathbf{n}_y \otimes \mathbf{1}_{N_x}) - \sin\psi_{r,i}(\mathbf{1}_{N_y} \otimes \mathbf{n}_x)\|^2|\Delta\psi_{r,i}|^2\big]. \tag{3.107}$$

Note that for arbitrary real values a and b, we obtain

$$\mathbb{E}\big[\sin^2\varphi_{r,i}|a\cos\psi_{r,i} - b\sin\psi_{r,i}|^2|\Delta\psi_{r,i}|^2\big] = \frac{a^2+b^2}{4}\mathbb{E}\big[(1+\cos(2\hat{\psi}_{r,i} + 2\Delta\psi_{r,i} + \alpha))|\Delta\psi_{r,i}|^2\big] \tag{3.108}$$

$$\begin{aligned}
&\overset{(a)}{=}\frac{a^2+b^2}{4}\mathbb{E}\big[||\Delta\psi_{r,i}|^2\big] && (3.109)\\
&= \frac{\pi^2(a^2+b^2)}{12W_{\mathrm{az}}^2}, && (3.110)
\end{aligned}$$

where $\tan\alpha = \frac{a}{b}$. Also, from $\hat{\psi}_{r,i} \sim \mathcal{U}_{\{\frac{2\pi}{W_{\mathrm{az}}}i|i=0,\cdots,W_{\mathrm{az}}-1\}}$, $\Delta\psi_{r,i} \sim \mathcal{U}_{[-\frac{\pi}{W_{\mathrm{az}}},\frac{\pi}{W_{\mathrm{az}}})}$, and $\int_y\int_x x^2\cos(x+y)dxdy = -x^2\cos(x+y) + 2x\sin(x+y) + 2\cos(x+y)$, we obtain $\mathbb{E}_{\Delta\psi_{r,i},\hat{\psi}_{r,i}}\big[|\Delta\psi_{r,i}|^2\cos(2\Delta\psi_{r,i} + 2\hat{\psi}_{r,i} + \alpha)\big] = 0$ from which we obtain (a). Thus, $\mathbb{E}\big[\|\mathbf{p}_i\|^2|\Delta\psi_{r,i}|^2\big]$ is computed as

$$\begin{aligned}
\mathbb{E}\big[\|\mathbf{p}_i\|^2|\Delta\psi_{r,i}|^2\big] &= \frac{\pi^4}{12W_{\mathrm{az}}^2}\sum_{x=0}^{N_x-1}\sum_{y=0}^{N_y-1}(x^2+y^2) && (3.111)\\
&= \frac{N\pi^4}{72W_{\mathrm{az}}^2}((N_x-1)(2N_x-1) + (N_y-1)(2N_y-1)). && (3.112)
\end{aligned}$$

Similarly, since $\hat{\varphi}_{r,i} \sim \mathcal{U}_{\{\frac{\pi}{W_{\text{el}}} i | i=-W_{\text{el}}/2,\cdots,W_{\text{el}}/2\}}$ and $\Delta\varphi_{r,i} \sim \mathcal{U}_{[-\frac{\pi}{2W_{\text{el}}},\frac{\pi}{2W_{\text{el}}})}$, we obtain

$$\mathbb{E}\big[\|\mathbf{q}_i\|^2|\Delta\varphi_{r,i}|^2\big] = \frac{N\pi^4}{288W_{\text{el}}^2}((N_x-1)(2N_x-1)+(N_y-1)(2N_y-1)). \quad (3.113)$$

By plugging (3.112) and (3.113) into (3.106), we obtain the first term of (3.99) as

$$\mathbb{E}\big[\|\Delta\boldsymbol{\Psi}\bar{\boldsymbol{\gamma}}\|^2\big] = \frac{MN\pi^4}{72}((N_x-1)(2N_x-1)+(N_y-1)(2N_y-1))\Big(\frac{1}{W_{\text{az}}^2}+\frac{1}{4W_{\text{el}}^2}\Big). \quad (3.114)$$

The second term of (3.99) can be computed as

$$\begin{aligned}\text{Re}\big\{j\mathbb{E}\big[\bar{\boldsymbol{\gamma}}^{\text{H}}\text{diag}(\mathbf{z}\otimes\mathbf{1}_{P_g})^{\text{H}}\boldsymbol{\Psi}^{\text{H}}\Delta\boldsymbol{\Psi}\bar{\boldsymbol{\gamma}}\big]\big\} &= \frac{1}{P_gP_r}\text{Re}\big\{j\mathbb{E}\big[\text{tr}(\text{diag}(\mathbf{z}\otimes\mathbf{1}_{P_g})^{\text{H}}\boldsymbol{\Psi}^{\text{H}}\Delta\boldsymbol{\Psi})\big]\big\} && (3.115)\\ &\overset{(a)}{=} \frac{MN\pi}{2P_gP_r}\mathbb{E}\big[\text{tr}(\text{diag}(\mathbf{z}\otimes\mathbf{1}_{P_g})^{\text{H}}(\text{diag}(\mathbf{z}\otimes\mathbf{1}_{P_g})))\big] && (3.116)\\ &= \frac{MN\pi}{2P_r}\sum_{i=1}^{P_r}\mathbb{E}\big[|x_i\Delta\psi_{r,i}+y_i\Delta\varphi_{r,i}|^2\big] && (3.117)\\ &\overset{(b)}{=} \frac{MN\pi^3}{24}((N_x-1)^2+(N_y-1)^2)\Big(\frac{1}{W_{\text{az}}^2}+\frac{1}{4W_{\text{el}}^2}\Big), && (3.118)\end{aligned}$$

where (a) is from the definition of $\boldsymbol{\Psi}$ and (3.96) and (b) is from (3.110).

Lastly, the third term of (3.99) can be computed as

$$\begin{aligned}\mathbb{E}\big[\|\boldsymbol{\Psi}\text{diag}(\mathbf{z}\otimes\mathbf{1}_{P_g})\bar{\boldsymbol{\gamma}}\|^2\big] &= \frac{1}{P_gP_r}\mathbb{E}\big[\text{tr}(\text{diag}(\mathbf{z}\otimes\mathbf{1}_{P_g})^{\text{H}}\boldsymbol{\Psi}^{\text{H}}\boldsymbol{\Psi}\text{diag}(\mathbf{z}\otimes\mathbf{1}_{P_g}))\big] && (3.119)\\ &= \frac{MN\pi^2}{12}((N_x-1)^2+(N_y-1)^2)\Big(\frac{1}{W_{\text{az}}^2}+\frac{1}{4W_{\text{el}}^2}\Big). && (3.120)\end{aligned}$$

Finally, by plugging (3.114), (3.118), and (3.120) into (3.99), we obtain the desired result.

Chapter 4

Transformer-based Channel Parameter Acquisition for Terahertz Ultra-Massive MIMO Systems

In this chapter, we introduce a channel estimation technique for time-division-duplexing (TDD)-based THz ultra-massive (UM) multiple-input multiple-output (MIMO) systems. THz UM-MIMO system is envisioned as a key technology to support ever-increasing data rates in 6G communication systems. To make the most of THz UM-MIMO systems, acquisition of accurate channel information is crucial. However, the THz channel acquisition is not easy due to the humongous pilot overhead that scales linearly with the number of antennas. In our work, we propose a novel deep learning (DL)-based channel acquisition technique for the THz UM-MIMO systems. By learning the complicated mapping function between the received pilot signal and the sparse channel parameters (e.g., angles, distances, path gains) using Transformer, the proposed scheme can make a fast yet accurate channel estimation with a relatively small amount of pilot resources. Moreover, using the attention mechanism of Transformer, we can promote the correlation structure of the received pilot signals in the feature extraction, thereby improving the channel parameter estimation quality significantly.

4.1 Introduction

As a key technology to meet the demand for ever-increasing data rate in 6G, terahertz (THz) ultra-massive multiple-input multiple-output (UM-MIMO) communication has received a great deal of attention recently [2]. By exploiting the plentiful spectrum resources in the THz frequency band ($0.1 \sim 10\,\text{THz}$) along with a large number of antennas, THz UM-MIMO communications can support way higher data rates than the conventional sub-6GHz and millimeter-wave communications can offer. To maximize the potential gain of THz UM-MIMO systems, the base station (BS) needs to acquire accurate downlink THz channel information. Main challenge of the THz UM-MIMO systems is that the channel exhibits the near-field characteristics since the array aperture of the massive number of antenna elements is comparable to the communication distance [52]. While the signal wavefront can be readily approximated as a planar wave in the conventional far-field region, the electromagnetic (EM) radiation is performed through the spherical wave in the near-field region [53, 54]. Due to the spherical wavefront, the near-field THz channel can be expressed as a function of a few parameters in the spherical domain including angles, distances, and path gains.

Recently, various techniques have been proposed for the acquisition of the THz channel parameters [55–59]. In [55, 56], compressed sensing (CS)-based channel acquisition approaches have been proposed. In [57–59], deep learning (DL)-based approaches that learn the mapping function between the received pilot signals and the channel parameters using deep neural network (DNN) have been proposed. Among various DNN architectures, a convolutional neural network (CNN) is popular due to its simplicity and ability to extract spatial features from the received pilot signals [59]. A major drawback of CNN, in the perspective of the THz channel parameter acquisition, is that it might not be effective in extracting the correlation between the spaced-apart pilot signals since the filter kernel and convolution operations are performed locally.

In the DL-based channel parameter estimator, a feature map is extracted from the DNN using the received pilot signals. By the feature map, we mean the low-dimensional

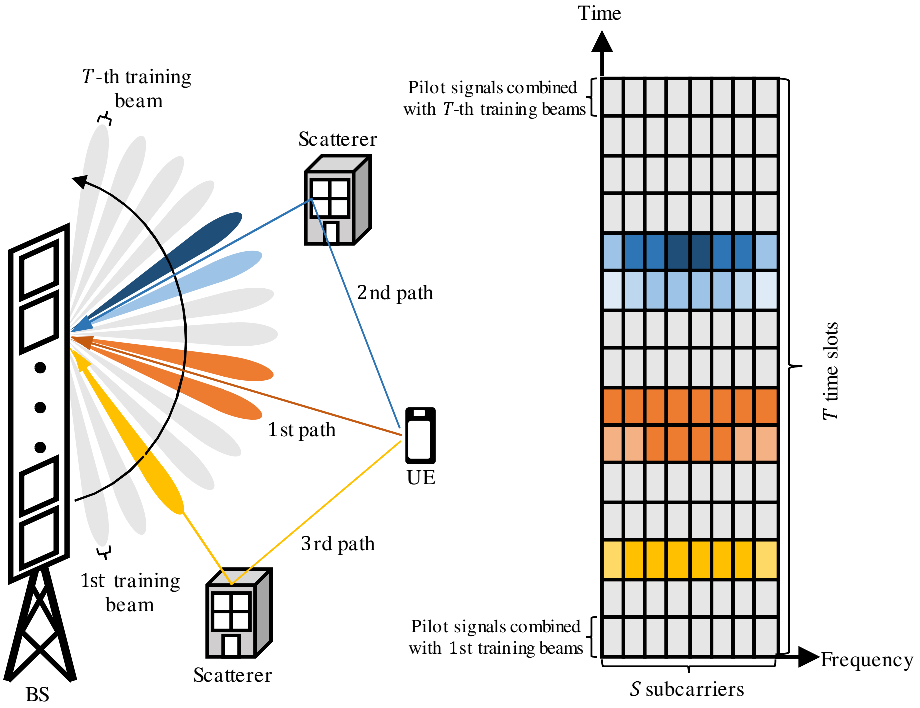

Figure 4.1: Correlation structure of the received pilot signal in THz UM-MIMO systems.

vector containing core information (e.g., MIMO antenna array structure, locations of scatterers, and mobility of user equipment (UE)) of the large-dimensional input. To facilitate the feature extraction, one should deliberately handle the correlation structure of the received pilot signals. Notable characteristics of the received pilot signal of THz UM-MIMO systems are twofold; First, the received pilot signals will have meaningful power only for a few time slots. During the channel acquisition process, the BS employs multiple sharp training beams, each of which is directed to distinct directions. Thus, the received pilot signal will have a high power only when the training beams are aligned with the direction of UE (see Fig. 1). Second, the THz channel is determined primarily by the scattering geometry around the BS so the received pilot signals for each and every subcarrier can be expressed as functions of the same geometric parameters (e.g. angles, distances), which means that the received pilot signals, irrespective of their subcarrier positions, are highly correlated.

An aim of this paper is to propose a DL-based channel acquisition technique for the THz UM-MIMO systems. The proposed technique, dubbed as *Transformer-based parametric THz channel acquisition* (T-PCA), estimates the channel parameters (angles, distances, path gains) using *Transformer*, a DL architecture that differentially weights the significance of each input data (in our case, the received pilot signals) via the attention mechanism [60]. To make the most of the correlation structures of the received pilot signal, we employ two distinct Transformer networks, viz., *temporal Transformer network* (TTN) and *spatial Transformer network* (STN). In TTN, using the received pilot signals as inputs, the temporally-correlated features are extracted from the product of the attention weight and the received pilot signal. Since only a small portion of received pilot signals have a meaningful power, Transformer in TTN is trained such that these dominant received pilot signals will have relatively high attention weights. In doing so, one can facilitate the extraction of the temporally-correlated features. After that, using the low-dimensional features generated from TTN as inputs, the spatio-temporally correlated features are extracted in STN. As mentioned, the received pilot signals for all subcarriers are expressed as functions of the same channel parameters so that all received pilot signals, regardless of their positions, are correlated to each other. Main purpose of Transformer in STN is to capture the correlated features of both the adjacent and spaced-apart received pilot signals. Finally, the extracted features are converted to the channel parameters via the fully-connected network.

From the simulation results, we demonstrate that T-PCA outperforms the conventional channel acquisition schemes in terms of the normalized mean square error (NMSE). For example, T-PCA achieves more than 5 dB NMSE gain over the CS-based scheme. Even when compared with the CNN-based scheme, T-PCA achieves around 2.5 dB NMSE gain.

4.2 Terahertz UM-MIMO System Model

We consider the THz UM-MIMO OFDM systems where a single-antenna UE transmits an uplink pilot signal to a BS equipped with a uniform linear array (ULA) of M antennas. Specifically, T time slots and S subcarriers are used for the uplink pilot transmission (see Fig. 1). By exploiting the channel reciprocity of time-division duplexing (TDD) systems, the BS can recycle the acquired uplink channel information for the downlink data transmission [61]. In case when the uplink and downlink channels are not exactly the same, one can bridge the gap between the uplink and downlink channels through the reciprocity calibration [62].

In this setup, the received pilot signal vector $\mathbf{y}_{t,s} \in \mathbb{C}^{N_r \times 1}$ of the s-th pilot subcarrier at t-th time slot is given by

$$\mathbf{y}_{t,s} = \mathbf{W}_t^{\mathrm{H}} \mathbf{h}_s x_{t,s} + \mathbf{W}_t^{\mathrm{H}} \mathbf{n}_{t,s} = \sqrt{P_{\text{tx}}} \mathbf{W}_t^{\mathrm{H}} \mathbf{h}_s + \tilde{\mathbf{n}}_{t,s}, \tag{4.1}$$

where N_r is the number of RF chains in BS, $x_{t,s} = \sqrt{P_{\text{tx}}}$ is the uplink pilot, P_{tx} is the transmit power of UE, $\mathbf{h}_s \in \mathbb{C}^{M \times 1}$ is the THz channel vector at s-th subcarrier, $\mathbf{W}_t \in \mathbb{C}^{M \times N_r}$ is the receive beamforming matrix at the t-th time slot, and $\mathbf{n}_{t,s} \sim \mathcal{CN}(\mathbf{0}, \sigma_n^2 \mathbf{I}_M)$ is the additive Gaussian noise. Note that $\mathbf{W}_t$ is generated from the column vectors of M-point DFT matrix. By concatenating the received pilot signals over T time slots, we obtain the received pilot signal matrix at the s-th subcarrier $\mathbf{Y}_s = [\mathbf{y}_{1,s} \cdots \mathbf{y}_{T,s}]^{\mathrm{T}} \in \mathbb{C}^{T \times N_r}$.

One notable characteristic of THz UM-MIMO systems is that the channel exhibits the near-field characteristics [52]. Since the signal wavefronts are spherical in the near-field channel, the phase difference between two antenna elements is affected by the distance r as well as the angle θ. Therefore, the near-field array steering vector is expressed as a function of spherical coordinates (θ, r). In fact, the near-field array steering vector $\mathbf{b}_s(\theta, r)$ at s-th subcarrier is given by [56]

$$\mathbf{b}_s(\theta, r) = \left[e^{-j \frac{2\pi}{\lambda}(1+\frac{f_s}{f_c})(r_1 - r)} \cdots e^{-j \frac{2\pi}{\lambda}(1+\frac{f_s}{f_c})(r_M - r)} \right]^{\mathrm{T}}, \tag{4.2}$$

where f_c is the carrier frequency, f_s is the baseband frequency of the s-th subcarrier, and r_m is the distance between the UE and the m-th BS antenna, given by

$$r_m = r - (m-1)d \sin\theta + (m-1)^2 \frac{d^2 \cos^2\theta}{2r}. \tag{4.3}$$

In this work, we use the near-field multipath THz channel model where the uplink channel vector $\mathbf{h}_s$ from the UE to the BS at the s-th subcarrier is expressed as

$$\mathbf{h}_s = \sum_{p=1}^{P} \alpha_p e^{-j2\pi f_s \tau_p} \mathbf{b}_s(\theta_p, r_p), \tag{4.4}$$

where P is the number of propagation paths, θ_p is the AoA, r_p is the distance, τ_p is the time delay, and α_p is the path gain of the p-th path. Let $\boldsymbol{\theta} = [\theta_1 \cdots \theta_P]^{\mathrm{T}}$ and $\mathbf{r} = [r_1 \cdots r_P]^{\mathrm{T}}$ be the angle and distance vectors, respectively, and $\boldsymbol{\alpha}_s = [\alpha_1 e^{-j2\pi f_s \tau_1} \dots \alpha_P e^{-j2\pi f_s \tau_P}]^{\mathrm{T}}$ be the path gain vector for the s-th subcarrier, then $\mathbf{h}_s$ can be succinctly expressed as a function of channel parameters:

$$\mathbf{h}_s = \mathbf{B}_s(\boldsymbol{\theta}, \mathbf{r})\boldsymbol{\alpha}_s, \tag{4.5}$$

where $\mathbf{B}_s(\boldsymbol{\theta}, \mathbf{r}) = [\mathbf{b}_s(\theta_1, r_1) \cdots \mathbf{b}_s(\theta_P, r_P)] \in \mathbb{C}^{M \times P}$ is the near-field array steering matrix. Note that $\mathbf{h}_s$ is parameterized by a few THz channel parameters, i.e., angles $\boldsymbol{\theta}$, distances $\mathbf{r}$, and path gains $\boldsymbol{\alpha}_s$, whose numbers are the same as the number of paths. Since the number of paths P (e.g., $P = 1 \sim 3$) is much smaller than the number of antennas M (e.g., $M = 256 \sim 1024$) in the THz UM-MIMO systems, one can significantly reduce the required number of measurements by estimating the sparse channel parameters instead of the full-dimensional channel vector $\mathbf{h}_s$ [41].

4.3 Transformer-based parametric Terahertz Channel Acquisition

Main goal of the proposed T-PCA is to estimate the sparse THz channel parameters (i.e., angles, distances, and path gains) using Transformer. Major benefit of T-PCA is that we can extract the features of the THz UM-MIMO received pilot signals using the attention mechanism of Transformer. In essence, the attention mechanism facilitates the generation of the attention weights that represent the correlations between input data. Using the product of the attention weights and the received pilot signals as input, one can extract the spatially and temporally-correlated features inherent in the THz UM-MIMO systems. Key ingredient of T-PCA is the combination of Transformer and fully-connected network to learn a complicated nonlinear mapping between the received pilot signals $\{\mathbf{Y}_s\}_{s=1}^S$ and the THz geometric channel parameters ($\boldsymbol{\theta}$, $\mathbf{r}$):

$$\{\hat{\boldsymbol{\theta}}, \hat{\mathbf{r}}\} = g\big(\{\mathbf{Y}_s\}_{s=1}^S; \boldsymbol{\Gamma}\big), \tag{4.6}$$

where g is the mapping function and $\boldsymbol{\Gamma}$ are the network parameters. Once $\hat{\boldsymbol{\theta}}$ and $\hat{\mathbf{r}}$ are acquired, the path gains $\{\hat{\boldsymbol{\alpha}}_s\}_{s=1}^S$ can be easily estimated using the conventional approaches such as the least squares (LS) estimator:

$$\hat{\boldsymbol{\alpha}}_s = \big(\sqrt{P}\mathbf{W}^{\mathrm{H}}\mathbf{B}_s(\hat{\boldsymbol{\theta}}, \hat{\mathbf{r}})\big)^{\dagger}\mathrm{vec}(\mathbf{Y}_s^{\mathrm{T}}), \quad s = 1, \cdots, S, \tag{4.7}$$

where $\mathbf{W} = [\mathbf{W}_1 \cdots \mathbf{W}_T] \in \mathbb{C}^{M \times TN_r}$. Using the obtained the channel parameters ($\hat{\boldsymbol{\theta}}$, $\hat{\mathbf{r}}$, $\{\hat{\boldsymbol{\alpha}}_s\}_{s=1}^S$), we can reconstruct the THz channels $\{\hat{\mathbf{h}}_s\}_{s=1}^S$:

$$\hat{\mathbf{h}}_s = \mathbf{B}_s(\hat{\boldsymbol{\theta}}, \hat{\mathbf{r}})\hat{\boldsymbol{\alpha}}_s, \quad s = 1, \cdots, S. \tag{4.8}$$

4.3.1 Basic of Transformer

In the conventional CNN-based acquisition technique, the features are extracted by performing the convolution operation of a 2D/3D-shaped weight matrix (called kernel) and a part of the received pilot signal [58]. While CNN is effective in extracting the locally correlated features (e.g. correlation among antennas), it might not be efficient in extracting the globally correlated feature due to the locality of the filter kernel. Also, since the same kernel is multiplied to all input signals, the nonuniform and irregular correlation structures of the received pilot signals cannot be captured properly.

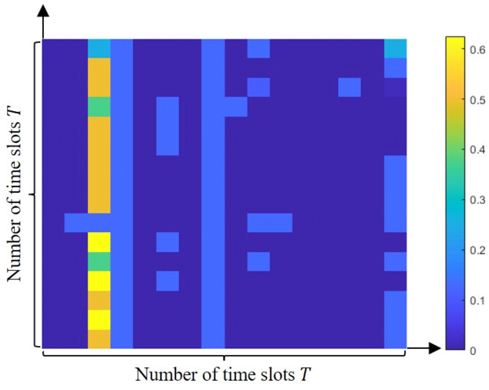

Figure 4.2: Attention map of TTN

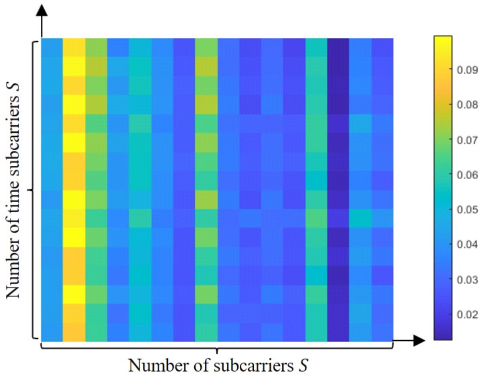

Figure 4.3: Attention map of STN

In a nutshell, Transformer extracts the features using the attention mechanism. In the attention layer of Transformer, the correlations between the input data (a.k.a., *attention weight* or *attention map*) are calculated and then multiplied to the input to generate the weighted input matrix [60]. Since the correlations between each and every element in the input sequences (a.k.a., token) are used for the attention weight generation, Transformer can extract both the locally and globally correlated features effectively.

To be specific, using the sequence of $D \times 1$ input vectors $\mathbf{Y} = [\mathbf{y}_1 \cdots \mathbf{y}_L]^{\mathrm{T}} \in \mathbb{C}^{L \times D}$, the attention layer constructs three different embedding matrices, i.e., the query $\mathbf{Q} = \mathbf{Y}\mathbf{W}_Q$, the key $\mathbf{K} = \mathbf{Y}\mathbf{W}_K$, and the value $\mathbf{V} = \mathbf{Y}\mathbf{W}_V$ where $\mathbf{W}_Q, \mathbf{W}_K, \mathbf{W}_V \in \mathbb{C}^{D \times D}$ are the weight matrices and L is the number of input sequences. Since the query $\mathbf{Q}$ and the key $\mathbf{K}$ contains the features of the input data, by performing the inner product of $\mathbf{Q}$ and $\mathbf{K}$, we obtain the attention map $\mathbf{M} \in \mathbb{C}^{L \times L}$:

$$\mathbf{M} = f_{\text{softmax}}\big(\mathbf{Q}\mathbf{K}^{\mathrm{T}}/\sqrt{D}\big), \tag{4.9}$$

where $f_{\text{softmax}}(\mathbf{Y})$ is a row-wise softmax function defined as $[f_{\text{softmax}}(\mathbf{Y})]_{i,j} = e^{\mathbf{Y}_{i,j}} / \sum_j e^{\mathbf{Y}_{i,j}}$. Finally, by multiplying the attention map $\mathbf{M}$ with the value $\mathbf{V}$, we obtain the weighted input matrix $\mathbf{Z} \in \mathbb{C}^{L \times D}$:

$$\mathbf{Z} = \mathbf{M}\mathbf{V} = f_{\text{softmax}}\big(\mathbf{Q}\mathbf{K}^{\mathrm{T}}/\sqrt{D}\big)\mathbf{V}, \tag{4.10}$$

After that $\mathbf{Z}$ passes through the fully-connected network, generating the output feature of Transformer.

To demonstrate the effect of the attention map in capturing the correlation structure of the received pilot signals, we plot the attention maps of TTN and STN in Fig. 4.2 and 4.3. From Fig. 4.2, one can observe that the attention weights of TTN are concentrated on a small number of column vectors. Due to the extremely narrow beamwidth of THz UM-MIMO systems, the received pilot signals will contain the noise only when the training beams are not aligned with the signal propagation paths. This means that only a few row vectors of the received pilot signal matrix $\mathbf{Y}_s = [\mathbf{y}_{1,s} \cdots \mathbf{y}_{T,s}]^{\mathrm{T}}$ have relatively high values (same for the key $\mathbf{K}$ generated from $\mathbf{Y}_s$). Since the attention map is constructed from the inner product of $\mathbf{Q}$ and $\mathbf{K}$, the attention weights are concentrated on a few column vectors corresponding to the dominant received pilot signals.

4.3.2 Network Architecture of T-PCA

In this subsection, we explain the detailed network architecture of T-PCA (see Fig. 2). In T-PCA, the received pilot signal $\mathbf{y}_{t,s}$ is first separated into the real and imaginary parts $\bar{\mathbf{y}}_{t,s} = [\mathrm{Re}(\mathbf{y}_{t,s})^{\mathrm{T}} \ \mathrm{Im}(\mathbf{y}_{t,s})^{\mathrm{T}}]^{\mathrm{T}} \in \mathbb{R}^{2N_r \times 1}$ and then the concatenated matrices $\mathbf{Y}_s = [\bar{\mathbf{y}}_{1,s} \cdots \bar{\mathbf{y}}_{T,s}]^{\mathrm{T}} \in \mathbb{R}^{T \times 2N_r}$ pass through the fully-connected network to generate $\mathbf{X}_s = \mathbf{Y}_s \mathbf{W}_e + \mathbf{b}_e \in \mathbb{R}^{T \times D}$ ($\mathbf{W}_e \in \mathbb{R}^{2N_r \times D}$ is the weight matrix and $\mathbf{b}_e \in \mathbb{R}^{D \times 1}$ is the bias vector). Then a representative vector $\mathbf{x}_{0,s} \in \mathbb{R}^{D \times 1}$, a trainable vector containing the correlated feature of the input data, is appended to the input matrices as $\bar{\mathbf{X}}_s = [\mathbf{x}_{0,s} \, \mathbf{X}_s^{\mathrm{T}}]^{\mathrm{T}} \in \mathbb{R}^{(T+1) \times D}$ [63]. Also, to indicate the position of each element in the input data sequence, a trainable matrix called positional embedding matrix $\mathbf{W}_{\mathrm{pos}} \in \mathbb{R}^{(T+1) \times D}$ is added as $\tilde{\mathbf{X}}_s = \bar{\mathbf{X}}_s + \mathbf{W}_{\mathrm{pos}}$. Then the encoded input sequences $\{\tilde{\mathbf{X}}_s\}_{s=1}^{S}$ sequentially pass through the multiple Transformer blocks. In the last Transformer block, the temporal feature vectors $\{\mathbf{f}_s^{\mathrm{ttn}}\}_{s=1}^{S}$ are obtained from the first row vector of the output matrix.

Once the temporal feature matrix $\mathbf{F}^{\mathrm{ttn}} = [\mathbf{f}_1^{\mathrm{ttn}} \cdots \mathbf{f}_S^{\mathrm{ttn}}]^{\mathrm{T}} \in \mathbb{R}^{S \times D}$ is obtained, $\mathbf{F}^{\mathrm{ttn}}$

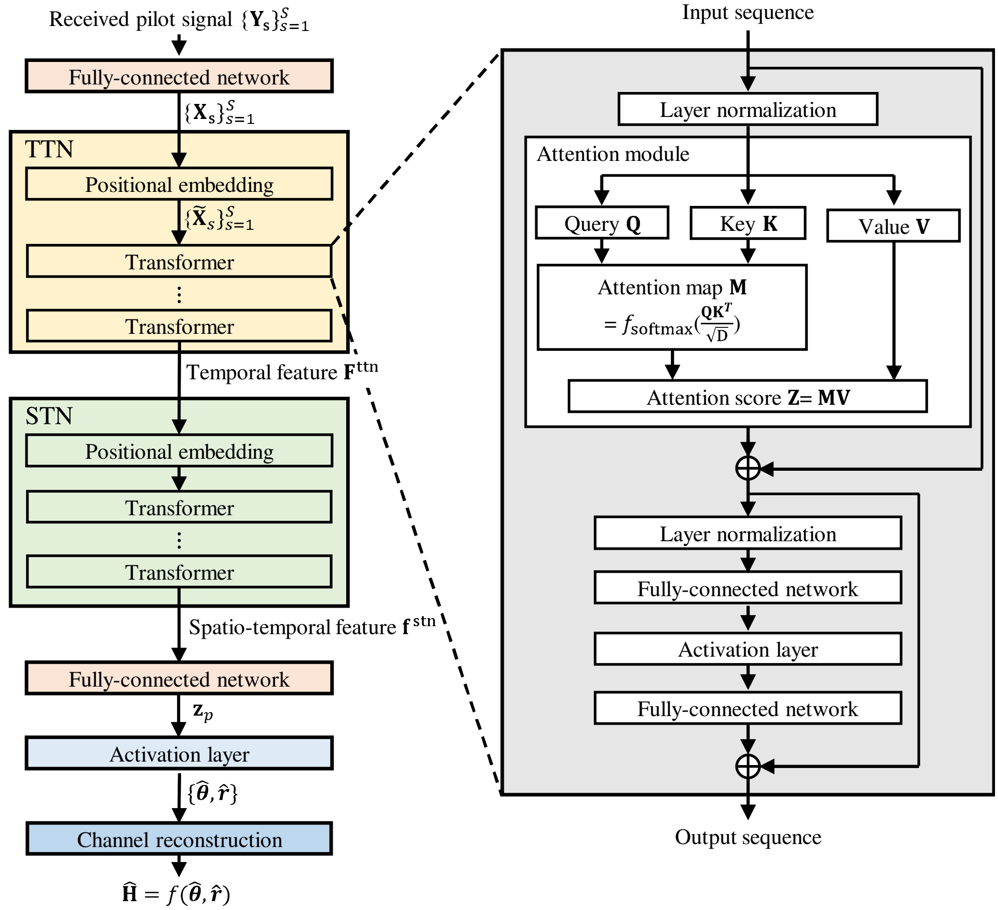

Figure 4.4: Overall structure of T-PCA.

is used as an input matrix of STN. Similar to TTN, the representative vector and the positional embedding matrix are added to $\mathbf{F}^{\text{ttn}}$ and then the output matrix passes through multiple Transformer blocks. Then the spatio-temporal feature vector $\mathbf{f}^{\text{stn}} \in \mathbb{R}^{D\times 1}$ is obtained from the first row vector of the output matrix of the last Transformer block.

The extracted spatio-temporal feature vector $\mathbf{f}^{\text{stn}}$ passes through the fully-connected network to generate the output vector $\mathbf{z}_p = \mathbf{W}_p\mathbf{f}^{\text{stn}} + \mathbf{b}_p \in \mathbb{R}^{2P\times 1}$ ($\mathbf{W}_p \in \mathbb{R}^{2P\times D}$ is the weight matrix and $\mathbf{b}_p \in \mathbb{R}^{2P\times 1}$ is the bias vector). After that, $\mathbf{z}_p$ passes through the hyperbolic tangent layer $f_{\text{tanh}}(x) = \frac{e^x - e^{-x}}{e^x + e^{-x}}$ to generate the desired THz channel parameters as $\{\hat{\boldsymbol{\theta}}, \hat{\mathbf{r}}\} = f_{\text{tanh}}(\mathbf{z}_p)$. The overall structure of T-PCA is depicted in Fig. 4.4.

4.3.3 Computational Complexity Analysis

In this subsection, we analyze the complexity of T-PCA in terms of the number of floating point operations (flops). Recall that the proposed T-PCA consists of input fully-connected network, TTN, STN, and output fully-connected network (see Fig. 3). Thus, the overall computational complexity $\mathcal{C}_{\text{T-PCA}}$ of T-PCA can be expressed as

$$\mathcal{C}_{\text{T-PCA}} = \mathcal{C}_{\text{in}} + \mathcal{C}_{\text{ttn}} + \mathcal{C}_{\text{stn}} + \mathcal{C}_{\text{out}}, \tag{4.11}$$

where $\mathcal{C}_{\text{in}}$, $\mathcal{C}_{\text{out}}$, $\mathcal{C}_{\text{ttn}}$, and $\mathcal{C}_{\text{stn}}$ are the computational complexities of input and output fully-connected networks, TTN, and STN, respectively.

In the input fully-connected network, the matrix multiplication and bias addition are performed for each subcarrier so the computational complexity $\mathcal{C}_{in}$ is

$$\mathcal{C}_{in} = 4N_r STD. \tag{4.12}$$

In TTN, the input vector passes through the positional embedding layer and Transformer layer consisting of N_b Transformer so the computational complexity $\mathcal{C}_{\text{ttn}}$ can be expressed as

$$\mathcal{C}_{\text{ttn}} = \mathcal{C}_{\text{pos}} + N_b \mathcal{C}_{\text{tf}}, \tag{4.13}$$

where $\mathcal{C}_{\text{pos}}$ and $\mathcal{C}_{\text{tf}}$ are the computational complexities of the positional embedding layer and Transformer layer, respectively. Also, N_b is the number of transformer blocks in TTN. In the positional embedding layer, the positional embedding matrix $\mathbf{W}_{\text{pos}}$ is added to the input matrix so that $\mathcal{C}_{\text{pos}} = S(T+1)D$. Also, since the Transformer block consists of the attention module ($S(T+1)(6D^2 + 4DT + 2T + 3)$ flops), the residual connection ($S(T+1)D$ flops), layer normalization ($4S(T+1)D$ flops), fully-connected network ($2S(T+1)D^2$ flops), activation layer ($S(T+1)D$ flops), and fully-connected network ($2S(T+1)D^2$ flops), the computational complexity $\mathcal{C}_{\text{tf}}$ of a Transformer block is $\mathcal{C}_{\text{tf}} = S(T+1)(10D^2 + 4DT + 2T + 10D + 3)$. By plugging $\mathcal{C}_{\text{pos}}$ and $\mathcal{C}_{\text{tf}}$ to (4.13), we obtain the computational complexity $\mathcal{C}_{\text{ttn}}$ of TTN:

$$\mathcal{C}_{\text{ttn}} = S(T+1)(D + N_b(10D^2 + 4DT + 2T + 10D + 3)). \tag{4.14}$$

Similarly, the computational complexity $\mathcal{C}_{\text{stn}}$ of STN is

$$\mathcal{C}_{\text{stn}} = (S+1)(D + N_b(10D^2 + 4DS + 2S + 10D + 3)). \tag{4.15}$$

In the output fully-connected network, the channel parameter estimates are extracted by multiplying the weight matrix, adding the bias vector, and passing through the tanh layer. Thus, the complexity of the output fully-connected network is

$$\mathcal{C}_{\text{out}} = (4D + 10)P. \tag{4.16}$$

In conclusion, by plugging (4.12)-(4.16) to (4.11), we obtain the computational complexity $\mathcal{C}_{\text{T-PCA}}$ of T-PCA:

$$\begin{aligned}\mathcal{C}_{\text{T-PCA}} =& 10P + (4N_rST + 4P + ST + 2S + 1)D \\ &+ N_b(S(T+1)(10D^2 + 4DT + 2T + 10D + 3) \\ &+ (S+1)(10D^2 + 4DS + 2S + 10D + 3)).\end{aligned} \tag{4.17}$$

4.4 Simulation Result

4.4.1 Simulation Setup

In our simulation, we consider the THz UM-MISO OFDM systems where a BS equipped with $M = 256$ antennas and $N_r = 4$ RF chains serves a single-antenna UE. The UE is located randomly around the BS within the cell radius of $R = 50\,\text{m}$. We use the wideband THz multi-path channel model where the number of paths is $P = 1$, the carrier frequency is $f_c = 0.1\,\text{THz}$, and the channel bandwidth is $B = 1\,\text{GHz}$[1]. We set

---

[1] In the THz systems, due to the severe path loss and directivity of THz band, the power of line-of-sight (LoS) component is almost 100 times stronger than that of the non-line-of-sight (NLoS) component [64].

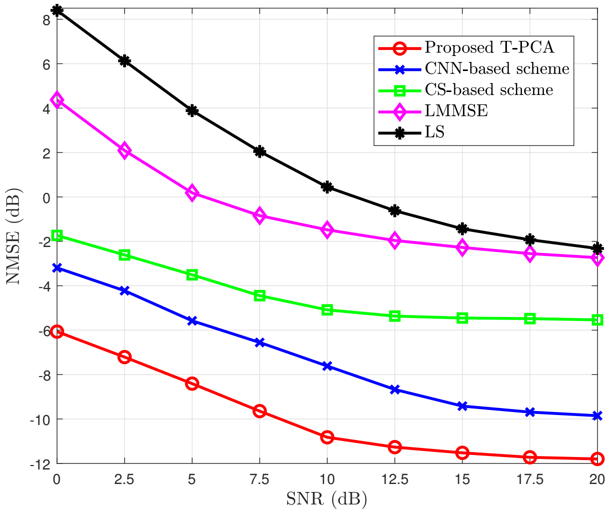

Figure 4.5: NMSE vs. SNR ($M = 256$, $N_r = 4$, $T = 32$, $S = 16$)

the numbers of subcarriers and time slots for pilot transmission to $S = 16$ and $T = 32$, respectively. Also, we use the path loss model in 3GPP Rel. 16 [17].

In the proposed T-PCA, each Transformer network consists of two Transformer blocks with the embedding dimension $D = 128$. For the network parameter training, we use the supervised learning strategy where the network parameters $\mathbf{\Gamma}$ are updated iteratively in a way to minimize the NMSE-based loss function $J(\mathbf{\Gamma})$:

$$J(\mathbf{\Gamma}) = \frac{1}{S}\sum_{s=1}^{S}\frac{\|\mathbf{h}_s - \hat{\mathbf{h}}_s\|^2}{\|\mathbf{h}_s\|^2}. \tag{4.18}$$

As a performance metric, we use the normalized mean square error (NMSE) defined as NMSE $= \frac{1}{S}\sum_{s=1}^{S}\frac{\|\hat{\mathbf{h}}_s - \mathbf{h}_s\|^2}{\|\mathbf{h}_s\|^2}$. Since it is very difficult to design a THz UM-MIMO testbed to acquire the real channel dataset, we instead used synthetically generated channels from the THz UM-MIMO simulator. Based on the property that the THz channel can be expressed as a function of a few geometric channel parameters (i.e., angles, distances, and path gains), we synthetically generated the scattering environment at the THz UM-MIMO simulator based on the 3GPP standard, using which we acquired the geometric channel parameters and THz channels. Specifically, we ran-

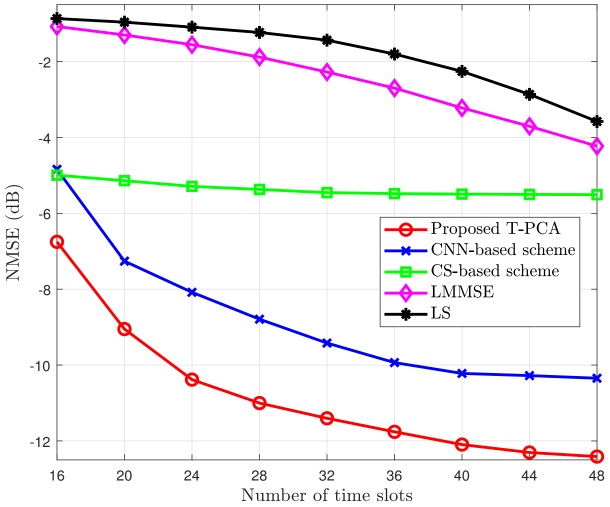

Figure 4.6: NMSE versus number of time slots ($M = 256$, $N_r = 4$, $S = 16$, SNR $=$ $15\,\text{dB}$)

domly generated the geometric channel parameters angles $\boldsymbol{\theta}$, distances $\mathbf{r}$, and path gains $\{\boldsymbol{\alpha}_s\}_{s=1}^{S}$ from $[-\pi, \pi)$, $(0\,\text{m}, 50\,\text{m})$, and $\mathcal{CN}(0, \rho)$ where ρ is the large-scale fading coefficient modeled by the path loss model in 3GPP TR 38.901, respectively [17]. Using the THz UM-MIMO simulator, we separately generate training and test datasets consisting of $300,000$ and $50,000$ independent channel realizations, respectively. The number of training epochs and the learning rate are set to $N_{\text{epoch}} = 1000$ and $\eta = 10^{-3}$, respectively. For comparison, we use four benchmark channel acquisition schemes: 1) CNN-based scheme [58], 2) compressed sensing (CS)-based scheme [55], 3) linear minimum mean square error (LMMSE) estimator, and 4) LS estimator.

4.4.2 Simulation Result

In Fig. 4.5, we plot the NMSE as a function of transmit SNR. We observe that T-PCA outperforms the conventional channel estimation techniques by a large margin. For example, when SNR $= 10\,\text{dB}$, T-PCA achieves significant (more than $9\,\text{dB}$ and $11\,\text{dB}$)

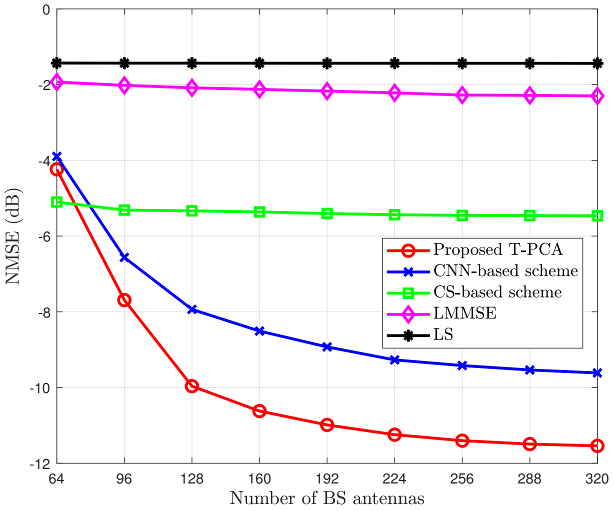

Figure 4.7: NMSE versus number of BS antennas ($N_r = 4$, $S = 16$, SNR $= 15\,$dB)

NMSE gains over the LMMSE and LS schemes, respectively. Even when compared with the CS-based scheme, T-PCA achieves around 6 dB NMSE gain. This is because the mismatch between the true channel parameters and the quantized channel parameters is considerable in the CS-based scheme while such is not the case for T-PCA since T-PCA estimates the channel parameters in the continuous domain.

In Fig. 4.6, we plot the NMSE as a function of the number of time slots. We observe that T-PCA achieves more than 33% pilot overhead reduction over the conventional schemes. For instance, to achieve the NMSE of $-10\,$dB, T-PCA requires 24 time slots while the conventional schemes require more than 36 time slots. This is not a surprise since the LMMSE and LS schemes estimate the full-dimensional THz channel vector $\mathbf{h}_s$ directly so that the required number of time slots is very large[2]. Whereas, by learning the complicated mapping between the received pilot signals and the THz

---

[2] In fact, to guarantee the accurate estimation of $\mathbf{h}_s$, the number of measurements TN_r should be larger than the number of antenna elements M. For example, when $M = 256$ and $N_r = 4$, we need to allocate more than 5 subframe (more than 50% of a frame in 5G NR) just for the pilot transmission (14 slots/subframe $\times$ 5 subframe $= 70 > M/N_r = 64$).

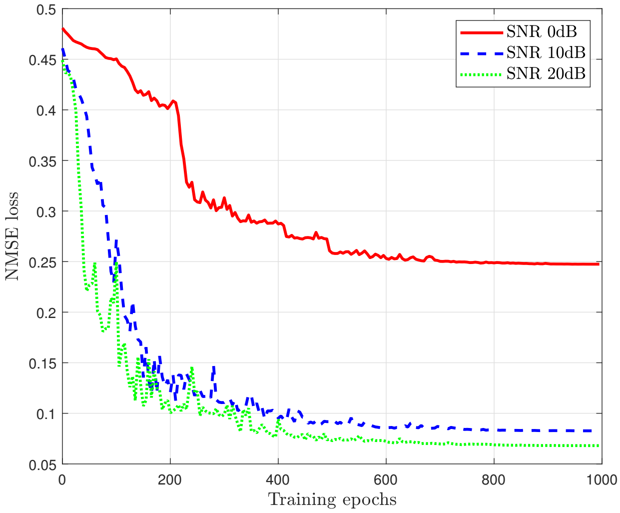

Figure 4.8: Training loss of T-PCA versus training epoch

channel parameters using Transformer, T-PCA can efficiently acquire the sparse THz channel parameters with a small amount of pilot resources.

In Fig. 4.7, we plot the NMSE as a function of the number of BS antennas M. We set the number of time slots $T = \lfloor \frac{M}{2N_r} \rfloor$ so that T increases linearly with M. We observe that the NMSE gain of T-PCA over the conventional techniques increases with M. For example, when M increases from 96 to 320, the NMSE gain of T-PCA over the CS-based scheme increases from 2.3 dB to 6.1 dB, which implies that T-PCA would be more effective in improving the channel estimation performance of the reconfigurable intelligent surface (RIS)-aided THz systems where the number of reflecting elements is extremely large.

In Fig. 4.8, we evaluate the NMSE loss of T-PCA as a function of the training epoch. By one epoch, we mean the period during which all training data has been used once to update the parameters of a DL model. We observe that as the training epoch increases, the NMSE loss of T-PCA decreases gradually and finally converges.

4.5 Summary

In recent years, a remarkable success of DL in various disciplines (e.g., image classification, speech recognition, and language translation) has stimulated increasing interest in applying this paradigm to wireless communication systems. In this chapter, we proposed a DL-based channel acquisition technique for the THz UM-MIMO systems. Intriguing feature of the proposed T-PCA is to promote the nonuniform and irregular correlation structures of the received pilot signals using Transformer, a DL architecture that differently weights each input data based on the correlations between the input data. By exploiting the attention mechanism of Transformer, T-PCA can facilitate the extraction of spatially and temporally-correlated features inherent in the THz UM-MIMO systems. In doing so, fast yet accurate channel parameter estimation can be made with small pilot overhead. From the simulation results, we demonstrated that T-PCA achieves more than $2.5\,\text{dB}$ NMSE gain and 33% pilot overhead reduction over the conventional channel acquisition techniques. In our work, we restricted our attention to channel estimation, but there are many interesting applications of T-PCA such as channel feedback, beam tracking, and resource allocation.

Chapter 5

Fast and Accurate Terahertz Beam Management via Frequency-dependent Beamforming

In this chapter, we introduce a beam management technique for wideband THz systems. One main difficulty of the THz communications is the severe attenuation of signal power caused by the high diffraction and penetration losses and atmospheric absorption. To compensate for the severe path loss, a beamforming technique realized by the massive multiple-input multiple-output (MIMO) has been widely used. Since the beamforming gain is maximized only when the beams are appropriately aligned with the signal propagation paths, acquisition of accurate beam directions is of great importance. A major issue of the conventional beam management schemes is the considerable latency being proportional to the number of training beams. In this chapter, we propose a THz beam management technique that simultaneously generates multiple frequency-dependent beams using the true time delay (TTD)-based phase shifters. By closing the gap between the frequency-dependent beamforming vectors and the desired directional beamforming vectors using the TTD-based signal propagation network called intensifier, we generate very sharp training beams maximizing the beamforming gain.

5.1 Introduction

Recently, terahertz (THz) communications have received much attention to alleviate spectrum bottleneck and support high data rates for 6G wireless communications [65, 66]. Using the abundant spectrum resource in the THz frequency band ($0.1 \sim 10$ THz), THz communications can support immersive mobile services such as digital twin, metaverse realized by XR devices, and high-fidelity mobile holographic displays [67,68]. Well-known drawback of the THz communications is the severe attenuation of the signal power caused by the high diffraction and penetration losses and atmospheric absorption [69]. To deal with the problem, a beamforming technique realized by the massive multiple-input multiple-output (MIMO) has been widely used [41, 56, 70, 71]. Since the beamforming gain is maximized only when the beams are properly aligned with the signal propagation paths, the base station (BS) needs to acquire the accurate channel information in a form of angle-of-arrivals (AoAs) and angle-of-departures (AoDs). The process to acquire the AoAs/AoDs associated with the paths between the BS and the mobile and then send the directional beams to the acquired directions is collectively called *beam management* [72, 73]. In general, the beam management of 5G NR consists of two steps: 1) *beam sweeping* and 2) *beam refinement*. In the beam sweeping step, the BS sequentially transmits the training beams carrying the reference signal and the mobile reports the index of the beam corresponding to the highest reference signal received power (RSRP) to the BS. After that, in the beam refinement step, the BS narrows down the direction of the mobile by sending multiple pilot signals (e.g., channel state information reference signal (CSI-RS)) to the direction obtained from the beam sweeping [74].

Over the years, various beam management schemes have been proposed [75–80]. In [75] and [76], beam management schemes using the hierarchical multi-level beam codebook have been proposed. In [77], a two-stage beam training scheme using a multi-resolution codebook for sub-THz communications has been proposed. In [78], a beam training scheme that exploits wide-beam codewords for the fast beam alignment in THz massive MIMO systems has been proposed. In [79], a fast beam tracking scheme that leverages the temporal variation of the physical direction has been proposed for THz massive MIMO systems. Also, in [80], a joint beam management and power allocation algorithm for the THz non-orthogonal multiple access (NOMA) systems has been proposed. A potential drawback of these schemes is that the BS can probe only one physical direction in each time slot, thereby inducing a beam management latency being proportional to the number of training beams. Recently, to speed up the beam management process, wideband beam training schemes that simultaneously generate multiple frequency-dependent training beams using the analog phase shifters and true time delay (TTD)-based phase shifters have been proposed [81–84]. TTD is a unit generating a specific time delay using multiple switched delay lines [85]. By controlling the propagation path of the RF transmission signals, TTD induces a phase shift being proportional to the product of the time delay and the signal frequency to the RF signal. Using the combination of TTD-based phase shifters and analog phase shifters, the BS can simultaneously generate multiple frequency-dependent training beams heading toward distinct physical directions, thereby achieving a considerable reduction of beam management latency. While this approach is promising, since micro-electromechanical systems (MEMS) relying on costly semiconductor lithographic process is used in switching the delay lines in the TTD, hardware complexity and implementation cost of the TTD are considerable[1]. To reduce the hardware complexity and the implementation cost, a partially-connected structure where one TTD is connected to multiple antennas has been suggested [82]. This so-called delay-phased precoding (DPP) scheme can save the hardware cost to some extent, but it will cause a severe degradation of the beamforming gain due to the strong sidelobe power of the generated beams.

An aim of this paper is to put forth an efficient THz beam management technique reducing the beam management latency without the loss of beamforming gain. The proposed scheme, henceforth referred to as *frequency-dependent beamforming*

---

[1] The cost of the TTD is nearly 10 times higher than that of the analog phase shifter [85].

(FDB), simultaneously generates multiple frequency-dependent training beams using the TTD-based phase shifters and the analog phase shifters. A distinctive feature of the FDB-based beam management over the previous efforts is that we exploit a deliberately designed TTD-based signal propagation network called *intensifier* to compensate for the difference between the desired directional beamforming vectors and the frequency-dependent beamforming vectors. Since the BS can search multiple directions simultaneously while suppressing the sidelobes of the beams, we can obtain a significant reduction in the beam management latency and at the same time achieve the maximum beamforming gain. The main contributions of this work are as follows:

- We propose a novel THz beamforming network that generates multiple frequency-dependent beams using TTDs and analog phase shifters. Specifically, the proposed FDB scheme consists of three signal propagation networks: 1) *analog network* generating the initial beamforming vector, 2) *time delay network* changing the physical directions of the beams, and 3) *intensifier network* suppressing the sidelobes of the subcarrier beams generated by the time delay network and the analog network. By controlling the parameters of these networks, FDB can generate the subcarrier beams heading toward the desired probing area while achieving the maximum beamforming gain.

- We propose the FDB-based THz beam management strategy that simultaneously searches multiple directions. The proposed strategy consists of two major operational steps: 1) *beam spraying* where the BS simultaneously transmits the FDB beams heading toward the whole angular area. After measuring these, a mobile feeds back the index of the FDB beam maximizing the RSRP to the BS and 2) *beam purification* where the BS performs the fine-tuning to the angular area identified in the beam spraying process to find out the precise beam direction. Since the number of FDB beams is the same as the number of subcarriers in the wideband THz systems (e.g., $64 \sim 256$), we can achieve a significant reduction in the beam management latency.

- We perform the beam misalignment probability analysis from which we show that the probability of FDB to find out the optimal beam direction is much higher than that of DPP. Also, from the numerical evaluations on the realistic THz systems, we demonstrate that FDB significantly reduces the beam management latency. In particular, FDB achieves more than 90% reduction on the beam management latency over the conventional beam management scheme in 5G NR. Even when compared with DPP, FDB achieves more than 70% beam management latency reduction.

Notation: Lower and upper case symbols are used to denote vectors and matrices, respectively. The superscript $(\cdot)^{\mathrm{T}}$, $(\cdot)^{\mathrm{H}}$, and $(\cdot)^{\dagger}$ denote transpose, hermitian transpose, and pseudo-inverse, respectively. $\|\mathbf{x}\|$ is the Euclidean norm of a vector $\mathbf{x}$ and $\|\mathbf{X}\|_{\mathrm{F}}$ is the Frobenius norm of a matrix $\mathbf{X}$. $\mathrm{Re}\{x\}$ and $\mathrm{Im}\{x\}$ are the real and imaginary parts of x, respectively. $\mathbf{a}_N(x) = \left[1, e^{jx}, \cdots, e^{j(N-1)x}\right]^{\mathrm{T}}$ is the $N \times 1$ array steering vector corresponding to x. Also, $\mathbf{X} \otimes \mathbf{Y}$ and $\mathbf{X} \odot \mathbf{Y}$ denote the Kronecker and Hadamard product of $\mathbf{X}$ and $\mathbf{Y}$, respectively.

5.2 Wideband Terahertz Systems

In this section, we briefly discuss the wideband THz MISO system model and true time delay, followed by a description of the conventional frequency-dependent beamforming technique.

5.2.1 Terahertz MISO-OFDM System Model

We consider a downlink THz MISO-OFDM system where a BS equipped with a uniform linear array (ULA) of N antennas[2] serves a single-antenna mobile. The number of

---

[2] In our work, we use $N \times 1$ linear antenna array systems but the proposed FDB scheme can be readily extended to the $N = N_x \times N_y$ planar antenna array systems by exploiting the property that the planar array steering vector $\mathbf{a}_N(\theta, \psi, f_i) \in \mathbb{C}^N$ can be expressed as a Kronecker product of two linear array steering vectors $\mathbf{a}_{N_x}(\theta, f_i) \in \mathbb{C}^{N_x}$ and $\mathbf{a}_{N_y}(\psi, f_i) \in \mathbb{C}^{N_y}$ as $\mathbf{a}_N(\theta, \psi, f_i) = \mathbf{a}_{N_x}(\theta, f_i) \otimes \mathbf{a}_{N_y}(\psi, f_i)$.

OFDM subcarriers is S, the carrier frequency is f_c, and the bandwidth is B. To reduce the hardware complexity, we consider the analog beamforming architecture where an RF chain is connected with N phase shifters[3]. Under this setup, the received signal y_i of the mobile at the i-th subcarrier is given by

$$y_i = \sqrt{P_t}\mathbf{h}_i^{\mathrm{H}}\mathbf{f}_i s_i + n_i, \quad i = 1, \cdots, S, \tag{5.1}$$

where P_t is the transmit power at each subcarrier, $\mathbf{h}_i \in \mathbb{C}^N$ is the downlink THz channel vector from the BS to the mobile, $\mathbf{f}_i \in \mathbb{C}^N$ is the frequency-dependent beamforming vector, s_i is the transmit symbol, and $n_i \sim \mathcal{CN}(0, \sigma_n^2)$ is the Gaussian noise at the i-th subcarrier. The corresponding data rate R of the mobile is given by

$$R = \sum_{i=1}^{S} \log_2 \left(1 + \frac{P_t |\mathbf{h}_i^{\mathrm{H}}\mathbf{f}_i|^2}{\sigma_n^2}\right). \tag{5.2}$$

As for the channel model, we use the far-field frequency-selective line-of-sight (LoS)-based THz channel model where the downlink i-th subcarrier channel vector $\mathbf{h}_i \in \mathbb{C}^N$ from the BS to the mobile is expressed as [86]

$$\mathbf{h}_i = \sqrt{\rho}\alpha_i e^{-j2\pi f_i \tau}\mathbf{a}_N(\phi, f_i), \quad i = 1, \cdots, S, \tag{5.3}$$

where ρ is the large-scale fading coefficient accounting for the path loss and the shadow fading, $\alpha_i \sim \mathcal{CN}(0, 1)$ is the small-scale fading coefficient, τ is the propagation delay, $f_i = f_c - \frac{B}{2} + \frac{B}{S-1}(i-1)$ is the i-th subcarrier frequency, and $\phi = \pi \sin\varphi$ is the physical direction, and φ is the AoD at the BS. Also, $\mathbf{a}_N(\phi, f_i) \in \mathbb{C}^N$ is the $N \times 1$ array steering vector of BS at the i-th subcarrier given by

$$\begin{aligned} \mathbf{a}_N(\phi, f_i) &= \left[1, e^{j\frac{f_i}{f_c}\phi}, \cdots, e^{j(N-1)\frac{f_i}{f_c}\phi}\right]^{\mathrm{T}} && (5.4) \\ &= \left[1, e^{j\frac{\phi}{\gamma_i}}, \cdots, e^{j(N-1)\frac{\phi}{\gamma_i}}\right]^{\mathrm{T}}, && (5.5) \end{aligned}$$

---

[3] The proposed scheme can be readily extended to the hybrid beamforming architecture scenario where multiple RF chains are connected to the phase shifters. In fact, when the number of RF chains is larger than one, one can generate the oversampled FDB beams between the FDB beams generated by the single RF chain.

where γ_i is the ratio between the i-th subcarrier frequency f_i and the central frequency f_c:

$$\gamma_i = \frac{f_c}{f_i}, \quad i = 1, \cdots, S. \tag{5.6}$$

Using $\mathbf{a}_N(\phi, f_i)$, one can define the physical direction ϕ_i of the beamforming vector $\mathbf{f}_i$ at the i-th subcarrier as [82]

$$\phi_i = \arg\max_{\theta} |\mathbf{f}_i^{\mathrm{H}} \mathbf{a}_N(\theta, f_i)|^2, \quad i = 1, \cdots, S. \tag{5.7}$$

From (5.2)-(5.5), one can easily see that the optimal beamforming vector $\mathbf{f}_i^*$ maximizing the achievable rate is $\mathbf{f}_i^* = \mathbf{a}_N(\phi, f_i)$ and the physical direction of $\mathbf{f}_i^*$ is $\phi_i = \phi$ for all subcarriers[4]. Note, to find out $\{\mathbf{f}_i^*\}_{i=1}^S$, one should acquire ϕ.

5.2.2 True Time Delay-based Phase Shifter

In 5G NR mmWave systems, analog phase shifters are often used for the training beam generation. Since the generated phase is invariant to the frequency, the subcarrier beams $\mathbf{f}_1, \cdots, \mathbf{f}_S$ are all the same (i.e., $\mathbf{f}_1 = \cdots = \mathbf{f}_S$). Also, since the subcarrier spacing is far smaller than the carrier frequency, the array steering vectors for all pilot subcarriers are almost identical (i.e., $\mathbf{a}_N(\theta, f_1) \approx \cdots \approx \mathbf{a}_N(\theta, f_S)$), meaning that the physical directions $\phi_1, \cdots, \phi_S$ of all subcarrier beams are fairly similar (i.e., $\phi_1 \approx \cdots \approx \phi_S$). Due to the fact that the BS can probe only one direction at a time, the beam management latency will be directly proportional to the number of training beams [74]. In fact, the time to complete the beam management process of 5G can easily exceed 20 ms so it might not be easy to support the mobility of human's movement even in very mild scenario (e.g., walking).

---

[4] Note that the optimal beamforming vector for each subcarrier is different. In the conventional mmWave systems, the difference between f_c and f_i is relatively small, and thus one can readily assume that $\gamma_i = \frac{f_c}{f_i} \approx 1$. This means that $\{f_i^*\}_{i=1}^S$ are almost identical. In the THz systems, however, the difference between f_c and f_i is no longer negligible due to the large bandwidth. Thus, γ_i can be larger or smaller than 1. This phenomenon where the optimal beamforming vector depends on the subcarrier frequency is called the *beam squint effect* [56, 87].

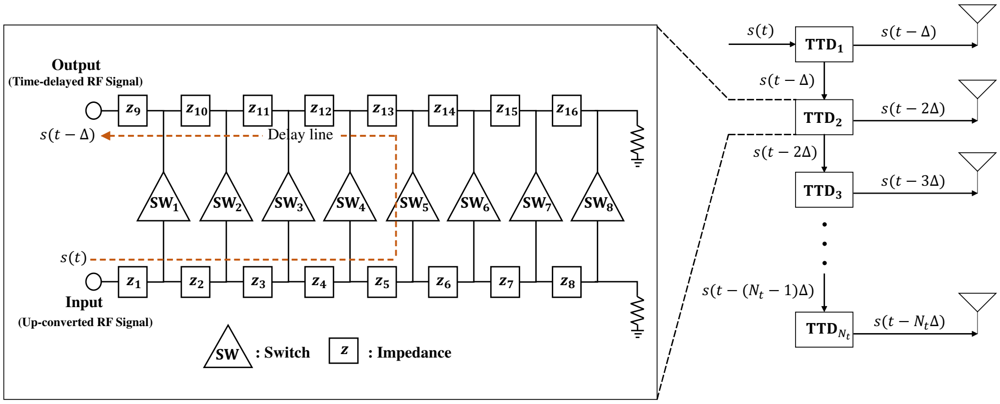

Figure 5.1: Structure of a 3-bit TTD and TTD array. The time delay is $\Delta = \frac{L}{c}$ where L is the length of the dotted delay line and c is the propagation speed of RF signal.

Recently, approaches to generate multiple frequency-dependent beams using the TTD-based phase shifters have been proposed [82, 88]. Essence of these approaches is to exploit TTD, a device consisting of multiple switches and electrical impedances, to change the phase of the RF signal. As illustrated in Fig. 5.1, when the fifth switch SW$_5$ is activated, the RF signal will propagate through the dotted delay line and the phase shift being proportional to the product of time delay $\Delta = \frac{L}{c}$ and the signal frequency f_i is induced. Specifically, if a time delay Δ is induced to an input RF signal (i.e., a sum of subcarrier signals) $s(t) = \sum_{i=1}^{S} s_i(t) = \sum_{i=1}^{S} s_i e^{j2\pi f_i t}$, then the output RF signal will be $s(t-\Delta) = \sum_{i=1}^{S} s_i e^{j2\pi f_i (t-\Delta)} = \sum_{i=1}^{S} s_i(t) e^{-j2\pi f_i \Delta}$ so that the frequency-dependent phase shift $-2\pi f_i \Delta$ is induced for each subcarrier signal $s_i(t)$.

Using the multiple TTD-based phase shifters, say N TTDs, one can generate multiple frequency-dependent beams. Specifically, let $x_{i,n}(t,\tau)$ be an output of the n-th TTD for the i-th subcarrier signal, then $x_{i,n}(t,\tau)$ can be expressed as $x_{i,n}(t,\tau) = s_i(t-(n-1)\tau) = s_i(t)e^{-j(n-1)2\pi f_i \tau}$. By stacking $x_{i,n}(t,\tau)$ of all N TTDs, one can

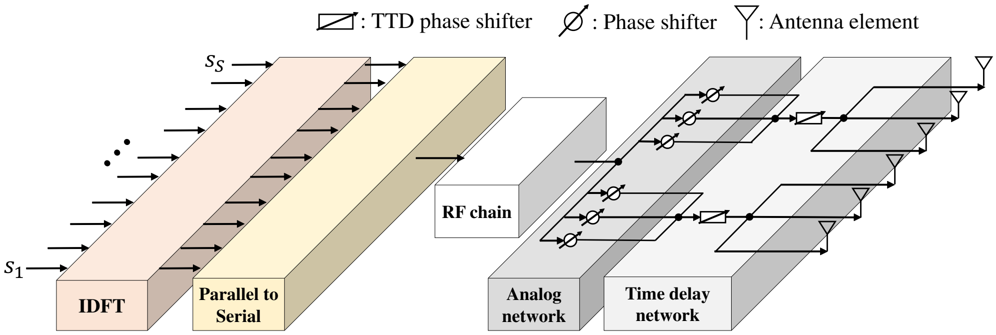

Figure 5.2: Overall structure of the conventional DPP scheme.

express the output vector $\mathbf{x}_i(t)$ of TTDs for the i-th subcarrier signal as

$$\begin{aligned}\mathbf{x}_i(t) &= [x_{i,1}(t,\tau), x_{i,2}(t,\tau), \cdots, x_{i,N}(t,\tau)]^{\mathrm{T}} && (5.8)\\ &= \left[1, e^{-j2\pi f_i \tau}, \cdots, e^{-j(N-1)2\pi f_i \tau}\right]^{\mathrm{T}} s_i(t) && (5.9)\\ &= \mathbf{f}_i(\tau) s_i(t) && (5.10)\\ &= \mathbf{a}_N(-2\pi f_c \tau, f_i) s_i(t). && (5.11)\end{aligned}$$

One can see that $\mathbf{f}_i(\tau) = \left[1, e^{-j2\pi f_i \tau}, \cdots, e^{-j(N-1)2\pi f_i \tau}\right]^{\mathrm{T}} = \mathbf{a}_N(-2\pi f_c \tau, f_i)$ is the TTD beamforming vector at the i-th subcarrier. In contrast to the beamforming vectors generated by the analog phase shifters, the TTD beamforming vectors at distinct subcarrier frequencies are different. However, since the physical direction ϕ_i of $\mathbf{f}_i(\tau)$ are identical for all subcarriers (i.e., $\phi_1 = \cdots = \phi_S = -2\pi f_c \tau$), one cannot generate frequency-dependent beams with distinct physical directions using only the TTD-based phase shifters.

5.2.3 Conventional Delay-phased Precoding

To simultaneously generate the multiple training beams heading toward distinct physical directions, DPP employs both TTDs and analog phase shifters [82, 83]. Let N and T^{dpp} be the numbers of analog phase shifters and TTDs, then each TTD is connected to $P^{\text{dpp}} = \frac{N}{T^{\text{dpp}}}$ analog phase shifters (see Fig. 5.2). The DPP beamforming vector

$\mathbf{f}_i^{\text{dpp}} \in \mathbb{C}^N$ at the i-th subcarrier is

$$\mathbf{f}_i^{\text{dpp}} = \mathbf{f}_i^{\text{td}}(\tau) \odot \mathbf{f}_i^{\text{ana}}(\theta), \quad i = 1, \cdots, S, \tag{5.12}$$

where $\mathbf{f}_i^{\text{ana}}(\theta) \in \mathbb{C}^N$ is the beamforming vector generated by the analog phase shifters:

$$\mathbf{f}_i^{\text{ana}}(\theta) = [1, e^{j\theta}, \cdots, e^{j(N-1)\theta}]^{\text{T}}. \tag{5.13}$$

Note that, since the phase generated by the analog phase shifter is invariant to the frequency, the analog beamforming vectors $\{\mathbf{f}_i^{\text{ana}}(\theta)\}_{i=1}^S$ of all subcarriers are the same. $\mathbf{f}_i^{\text{td}}(\tau) \in \mathbb{C}^N$ is the beamforming vector generated by the TTDs:

$$\mathbf{f}_i^{\text{td}}(\tau) = \left[1, e^{-j2\pi f_i \tau}, \cdots, e^{-j(T^{\text{dpp}}-1)2\pi f_i \tau}\right]^{\text{T}} \otimes \mathbf{1}_{P^{\text{dpp}}}, \tag{5.14}$$

Noting that $\mathbf{f}_i^{\text{ana}}(\theta) = \mathbf{a}_N(\theta, f_c) = \mathbf{a}_N(\gamma_i\theta, f_i)$ and $\mathbf{f}_i^{\text{td}}(\tau) = \mathbf{a}_{T^{\text{dpp}}}(-2\pi f_c \tau, f_i) \otimes \mathbf{1}_{P^{\text{dpp}}}$, one can re-express $\mathbf{f}_i^{\text{dpp}}$ as

$$\begin{aligned}
\mathbf{f}_i^{\text{dpp}} &= \mathbf{f}_i^{\text{td}}(\tau) \odot \mathbf{f}_i^{\text{ana}}(\theta) && (5.15)\\
&\overset{(a)}{=} (\mathbf{a}_{T^{\text{dpp}}}(-2\pi f_c\tau, f_i) \otimes \mathbf{1}_{P^{\text{dpp}}}) \odot (\mathbf{a}_{T^{\text{dpp}}}(P\gamma_i\theta, f_i) \otimes \mathbf{a}_{P^{\text{dpp}}}(\gamma_i\theta, f_i)) && (5.16)\\
&\overset{(b)}{=} (\mathbf{a}_{T^{\text{dpp}}}(-2\pi f_c\tau, f_i) \odot \mathbf{a}_{T^{\text{dpp}}}(P\gamma_i\theta, f_i)) \otimes (\mathbf{1}_{P^{\text{dpp}}} \odot \mathbf{a}_{P^{\text{dpp}}}(\gamma_i\theta, f_i)) && (5.17)\\
&\overset{(c)}{=} \mathbf{a}_{T^{\text{dpp}}}(P^{\text{dpp}}\gamma_i\theta - 2\pi f_c\tau, f_i) \otimes \mathbf{a}_{P^{\text{dpp}}}(\gamma_i\theta, f_i), && (5.18)
\end{aligned}$$

where (a), (b), and (c) follow from $\mathbf{a}_N(\theta, f_i) = \mathbf{a}_T(P\theta, f_i) \otimes \mathbf{a}_P(\theta, f_i)$, $(\mathbf{A} \otimes \mathbf{B}) \odot (\mathbf{C} \otimes \mathbf{D}) = (\mathbf{A} \odot \mathbf{C}) \otimes (\mathbf{B} \odot \mathbf{D})$, and $\mathbf{a}_N(\phi_1, f_i) \odot \mathbf{a}_N(\theta_2, f_i) = \mathbf{a}_N(\phi_1 + \theta_2, f_i)$, respectively[5].

By properly controlling τ and θ, one can generate S DPP beams $\{\mathbf{f}_i^{\text{dpp}}\}_{i=1}^S$ heading toward the desired physical directions. In the following Lemma, we express the physical direction of DPP beam as a function of θ and τ.

Lemma 6. *The physical direction ϕ_i of the DPP beam $\mathbf{f}_i^{\text{DPP}}$ is $\phi_i = \gamma_i\theta - \frac{2\pi f_c \tau}{P^{\text{dpp}}}$ [82].*

---

[5] For example, when $N = 6$, $T = 2$, and $P = 3$, then $\mathbf{a}_N(\theta, f_i)$ can be re-expressed as $\mathbf{a}_6(\theta, f_i) = \left[1, e^{j\frac{1}{\gamma_i}}, \cdots, e^{j\frac{5\theta}{\gamma_i}}\right]^{\text{T}} = \left[[1\, e^{j\frac{\theta}{\gamma_i}}\, e^{j\frac{2\theta}{\gamma_i}}]^{\text{T}}\, e^{j\frac{3\theta}{\gamma_i}}[1\, e^{j\frac{\theta}{\gamma_i}}\, e^{j\frac{2\theta}{\gamma_i}}]^{\text{T}}\right] = \left[1\, e^{j\frac{3\theta}{\gamma_i}}\right]^{\text{T}} \otimes \left[1\, e^{j\frac{\theta}{\gamma_i}}\, e^{j\frac{2\theta}{\gamma_i}}\right]^{\text{T}} = \mathbf{a}_2(3\theta, f_i) \otimes \mathbf{a}_3(\theta, f_i)$.

Due to the partially-connected structure where one TTD is connected to multiple analog phase shifters, DPP cannot generate sharp training beams. To measure the difference between the DPP beamforming vector $\mathbf{f}_i^{\text{dpp}}$ and the desired directional beamforming vector $\mathbf{a}_N(\phi_i, f_i)$, one can re-express $\mathbf{a}_N(\phi_i, f_i)$ as

$$\begin{aligned}\mathbf{a}_N(\phi_i, f_i) &= \mathbf{a}_{T^{\text{dpp}}}(P^{\text{dpp}}\phi_i, f_i) \otimes \mathbf{a}_{P^{\text{dpp}}}(\phi_i, f_i) && (5.19)\\ &\overset{(a)}{=} \mathbf{a}_{T^{\text{dpp}}}(P^{\text{dpp}}\gamma_i\theta - 2\pi f_c\tau, f_i) \otimes \mathbf{a}_{P^{\text{dpp}}}\Big(\gamma_i\theta - \frac{2\pi f_c\tau}{P^{\text{dpp}}}, f_i\Big), && (5.20)\end{aligned}$$

where (a) is from Lemma 1. It is clear from (5.18) and (5.20) that $\mathbf{f}_i^{\text{dpp}}$ and $\mathbf{a}_N(\phi_i, f_i)$ are not the same due to the difference between $\mathbf{a}_{P^{\text{dpp}}}\big(\gamma_i\theta - \frac{2\pi f_c\tau}{P^{\text{dpp}}}, f_i\big)$ and $\mathbf{a}_{P^{\text{dpp}}}(\gamma_i\theta, f_i)$. Since $\mathbf{f}_i^{\text{dpp}}$ and $\mathbf{a}_N(\phi_i, f_i)$ are different, the transmit signal is not fully concentrated on the mainlobe, causing a considerable degradation of beamforming gain. To quantify this behavior, we evaluate the beamforming gain $G_i^{\text{dpp}} = |\frac{1}{N}\mathbf{f}_i^{\text{dpp,H}}\mathbf{a}_N(\phi_i, f_i)|^2$ of the DPP beam $\mathbf{f}_i^{\text{dpp}}$ at the i-th subcarrier:

$$\begin{aligned}G_i^{\text{dpp}} =& \Big|\frac{1}{N}\mathbf{f}_i^{\text{dpp,H}}\mathbf{a}_N(\phi_i, f_i)\Big|^2 && (5.21)\\ =& \Big|\frac{1}{N}\Big(\mathbf{a}_{T^{\text{dpp}}}(P^{\text{dpp}}\gamma_i\theta - 2\pi f_c\tau, f_i) \otimes \mathbf{a}_{P^{\text{dpp}}}(\gamma_i\theta, f_i)\Big)^{\text{H}} \\ & \Big(\mathbf{a}_{T^{\text{dpp}}}(P^{\text{dpp}}\gamma_i\theta - 2\pi f_c\tau, f_i) \otimes \mathbf{a}_{P^{\text{dpp}}}\Big(\gamma_i\theta - \frac{2\pi f_c\tau}{P^{\text{dpp}}}, f_i\Big)\Big)\Big|^2 && (5.22)\\ =& \Big|\frac{1}{P^{\text{dpp}}}\mathbf{a}_{P^{\text{dpp}}}^{\text{H}}(\gamma_i\theta, f_i)\mathbf{a}_{P^{\text{dpp}}}\Big(\gamma_i\theta - \frac{2\pi f_c\tau}{P^{\text{dpp}}}, f_i\Big)\Big|^2 && (5.23)\\ =& \left|\frac{\sin(\pi f_c\tau)}{P^{\text{dpp}}\sin\frac{\pi f_c\tau}{P^{\text{dpp}}}}\right|^2. && (5.24)\end{aligned}$$

One can see that G_i^{dpp} is a function of P^{dpp} and achieves the maximum value at $P^{\text{dpp}} = \frac{N}{T^{\text{dpp}}} = 1$. To achieve $P^{\text{dpp}} = 1$, the number of TTDs T^{dpp} should be the same with the number of analog phase shifters N. However, due to the considerable hardware complexity and implementation cost of TTD, it might not be easy to use such a large number of TTDs. Thus, in many practical scenarios where T^{dpp} is smaller than N, the degradation of DPP beamforming gain is unavoidable. Indeed, as shown in Fig. 5.3, the mainlobe of the DPP beam $\mathbf{f}_i^{\text{dpp}}$ is 2 dB lower than that of the desired directional beam $\mathbf{a}_N(\phi_i, f_i)$.

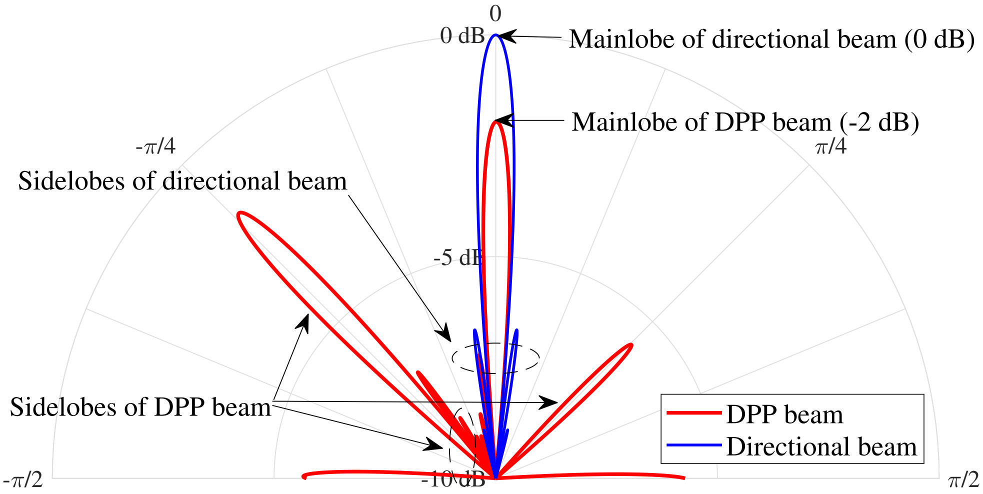

Figure 5.3: Beamforming gains of DPP beam and directional beam ($N = 32$, $f_i = 10\,\text{GHz}$, $f_c = 100\,\text{GHz}$, $B = 10\,\text{GHz}$, $S = 16$, $T^{\text{dpp}} = 8$, $P^{\text{dpp}} = 4$, $\theta = -0.25$, and $\tau = -4.2 \times 10^{-10}$). One can see that the sidelobe leakage of DPP beam is much larger than that of directional beam.

5.3 Frequency-dependent Beamforming for Wideband Terahertz Systems

Main purpose of the proposed FDB is to simultaneously generate multiple frequency-dependent beams achieving the maximum beamforming gain. To this end, FDB employs three signal propagation networks (see Fig. 5.4): 1) *analog network* generating the initial beamforming vector, 2) *time delay network* changing the physical directions of the beams using the TTD-based phase shifters, and 3) *intensifier network* suppressing the sidelobes of the subcarrier beams generated by the time delay network and the analog network. Among these, the key distinctive block of FDB over DPP is the intensifier network compensating for the difference between the subcarrier beams and the desired directional beams. Using the intensifier network to adjust the beam patterns of the generated beams, FDB can achieve the maximum beamforming gain with much smaller number of TTDs than those required by DPP.

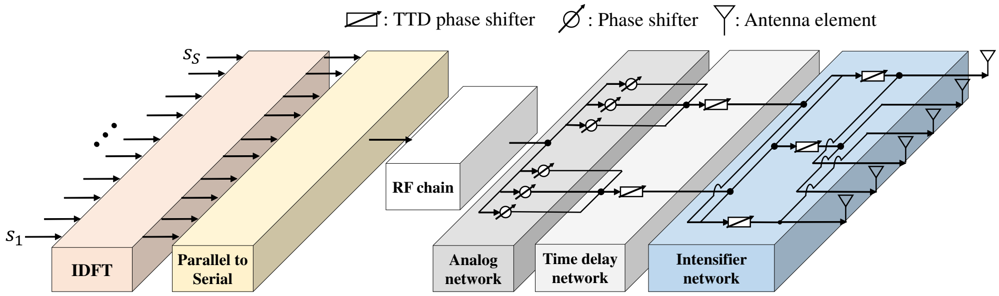

Figure 5.4: Overall structure of the proposed FDB scheme.

5.3.1 Overall Operation of Frequency-dependent Beamforming

After passing through three networks, the FDB beamforming vector $\mathbf{f}_i \in \mathbb{C}^N$ can be expressed as

$$\mathbf{f}_i = \mathbf{f}_i^{\text{it}}(\eta) \odot \mathbf{f}_i^{\text{td}}(\tau) \odot \mathbf{f}_i^{\text{ana}}(\theta), \quad i = 1, \cdots, S, \tag{5.25}$$

where $\mathbf{f}_i^{\text{ana}}(\theta)$, $\mathbf{f}_i^{\text{td}}(\tau)$, and $\mathbf{f}_i^{\text{it}}(\eta) \in \mathbb{C}^N$ are the beamforming vectors generated by the analog network, time delay network, and intensifier network, respectively. Also, θ is the phase shift of the analog phase shifters and τ and η are the time delays provided by the TTDs in the time delay network and intensifier network, respectively. By deliberately controlling the FDB parameters (θ, τ, η), we can design the beamforming vectors such that $\{\mathbf{f}_i\}_{i=1}^S$ are directed to the desired probing area $[\phi_{\text{min}}, \phi_{\text{max}}]$.

We start by defining the notions used in the FDB beamforming. First, the angular range of $\{\mathbf{f}_i\}_{i=1}^S$ is defined as

$$\text{Range}(\{\mathbf{f}_i\}_{i=1}^S) = \big[\phi_1, \, \phi_S\big], \tag{5.26}$$

where $\phi_i = \arg\max_\theta |\mathbf{f}_i^{\text{H}} \mathbf{a}_N(\theta, f_i)|^2$ is the physical direction of $\mathbf{f}_i$ (see (5.7)). Note that $\text{Range}(\{\mathbf{f}_i\}_{i=1}^S)$ is a function of the central direction and the width given by

$$\text{Center}(\{\mathbf{f}_i\}_{i=1}^S) = \frac{1}{2}(\phi_1 + \phi_S), \tag{5.27}$$

$$\text{Width}(\{\mathbf{f}_i\}_{i=1}^S) = \phi_S - \phi_1. \tag{5.28}$$

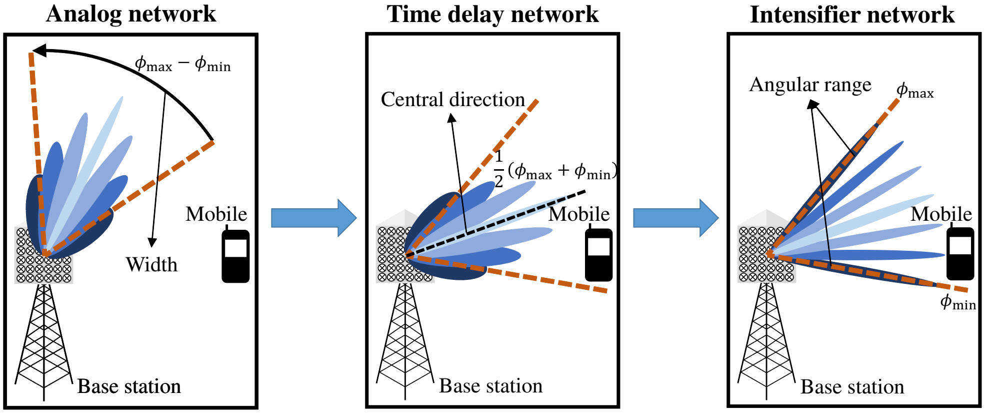

Set the width of FDB beams

Set the central direction of FDB beams

Modify the beam pattern

Figure 5.5: FDB beam generation via analog network, time delay network, and intensifier network.

To enforce $\mathrm{Range}(\{\mathbf{f}_i\}_{i=1}^S) = [\phi_{\min}, \phi_{\max}]$, we should set $\mathrm{Center}(\{\mathbf{f}_i\}_{i=1}^S) = \frac{1}{2}(\phi_{\min} + \phi_{\max})$ and $\mathrm{Width}(\{\mathbf{f}_i\}_{i=1}^S) = \phi_{\max} - \phi_{\min}$.

The overall operation of FDB is as follows (see Fig. 5.5):

- **Analog network**: By controlling the phase shift θ in the analog network, the subcarrier beams $\{\mathbf{f}_i^{\mathrm{ana}}(\theta)\}_{i=1}^S$ satisfying $\mathrm{Width}(\{\mathbf{f}_i^{\mathrm{ana}}(\theta)\}_{i=1}^S) = \phi_{\max} - \phi_{\min}$ is generated.

- **Time delay network**: By controlling the time delay τ in the time delay network, the central direction of the generated beams $\{\mathbf{f}_i^{\mathrm{td}}(\tau) \odot \mathbf{f}_i^{\mathrm{td}}(\tau)\}_{i=1}^S$ is set to $\mathrm{Center}(\{\mathbf{f}_i^{\mathrm{td}}(\tau) \odot \mathbf{f}_i^{\mathrm{td}}(\tau)\}_{i=1}^S) = \frac{1}{2}(\phi_{\min} + \phi_{\max})$ (Note that the width remains unchanged).

- **Intensifier network**: By controlling the time delay η in the intensifier network, we can bridge the gap between the FDB beamforming vectors $\{\mathbf{f}_i^{\mathrm{it}}(\eta) \odot \mathbf{f}_i^{\mathrm{td}}(\tau) \odot \mathbf{f}_i^{\mathrm{ana}}(\theta)\}_{i=1}^S$ and the desired directional beamforming vectors $\{\mathbf{a}_N(\phi_i, f_i)\}_{i=1}^S$.

5.3.2 Frequency-dependent Beam Generation

In this subsection, we explain the detailed operation of the FDB beam generation. As shown in Fig. 4, the analog network, time delay network, and intensifier network consist of N analog phase shifters, T TTD-based phase shifters, and $P = \frac{N}{T}$ TTD-based phase shifters, respectively.

Analog Network

In the analog network, S subcarrier beams $\{\mathbf{f}_i^{\text{ana}}(\theta)\}_{i=1}^S$ are generated using N analog phase shifters. The beamforming vector $\mathbf{f}_i^{\text{ana}}(\theta)$ of the analog network at the i-th subcarrier is

$$\mathbf{f}_i^{\text{ana}}(\theta) = [1, e^{j\theta}, \cdots, e^{j(N-1)\theta}]^{\text{T}} = \mathbf{a}_N(\theta, f_c) = \mathbf{a}_N(\gamma_i\theta, f_i). \tag{5.29}$$

From the definition of physical direction in (5.7), the physical direction of $\mathbf{f}_i^{\text{ana}}(\theta)$ is given by $\phi_i = \gamma_i\theta$ so that $\text{Width}(\{\mathbf{f}_i^{\text{ana}}(\theta)\}_{i=1}^S) = (\gamma_S - \gamma_1)\theta$. Thus, by setting θ as

$$\theta = \frac{\phi_{\text{max}} - \phi_{\text{min}}}{\gamma_S - \gamma_1}, \tag{5.30}$$

we can enforce $\text{Width}(\{\mathbf{f}_i^{\text{ana}}(\theta)\}_{i=1}^S) = \phi_{\text{max}} - \phi_{\text{min}}$. Note that the central direction of the generated beams $\{\mathbf{f}_i^{\text{ana}}(\theta)\}_{i=1}^S$ is $\text{Center}(\{\mathbf{f}_i^{\text{ana}}(\theta)\}_{i=1}^S) = \frac{1}{2}(\gamma_1 + \gamma_S)\theta = \frac{(\gamma_1+\gamma_S)}{2(\gamma_S-\gamma_1)}(\phi_{\text{max}} - \phi_{\text{min}})$.

Time Delay Network

In the time delay network, the central direction $\frac{(\gamma_1+\gamma_S)}{2(\gamma_S-\gamma_1)}(\phi_{\text{max}} - \phi_{\text{min}})$ of the beams generated from the analog network is changed to $\frac{1}{2}(\phi_{\text{min}} + \phi_{\text{max}})$ using T TTD-based phase shifters, each of which is connected to $P = \frac{N}{T}$ analog phase shifters in the analog network. The beamforming vector $\mathbf{f}_i^{\text{td}}(\tau)$ of the time delay network at the i-th subcarrier is

$$\mathbf{f}_i^{\text{td}}(\tau) = [1, e^{-j2\pi f_i\tau}, \cdots, e^{-j(T-1)2\pi f_i\tau}]^{\text{T}} \otimes \mathbf{1}_P = \mathbf{a}_T(-2\pi f_c\tau, f_i) \otimes \mathbf{1}_P. \tag{5.31}$$

Using (5.29) and (5.31), the i-th subcarrier beam $\mathbf{f}_i^{\text{td}}(\tau) \odot \mathbf{f}_i^{\text{ana}}(\theta)$ generated by the analog network and time delay network can be expressed as

$$\begin{aligned}
\mathbf{f}_i^{\text{td}}(\tau) \odot \mathbf{f}_i^{\text{ana}}(\theta) &= (\mathbf{a}_T(-2\pi f_c \tau, f_i) \otimes \mathbf{1}_P) \odot \mathbf{a}_N(\gamma_i \theta, f_i) && (5.32)\\
&= (\mathbf{a}_T(-2\pi f_c \tau, f_i) \otimes \mathbf{1}_P) \odot (\mathbf{a}_T(P\gamma_i \theta, f_i) \otimes \mathbf{a}_P(\gamma_i \theta, f_i)) && (5.33)\\
&= \mathbf{a}_T(P\gamma_i\theta - 2\pi f_c \tau, f_i) \otimes \mathbf{a}_P(\gamma_i \theta, f_i). && (5.34)
\end{aligned}$$

Using Lemma 1 and (5.30), one can see that the physical direction of $\mathbf{f}_i^{\text{td}}(\tau) \odot \mathbf{f}_i^{\text{ana}}(\theta)$ is $\phi_i = \gamma_i\theta - \frac{2\pi f_c \tau}{P} = \frac{\gamma_i}{\gamma_S - \gamma_1}(\phi_{\text{max}} - \phi_{\text{min}}) - \frac{2\pi f_c \tau}{P}$. Since $\text{Center}(\{\mathbf{f}_i^{\text{td}}(\tau) \odot \mathbf{f}_i^{\text{ana}}(\theta)\}_{i=1}^S) = \frac{\gamma_1 + \gamma_S}{2(\gamma_S - \gamma_1)}(\phi_{\text{max}} - \phi_{\text{min}}) - \frac{2\pi f_c \tau}{P}$, by setting τ as

$$\tau = \frac{P}{2\pi f_c}\left(\frac{\gamma_1 + \gamma_S}{2(\gamma_S - \gamma_1)}(\phi_{\text{max}} - \phi_{\text{min}}) - \frac{\phi_{\text{min}} + \phi_{\text{max}}}{2}\right) = \frac{P(\gamma_1 \phi_{\text{max}} - \gamma_S \phi_{\text{min}})}{2\pi f_c (\gamma_S - \gamma_1)}, \tag{5.35}$$

we can enforce $\text{Center}(\{\mathbf{f}_i^{\text{td}}(\tau) \odot \mathbf{f}_i^{\text{ana}}(\theta)\}_{i=1}^S) = \frac{1}{2}(\phi_{\text{min}} + \phi_{\text{max}})$. Note that the physical direction ϕ_i of the generated beam $\mathbf{f}_i^{\text{td}}(\tau) \odot \mathbf{f}_i^{\text{ana}}(\theta)$ is given by

$$\phi_i = \gamma_i \theta - \frac{2\pi f_c \tau}{P} = \frac{(\gamma_i - \gamma_1)\phi_{\text{max}} + (\gamma_S - \gamma_i)\phi_{\text{min}}}{\gamma_S - \gamma_1}. \tag{5.36}$$

One can easily see that $\phi_1 = \phi_{\text{min}}$ and $\phi_S = \phi_{\text{max}}$.

In summary, by setting τ and θ as (5.30) and (5.35), respectively, we can set the angular range of $\{\mathbf{f}_i^{\text{td}}(\tau) \odot \mathbf{f}_i^{\text{ana}}(\theta)\}_{i=1}^S$ to $\text{Range}(\{\mathbf{f}_i^{\text{td}}(\tau) \odot \mathbf{f}_i^{\text{ana}}(\theta)\}_{i=1}^S) = [\phi_{\text{min}}, \phi_{\text{max}}]$.

Intensifier Network

Although the angular range of the generated beams is set to the desired probing area $[\phi_{\text{min}}, \phi_{\text{max}}]$, the generated beams suffer from a severe degradation of beamforming gain due to the high sidelobe leakage (see (5.21)-(5.24)). Main purpose of the intensifier network is to concentrate the signal power to the mainlobe by closing the gap between the FDB beam $\mathbf{f}_i$ and the desired directional beamforming vector $\mathbf{a}_N(\phi_i, f_i)$. Note that ϕ_i is the physical direction of $\mathbf{f}_i$ (see (5.36)).

In essence, the intensifier network consists of P TTDs, each of which is fully-connected to $T = \frac{N}{P}$ TTDs in the time delay network. The intensifier beamforming vector $\mathbf{f}_i^{\text{it}}(\eta)$ at the i-th subcarrier is

$$\mathbf{f}_i^{\text{it}}(\eta) = \mathbf{1}_T \otimes [1, e^{-j2\pi f_i \eta}, \cdots, e^{-j(P-1)2\pi f_i \eta}]^{\text{T}} = \mathbf{1}_T \otimes \mathbf{a}_P(-2\pi f_c \eta, f_i). \quad (5.37)$$

Substituting (5.34) and (5.37) into (5.25), the FDB beam $\mathbf{f}_i$ can be re-expressed as

$$\begin{aligned}
\mathbf{f}_i &= \mathbf{f}_i^{\text{it}}(\eta) \odot (\mathbf{f}_i^{\text{td}}(\tau) \odot \mathbf{f}_i^{\text{ana}}(\theta)) && (5.38)\\
&= (\mathbf{1}_T \otimes \mathbf{a}_P(-2\pi f_c \eta, f_i)) \odot (\mathbf{a}_T(P\gamma_i \theta - 2\pi f_c \tau, f_i) \otimes \mathbf{a}_P(\gamma_i \theta, f_i)) && (5.39)\\
&= \mathbf{a}_T(P\gamma_i \theta - 2\pi f_c \tau, f_i) \otimes \mathbf{a}_P(\gamma_i \theta - 2\pi f_c \eta, f_i) && (5.40)\\
&\overset{(a)}{=} \mathbf{a}_T(P\phi_i, f_i) \otimes \mathbf{a}_P\left(\phi + \frac{2\pi f_c \tau}{P} - 2\pi f_c \eta, f_i\right), && (5.41)
\end{aligned}$$

where (a) is from (5.36). Also, using the property that $\mathbf{a}_N(\theta, f_i) = \mathbf{a}_T(P\theta, f_i) \otimes \mathbf{a}_P(\theta, f_i)$ for every T and P satisfying $TP = N$, the desired directional beam $\mathbf{a}_N(\phi_i, f_i)$ can be expressed as

$$\mathbf{a}_N(\phi_i, f_i) = \mathbf{a}_T(P\phi_i, f_i) \otimes \mathbf{a}_P(\phi_i, f_i). \quad (5.42)$$

From (5.41) and (5.42), one can easily see that η satisfying $\mathbf{f}_i = \mathbf{a}_N(\phi_i, f_i)$ is

$$\eta = \frac{\tau}{P} = \frac{\gamma_1 \phi_{\text{max}} - \gamma_S \phi_{\text{min}}}{2\pi f_c(\gamma_S - \gamma_1)}. \quad (5.43)$$

In summary, by setting the FDB parameters (θ, τ, η) as in (5.30), (5.35), and (5.43), one can generate S FDB beams $\{\mathbf{f}_i\}_{i=1}^{S}$ heading toward the desired probing area $[\phi_{\text{min}}, \phi_{\text{max}}]$. As shown in Fig. 5.6 and 5.7, FDB beams achieve the maximum beamforming gain:

$$\begin{aligned}
G_i^{\text{-5-fig4}} &= \left|\frac{1}{N}\mathbf{f}_i^{\text{H}} \mathbf{a}_N(\phi_i, f_i)\right|^2 && (5.44)\\
&= \left|\frac{1}{N}\mathbf{a}_N^{\text{H}}(\phi_i, f_i) \mathbf{a}_N(\phi_i, f_i)\right|^2 && (5.45)\\
&= 1. && (5.46)
\end{aligned}$$

It is worth mentioning that for every T and P satisfying $TP = N$, the FDB beams achieve the maximum beamforming gain. Moreover, since $T + P \geq 2\sqrt{TP} = 2\sqrt{N}$, the minimum number of TTDs required to achieve the maximum beamforming gain of

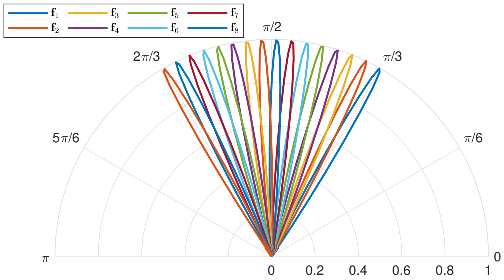

Figure 5.6: FDB beam pattern

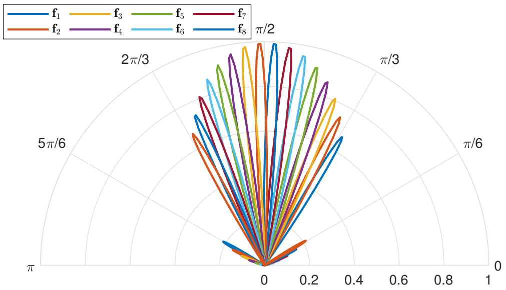

Figure 5.7: DPP beam pattern

FDB scheme is $T^{\text{min}} = K + \frac{N}{K}$ where K is the integer closest to $\sqrt{N}$ such that $\frac{N}{K}$ is an integer. For example, when $N = 256$, K would be 16, meaning that $T^{\text{min}} = K + \frac{N}{K} = 32$.

We now briefly explain the computational complexity of the intensifier network in terms of flops. First, the number of flops required for the computation of η in (5.43) is 7. Second, the number of flops required for the computation of $\mathbf{a}_P(-2\pi f_c \eta, f_i)$ is $5P$. Third, the number of flops required for the element-wise multiplication with the beamforming vectors generated by the time delay network and analog network is NS. Summing up these, the total computational complexity of the intensifier network is $\mathcal{C} = NS + 5P + 7$.

5.4 Frequency-dependent Beamforming-based Terahertz Beam Management

As mentioned, the conventional beam management schemes rely on the analog phase shifters exclusively, so that the BS can search only one direction at a time. In the FDB-based beam management, we search multiple directions simultaneously using the frequency-dependent beams. The essence of the proposed scheme is to deliberately design the FDB parameters, i.e., the phase shift of the analog network θ (see (5.30)), the time delay of the time delay network τ (see (5.35)), the time delay of the intensifier

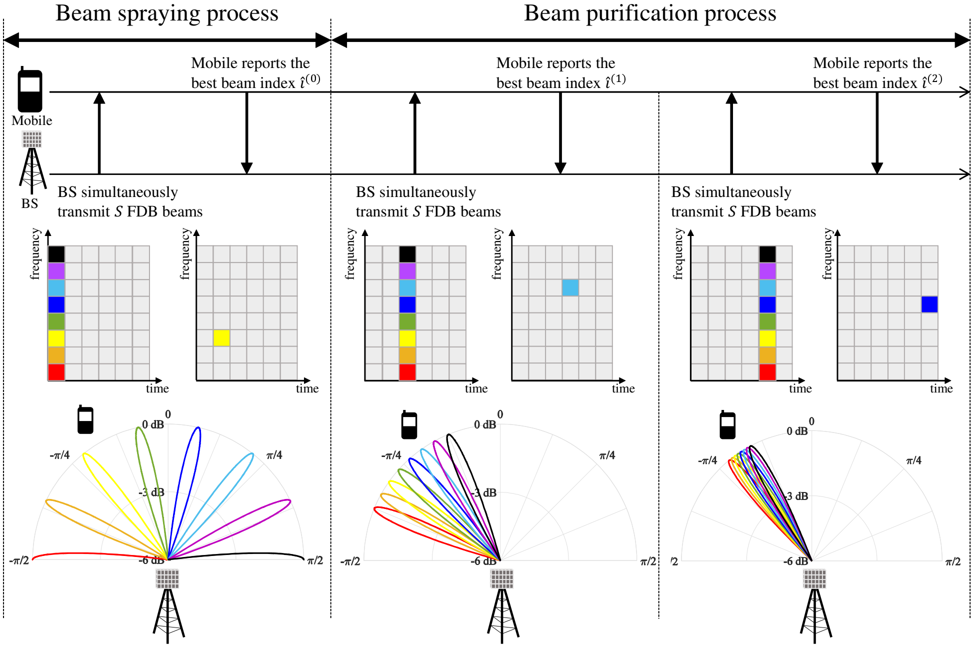

Figure 5.8: Illustration of the proposed FDB-based beam management.

network η (see (5.43)), to direct the FDB beams to the desired probing area. Since the BS can probe multiple directions, as many as the number of subcarriers in the THz systems, we can achieve a significant reduction in the beam management latency. Also, since the sidelobes of the FDB beams are controlled by the intensifier network, the chance of finding out the optimal beam direction increases significantly.

The proposed scheme consists of two major operational steps (see Fig. 5.8). In the first step called *beam spraying*, the BS simultaneously transmits the FDB beams directed to the whole angular area and then the mobile feeds back the index of the FDB beam maximizing the RSRP to the BS. In the second step called *beam purification*, to find out the precise beam direction, the BS performs the fine-tuning to the narrow angular area identified in the first step[6].

---

[6] Note that to narrow down the beam direction, one can perform multiple beam purification processes.

5.4.1 Beam Spraying Process

In the beam spraying process, to acquire the rough estimate of the physical direction ϕ of the channel, the BS transmits the FDB beams $\{\mathbf{f}_i^{(0)}\}_{i=1}^{S}$ whose physical directions are distributed in $\big[-\pi, -\pi + \frac{2\pi(S-1)}{S}\big]$. This task is performed by setting the FDB parameters to

$$(\theta^{(0)}, \tau^{(0)}, \eta^{(0)}) = \left(\frac{2\pi(S-1)}{S(\gamma_S - \gamma_1)}, \frac{P}{2f_c} + \frac{P(S-1)\gamma_1}{f_c S(\gamma_S - \gamma_1)}, \frac{1}{2f_c} + \frac{(S-1)\gamma_1}{f_c S(\gamma_S - \gamma_1)}\right). \tag{5.47}$$

In doing so, the generated FDB beam $\mathbf{f}_i^{(0)}$ at the i-th subcarrier is heading toward the physical direction $\phi_i^{(0)} = -\pi + \frac{2\pi(S-1)(\gamma_i - \gamma_1)}{S(\gamma_S - \gamma_1)} \in [-\pi, \pi]$ (see (5.36)). After the FDB beam generation, the BS simultaneously transmits the frequency-selective pilot signals using $\{\mathbf{f}_i^{(0)}\}_{i=1}^{S}$. Then the received signal $y_i^{(0)}$ of the mobile at the i-th subcarrier is

$$y_i^{(0)} = \mathbf{h}_i^{\mathrm{H}} \mathbf{f}_i^{(0)} s + n_i^{(0)}, \quad i = 1, \cdots, S, \tag{5.48}$$

where s is the pilot symbol and n_i is additive Gaussian noise. In the mobile, a subcarrier index $\hat{i}^{(0)}$ of the FDB beam $\mathbf{f}_{\hat{i}^{(0)}}^{(0)}$ maximizing the RSRP is fed back to the BS:

$$\hat{i}^{(0)} = \arg \max_{i=1,\cdots,S} \big|y_i^{(0)}\big|^2. \tag{5.49}$$

Since the RSRP is maximized when the FDB beamforming vectors are properly aligned with the subcarrier channel vectors, the BS can acquire the estimates of the physical direction ϕ of the channel from the FDB beam index feedback $\hat{i}^{(0)}$.

Lemma 7. *The angular area* $[\phi_{\text{min}}^{(1)}, \phi_{\text{max}}^{(1)}]$ *of the physical direction of the channel* $\phi = \pi \sin \varphi$ *designated by the chosen FDB beam* $\mathbf{f}_{\hat{i}^{(0)}}$ *is given by*

$$[\phi_{\text{min}}^{(1)}, \phi_{\text{max}}^{(1)}] = \left[\frac{\gamma_{\hat{i}^{(0)}} \phi_{\hat{i}^{(0)}-1}^{(0)} + \gamma_{\hat{i}^{(0)}-1} \phi_{\hat{i}^{(0)}}^{(0)}}{\gamma_{\hat{i}^{(0)}-1} + \gamma_{\hat{i}^{(0)}}}, \frac{\gamma_{\hat{i}^{(0)}+1} \phi_{\hat{i}^{(0)}}^{(0)} + \gamma_{\hat{i}^{(0)}} \phi_{\hat{i}^{(0)}+1}^{(0)}}{\gamma_{\hat{i}^{(0)}} + \gamma_{\hat{i}^{(0)}+1}}\right]. \tag{5.50}$$

Proof. See Appendix A. □

Due to the large number of subcarriers S in the wideband THz systems (e.g., $S = 128 \sim 512$), the angular area covered by the FDB beam is much smaller than that of the synchronization signal block (SSB) beam in 5G NR. In 5G NR, up to 64 SSB beams are transmitted so that the angular area covered by each SSB beam is around $\frac{360^\circ}{64} \approx 5.6^\circ$ [89]. In contrast, when $S = 256$, the angular area covered by each FDB beam is around $\frac{360^\circ}{256} \approx 1.4^\circ$. After the beam spraying process, the BS transmits the FDB beams toward the angular range $\left[\frac{\gamma_{\hat{i}^{(0)}}\phi^{(0)}_{\hat{i}^{(0)}-1}+\gamma_{\hat{i}^{(0)}-1}\phi^{(0)}_{\hat{i}^{(0)}}}{\gamma_{\hat{i}^{(0)}-1}+\gamma_{\hat{i}^{(0)}}}, \frac{\gamma_{\hat{i}^{(0)}+1}\phi^{(0)}_{\hat{i}^{(0)}}+\gamma_{\hat{i}^{(0)}}\phi^{(0)}_{\hat{i}^{(0)}+1}}{\gamma_{\hat{i}^{(0)}}+\gamma_{\hat{i}^{(0)}+1}}\right]$ to narrow down the beam direction.

5.4.2 Beam Purification Process

In the beam purification process, to find out the precise beam direction, the BS transmits the FDB beams toward the angular area determined by the beam spraying process. The beam purification process is similar in spirit to the beam spraying process in the sense that the FDB beams are transmitted to the probing area. The difference is that the probing area of the beam spraying process is the whole angular area but that of the beam purification process is the narrow angular area designated by the FDB beam chosen at the beam spraying process.

The FDB beams $\{\mathbf{f}_i^{(1)}\}_{i=1}^S$ directing toward $[\phi^{(1)}_{\text{min}}, \phi^{(1)}_{\text{max}}] = \left[\frac{\gamma_{\hat{i}^{(0)}}\phi^{(0)}_{\hat{i}^{(0)}-1}+\gamma_{\hat{i}^{(0)}-1}\phi^{(0)}_{\hat{i}^{(0)}}}{\gamma_{\hat{i}^{(0)}-1}+\gamma_{\hat{i}^{(0)}}}, \frac{\gamma_{\hat{i}^{(0)}+1}\phi^{(0)}_{\hat{i}^{(0)}}+\gamma_{\hat{i}^{(0)}}\phi^{(0)}_{\hat{i}^{(0)}+1}}{\gamma_{\hat{i}^{(0)}}+\gamma_{\hat{i}^{(0)}+1}}\right]$ are generated by setting the FDB parameters as

$$(\theta^{(1)}, \tau^{(1)}, \eta^{(1)}) = \left(\frac{\phi^{(1)}_{\text{max}} - \phi^{(1)}_{\text{min}}}{\gamma_S - \gamma_1}, \frac{P(\gamma_1\phi^{(1)}_{\text{max}} - \gamma_S\phi^{(1)}_{\text{min}})}{2\pi f_c(\gamma_S - \gamma_1)}, \frac{\gamma_1\phi^{(1)}_{\text{max}} - \gamma_S\phi^{(1)}_{\text{min}}}{2\pi f_c(\gamma_S - \gamma_1)}\right). \tag{5.51}$$

Note that each FDB beam $\mathbf{f}_i^{(1)}$ is heading toward the physical direction $\phi_i^{(1)} = \frac{(\gamma_i-\gamma_1)\phi^{(1)}_{\text{max}}+(\gamma_S-\gamma_i)\phi^{(1)}_{\text{min}}}{\gamma_S-\gamma_1}$ (see (5.36)). Then the received signal $y_i^{(1)}$ of the mobile at the i-th subcarrier is

$$y_i^{(1)} = \mathbf{h}_i^{\text{H}}\mathbf{f}_i^{(1)}s + n_i^{(1)}, \quad i = 1, \cdots, S. \tag{5.52}$$

After that, the mobile measures the RSRP and feeds back the subcarrier index $\hat{i}^{(1)}$ of the FDB beam $\mathbf{f}^{(1)}_{\hat{i}^{(1)}}$ maximizing the RSRP:

$$\hat{i}^{(1)} = \arg\max_{i=1,\cdots,S} |y_i^{(1)}|^2. \tag{5.53}$$

Using the beam index $\hat{i}^{(1)}$ fed back from the mobile, the BS acquires the physical channel direction estimate $\hat{\phi}$ as

$$\hat{\phi} = \phi^{(1)}_{\hat{i}^{(1)}} = \frac{(\gamma_{\hat{i}^{(1)}} - \gamma_1)\phi^{(1)}_{\text{max}} + (\gamma_S - \gamma_{\hat{i}^{(1)}})\phi^{(1)}_{\text{min}}}{\gamma_S - \gamma_1}. \tag{5.54}$$

Note that to narrow down the beam direction, one needs to perform multiple beam purification processes.

Once the physical direction of the channel is identified, the BS performs the downlink transmission (i.e., frequency-dependent data beamforming) to the mobile. The overall procedures of the FDB-based beam management are summarized in Table 5.1.

5.4.3 Beam Misalignment Probability Analysis

In this subsection, we provide the beam misalignment probability analysis of FDB. By the beam misalignment probability, we mean the probability that the beam chosen in the beam spraying process is different from the optimal beam. For simplicity, we analyze the beam misalignment probability of the beam spraying process but the extension to the beam purification process is straightforward since the mechanical process is exactly the same.

Let ϕ_i be the physical direction of the i-th FDB beamforming vector $\mathbf{f}_i$. Then the optimal beam direction index i^* is defined as the subcarrier index of the FDB beam $\mathbf{f}_{i^*}$ whose physical direction ϕ_{i^*} is closest to the channel direction ϕ:

$$i^* = \arg \min_{i=1,\cdots,S} |\phi - \phi_i| \tag{5.55}$$

where φ is the AoD at the BS. Also, the chosen beam direction index $\hat{i}$ is defined as the subcarrier index of the FDB beam maximizing the RSRP:

$$\begin{aligned}
\hat{i} &= \arg \max_{i=1,\cdots,S} |y_i|^2 && (5.56)\\
&= \arg \max_{i=1,\cdots,S} |\mathbf{h}_i^{\mathrm{H}}\mathbf{f}_i + n_i|^2 && (5.57)\\
&= \arg \max_{i=1,\cdots,S} \left|\sqrt{\rho}\alpha_i \mathbf{a}_N^{\mathrm{H}}\left(\frac{f_i}{f_c}\frac{2\pi d \sin\varphi}{\lambda_c}, f_c\right)\mathbf{f}_i + n_i\right|^2. && (5.58)
\end{aligned}$$

Table 5.1 Frequency-dependent beamforming based THz beam management

Input: The numbers of BS and mobile antennas N and N_r, the numbers of TTDs in the time delay network and intensifier network T and P ($TP = N$), the central frequency f_c, the subcarrier frequency ratios $\{\gamma_i\}_{i=1}^{S}$, the number of time slots for BS beam purification L

```
Beam spraying process:
$[\phi_{\text{min}}^{(0)}, \phi_{\text{max}}^{(0)}] = \left[ -\pi, -\pi + \frac{2\pi(S-1)}{S} \right]$
$(\theta^{(0)}, \tau^{(0)}, \eta^{(0)}) = \left( \frac{2\pi(S-1)}{S(\gamma_S-\gamma_1)}, \frac{P}{2f_c} + \frac{P(S-1)\gamma_1}{f_c S(\gamma_S-\gamma_1)}, \frac{1}{2f_c} + \frac{(S-1)\gamma_1}{f_c S(\gamma_S-\gamma_1)} \right)$
$\phi_i^{(0)} = -\pi + \frac{2\pi(S-1)(\gamma_i-\gamma_1)}{S(\gamma_S-\gamma_1)}, \quad i = 1, \cdots, S$
BS simultaneously transmits the FDB beams $\{\mathbf{f}_i^{(0)}\}_{i=1}^{S}$ toward $\{\phi_i^{(0)}\}_{i=1}^{S}$
$\hat{i}^{(0)} = \arg\max_{i=1,\cdots,S} \left| y_i^{(0)} \right|^2$
Mobile feeds back the subcarrier index $\hat{i}^{(0)}$ to the BS

Beam purification process:
for $l = 1, \cdots, L$ do
    $[\phi_{\text{min}}^{(l)}, \phi_{\text{max}}^{(l)}] = \left[ \frac{\gamma_{\hat{i}^{(l-1)}}\phi^{(l-1)}_{\hat{i}^{(l-1)}-1} + \gamma_{\hat{i}^{(l-1)}-1}\phi^{(l-1)}_{\hat{i}^{(l-1)}}}{\gamma_{\hat{i}^{(l-1)}-1} + \gamma_{\hat{i}^{(l-1)}}}, \frac{\gamma_{\hat{i}^{(l-1)}+1}\phi^{(l-1)}_{\hat{i}^{(l-1)}} + \gamma_{\hat{i}^{(l-1)}}\phi^{(l-1)}_{\hat{i}^{(l-1)}+1}}{\gamma_{\hat{i}^{(l-1)}} + \gamma_{\hat{i}^{(l-1)}+1}} \right]$
    $(\theta^{(l)}, \tau^{(l)}, \eta^{(l)}) = \left( \frac{\phi_{\text{max}}^{(l)} - \phi_{\text{min}}^{(l)}}{\gamma_S-\gamma_1}, \frac{P(\gamma_1\phi_{\text{max}}^{(l)} - \gamma_S\phi_{\text{min}}^{(l)})}{2\pi f_c(\gamma_S-\gamma_1)}, \frac{\gamma_1\phi_{\text{max}}^{(l)} - \gamma_S\phi_{\text{min}}^{(l)}}{2\pi f_c(\gamma_S-\gamma_1)} \right)$
    $\phi_i^{(l)} = \frac{(\gamma_i-\gamma_1)\phi_{\text{max}}^{(l)} + (\gamma_S-\gamma_i)\phi_{\text{min}}^{(l)}}{\gamma_S-\gamma_1}, \quad i = 1, \cdots, S$
    BS simultaneously transmits the FDB beams $\{\mathbf{f}_i^{(l)}\}_{i=1}^{S}$ toward $\{\phi_i^{(l)}\}_{i=1}^{S}$
    $\hat{i}^{(l)} = \arg\max_{i=1,\cdots,S} \left| y_i^{(l)} \right|^2$
    Mobile feeds back the subcarrier index $\hat{i}^{(l)}$ to the BS
end for
$\hat{\phi} = \frac{(\gamma_{\hat{i}^{(L)}}-\gamma_1)\phi_{\text{max}}^{(L)} + (\gamma_S-\gamma_{\hat{i}^{(L)}})\phi_{\text{min}}^{(L)}}{\gamma_S-\gamma_1}$
```

Output: Physical direction of channel $\hat{\phi}$

Then the beam misalignment probability P_{miss} is defined as

$$\begin{aligned} P_{\text{miss}} &= \Pr(\hat{i} \neq i^*) && (5.59) \\ &= \Pr\big(|y_{i^*}|^2 < |y_{\hat{i}}|^2\big) && (5.60) \\ &\overset{(a)}{=} \frac{1}{2\pi}\int_{-\pi}^{\pi} \Pr\big(|y_{i^*}|^2 < |y_{\hat{i}}|^2 \mid \varphi\big) d\varphi && (5.61) \\ &= \frac{1}{2\pi}\int_{-\pi}^{\pi} \Pr\Bigg(\bigcup_{\hat{i}\neq i^*} \{|y_{i^*}|^2 < |y_{\hat{i}}|^2\} \,\Bigg|\, \varphi\Bigg) d\varphi, && (5.62) \end{aligned}$$

where (a) is from the fact that φ is uniformly distributed in $[-\pi, \pi)$. Using the Boole's inequality, P_{miss} is bounded by [90]

$$P_{\text{miss}} \leq \frac{1}{2\pi}\int_{-\pi}^{\pi} \sum_{\hat{i}\neq i^*}^{S} \Pr\big(|y_{i^*}|^2 < |y_{\hat{i}}|^2 \mid \varphi\big) d\varphi. \tag{5.63}$$

It is worth noticing that $y_i = \sqrt{\rho}\alpha_i \mathbf{a}_N^{\mathrm{H}}\Big(\frac{f_i}{f_c}\frac{2\pi d \sin\varphi}{\lambda_c}, f_c\Big)\mathbf{f}_i + n_i$ is a sum of two independent complex Gaussian random variables $\sqrt{\rho}\alpha_i \mathbf{a}_N^{\mathrm{H}}\Big(\frac{f_i}{f_c}\frac{2\pi d \sin\varphi}{\lambda_c}, f_c\Big)\mathbf{f}_i \sim \mathcal{CN}\Big(0, \rho\Big|\mathbf{a}_N^{\mathrm{H}}\Big(\frac{f_i}{f_c}\frac{2\pi d \sin\varphi}{\lambda_c}, f_c\Big)\mathbf{f}_i\Big|^2\Big)$ and $n_i \sim \mathcal{CN}(0, \sigma_n^2)$. Thus, $y_i \sim \mathcal{CN}\Big(0, \rho\Big|\mathbf{a}_N^{\mathrm{H}}\Big(\frac{f_i}{f_c}\frac{2\pi d \sin\varphi}{\lambda_c}, f_c\Big)\mathbf{f}_i\Big|^2 + \sigma_n^2\Big)$, which means that $\frac{|y_i|^2}{\rho\left|\mathbf{a}_N^{\mathrm{H}}\left(\frac{f_i}{f_c}\frac{2\pi d \sin\varphi}{\lambda_c}, f_c\right)\mathbf{f}_i\right|^2 + \sigma_n^2}$ is a chi-square random variable[7] with degrees of freedom 2.

By denoting $\lambda_i = \frac{|y_i|^2}{\rho\left|\mathbf{a}_N^{\mathrm{H}}\left(\frac{f_i}{f_c}\frac{2\pi d \sin\varphi}{\lambda_c}, f_c\right)\mathbf{f}_i\right|^2 + \sigma_n^2} \sim \chi^2(2)$, we obtain the upper bound

---

[7] The degree of freedom of $\frac{|y_i|^2}{\rho\left|\mathbf{a}_N^{\mathrm{H}}\left(\frac{f_i}{f_c}\frac{2\pi d \sin\varphi}{\lambda_c}, f_c\right)\mathbf{f}_i\right|^2 + \sigma_n^2}$ is 2 since $\mathrm{Re}\{y_i\} \sim \mathcal{N}\Big(0, \rho\Big|\mathbf{a}_N^{\mathrm{H}}\Big(\frac{f_i}{f_c}\frac{2\pi d \sin\varphi}{\lambda_c}, f_c\Big)\mathbf{f}_i\Big|^2 + \sigma_n^2\Big)$ and $\mathrm{Im}\{y_i\} \sim \mathcal{N}\Big(0, \rho\Big|\mathbf{a}_N^{\mathrm{H}}\Big(\frac{f_i}{f_c}\frac{2\pi d \sin\varphi}{\lambda_c}, f_c\Big)\mathbf{f}_i\Big|^2 + \sigma_n^2\Big)$.

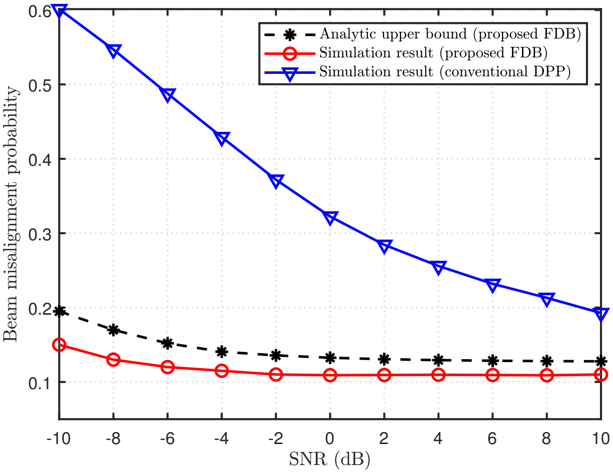

Figure 5.9: Beam misalignment probability vs. SNR ($N = 256$, $T = 16$, $P = 16$, and $S = 128$)

of P_{miss} as

$$\begin{aligned}
P_{\text{miss}} &\leq \frac{1}{2\pi}\int_{-\pi}^{\pi}\sum_{\hat{i}\neq i^*}^{S}\Pr(|y_{i^*}|^2 < |y_{\hat{i}}|^2 \mid \varphi)d\varphi \\
&= \frac{1}{2\pi}\int_{-\pi}^{\pi}\sum_{\hat{i}\neq i^*}^{S}\Pr\left(\frac{\lambda_{i^*}}{\lambda_{\hat{i}}} < \frac{\rho\left|\mathbf{a}_N^{\mathrm{H}}\left(\frac{f_{\hat{i}}}{f_c}\frac{2\pi d\sin\varphi}{\lambda_c}, f_c\right)\mathbf{f}_{\hat{i}}\right|^2 + \sigma_n^2}{\rho\left|\mathbf{a}_N^{\mathrm{H}}\left(\frac{f_{i^*}}{f_c}\frac{2\pi d\sin\varphi}{\lambda_c}, f_c\right)\mathbf{f}_{i^*}\right|^2 + \sigma_n^2}\,\middle|\,\varphi\right)d\varphi \\
&\overset{(a)}{=} \frac{1}{2\pi}\int_{-\pi}^{\pi}\sum_{\hat{i}\neq i^*}^{S}F_{\text{cdf}}\left(\frac{\rho\left|\mathbf{a}_N^{\mathrm{H}}\left(\frac{f_{\hat{i}}}{f_c}\frac{2\pi d\sin\varphi}{\lambda_c}, f_c\right)\mathbf{f}_{\hat{i}}\right|^2 + \sigma_n^2}{\rho\left|\mathbf{a}_N^{\mathrm{H}}\left(\frac{f_{i^*}}{f_c}\frac{2\pi d\sin\varphi}{\lambda_c}, f_c\right)\mathbf{f}_{i^*}\right|^2 + \sigma_n^2}\right)d\varphi \\
&\overset{(b)}{=} \frac{1}{2\pi}\int_{-\pi}^{\pi}\sum_{\hat{i}\neq i^*}^{S}\frac{\rho\left|\mathbf{a}_N^{\mathrm{H}}\left(\frac{f_{\hat{i}}}{f_c}\frac{2\pi d\sin\varphi}{\lambda_c}, f_c\right)\mathbf{f}_{\hat{i}}\right|^2 + \sigma_n^2}{\rho\left|\mathbf{a}_N^{\mathrm{H}}\left(\frac{f_{\hat{i}}}{f_c}\frac{2\pi d\sin\varphi}{\lambda_c}, f_c\right)\mathbf{f}_{\hat{i}}\right|^2 + \rho\left|\mathbf{a}_N^{\mathrm{H}}\left(\frac{f_{i^*}}{f_c}\frac{2\pi d\sin\varphi}{\lambda_c}, f_c\right)\mathbf{f}_{i^*}\right|^2 + 2\sigma_n^2}d\varphi,
\end{aligned} \tag{5.64}$$

where (a) is from the fact that the ratio $\lambda_{i^*}/\lambda_{\hat{i}}$ of two chi-square random variables λ_i^* and $\lambda_{\hat{i}}$ is an F-distributed random variable and $F_{\text{cdf}}(x) = \Pr(X \leq x)$ is the cumulative distribution function (CDF) of F-distributed random variable X. Also, (b) is from $F_{\text{cdf}}(x) = \frac{x}{x+1}$ [91].

In Fig. 5.9, we plot the beam misalignment probability as a function of SNR. We

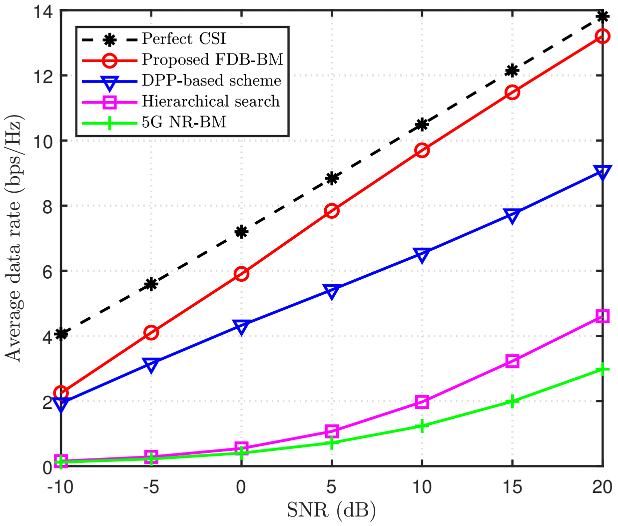

Figure 5.10: Average data rate vs. transmit SNR ($N = 256$, $L = 5$, $T = 16$, $P = 16$, and $S = 128$).

observe that the obtained analytic upper bound in (5.64) is close to the simulation result. We also observe that the beam misalignment probability of FDB is far smaller than that of the conventional DPP scheme. This is because FDB minimizes the sidelobe leakage of the subcarrier using the intensifier network so that the ratio of RSRPs of the misaligned beam and the optimal beams $\frac{\rho\left|\mathbf{a}_N^{\mathrm{H}}\left(\frac{f_{\hat{i}}}{f_c}\frac{2\pi d\sin\varphi}{\lambda_c},f_c\right)\mathbf{f}_{\hat{i}}\right|^2+\sigma_n^2}{\rho\left|\mathbf{a}_N^{\mathrm{H}}\left(\frac{f_{i*}}{f_c}\frac{2\pi d\sin\varphi}{\lambda_c},f_c\right)\mathbf{f}_{i*}\right|^2+\sigma_n^2}$ is much smaller than that of the conventional DPP scheme.

5.5 Simulation Results

5.5.1 Simulation Setup

In this section, we investigate the performance of the proposed FDB scheme. In our simulations, we consider THz MISO-OFDM systems where the BS equipped with $N = 256$ antennas serves a single-antenna mobile. The mobile is located randomly around the BS within the cell radius of $r = 100\,\mathrm{m}$. We use the wideband THz LoS

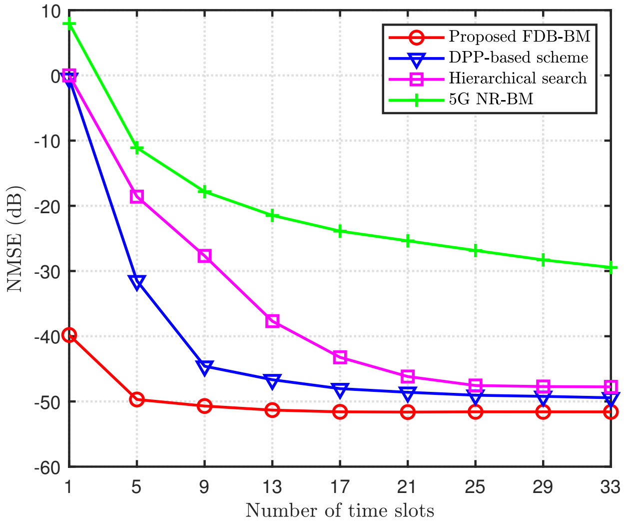

Figure 5.11: NMSE vs. the number of time slots ($N = 256$, $T = 16$, $P = 16$, and $S = 128$).

channel model where the carrier frequency is $f_c = 1\,\text{THz}$, the bandwidth is $B = 40\,\text{GHz}$, and the number of subcarriers is $S = 128$. The large-scale fading coefficients are modeled as $\rho = \text{PL} \times 10^{\frac{\sigma_{\text{sh}} z_{\text{sh}}}{10}}$ where PL represents the path loss and $10^{\frac{\sigma_{\text{sh}} z_{\text{sh}}}{10}}$ represents the shadow fading ($\sigma_{\text{sh}} = 4\,\text{dB}$ and $z_{\text{sh}} \sim \mathcal{CN}(0,1)$). We use the path loss model in 3GPP Rel. 16 [17]. The small-scale fading coefficients are generated according to the complex normal distribution (i.e. $\alpha_i \sim \mathcal{CN}(0,1)$). The number of time slots used for the beam management is $L = 5$. We set the transmit SNR to $20\,\text{dB}$. The numbers of TTDs used in the time delay network and the intensifier network are set to $T = P = \sqrt{N}$. As performance metrics, we use the average data rate defined as $R = \frac{1}{S}\sum_{i=1}^{S}\log_2\left(1 + \frac{P_t|\mathbf{h}_i^{\text{H}}\mathbf{f}_i|^2}{\sigma_n^2}\right)$ and the normalized mean square error (NMSE) defined as $\text{NMSE} = 10\log_{10}\left(\frac{1}{S}\sum_{i=1}^{S}\left(\frac{\phi_i - \hat{\phi}_i}{\phi_i}\right)^2\right)$. In each point of the plots, we test at least $100,000$ randomly generated wideband THz systems.

For comparison, we use four benchmark schemes: 1) ideal system with the perfect channel information, 2) DPP-based beam management scheme [82], 3) hierarchical

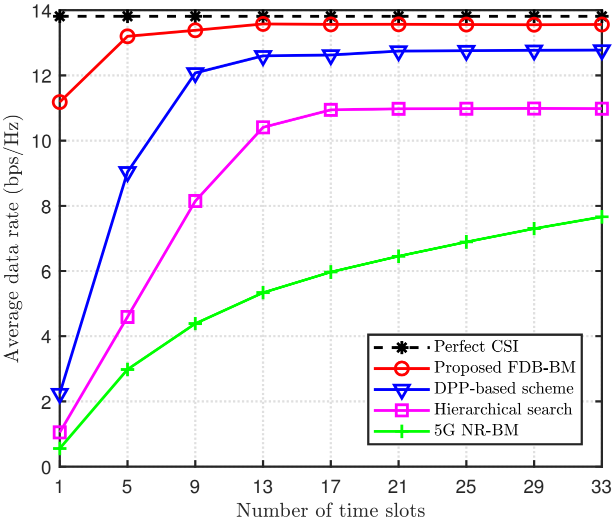

Figure 5.12: Average data rate vs. the number of time slots ($N = 256$, $T = 16$, $P = 16$, and $S = 128$).

beam management scheme generating the hierarchical beam codebook [76], and 4) 5G NR beam management scheme based on the beam sweeping process [74]. Note, to make a fair comparison between the DPP and FDB, the number of TTDs used for the DPP beam generation is set to be the same as the total number of TTDs used for the FDB beam generation ($T^{\text{dpp}} = T + P$).

5.5.2 Simulation Results

In Fig. 5.10, we plot the average data rate as a function of the transmit SNR. We observe that FDB outperforms the conventional beam management schemes by a large margin. For example, when SNR $= 10\,$dB, FDB achieves a significant rate gain (more than 390% data rate improvement) over the hierarchical beam management scheme. As mentioned, a phase shift of the conventional schemes relying on the analog phase shifters is invariant to the frequency so the beams for all subcarriers are all the same. However, the optimal beamforming vector maximizing the data rate is different for

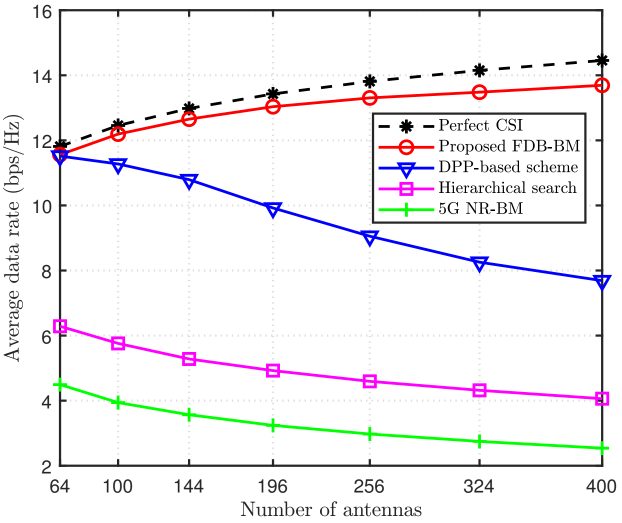

Figure 5.13: Average data rate vs. the number of antennas ($L = 5$, $T = P = \sqrt{N}$, and $S = 128$).

each subcarrier due to the beam squint effect. This mismatch between the optimal frequency-dependent beamforming vectors and the frequency-invariant beamforming vectors generated by the analog phase shifters causes a significant data rate loss in the conventional schemes. Whereas, in the proposed scheme, multiple frequency-dependent beams are generated using the TTD-based phase shifters so that the data rate loss caused by the beam squint effect can be effectively mitigated.

In Fig. 5.11, we set the transmit SNR to 20 dB and plot the NMSE as a function of the number of time slots L. We observe that FDB achieves significant NMSE gains over the conventional schemes. For example, when $L = 5$, FDB achieves more than 31.1 dB and 38.6 dB NMSE gains over the hierarchical beam management technique and the 5G NR beam management scheme. This is not quite a surprise since the conventional schemes search one direction at a time but FDB simultaneously searches $S = 128$ directions. Interestingly, as shown in Fig. 5.11, FDB can identify pretty accurate beam direction even in a single time slot. Even when compared to DPP, the NMSE gain

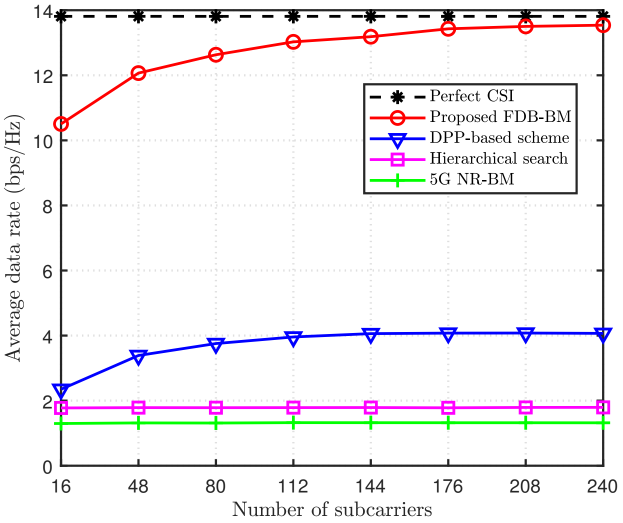

Figure 5.14: Average data rate vs. the number of subcarriers ($N = 256$, $L = 5$, $T = 16$, and $P = 16$).

of the FDB is more than 18 dB since the high sidelobe leakage of DPP will cause a degradation of the beam alignment performance but such is not the case for FDB due to the effective suppression of the sidelobe leakage at the intensifier network.

In Fig. 5.12, we plot the average data rate as a function of the number of time slots L. We observe that the proposed scheme achieves more than 70% reduction in the beam management latency over the conventional approaches. For instance, to achieve the average data rate of 13 bps/Hz, FDB requires only $L = 5$ time slots but DPP requires around $L = 17$ time slots. Since FDB can generate very sharp beams achieving the maximum beamforming gain, we also observe that when $L \geq 5$, FDB performs similar to the ideal system with the perfect CSI.

In Fig. 5.13, we plot the average data rate as a function of the number of transmit antennas N. Interestingly, we observe that the data rate gain of FDB over the conventional schemes increases with the number of antennas. For example, when $N = 100$, FDB shows around 0.9 bps/Hz data rate gain over DPP but it increases up to 6 bps/Hz when

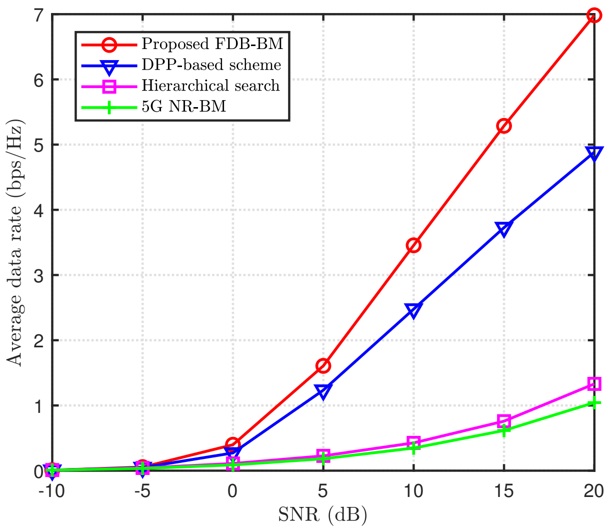

Figure 5.15: Average data rate vs. transmit SNR in the multipath scenario ($N = 256$, $L = 5$, $T = 16$, $P = 16$, $S = 128$, $N_{\text{path}} = 3$, and $\kappa = 100$).

$N = 400$. This is because when the number of antennas increases, the number of analog phase shifters connected to TTD also increases so that the loss of the beamforming gain caused by the mismatch between the DPP beam and the directional beam also increases (see (5.21)-(5.24)). In contrast, the beamwidth of FDB beams is inversely proportional to the number of antennas so the beam direction accuracy increases with the number of antennas. This implies that FDB would be more effective in the THz ultra-massive MIMO systems where the number of antennas is extremely large.

In Fig. 5.14, we set the number of time slots to $L = 2$ and plot the average data rate as a function of the number of subcarriers S. We observe that the performance gain of FDB increases with the number of subcarriers. Specifically, when the number of subcarriers increases from $S = 16$ to $S = 240$, the data rate gain of FDB over the conventional DPP-based scheme increases from 7.1 bps/Hz to 9.5 bps/Hz. This is because FDB hierarchically finds out the beam direction so that the beam direction accuracy increases exponentially with the number of subcarrier beams. Whereas, DPP

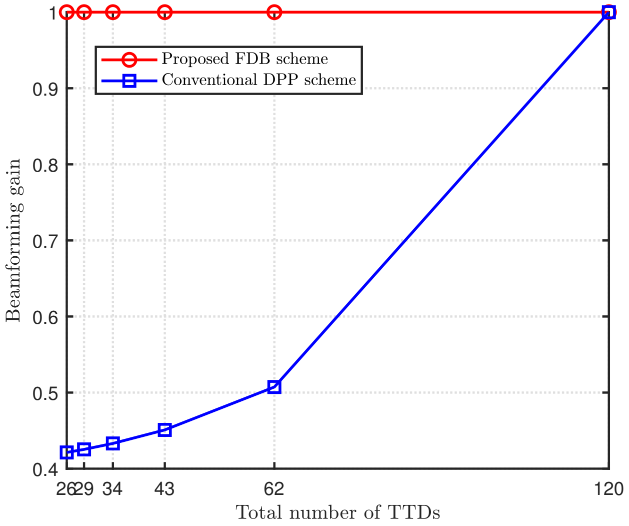

Figure 5.16: Beamforming gains of FDB and DPP vs. total number of TTDs ($N = 120$).

uniformly splits the probing area and then sequentially searches the divided areas so that the beam direction accuracy increases linearly with the number of subcarrier beams.

In Fig. 5.15, we plot the average data rate as a function of the transmit SNR in the multipath scenario where the number of propagation paths is $N_{\text{path}} = 3$. In this figure, we set the Rician K-factor[8] as $\kappa = 100$. We observe the proposed FDB scheme works well even in the multipath scenarios. For example, when SNR $= 20\,$dB, FDB achieves more than 40% data rate improvement over DPP.

In Fig. 15, we set $N = 120$ and plot the beamforming gains $G_i^{\text{-5-fig4}}$ and G_i^{dpp} as functions of the total number of TTDs $T + P$ for various (T, P) satisfying $TP = N$. To make a fair comparison between FDB and DPP, we use the same number of TTDs at FDB and DPP (i.e., $T^{\text{-5-fig4}} = T^{\text{dpp}} = T + P$). We observe that FDB outperforms DPP for every point under test. This is because FDB can achieve the maximum beamforming gain whenever (T, P) satisfies $TP = N$ but DPP can achieve the same performance

---

[8] The Rician K-factor denotes the ratio of the power of LoS path over the sum of powers of non-line-of-sight (NLoS) paths. In our work, we set $\kappa = 100$ so that the power of Los path is $20\,$dB larger than the sum of powers of all NLoS paths [2]

only when $T^{\text{dpp}} = N$.

5.6 Summary

In this chapter, we proposed a THz beam management scheme that simultaneously generates multiple frequency-dependent beams using the TTD-based phase shifters. By employing the generated FDB beams as the training beams, the proposed technique can search multiple directions simultaneously, thereby reducing the beam management latency. Intriguing feature of the proposed FDB is to exploit a deliberately designed TTD-based signal propagation network called intensifier to bridge the gap between the desired beamforming vectors and the frequency-dependent beamforming vectors. In doing so, RSRP of the beam aligned with the channel propagation path gets larger while those of the misaligned beams get smaller, resulting in a significant improvement of the beam direction accuracy. From the beam misalignment probability analysis and the numerical evaluations on 6G THz environment, we demonstrated that FDB is very effective in improving the beam direction accuracy and also reducing the beam management latency. In our work, we restricted our attention to THz communications, but there are many interesting applications of FDB including vehicle-to-everything (V2X) communications and reconfigurable intelligent surface (RIS)-assisted communications.

5.7 Proofs

5.7.1 Proof of Lemma 2

Using the fact that $\phi_{\hat{i}^{(0)}}$ is closest to ϕ, we obtain

$$f_{\hat{i}^{(0)}}(\phi - \phi_{\hat{i}^{(0)}}) \leq f_{\hat{i}^{(0)}+1}(\phi_{\hat{i}^{(0)}+1} - \phi). \tag{5.65}$$

Thus, the upper bound of ϕ is

$$\phi \leq \frac{f_{\hat{i}^{(0)}}\phi_{\hat{i}^{(0)}} + f_{\hat{i}^{(0)}+1}\phi_{\hat{i}^{(0)}+1}}{f_{\hat{i}^{(0)}} + f_{\hat{i}^{(0)}+1}} \overset{(a)}{=} \frac{\gamma_{\hat{i}^{(0)}+1}\phi_{\hat{i}^{(0)}} + \gamma_{\hat{i}^{(0)}}\phi_{\hat{i}^{(0)}+1}}{\gamma_{\hat{i}^{(0)}} + \gamma_{\hat{i}^{(0)}+1}}, \tag{5.66}$$

where (a) is from $\gamma_i = \frac{f_c}{f_i}$. Similarly, the lower bound of ϕ is

$$\phi \geq \frac{\gamma_{\hat{i}^{(0)}-1}\phi_{\hat{i}^{(0)}} + \gamma_{\hat{i}^{(0)}}\phi_{\hat{i}^{(0)}-1}}{\gamma_{\hat{i}^{(0)}} + \gamma_{\hat{i}^{(0)}-1}}. \tag{5.67}$$

Combining (5.66) and (5.67), we have

$$\frac{\gamma_{\hat{i}^{(0)}-1}\phi_{\hat{i}^{(0)}} + \gamma_{\hat{i}^{(0)}}\phi_{\hat{i}^{(0)}-1}}{\gamma_{\hat{i}^{(0)}} + \gamma_{\hat{i}^{(0)}-1}} \leq \phi \leq \frac{\gamma_{\hat{i}^{(0)}+1}\phi_{\hat{i}^{(0)}} + \gamma_{\hat{i}^{(0)}}\phi_{\hat{i}^{(0)}+1}}{\gamma_{\hat{i}^{(0)}} + \gamma_{\hat{i}^{(0)}+1}}. \tag{5.68}$$

Chapter 6

Conclusion

In this dissertation, THz channel acquisition schemes for 6G have been extensively studied. Specifically, we have made the following contributions.

- In Chapter 2, we proposed a novel feedback reduction technique for FDD-based cell-free systems. The key feature of the proposed scheme is to choose a few dominating paths among all possible propagation paths and then feed back the PGI of the chosen paths. Key observations in our work are that 1) the spatial domain channel is represented by a small number of multi-path components (AoDs and path gains) and 2) the AoDs are quite similar in the uplink and downlink channel owing to the angle reciprocity so that the BSs can acquire AoD information directly from the uplink pilot signal. Thus, by choosing a few dominating paths and only feed back the path gain of the chosen paths, we can achieve a significant reduction in the feedback overhead. We observed from the extensive simulations that the proposed scheme can achieve more than 60% of feedback overhead reduction over the conventional schemes relying on the CSI feedback.

- In Chapter 3, we proposed an efficient channel estimation framework to reduce the pilot overhead of RIS-aided mmWave systems. Key idea of the proposed

TAD-CE scheme is to decompose the RIS reflected channel into three major components, i.e., static BS-RIS angles, quasi-static RIS-UE angles, and time-varying BS-RIS-UE path gains, and then estimate these components in different time scales. In doing so, the number of channel parameters to be estimated at each stage can be reduced significantly, resulting in a reduction of pilot overhead. Also, by optimizing the RIS phase shifts using the channel components with relatively long coherence time, we could further improve the channel estimation accuracy without requiring additional pilot resources. We demonstrated from the channel estimation error and pilot overhead analyses and numerical evaluations that the proposed TAD-CE scheme is effective in saving the pilot resources. In our work, we assumed the ideal phase shift model where the reflection amplitude and the phase shifts are independent, but an extension to the realistic scenarios where the reflection is imperfect and is affected by the RIS phase shifts would be an interesting future work worth pursuing.

- In Chapter 4, we proposed a DL-based channel acquisition technique for the THz UM-MIMO systems. In recent years, a remarkable success of DL in various disciplines (e.g., image classification, speech recognition, and language translation) has stimulated increasing interest in applying this paradigm to wireless communication systems. Intriguing feature of the proposed T-PCA is to promote the nonuniform and irregular correlation structures of the received pilot signals using Transformer, a DL architecture that differently weights each input data based on the correlations between the input data. By exploiting the attention mechanism of Transformer, T-PCA can facilitate the extraction of spatially and temporally-correlated features inherent in the THz UM-MIMO systems. In doing so, fast yet accurate channel parameter estimation can be made with small pilot overhead. From the simulation results, we demonstrated that T-PCA achieves more than $2.5\,\mathrm{dB}$ NMSE gain and 33% pilot overhead reduction over the conventional channel acquisition techniques. In our work, we restricted our attention to channel estimation, but there are many interesting applications of T-PCA such as channel feedback, beam tracking, and resource allocation.

- In Chapter 5, we proposed a THz beam management scheme that simultaneously generates multiple frequency-dependent beams using the TTD-based phase shifters. By employing the generated FDB beams as the training beams, the proposed technique can search multiple directions simultaneously, thereby reducing the beam management latency. Intriguing feature of the proposed FDB is to exploit a deliberately designed TTD-based signal propagation network called intensifier to bridge the gap between the desired beamforming vectors and the frequency-dependent beamforming vectors. In doing so, RSRP of the beam aligned with the channel propagation path gets larger while those of the misaligned beams get smaller, resulting in a significant improvement of the beam direction accuracy. From the beam misalignment probability analysis and the numerical evaluations on 6G THz environment, we demonstrated that FDB is very effective in improving the beam direction accuracy and also reducing the beam management latency. In our work, we restricted our attention to THz communications, but there are many interesting applications of FDB including vehicle-to-everything (V2X) communications and reconfigurable intelligent surface (RIS)-assisted communications.

Bibliography

[1] Z. Chen, X. Ma, B. Zhang, Y. Zhang, Z. Niu, N. Kuang, W. Chen, L. Li, and S. Li, "A survey on terahertz communications," *China Commun.*, vol. 16, no. 2, pp. 1–35, 2019.

[2] C. Han, Y. Wang, Y. Li, Y. Chen, N. A. Abbasi, T. Kürner, and A. F. Molisch, "Terahertz wireless channels: A holistic survey on measurement, modeling, and analysis," *IEEE Commun. Surveys Tuts.*, vol. 24, no. 3, pp. 1670–1707, 2022.

[3] M. Cui and L. Dai, "Channel estimation for extremely large-scale MIMO: Far-field or near-field?" *IEEE Trans. Commun.*, vol. 70, no. 4, pp. 2663–2677, 2022.

[4] M. Series, "IMT Vision–Framework and overall objectives of the future development of IMT for 2020 and beyond," *Recommendation ITU*, pp. 2083–0, 2015.

[5] H. Q. Ngo, A. Ashikhmin, H. Yang, E. G. Larsson, and T. L. Marzetta, "Cell-free massive MIMO versus small cells," *IEEE Trans. Wireless Commun.*, vol. 16, no. 3, pp. 1834–1850, 2017.

[6] B. Lee, J. Choi, J.-Y. Seol, D. J. Love, and B. Shim, "Antenna grouping based feedback compression for FDD-based massive MIMO systems," *IEEE Trans. on Commun.*, vol. 63, no. 9, pp. 3261–3274, 2015.

[7] W. Shen, L. Dai, Y. Shi, B. Shim, and Z. Wang, "Joint Channel Training and Feedback for FDD Massive MIMO Systems," *IEEE Trans. Veh. Technol.*, vol. 65, no. 10, pp. 8762–8767, 2016.

[8] E. Nayebi, A. Ashikhmin, T. L. Marzetta, H. Yang, and B. D. Rao, “Precoding and power optimization in cell-free massive MIMO systems,” *IEEE Trans. Wireless Commun.*, vol. 16, no. 7, pp. 4445–4459, 2017.

[9] H. Q. Ngo, L.-N. Tran, T. Q. Duong, M. Matthaiou, and E. G. Larsson, “On the total energy efficiency of cell-free massive MIMO,” *IEEE Trans. Green Commun. Netw.*, vol. 2, no. 1, pp. 25–39, 2018.

[10] J. Jose, A. Ashikhmin, T. L. Marzetta, and S. Vishwanath, “Pilot contamination and precoding in multi-cell TDD systems,” *IEEE Trans. Wireless Commun.*, vol. 10, no. 8, pp. 2640–2651, 2011.

[11] N. Jindal, “MIMO broadcast channels with finite rate feedback,” *IEEE Trans. Inf. Theory*, vol. 52, no. 11, pp. 5045–5059, 2006.

[12] R. B. Ertel, P. Cardieri, K. W. Sowerby, T. S. Rappaport, and J. H. Reed, “Overview of spatial channel models for antenna array communication systems,” *IEEE Personal Commun.*, vol. 5, no. 1, pp. 10–22, 1998.

[13] H. Xie, F. Gao, and S. Jin, “An overview of low-rank channel estimation for massive MIMO systems,” *IEEE Access*, vol. 4, pp. 7313–7321, 2016.

[14] D. Tse and P. Viswanath, *Fundamentals of Wireless Communication*. Cambridge university press, 2005.

[15] W. Shen, L. Dai, B. Shim, Z. Wang, and R. W. Heath, “Channel feedback based on AoD-adaptive subspace codebook in FDD massive MIMO systems,” *IEEE Trans. on Commun.*, vol. 66, no. 11, pp. 5235–5248, 2018.

[16] T. S. Rappaport, S. Sun, R. Mayzus, H. Zhao, Y. Azar, K. Wang, G. N. Wong, J. K. Schulz, M. Samimi, and F. Gutierrez Jr, “Millimeter wave mobile communications for 5G cellular: It will work!” *IEEE Access*, vol. 1, no. 1, pp. 335–349, 2013.

[17] "Study on channel model for frequencies from 0.5 to 100 GHz," *3GPP TR, 38.901, V16.1.0*, 2020.

[18] Q. Zhang, S. Jin, M. McKay, D. Morales-Jimenez, and H. Zhu, "Power allocation schemes for multicell massive MIMO systems," *IEEE Trans. Wireless Commun.*, vol. 14, no. 11, pp. 5941–5955, 2015.

[19] P. Series, "Propagation data and prediction methods for the planning of indoor radiocommunication systems and radio local area networks in the frequency range 900 MHz to 100 GHz," *Recommendation ITU-R*, pp. 1238–7, 2012.

[20] R. Schmidt, "Multiple emitter location and signal parameter estimation," *IEEE Trans. Antennas. Propagat.*, vol. 34, no. 3, pp. 276–280, 1986.

[21] R. Roy and T. Kailath, "ESPRIT-estimation of signal parameters via rotational invariance techniques," *IEEE Trans. Acoust. Speech. Signal. Process.*, vol. 37, no. 7, pp. 984–995, 1989.

[22] J. Capon, "High-resolution frequency-wavenumber spectrum analysis," *Proceedings of the IEEE*, vol. 57, no. 8, pp. 1408–1418, 1969.

[23] P. Stoica and K. C. Sharman, "Maximum likelihood methods for direction-of-arrival estimation," *IEEE Trans. Acoust. Speech. Signal. Process.*, vol. 38, no. 7, pp. 1132–1143, 1990.

[24] M. Sadek, A. Tarighat, and A. H. Sayed, "A leakage-based precoding scheme for downlink multi-user MIMO channels," *IEEE Trans. Wireless Commun.*, vol. 6, no. 5, 2007.

[25] E. Bjornson, R. Zakhour, D. Gesbert, and B. Ottersten, "Cooperative multicell precoding: Rate region characterization and distributed strategies with instantaneous and statistical CSI," *IEEE Trans. Sig. Proc.*, vol. 58, no. 8, pp. 4298–4310, 2010.

[26] C. Lim, T. Yoo, B. Clerckx, B. Lee, and B. Shim, “Recent trend of multiuser MIMO in LTE-advanced,” *IEEE Commun. Mag.*, vol. 51, no. 3, pp. 127–135, 2013.

[27] J. Choi, D. J. Love, and P. Bidigare, “Downlink training techniques for FDD massive MIMO systems: Open-loop and closed-loop training with memory,” *IEEE J. Sel. Topics Signal Process*, vol. 8, no. 5, pp. 802–814, 2014.

[28] R. Zhang and L. Hanzo, “Joint and distributed linear precoding for centralised and decentralised multicell processing,” in *2010 IEEE 72nd Vehicular Technology Conference-Fall.* IEEE, 2010, pp. 1–5.

[29] J. Wu, S. Kim, and B. Shim, “Energy-Efficient Power Control and Beamforming for Reconfigurable Intelligent Surface-Aided Uplink IoT Networks,” *IEEE Trans. Wireless Commun.*, vol. 21, no. 12, pp. 10 162–10 176, 2022.

[30] E. M. Mohamed, S. Hashima, N. Anjum, K. Hatano, W. E. Shafai, and B. M. Elhalawany, “Reconfigurable intelligent surface-aided millimetre wave communications utilizing two-phase minimax optimal stochastic strategy bandit,” *IET Commun.*, vol. 16, no. 18, pp. 2200–2207, 2022.

[31] E. M. Mohamed, S. Hashima, K. Hatano, and S. A. Aldossari, “Two-stage multi-armed bandit for reconfigurable intelligent surface aided millimeter wave communications,” *Sensors*, vol. 22, no. 6, p. 2179, 2022.

[32] Y. Yang, B. Zheng, S. Zhang, and R. Zhang, “Intelligent reflecting surface meets OFDM: Protocol design and rate maximization,” *IEEE Trans. Commun.*, vol. 68, no. 7, pp. 4522–4535, 2020.

[33] H. Alwazani, A. Kammoun, A. Chaaban, M. Debbah, M.-S. Alouini *et al.*, “Intelligent reflecting surface-assisted multi-user MISO communication: Channel estimation and beamforming design,” *IEEE Open J. Commun. Soc.*, vol. 1, pp. 661–680, 2020.

[34] G. T. de Araújo, A. L. De Almeida, and R. Boyer, "Channel estimation for intelligent reflecting surface assisted MIMO systems: A tensor modeling approach," *IEEE J. Sel. Topics Signal Process.*, vol. 15, no. 3, pp. 789–802, 2021.

[35] C. Hu, L. Dai, S. Han, and X. Wang, "Two-timescale channel estimation for reconfigurable intelligent surface aided wireless communications," *IEEE Trans. Commun.*, vol. 69, no. 11, pp. 7736–7747, 2021.

[36] P. Wang, J. Fang, H. Duan, and H. Li, "Compressed channel estimation for intelligent reflecting surface-assisted millimeter wave systems," *IEEE Sig. Process. Lett.*, vol. 27, pp. 905–909, 2020.

[37] X. Wei, D. Shen, and L. Dai, "Channel estimation for RIS assisted wireless communications—Part II: An improved solution based on double-structured sparsity," *IEEE Commun. Lett.*, vol. 25, no. 5, pp. 1403–1407, 2021.

[38] Z.-Q. He and X. Yuan, "Cascaded channel estimation for large intelligent metasurface assisted massive MIMO," *IEEE Wireless Commun. Lett.*, vol. 9, no. 2, pp. 210–214, 2019.

[39] T. Lin, X. Yu, Y. Zhu, and R. Schober, "Channel estimation for IRS-assisted millimeter-wave MIMO systems: Sparsity-inspired approaches," *IEEE Trans. Commun.*, 2022.

[40] V. Va, J. Choi, and R. W. Heath, "The impact of beamwidth on temporal channel variation in vehicular channels and its implications," *IEEE Transactions on Vehicular Technology*, vol. 66, no. 6, pp. 5014–5029, 2017.

[41] S. Kim, J. W. Choi, and B. Shim, "Downlink pilot precoding and compressed channel feedback for FDD-based cell-free systems," *IEEE Trans. Wireless Commun.*, vol. 19, no. 6, pp. 3658–3672, 2020.

[42] Q. Wu, S. Zhang, B. Zheng, C. You, and R. Zhang, “Intelligent reflecting surface aided wireless communications: A tutorial,” *IEEE Trans. Commun.*, 2021.

[43] G. Zhou, C. Pan, H. Ren, P. Popovski, and A. L. Swindlehurst, “Channel estimation for RIS-aided multiuser millimeter-wave systems,” *IEEE Trans. Signal Process.*, vol. 70, pp. 1478–1492, 2022.

[44] A. L. Swindlehurst, G. Zhou, R. Liu, C. Pan, and M. Li, “Channel estimation with reconfigurable intelligent surfaces—A general framework,” *Proc. IEEE*, vol. 110, no. 9, pp. 1312–1338, 2022.

[45] J. W. Choi, B. Shim, Y. Ding, B. Rao, and D. I. Kim, “Compressed sensing for wireless communications: Useful tips and tricks,” *IEEE Commun. Surveys Tuts.*, vol. 19, no. 3, pp. 1527–1550, 2017.

[46] R. Ward, “Compressed sensing with cross validation,” *IEEE Trans. Inf. Theory*, vol. 55, no. 12, pp. 5773–5782, 2009.

[47] S. Boyd and L. Vandenberghe, *Convex optimization*. Cambridge university press, 2004.

[48] Y. Nesterov and A. Nemirovskii, *Interior-point polynomial algorithms in convex programming*. SIAM, 1994.

[49] S. M. Kay, *Fundamentals of statistical signal processing: estimation theory*. Prentice-Hall, Inc., 1993.

[50] A. Maleki and D. L. Donoho, “Optimally tuned iterative reconstruction algorithms for compressed sensing,” *IEEE J. Sel. Topics Signal Process.*, vol. 4, no. 2, pp. 330–341, 2010.

[51] T. Lin, X. Yu, Y. Zhu, and R. Schober, “Channel estimation for intelligent reflecting surface-assisted millimeter wave MIMO systems,” in *Proc. IEEE Global Commun. Conf. (GLOBECOM)*, 2020, pp. 1–6.

[52] X. Wei and L. Dai, "Channel estimation for extremely large-scale massive MIMO: far-field, near-field, or hybrid-field?" *IEEE Commun. Lett.*, vol. 26, no. 1, pp. 177–181, 2022.

[53] A. Guerra, F. Guidi, D. Dardari, and P. M. Djurić, "Near-field tracking with large antenna arrays: Fundamental limits and practical algorithms," *IEEE Trans. Sig. Process.*, vol. 69, pp. 5723–5738, 2021.

[54] X. Zhang, H. Zhang, and Y. C. Eldar, "Near-field sparse channel representation and estimation in 6G wireless communications," *arXiv preprint arXiv:2212.13527*, 2022.

[55] K. Dovelos, M. Matthaiou, H. Q. Ngo, and B. Bellalta, "Channel estimation and hybrid combining for wideband terahertz massive MIMO systems," *IEEE J. Sel. Areas Commun.*, vol. 39, no. 6, pp. 1604–1620, 2021.

[56] J. Wu, S. Kim, and B. Shim, "Parametric Sparse Channel Estimation for RIS Assisted Terahertz Systems," *to appear in IEEE Trans. Commun.*, 2022.

[57] H. Huang, J. Yang, H. Huang, Y. Song, and G. Gui, "Deep learning for super-resolution channel estimation and DoA estimation based massive MIMO system," *IEEE Trans. Veh. Technol.*, vol. 67, no. 9, pp. 8549–8560, 2018.

[58] J. Kim, Y. Ahn, S. Kim, and B. Shim, "Parametric sparse channel estimation using long short-term memory for mmwave massive MIMO systems," in *Proc. IEEE Int. Conf. Commun. (ICC)*, 2022, pp. 1397–1402.

[59] S. Bhattacharya and A. K. Gupta, "Deep learning for THz channel estimation and beamforming prediction via sub-6GHz channel," in *Proc. IEEE Int. Conf. Sig. Process Commun. (SPCOM)*, 2022, pp. 1–5.

[60] A. Vaswani, N. Shazeer, N. Parmar, J. Uszkoreit, L. Jones, A. N. Gomez, Ł. Kaiser, and I. Polosukhin, "Attention is all you need," *Adv Neural Inf Process Syst*, vol. 30, 2017.

[61] L. You, X. Gao, G. Y. Li, X.-G. Xia, and N. Ma, "BDMA for millimeter-wave/terahertz massive MIMO transmission with per-beam synchronization," *IEEE J. Sel. Areas Commun.*, vol. 35, no. 7, pp. 1550–1563, 2017.

[62] J. Vieira, F. Rusek, O. Edfors, S. Malkowsky, L. Liu, and F. Tufvesson, "Reciprocity calibration for massive MIMO: Proposal, modeling, and validation," *IEEE Trans. Wireless Commun.*, vol. 16, no. 5, pp. 3042–3056, 2017.

[63] A. Dosovitskiy, L. Beyer, A. Kolesnikov, D. Weissenborn, X. Zhai, T. Unterthiner, M. Dehghani, M. Minderer, G. Heigold, S. Gelly *et al.*, "An image is worth 16x16 words: Transformers for image recognition at scale," *arXiv preprint arXiv:2010.11929*, 2020.

[64] H. Do, S. Cho, J. Park, H.-J. Song, N. Lee, and A. Lozano, "Terahertz line-of-sight MIMO communication: Theory and practical challenges," *IEEE Commun. Mag.*, vol. 59, no. 3, pp. 104–109, 2021.

[65] Z. Zhang, Y. Xiao, Z. Ma, M. Xiao, Z. Ding, X. Lei, G. K. Karagiannidis, and P. Fan, "6G wireless networks: Vision, requirements, architecture, and key technologies," *IEEE Veh. Technol. Mag.*, vol. 14, no. 3, pp. 28–41, 2019.

[66] M. Giordani, M. Polese, M. Mezzavilla, S. Rangan, and M. Zorzi, "Toward 6G networks: Use cases and technologies," *IEEE Commun. Mag.*, vol. 58, no. 3, pp. 55–61, 2020.

[67] I. F. Akyildiz, C. Han, Z. Hu, S. Nie, and J. M. Jornet, "Terahertz band communication: An old problem revisited and research directions for the next decade," *IEEE Trans. Commun.*, vol. 70, no. 6, pp. 4250–4285, 2022.

[68] I. F. Akyildiz, J. M. Jornet, and C. Han, “TeraNets: Ultra-broadband communication networks in the terahertz band,” *IEEE Wireless Commun.*, vol. 21, no. 4, pp. 130–135, 2014.

[69] C. Han and Y. Chen, “Propagation modeling for wireless communications in the terahertz band,” *IEEE Commun. Mag.*, vol. 56, no. 6, pp. 96–101, 2018.

[70] H. Ji, Y. Kim, J. Lee, E. Onggosanusi, Y. Nam, J. Zhang, B. Lee, and B. Shim, “Overview of full-dimension MIMO in LTE-advanced pro,” *IEEE Commun. Mag.*, vol. 55, no. 2, pp. 176–184, 2016.

[71] S. Kim, J. Son, and B. Shim, “Energy-efficient ultra-dense network using LSTM-based deep neural networks,” *IEEE Trans. Wireless Commun.*, vol. 20, no. 7, pp. 4702–4715, 2021.

[72] Y.-N. R. Li, B. Gao, X. Zhang, and K. Huang, “Beam management in millimeter-wave communications for 5G and beyond,” *IEEE Access*, vol. 8, pp. 13 282–13 293, 2020.

[73] Y. Ahn, J. Kim, S. Kim, K. Shim, J. Kim, S. Kim, and B. Shim, “Towards intelligent millimeter and terahertz communication for 6G: Computer vision-aided beamforming,” *IEEE Wireless Commun.*, 2023.

[74] M. Giordani, M. Polese, A. Roy, D. Castor, and M. Zorzi, “A tutorial on beam management for 3GPP NR at mmWave frequencies,” *IEEE Commun. Surv. Tuts.*, vol. 21, no. 1, pp. 173–196, 2018.

[75] A. Alkhateeb, O. El Ayach, G. Leus, and R. W. Heath, “Channel estimation and hybrid precoding for millimeter wave cellular systems,” *IEEE J. Sel. Topics Sig. Process.*, vol. 8, no. 5, pp. 831–846, 2014.

[76] Z. Xiao, T. He, P. Xia, and X.-G. Xia, “Hierarchical codebook design for beamforming training in millimeter-wave communication,” *IEEE Trans. Wireless Commun.*, vol. 15, no. 5, pp. 3380–3392, 2016.

[77] C. Lin, G. Y. Li, and L. Wang, “Subarray-based coordinated beamforming training for mmWave and sub-THz communications,” *IEEE J. Sel. Areas Commun.*, vol. 35, no. 9, pp. 2115–2126, 2017.

[78] B. Ning, T. Wang, C. Huang, Y. Zhang, and Z. Chen, “Wide-beam designs for terahertz massive MIMO: SCA-ATP and S-SARV,” *IEEE Internet Things J.*, 2023.

[79] X. Gao, L. Dai, Y. Zhang, T. Xie, X. Dai, and Z. Wang, “Fast channel tracking for terahertz beamspace massive MIMO systems,” *IEEE Trans. Veh. Technol.*, vol. 66, no. 7, pp. 5689–5696, 2016.

[80] Z. Ding and H. V. Poor, “Joint Beam Management and Power Allocation in THz-NOMA Networks,” *to appear in IEEE Trans. Commun.*, 2023.

[81] V. Boljanovic, H. Yan, E. Ghaderi, D. Heo, S. Gupta, and D. Cabric, “Design of millimeter-wave single-shot beam training for true-time-delay array,” in *Proc. IEEE 21st Int. Workshops Sig. Process. Adv. Wireless Commun. (SPAWC)*, May 2020.

[82] J. Tan and L. Dai, “Wideband beam tracking in THz massive MIMO systems,” *IEEE J. Sel. Areas Commun.*, vol. 39, no. 6, pp. 1693–1710, 2021.

[83] L. Dai, J. Tan, Z. Chen, and H. V. Poor, “Delay-phase precoding for wideband THz massive MIMO,” *IEEE Trans. Wireless Commun.*, 2022.

[84] Y. Wu, G. Song, H. Liu, L. Xiao, and T. Jiang, “3-D Hybrid Beamforming for Terahertz Broadband Communication System With Beam Squint,” *IEEE Trans. Broadcast.*, vol. 69, no. 1, pp. 264–275, 2023.

[85] H. Hashemi, T.-S. Chu, and J. Roderick, "Integrated true-time-delay-based ultra-wideband array processing," *IEEE Commun. Mag.*, vol. 46, no. 9, pp. 162–172, 2008.

[86] A. Faisal, H. Sarieddeen, H. Dahrouj, T. Y. Al-Naffouri, and M.-S. Alouini, "Ultramassive MIMO systems at terahertz bands: Prospects and challenges," *IEEE Veh. Technol. Mag.*, vol. 15, no. 4, pp. 33–42, 2020.

[87] J. Wu, S. Kim, and B. Shim, "Parametric Sparse Channel Estimation for RIS-Assisted Terahertz Systems," *submitted to IEEE Trans. Commun.*, 2023.

[88] B. Zhai, A. Tang, C. Peng, and X. Wang, "SS-OFDMA: Spatial-spread orthogonal frequency division multiple access for terahertz networks," *IEEE J. Sel. Areas Commun.*, vol. 39, no. 6, pp. 1678–1692, 2021.

[89] 3GPP, "Study on New Radio (NR) Access Technology - Physical Layer Aspects - Release 14," 3rd Generation Partnership Project (3GPP), TR 38.802, 2017.

[90] P. Diananda and M. Bartlett, "Some probability limit theorems with statistical applications," in *Proc. Cambridge Philos. Soc.*, vol. 49, no. 2. Cambridge University Press, 1953, pp. 239–246.

[91] W. Wells, R. Anderson, and J. W. Cell, "The distribution of the product of two central or non-central chi-square variates," *Ann. Math. Statist.*, vol. 33, no. 3, pp. 1016–1020, 1962.

초록

최근 테라헤르츠 통신은 스펙트럼 병목 현상을 완화하고 6G 무선 통신을 위한 높은 데이터 속도를 지원하기 위해 많은 관심을 받고 있다. 테라헤르츠 주파수 대역의 풍부한 스펙트럼 자원을 이용하여 THz 통신은 디지털 트윈, XR 장치가 실현하는 메타버스, 고충실도 모바일 홀로그래픽 디스플레이와 같은 몰입형 모바일 서비스를 지원할 수 있다. 테라헤르츠 통신의 잘 알려진 단점은 높은 회절 및 침투 손실과 대기 흡수로 인한 신호 전력의 심각한 감쇠이다. 이 문제를 해결하기 위해 대규모 다중입출력 시스템으로 실현된 빔포밍 기법이 널리 사용되었다. 빔 형성 이득은 빔이 신호 전파 경로와 적절하게 정렬되어야만 최대화되므로, 기지국은 정확한 채널 정보를 획득해야 한다.

논문의 첫 번째 부분에서, 우리는 주파수 분할 이중화 기반 셀 프리 밀리미터 및 테라헤르츠 시스템에 대한 채널 피드백 기술을 연구한다. 기지국 그룹이 사용자에게 협력적으로 서비스를 제공하는 셀 프리 시스템은 미래 무선 시스템의 유망한 기술로 많은 관심을 받아왔다. 셀 프리 시스템에서 협력 이득을 극대화하려면 BS에서 다운링크 채널 상태 정보를 획득하는 것이 중요하다. 이 작업은 채널 상호성으로 인해 시간 분할 이중화 시스템에서는 비교적 쉬운 반면, 채널 피드백 오버헤드로 인해 주파수 분할 이중화 시스템에서는 쉽지 않다. 사용자가 여러 기지국의 채널정보를 피드백해야 하기 때문에 이 문제는 셀이 없는 시스템에서 훨씬 더 두드러진다. 본 연구에서는 주파수 분할 이중화 기반 셀프리 시스템에 대한 새로운 피드백 감소 기술을 제안한다. 제안된 기술의 주요 특징은 몇 가지 지배적인 경로를 선택한 다음 선택한 경로의 경로 이득 정보를 피드백하는 것이다. 출발 각도가 업링크 및 다운링크 채널에서 상당히 유사하다는 특성(이 특성을 각도 상호성이라고 함)을 이용하여

BS는 업링크 파일럿 신호로부터 직접 출발 각도를 얻는다.

논문의 두 번째 부분에서, 우리는 재구성 가능한 지능형 반사평면 기반 테라헤르츠 시스템을 위한 채널 추정 기술을 연구한다. 최근, 입사 신호의 반사 특성을 제어하는 지능형 반사평면이 큰 주목을 받고 있다. 지능형 반사평면 지원 시스템을 최대한 활용하려면 기지국에서 채널 정보를 획득하는 것이 중요하다. 그러나 많은 반사 요소에 의해 유도되는 파일럿 오버헤드 때문에 이 작업은 결코 쉽지 않다. 본 연구에서는 지능형 반사평면 기반 밀리미터 시스템의 파일럿 오버헤드를 줄이는 효율적인 채널 추정 및 위상 편이 제어 기술을 제안한다. 제안된 체계의 핵심 아이디어는 지능형 반사평먼의 반사 채널을 정적 기지국-지능형 반사평면 각도, 준정적 지능형 반사평면-단말 각도 및 시간 변동 기지국-지능형 반사평면-단말 경로 이득의 세 가지 주요 구성 요소로 분해한 다음 다른 시간 척도로 추정하는 것이다. 제안된 체계는 기지국-지능형 반사평면 및 지능형 반사평면-단말 각도를 가끔 추정하고 경로 이득만 자주 추정함으로써 파일럿 오버헤드를 크게 감소시킨다. 또한, 비교적 긴 일관성 시간을 가진 채널 구성 요소를 사용하여 위상 이동을 최적화함으로써 채널 추정 정확도를 향상시킬 수 있다.

논문의 세 번째 부분에서는 시분할 이중화 기반 테라헤르츠 초거대 다중입출력 시스템에 대한 채널 추정 기법을 연구한다. 초거대 다중입출력 시스템은 6G 통신 시스템에서 계속 증가하는 데이터 속도를 지원하는 핵심 기술로 구상된다. 테라헤르츠 초거대 다중입출력 시스템을 최대한 활용하려면 정확한 채널 정보를 획득하는 것이 중요하다. 그러나 안테나 수에 따라 선형으로 확장되는 막대한 파일럿 오버헤드로 인해 테라헤르츠 채널 획득은 쉽지 않다. 본 연구에서는 테라헤르츠 초거대 다중입출력 시스템을 위한 새로운 딥러닝 기반 채널 획득 기술을 제안한다. 트랜스포머를 사용하여 수신된 파일럿 신호와 희소 채널 매개 변수(예: 각도, 거리, 경로 이득) 사이의 복잡한 매핑 기능을 학습함으로써, 제안된 체계는 상대적으로 적은 양의 파일럿 리소스로 빠르지만 정확한 채널 추정을 할 수 있다. 또한 트랜스포머의 주의 메커니즘을 사용하여 기능 추출에서 수신된 파일럿 신호의 상관 구조를 촉진하여 채널 매개 변수 추정 품질을 크게 향상시킬 수 있다.

논문의 네 번째 부분에서, 우리는 광대역 테라헤르츠 시스템을 위한 빔 관리 기

술을 연구한다. 테라헤르츠 통신의 주요 어려움 중 하나는 높은 회절 및 침투 손실과 대기 흡수로 인한 신호 전력의 심각한 감쇠이다. 심각한 경로 손실을 보상하기 위해 초거대 다중입출력 시스템에 의해 실현된 빔 포밍 기술이 널리 사용되었다. 빔 형성 이득은 빔이 신호 전파 경로와 적절하게 정렬되어야만 최대화되므로, 정확한 빔 방향의 획득이 매우 중요하다. 기존 빔 관리 체계의 주요 문제는 훈련 빔의 수에 비례하는 상당한 지연 시간이다. 본 논문에서는 실시간 지연기 기반 위상 시프트를 사용하여 여러 주파수 의존 빔을 동시에 생성하는 테라헤르츠 빔 관리 기법을 제안한다. 인텐시파이어라는 실시간 지연기 기반 신호 전파 네트워크를 사용하여 주파수 의존적 빔포밍 벡터와 원하는 방향 빔포밍 벡터 사이의 간격을 좁힘으로써 빔포밍 이득을 극대화하는 매우 날카로운 훈련 빔을 생성한다.

주요어: 6G, 무선 통신, 테라헤르츠, 채널 추정, 채널 피드백, 빔 관리

학번: 2016-25925

감사의 글

박사 과정을 시작한지 얼마 되지 않은것 같은데 벌써 졸업을 앞두고 있습니다. 많은 분들의 도움으로 짧은 시간동안 학문적으로, 인격적으로 배우고 성장하였습니다. 소중한 인연들에게 짧은 글로나마 감사의 마음을 전하고자 합니다.

우선 박사 학위동안 열성적으로 지도해주신 심병효 교수님께 감사의 말씀을 전합니다. 항상 연구에 전념할 수 있도록 환경을 조성해 주시고 연구에 조언을 마다하지 않으시며, 밤낮 주말을 가리지 않고 지도해 주셔서 좋은 성과를 내고 성장할 수 있었습니다. 학위 논문 심사과정에서 위원장을 맡아주시고 심사해주신 김성철 교수님께 감사드립니다. 아울러 심사위원을 맡아 주시고 조언해주신 이경한 교수님, 한양대학교 최준원 교수님, 인천대학교 이병주 교수님께도 깊은 감사를 드립니다.

대학원 생활 동안 함께한 소중한 연구실 동료에게도 감사드립니다. 신입생 시절 선배로서 많은 조언을 해주신 지형주 선배님, 박선호 선배님께 감사드립니다. 또한, 먼저 졸업했지만 오랜 기간 같이 연구했던 상태형, 원준이형, 준한이형, 규홍이형과 연구실에서 같이 생활했던 쟈오, 진홍이형, 현규형, 지훈, 현수, 용준, 지섭, 선우, 콰, 용석이형, 정재, 안호, 동훈, 의영, 인국, 진우, 석현, 구상에게 고마웠습니다. 더불어 항상 옆에서 응원해준 소중한 친구 재현이형, 영광이형, 대호형에게도 고맙다는 말을 전합니다.

마지막으로 사랑하는 가족에게 깊은 감사를 전합니다. 아들의 선택을 지켜봐 주시고 묵묵히 응원해주신 아버지 김보현, 항상 아픈곳은 없는지 부족한 것은 없는지 걱정하고 채워주신 어머니 천미화, 자신의 일처럼 옆에서 같이 고민해준 동생 김예은에게도 표현할 수 없는 감사와 고마움을 전합니다.

2023년 8월 7일

김 승 년